
European Coordination for Accelerator Research and Development

**PUBLICATION**

# Complex Envelope Control of Pulsed Accelerating Fields in Superconducting Cavities; EuCARD Editorial Series on Accelerator Science and Technology, Vol.07

Czarski, T (Warsaw University of Technology, Poland)

17 August 2012

The research leading to these results has received funding from the European Commission under the FP7 Research Infrastructures project EuCARD, grant agreement no. 227579.

This work is part of EuCARD Work Package **4: AccNet: Accelerator Science Networks**.

The electronic version of this EuCARD Publication is available via the EuCARD web site <http://cern.ch/eucard> or on the CERN Document Server at the following URL : <http://cdsweb.cern.ch/record/1473435

Tomasz Czarski

# COMPLEX ENVELOPE CONTROL OF PULSED ACCELERATING FIELD IN SUPERCONDUCTING CAVITY RESONATORS

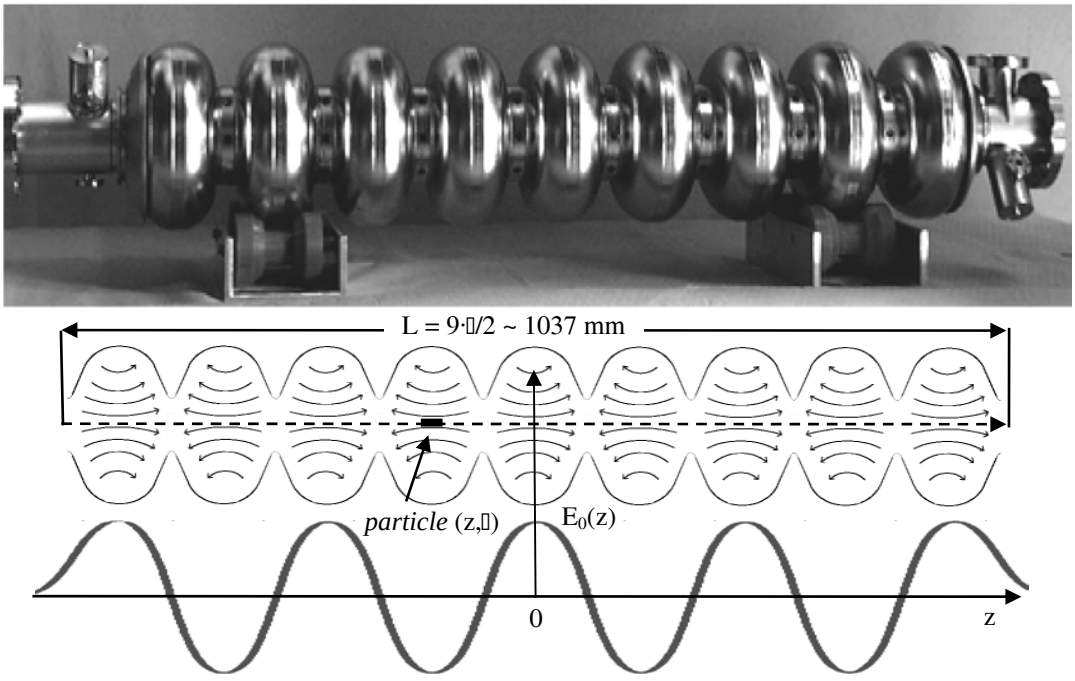


Editorial Series on ACCELERATOR RESEARCH

Institute of Electronic Systems

Publishing House of Warsaw University of Technology

Warszawa 2009

## STRESZCZENIE

Praca przedstawia system sterowania akceleratora linowego w technologii TESLA (TeV–Energy Superconducting Linear Akcelerator). Sterowanie nadprzewodzącej wnęki z wykorzystaniem układów FPGA zrealizowane zostało w ośrodku DESY w Hamburgu. Przeprowadzone testy koncentrowały się na rozpoznaniu obiektu i weryfikacji proponowanych metod sterowania. Elementarna analiza rezonatora wnękowego w oparciu o uproszczony model elektryczny obejmuje rozważania sygnałowe i energetyczne. Identyfikacja parametrów wnęki pozwala osiągnąć wymagane warunki pracy: napełnianie wnęki polem EM w warunkach rezonansu a następnie stabilizację pola z dopuszczalnym poborem mocy. Sterowanie bezpośrednie w układzie otwartym zgodnie z modelem procesu jest skutecznym wspomaganiem metody sprzężenia zwrotnego. Kalibracja i korekcja toru sygnałowego stanowi kluczowy fragment procedury.

Projektowany system sterowania akceleratora ma zapewnić kontrolowane przyśpieszanie cząstek poprzez skuteczną stabilizację pola wnęki. Sekcja sterująca zasilana przez jeden klistron separowany cyrkulatorem może zawierać wiele modułów wnęk rezonansowych sprzężonych z falowodem. Szybka kontrola amplitudy i fazy pola wnęki realizowana jest poprzez modulację sygnału sterującego klistronem. Rezonator pobudzany jest impulsowo przez okres ok. 1.3 ms z częstotliwością 10 Hz, a przeciętne natężenie pola sięga 25 MV/m. Sygnał wyjściowy wnęki przetwarzany jest do częstotliwości pośredniej 250 kHz zachowując informację o amplitudzie i fazie pola. Przetworniki A/C i C/A łączą część analogową i cyfrową systemu z częstotliwością próbkowania 1 MHz. W procesie cyfrowego przetwarzania następuje detekcja obwiedni zespolonej (demodulacja), kalibracja i filtrowanie sygnału. Układ sprzężenia zwrotnego reguluje sumę wektorową pola przyśpieszającego w przypadku wielu rezonatorów. Cyfrowy kontroler stabilizuje obwiednię zespoloną reprezentowaną przez składową rzeczywistą (I - synfazową) i urojoną (Q - kwadraturową) dekodowanego sygnału zgodnie z zadanym odniesieniem (*set-point*). Ponadto, dodatkowy sygnał bezpośredni (*feed-forward*) w oparciu o model procesu iteracyjnie kompensuje powtarzalne zakłócenia. Układ sterowania na podstawie estymowanych parametrów procesu generuje odpowiednie dane (tablice sterujące) dla układu wykonawczego kontrolera. Przedstawiono wybrane rezultaty testów w typowych warunkach pracy rezonatora.

## ABSTRACT

A digital control system for superconducting cavities of a linear accelerator is presented in this work. FPGA (Field Programmable Gate Arrays) based controller, managed by MATLAB, was developed to investigate a novel firmware implementation. The LLRF - Low Level Radio Frequency system for FLASH project in DESY is introduced. Essential modeling of a cavity resonator with signal and power analysis is considered as a key approach to the control methods. An electrical model is represented by the non-stationary state space equation for the *complex envelope* of the cavity voltage driven by the current generator and the beam loading. The electromechanical model of the superconducting cavity resonator including the Lorentz force detuning has been developed for a simulation purpose. The digital signal processing is proposed for the field vector detection. The field vector sum control is considered for multiple cavities driven by one klystron. An algebraic, complex domain model is proposed for the system analysis. The calibration procedure of a signal path is considered for a multi-channel control. Identification of the system parameters is carried out by the *least squares* method application. The FPGA based controller executes a procedure according to the following prearranged control tables: Feed-Forward, Set-Point and Gain. The control tables are determined for the required cavity performance, according to the recognized process. Nonlinearities and deterministic disturbances are compensated by the feed-forward table for the open loop operation. The closed loop correction for the feed-back mode is performed by the complex gain of the corrector table. The adaptive control algorithm is applied for the feed-forward and feedback modes according to the recognized process. The presented method is useful for the repetitive, deterministic condition. It has been verified experimentally in the case of a pulsed mode of an accelerator operation. Experimental results, based on the field measurement, are presented for a cavity representative operation. The results of the project accomplishment can be presented and used physically by driving the real cavity module according to the given control algorithm.

**CONTENTS**

# 1. INTRODUCTION

## 1.1 Origin and subject of the thesis

The Institute of Electronic Systems of Warsaw University of Technology has been involved in the accelerator technology program of CARE – Coordinated Accelerator Research in Europe within the 6th European Framework Program [1]. Consequently, a dedicated laboratory in the area of electronics systems for accelerators - ELHEP - Electronics for High Energy Physics has been established. The work of ELHEP laboratory is closely associated with the international research on superconducting accelerator technology coordinated by DESY – Deutsches Elektronen-Synchrotron in Hamburg. The team of the laboratory has been participating in the development of the control and measurement system design for the accelerator part of the X-ray free electron laser - XFEL facility in DESY. The activity of the laboratory group embraces applied research, design, construction and tests of hardware and software for the Low Level Radio Frequency – LLRF system of a superconducting linear accelerator. Significant contribution to the LLRF control system has been done by the ELHEP group especially in the area of dedicated hardware and software. Novel firmware implementation has been developed to improve the control methods for the LLRF system. Digital control of the superconductive cavity resonator has been performed by applying FPGA technology system involving VHDL programming. A controller and cavity simulator has been implemented as the SIMCON board to manage the modules of FLASH set up. FLASH, stands for "F"reie-Elektronen-"LAS"er in "H"amburg, is a user facility providing laser-like radiation in the VUV and soft X-ray range to various user experiments in many scientific fields. It is also a pilot facility for the future European XFEL machine. A control algorithm based on system identification has been experimentally introduced in a dedicated laboratory setup named CHECHIA and in the first module ACC1 of FLASH. Moreover, the cavity resonator module at FERMILAB in the USA and Module Test Stand (MTS) setup at DESY has been experimentally controlled remotely from the ELHEP laboratory in Warsaw.

Regulation of the bunched electron beam (stream of accelerated particles) by the control of a cavity resonator electromagnetic field is the main issue of the LLRF work package. The digital control system for a resonator of a linear accelerator is considered in this work. Since the software support and hardware implementation coordinated with the total system is required, the work is strongly dependent on the efforts of many others involved in the project. The presented work deals with a part of that large common effort and is

synchronized with the XFEL facility in DESY. **A precise control of pulsed accelerating microwave fields in superconducting cavities is the subject of this thesis.**

## 1.2 Objective and thesis of the work

Hardware and software improvement of the LLRF system goes with the algorithm development which is essential for the control optimization. The current technology for digital signal processing is based on programmable, reconfigurable circuits: FPGA, DSP and embedded general purpose processor like PowerPC, respectively to the function and requirements of executed procedures. Novel firmware allows implementation of sophisticated algorithms to improve the beam regulation by the cavity field control. Several proposed solutions, applying FPGA based controller, are still under development. This work is a continuation of previous and parallel efforts for the cavity control system development. It presents the investigation of the cavity control by the system analyzing, modeling, simulations, process identification, digital signal processing, stochastic estimations, testing and verification.

A very low energy spread is required during the acceleration process to obtain extremely small particles' interaction point and high beam luminosity. A complex control system for the relativistic beam has been developed to cope with signals disturbances, non-linearity and with time-varying parameters, in order to stabilize the accelerating fields of resonators. **The objective of the work is the control algorithm improvement for pulsed accelerating fields in superconducting cavities.** The control algorithm based on the non-linear system identification is the authors proposal verified by the preliminary experimental results. The thesis of the work can be formulated as follows:

**Application of the results of the LLRF system analysis based on the complex envelope signal representation and the plant model in time domain for the repetitive no stationary process recognized by system identification leads to the efficient field control of the cavity resonator.**

This thesis is realized in this work by performing of the following particular tasks:

- cavity resonator modeling
- cavity simulator design based on electromechanical model

- multi-cavity system modeling
- identification of particular components
- control algorithms based on the system identification
- digital controller design.

The result of this work, based on the above thesis, is a considerable improvement to the existing methods of accelerator control.

## 1.3 Linear accelerator outline

The biggest world projects of linear accelerators (linacs): the International Linear Collider (ILC) and the European X-ray Free Electron Laser (XFEL) share the basic design of the accelerating cavity, based on the TESLA technology [2, 3]. TESLA stands for TeV–Energy Superconducting Linear Accelerator – the residual name of the previous primary project of the electron-positron collider [4]. It is planned to reach a target collision energy of TeV for the ILC experiment. The particles and interactions described by the current Standard Model of particle physics, and beyond this model, are expected to be discovered and precisely measured, by the ILC, in conjunction with LHC – Large Hadron Collider experiment.

FELs use a relativistic electron beam as the lasing medium, through the process of Self-Amplified Spontaneous Emission (SASE) [5]. Free electron lasers can achieve very high peak power. Their tunability makes them highly desirable in several disciplines, including medical diagnosis, non-destructive testing and military applications. Currently, the Free electron LASer in Hamburg (FLASH) has already demonstrated SASE principle to soft X-ray generation [6]. The FLASH set up is also used as a test facility for the ILC and the XFEL under the name TESLA Test Facility-Phase 2 (TTF2).

A particle accelerator consists of a particle source, accelerating structures and focusing system. A brief scheme of the FLASH facility is showed in Fig.1.3-1.

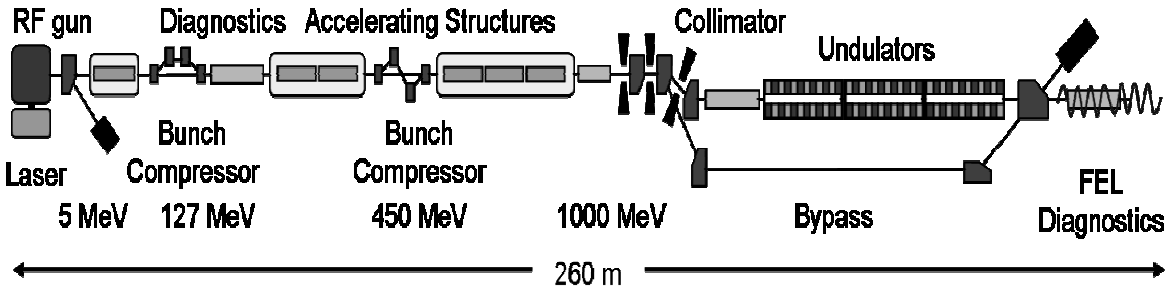


Fig. 1.3-1. The scheme of FLASH facility

The electron bunches are produced in a laser-driven photo-injector and accelerated by a superconducting linear accelerator. The photoelectric RF gun generates up to 800 electron bunches per train, with the energy of 5 MeV. The heart of the accelerator complex is the L-band (1.3 GHz) electron linac operating at an accelerating gradient of ~20 MV/m. The accelerating modules, each containing eight superconducting cavities, accelerate the beam to a total energy of 1000 MeV. At intermediate energies of 127 and 450 MeV, the 1 nC electron bunches are longitudinally compressed, thereby increasing the peak current from initially 50 - 80 A to approximately 1-2 kA as required for the FEL operation. The initial bunch length is ~5.7 ps. Two bunch compressors reduce the length of part of each bunch to ~50 fs. In the 30 m arrangement of magnets (undulator), the accelerated electrons — traveling at close to the speed of light — are induced to produce flashes of intense VUV light with a wavelength between 32 and 13 nm, based on SASE process. The FEL radiation propagates to the user experimental hall, while the electrons are deflected to a dump. The bypass line is used during commissioning and accelerator studies in order to protect the undulators.

## 1.4 Low Level RF system introduction

An actual linear accelerator (linac) is composed of RF stations supplying high power at 1.3 GHz for the superconducting cavities contained by the contiguous cryo-modules. One control section may consist of many independent accelerating cavities (up to 32) driven by a common klystron in a pulsed mode. The 10 MW klystron supplies the RF power to the cavities through the coupled wave-guide with a circulator. The Low Level RF system (fig.

1.4-1) is essential for producing a high-quality particle beam. Its fundamental purpose is field regulation in RF cavities; it also serves as the primary interface between the operation team and the RF system as a whole [7-10].

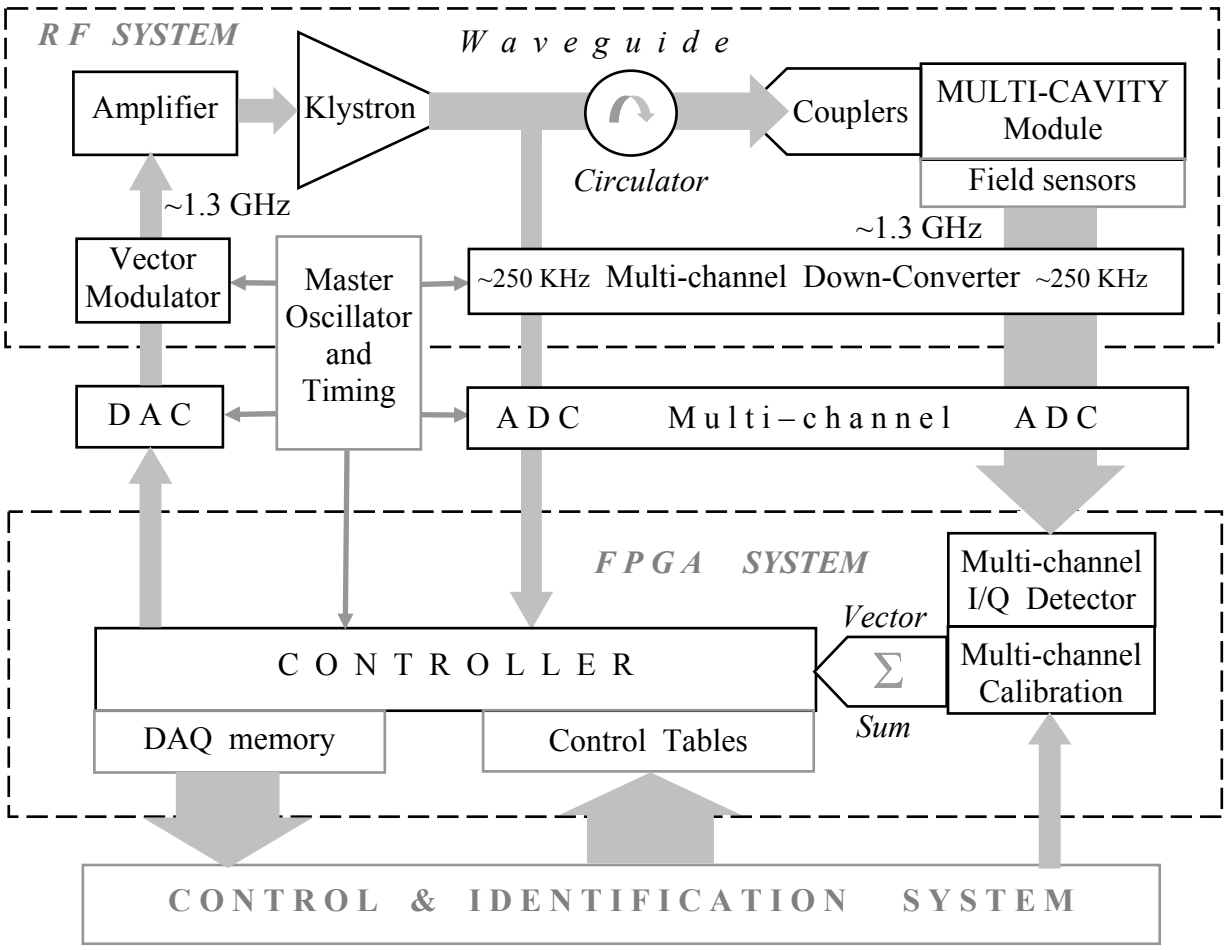


Fig 1.4-1. Functional block diagram of LLRF control structure

Fast amplitude and phase control of the cavity field is accomplished by modulation of a signal driving the klystron through a *vector modulator*. The cavities are driven with 1.3 ms pulses with frequency of 10 Hz. Average accelerating gradient is up to 20 MV/m. A typical single pulse structure of cavity field amplitude with three time stages: *filling* (0.5 ms), *flattop* (0.8 ms) and *decay* is presented in figure 1.4-2. The cavity RF signal is *down-converted* to intermediate frequency of 250 KHz, while preserving the amplitude and phase information. ADC and DAC converters link the analog and digital parts of the system with a sampling interval of 1 μs. Digital signal processing is executed in the FPGA system to obtain field vector detection, calibration and filtering. Control feedback system regulates the vector sum

of the pulsed accelerating fields in multiple cavities. The FPGA based controller stabilizes the detected real and imaginary components of the incident wave according to given control tables. Internal memory module of data acquisition (DAQ) gathers selected data during the pulse for the analysis purpose between pulses. The klystron output signal is also considered for the system analysis. A control block employs the values of the process parameters, estimated in the identification system, and generates the required data for the controller. A system model was developed for investigating the efficient control methods of achieving the required cavity performance: driving in the resonance during *filling* and the field stabilization for *flattop* range. The control system was experimentally introduced in the first cryo-module with 8 cavities – ACC1 of FLASH laser in DESY.

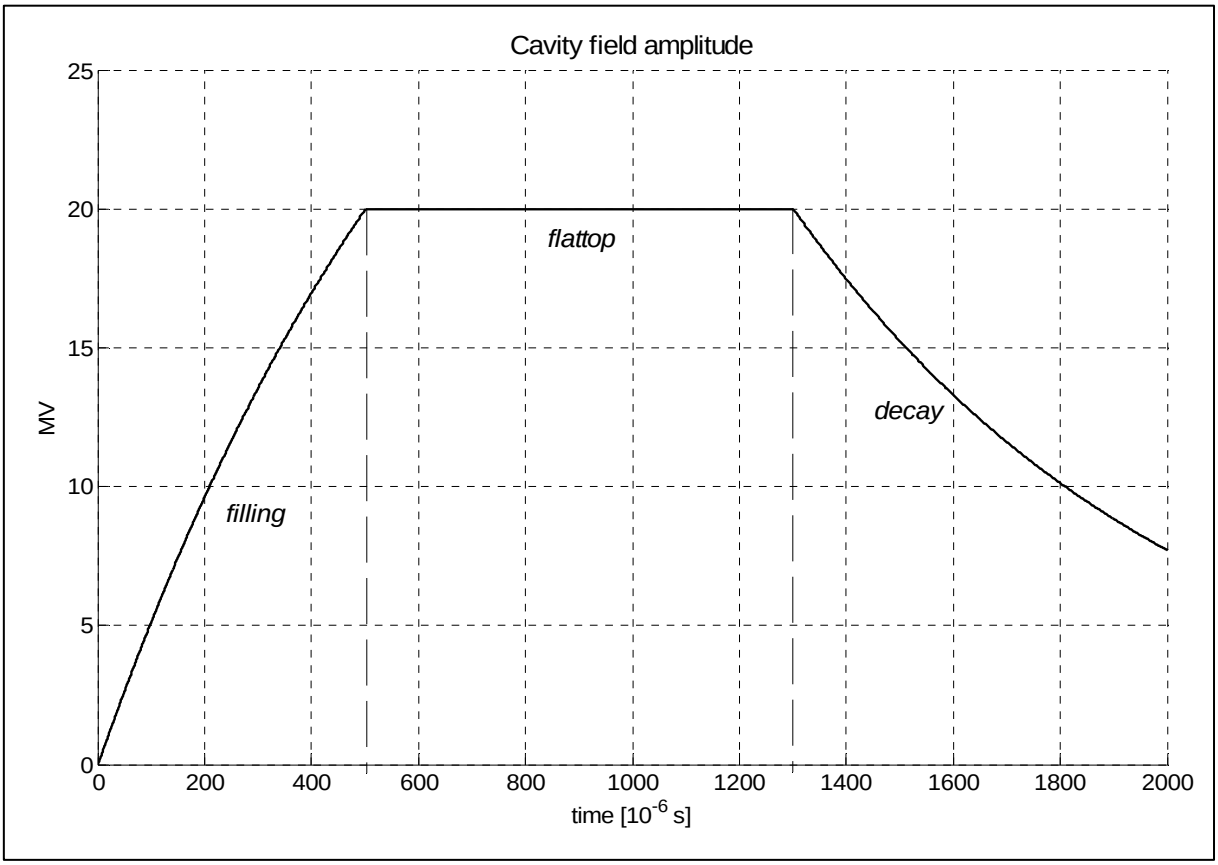


Fig 1.4-2. A single pulse structure of cavity field amplitude with three time stages: *filling*, *flattop* and *decay*.

# 2. CAVITY RESONATOR MODELING

## 2.1. Basic physical features of TESLA cavity

A microwave resonant cavity based on the superconducting technology is presently used to accelerate, light enough, charged particles (electrons and positrons) close to the speed of light. TESLA technology bases on nine-cell super conducting niobium resonators. (figure 2.1-1) [2-4, 11, 13]. The vacuum resonator works in helium liquid at 2 K. A multi-cell structure is applied to maximize the active acceleration space. It is limited by the field homogeneity requirements and parasitic pass-band modes. The nine-cell coupled resonators can oscillate in 9 modes for each resonance field pattern. Each mode is an eigenvector of a single (uncoupled) cell. The 9 modes, which differ in frequency and cell-to-cell phase advance, form the pass-band. The $TM_{010}$ like resonance pattern is utilized for particle acceleration in the TESLA structure. The acceleration structure is operated in a standing $\pi$-mode wave at the frequency of 1,3 GHz with the bandwidth of about 430 Hz.

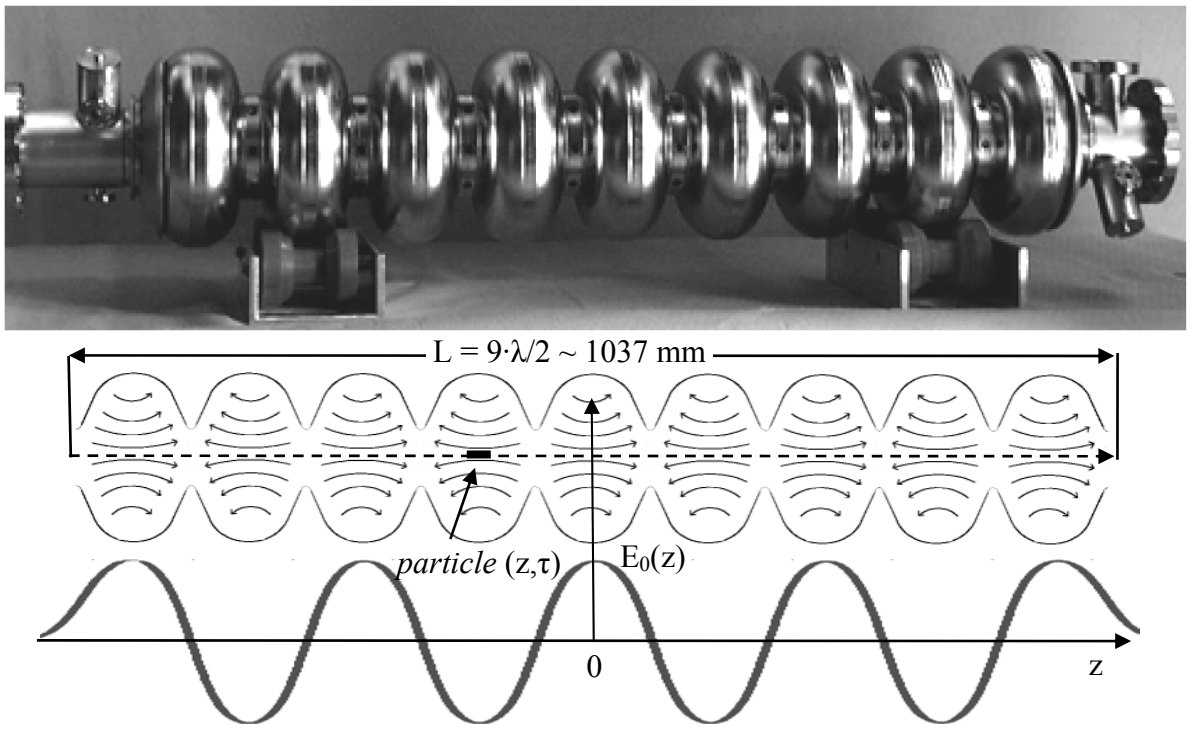


Fig. 2.1-1. The superconducting 9-cell TESLA structure: the photograph and simplified cross-section with electric field distribution and accelerating gradient along the cavity axis.

The RF oscillating field is synchronized with the motion of a particle moving close to light velocity c across the cavity. The axial length of each cell is equal to half of the free space wavelength $\lambda$ of the fundamental (accelerating) resonant mode. At the operating TESLA frequency $f_g$ = 1.3 GHz the cell length is $\lambda/2$ = 115.3 mm.

The cavity voltage is defined by the energy gain of the unity charge passing the accelerating field along the resonator axis (figure.2.1-1). The accelerating field on a cavity axis z at time $\tau$ is described as follows:

$$E(z, \tau) = E_0(z)\cdot\cos(\omega_g\tau), \quad \text{for } \omega_g = 2\pi f_g. \tag{2.1-1}$$

Let us consider a hypothetical relativistic, point-like particle, as a reference unit, determined by the coordinates $(z, \tau)$, crossing the center of a cavity ($z = 0$) in time $\tau = t$. Consequently, the position $z = c\cdot(\tau - t)$ determines the time $\tau = z/c + t$, and the field, accelerating the particle, is as follows:

$$E(z, z/c + t) = E_0(z)\cdot\cos(kz + \omega_g t), \quad \text{for } k = 2\pi/\lambda. \tag{2.1-2}$$

The resultant accelerating cavity voltage v(t), related to the moving particle, is calculated for a given time t as follows:

$$v(t) = \int_{-L/2}^{L/2} E_0(z)\cos(kz + \omega_g t)dz, \quad \text{for the cavity length } L = 9\cdot\lambda/2. \tag{2.1-3}$$

For a symmetric field distribution, $E_0(z) = E_0(-z)$, the equation 2.1-3 is simplified:

$$v(t) = \cos(\omega_g t)\cdot\int_{-L/2}^{L/2} E_0(z)\cos(kz)dz = v_m\cdot\cos(\omega_g t), \tag{2.1-4}$$

where $v_m = \int_{-L/2}^{L/2} E_0(z)\cos(kz)dz$ is the maximum accelerating cavity voltage for $t = 0$. Assuming approximation for the field distribution on a cavity axis $E_0(z) = 2E_{acc}\cdot\cos(kz)$, results in a cavity voltage amplitude $v_m = E_{acc}\cdot L$, where $E_{acc}$ is called accelerating cavity field gradient.

The actual electron beam current has, typically, a bunch charge $q = -8$ nC with ~2 ps Gaussian dispersion, $f_b = 1$ MHz rate and an average value of $i_{B0} = q\cdot f_b = -8$ mA. Due to the very low duty cycle ($\sim 10^{-6}$), the beam current can be modeled in the time domain as a cyclic Dirac pulsed structure (Ш - function), described equivalently by the Fourier series [15]

$$i_B(t) = i_{B0}\sum_{n\in Z}\exp(\boldsymbol{j}\omega_n t) = i_{B0} + 2i_{B0}\cdot\sum_{n\in N}\cos(\omega_n t), \quad \text{for } \omega_n = n\cdot 2\pi f_b. \tag{2.1-5}$$

For a relativistic bunch with charge q and mass *m*, crossing the center of the cavity at the time $t = t_b$, the energy gain equals

$$\Delta E = \Delta mc^2 = q\cdot v(t_b) = q\cdot v_m\cdot\cos\varphi_b, \tag{2.1-6}$$

where *injection* phase $\varphi_b = \omega_g t_b$ is called beam phase related to the cavity voltage.

The expended electric power for beam acceleration is as follows:

$$P_b = \Delta E\cdot f_b = i_{B0}\cdot v_m\cdot\cos\varphi_b. \tag{2.1-7}$$

At the operating condition: $v_m = 25$ MV ($E_{acc} \approx 25$ MV/m), $\varphi_b = 0$ (*injection on crest*), the required power is $P = 200$ kW for beam acceleration in one cavity. Stability of accelerating power is essential for the preservation of the beam quality.

Taking into account equations 2.1-4 and 2.1-7, and relating to the equivalent electrical circuit model with harmonic signals of frequency $\omega_g$, the substituted beam loading current is

$$i_{Bg}(t) = 2i_b(t) \qquad \text{for} \qquad i_b(t) = i_{B0}\cdot\cos(\omega_g t + \varphi_b). \tag{2.1-8}$$

Therefore, only the RF Fourier component for $f_g = 1.3$ GHz of the series 2.1-5 takes away effective power and is considered in the model of a beam loading current. The other components of the series are orthogonal to the cavity voltage 2.1-4 (for π mode), but can excite the higher order modes (HOM) of a cavity [11].

## 2.2 Electrical circuit model

The cavity resonator feature is dominant in the RF structure of the control loop and its dynamics determines behavior of the system (refer to figure 1.4-1). This chapter is devoted to the modeling of a cavity for the control purpose.

The equivalent representation of the chain of nine cells are resonant RLC circuits, which are magnetically coupled [11-13]. The following considerations are limited to the π-mode of one cavity represented as a single lumped parallel RLC circuit. This simplified approach has been assumed for the purpose of the cavity control modeling. The primary parameters: R-resistance, L-inductance, C-capacitance, of the cavity model correspond to the secondary parameters of a resonant circuit, as follows:

resonance angular frequency $\equiv \omega_0 = 2\pi f_0 = 1/\sqrt{LC}$,

characteristic resistance (*shunt* impedance) $\equiv \rho = \sqrt{L/C}$ ,

quality factor $\equiv Q_0 = R/\rho$.

The resonance frequency $f_0$ and characteristic resistance $\rho$ is the invariant feature of the stationary circuit and are considered as the basic parameters with well-defined nominal values: $f_0 = 1.3$ GHz, $\rho = 520\ \Omega$ for TESLA cavity. The super-conducting resonator has an extremely high quality factor (unloaded) $Q_0 \sim 10^{10}$, so an intrinsic resistance is $R \sim 5 \cdot 10^{12}\ \Omega$.

The circuit linear model of the cavity coupled to a waveguide driven by a klystron is presented in figure 3.2-1. The time domain signals $i(t)$ and $v(t)$, for current and voltage, respectively, are represented in *Laplace space*, as follows:

$$i(t) \leftrightarrow I(\mathbf{s}) \text{ and } v(t) \leftrightarrow V(\mathbf{s}), \quad \text{or simply,} \quad i \leftrightarrow I \text{ and } v \leftrightarrow V.$$

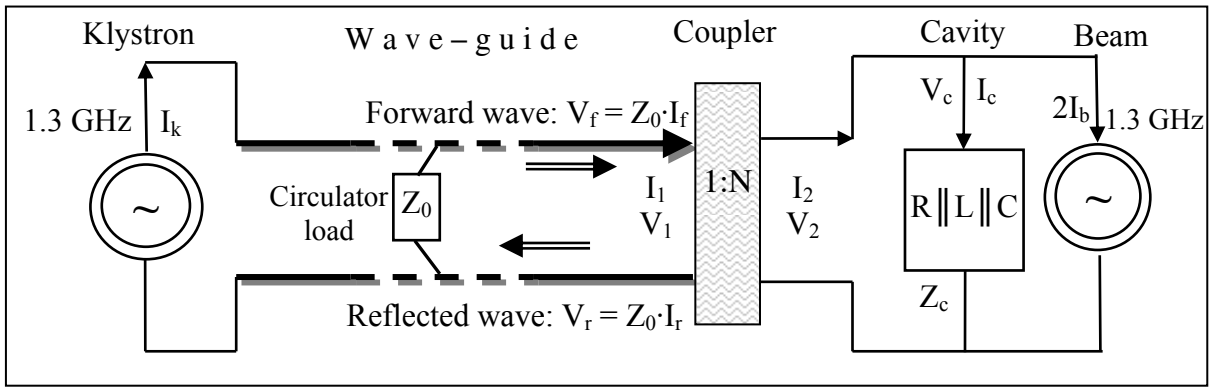


Fig. 2.2-1. Electrical circuit model (*Laplace space*) of cavity environment.

The klystron as a power amplifier is modeled by the RF current generator $i_k \leftrightarrow I_k$ driving the waveguide via a circulator. The RF generator delivers an AC current with harmonic time dependence and frequency $f_g = 1.3$ GHz. The waveguide, as a transmission line, is parameterized by characteristic impedance $Z_0$ and time delay $T_w$. The cavity is represented as a resonant parallel RLC circuit, coupled to the waveguide, with impedance

$$Z_c = \frac{1}{\frac{1}{R} + \frac{1}{\mathbf{s}L} + \mathbf{s}C}. \qquad (2.2\text{-}1)$$

According to the electric coupling between a cavity and a beam, described in terms of the power by equation 2.1-7, the beam loading is modeled as a current sink source $2i_b \leftrightarrow 2I_b$, determined by equation 2.1-8 and fed by the electromagnetic field of the cavity.

The *forward wave* of the wave-guide is represented by current $i_f \leftrightarrow I_f$ and voltage $v_f \leftrightarrow V_f = Z_0 \cdot I_f$. The *reflected wave*, represented by current $i_r \leftrightarrow I_r$ and voltage $v_r \leftrightarrow V_r = Z_0 \cdot I_r$, is isolated by circulator and absorbed by the load $Z_0$ matched to the wave-guide, so there is no feedback signal to the klystron output. Consequently, the forward current equals to the klystron current $(I_f = I_k)$. Superposition of the forward and reflected wave, represented by current $i_1 \leftrightarrow I_1 = I_f - I_r$ and voltage $v_1 \leftrightarrow V_1 = V_f + V_r = (2I_k - I_1) \cdot Z_0$ drives the coupler, which converts the signal according to transformation ratio 1:N. The output signal of the coupler is represented by current $i_2 \leftrightarrow I_2 = I_1/N$ and voltage $v_2 \leftrightarrow V_2 = NV_1 = N(2I_k - I_1) \cdot Z_0 = (2I_k/N - I_2) \cdot N^2 Z_0 = V_c$.

Defining the transformed generator current $i_g \leftrightarrow I_g \equiv I_k/N$, and introducing the transformed impedance $Z_{ext} = N^2 Z_0$ results in the substituted, reduced circuit presented in figure 2.2-2, according to equation $V_c = (2I_g - I_2) \cdot Z_{ext}$.

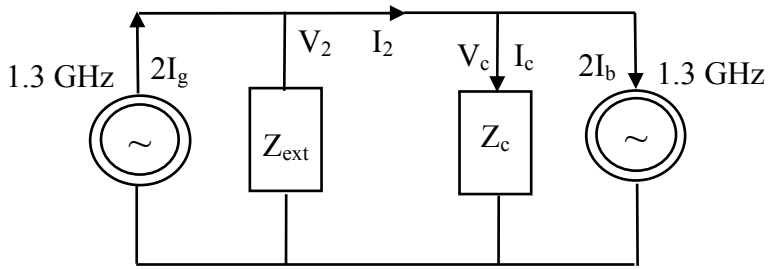


Fig. 2.2-2. Equivalent electrical circuit model of cavity setup

Superposition of the output current of the coupler $I_2$ and beam loading $-2I_b$ results in the cavity current $i_c \leftrightarrow I_c = I_2 - 2I_b$ and the cavity voltage $v_c \leftrightarrow V_c = Z_c \cdot I_c$. Introducing the cavity loaded impedance $Z_L = Z_{ext} \parallel Z_c$, as a parallel connection of the external loading and intrinsic impedance, results in the final model of the cavity setup presented in figure 2.2-3, where

$$i \leftrightarrow I = I_g - I_b \qquad \text{and} \qquad v \leftrightarrow V = V_c = (2I_g - 2I_b) \cdot Z_L = 2I \cdot Z_L \qquad (2.2\text{-}2)$$

is the resultant current and voltage, respectively.

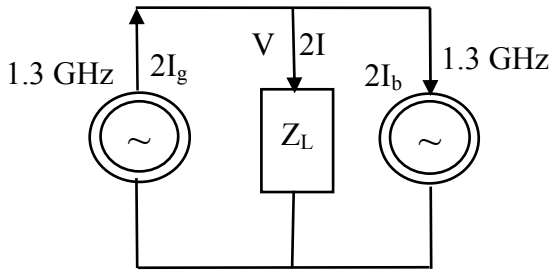


Fig. 2.2-3. Final model of cavity setup

Diverse operational conditions influence the loading of the resonator and determine mutually corresponding parameters with typical values for TESLA cavity:

- shunt resistance $R_L \equiv Z_{ext} \,\|\, R$ $\sim 1.5\cdot 10^9\ \Omega$.

- loaded quality factor $Q_L = \dfrac{R_L}{\rho}$ $\sim 3\cdot 10^6$

- coupling factor $\beta = \dfrac{R}{Z_{ext}} = \dfrac{Q_0}{Q_L} - 1$ $\sim 10^3 \div 10^4$

- half-bandwidth $\omega_{1/2} = 2\pi f_{1/2} = \dfrac{1}{2R_L C} = \dfrac{\omega_0}{2Q_L}$ $\sim 2\pi \cdot 217$ Hz

The useful approximation for the external loading is as follows:

$$Z_{ext} = N^2 Z_0 = (1+1/\beta)R_L \approx R_L, \quad \text{for } \beta >> 1.$$

Consequently, the useful representation for forward and reflected voltage is, respectively:

$$V_g = NV_f = R_L \cdot I_g, \qquad NV_r = V - R_L \cdot I_g. \tag{2.2-3}$$

Finally, the resultant cavity loaded impedance can be represented by the transfer function, in the corresponding forms:

$$Z_L(\mathbf{s}) = \frac{1}{\dfrac{1}{R_L} + \dfrac{1}{\mathbf{s}L} + \mathbf{s}C} = \frac{\omega_0 \rho}{2\omega_{1/2} + \dfrac{\mathbf{s}^2 + \omega_0^2}{\mathbf{s}}}. \tag{2.2-4}$$

## 2.3. RF signal modelling

Amplitude and phase control of the cavity field is accomplished by modulation of a RF signal driving the klystron through a *vector modulator* (refer to figure 1.2-1). The general idea of signal conversion for the cavity control system is presented in figure 2.3-1.

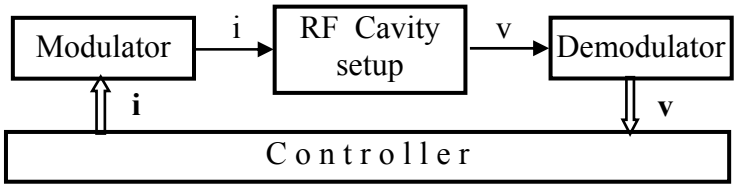


Fig. 2.3-1. The scheme of signal conversion for the cavity control system

The essential signal modeling for the superconducting cavity resonator with its narrowband assumes a relatively slow modulation of the RF carrier with a constant frequency $f_g$ =1.3GHz. Therefore, the RF signal can be modeled in the *time domain* as a *generalized oscillation* [14], according to the expression, for the cavity voltage case:

$$v(t) = v_m(t) \cdot \cos \Phi(t) \quad \text{for} \quad \Phi(t) = \omega_g t + \varphi(t), \tag{2.3-1}$$

where the amplitude $v_m(t)$ and the phase $\varphi(t)$ are slowly time-varying, relatively to the RF signal carrier with the angular frequency $\omega_g = 2\pi f_g$. The unique representation (2.3-1) can be established jointly with its *Hilbert transform* $\hat{v}(t)$ modeled by the $\pi/2$ shifted signal

$$\hat{v}(t) = v_m(t) \cdot \sin \Phi(t) \quad \text{for} \quad \Phi(t) = \omega_g t + \varphi(t) \tag{2.3-2}$$

The ordered pair of the complementary signals, as the real (2.3-1) and the imaginary (2.3-2) part, creates the *analytic signal* $\breve{\mathbf{v}}(t) \equiv v(t) + \boldsymbol{j}\hat{v}(t)$ in the *complex domain* [14, 15]. The representation in polar coordinates definitely determines the amplitude $v_m(t)$ and the phase $\varphi(t)$ for a given frequency $\omega_g$, as follows:

$$\breve{\mathbf{v}}(t) \equiv v(t) + \boldsymbol{j}\hat{v}(t) = v_m(t) \cdot e^{j\Phi(t)}. \tag{2.3-3}$$

The low-pass frequency representation of the RF signal in the *time domain*, called a *complex envelope* [14, 15], is introduced for the control purpose. It is derived by a complex demodulation of the *analytic signal* (down conversion to the *base-band*) for a given frequency $\omega_g$, according to the expression, for the voltage case:

$$\mathbf{v}(t) \equiv \breve{\mathbf{v}}(t) \cdot \exp(-\boldsymbol{j}\omega_g t) = v_m(t) \cdot e^{j\varphi(t)} = I + \boldsymbol{j}Q \tag{2.3-4}$$

where, in-phase component $I = v_m(t) \cdot \cos\varphi(t)$ and quadrature component $Q = v_m(t) \cdot \sin\varphi(t)$, are the real and imaginary parts of the *complex envelope*, respectively.

*Vice versa*, the complex modulation of the *complex envelope* (up conversion to the *pass-band*) is obtained by applying the operator $\exp(\boldsymbol{j}\omega_g t)$ for a given frequency $\omega_g$.

Analogically, the cavity RF current $i(t) = i_g(t) - i_b(t)$ (refer to equation 2.2-2) is modeled, as an *analytic signal* $\breve{\mathbf{i}}(t) = \breve{\mathbf{i}}_g(t) - \breve{\mathbf{i}}_b(t)$, and *complex envelope* $\mathbf{i}(t) = \mathbf{i}_g(t) - \mathbf{i}_b(t)$, is according to the relation: $\mathbf{i}(t) \equiv \breve{\mathbf{i}}(t) \cdot \exp(-\boldsymbol{j}\omega_g t)$, for a given frequency $\omega_g$.

In the LLRF control system, the *base-band* signals are only available for the actual controller, according to the scheme of figure 2.3-1. Therefore, the *complex envelope* is the primary signal representation for the control purpose. However, the cavity model can be driven with an arbitrary low-pass complex signal by the controller. Thus, the complex *pass-band* signal obtained by the complex modulation is not necessary as an *analytic* one according to the definition 2.3-3 (except for the case of a stable phase). Consequently, the primary definition 2.3-4 is not valid generally for the *complex envelope* detection.

Nevertheless, the notion of the "*complex envelope*" remains in the more general meaning according to the scheme of the signal conversion (refer to figure 2.3-1) modeled by the signal-flow graph in figure 2.3-2. The time domain *complex* signals $\mathbf{i}(t)$ and $\mathbf{v}(t)$, for current and voltage, respectively, are represented in the *Laplace space*, as follows:

$$\mathbf{i}(t) \leftrightarrow \mathbf{I}(\mathbf{s}) \text{ and } \mathbf{v}(t) \leftrightarrow \mathbf{V}(\mathbf{s}).$$

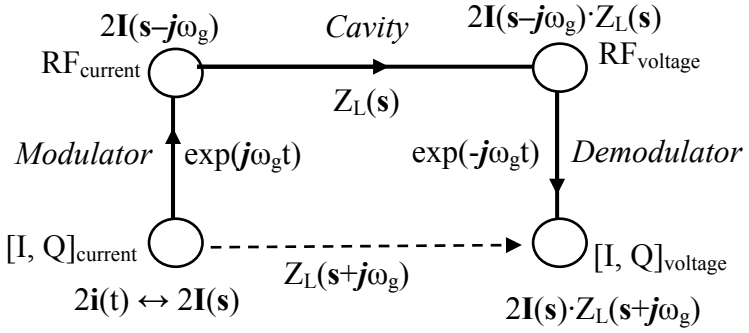


Fig. 2.3-2. Cavity signal-flow for complex signals in time domain and *Laplace* space.

The successive operations: complex modulation, cavity transfer function and complex demodulation, yields the direct relation for the *complex envelope* between the cavity input $2\mathbf{i}(t) \leftrightarrow 2\mathbf{I}(\mathbf{s})$ and the output $\mathbf{v}(t) \leftrightarrow \mathbf{V}(\mathbf{s})$ as follows (refer to equation 2.2-2)

$$\mathbf{V}(\mathbf{s}) = 2\mathbf{I}(\mathbf{s}) \cdot Z_L(\mathbf{s} + \boldsymbol{j}\omega_g) \quad \text{for} \quad \mathbf{I}(\mathbf{s}) = \mathbf{I}_g(\mathbf{s}) - \mathbf{I}_b(\mathbf{s}). \tag{2.3-5}$$

Thus, the low-pass transformation determines the resultant, substituted cavity transfer function $Z_L(\mathbf{s} + \boldsymbol{j}\omega_g)$. The expression for this impedance can be simplified for signals with a narrow spectral range in comparison with the generator frequency, which is close to the cavity resonance frequency. According to equation 2.2-4, successive modifications lead to the effective simplification, under the condition that $|\mathbf{s}| << \omega_g \approx \omega_0$, as follows:

$$Z_L(\mathbf{s} + \boldsymbol{j}\omega_g) = \frac{\omega_0\rho}{2\omega_{1/2} + \dfrac{(\mathbf{s} + \boldsymbol{j}\omega_g)^2 + \omega_0^2}{\mathbf{s} + \boldsymbol{j}\omega_g}} = \frac{\omega_0\rho}{2\omega_{1/2} + \dfrac{\mathbf{s}(\mathbf{s} + 2\boldsymbol{j}\omega_g) + (\omega_0 + \omega_g)(\omega_0 - \omega_g)}{\mathbf{s} + \boldsymbol{j}\omega_g}} \approx$$

$$\approx \frac{\omega_0\rho}{2(\mathbf{s} - \mathbf{A})}, \tag{2.3-6}$$

where $\mathbf{A}_e = -\omega_{1/2} + \boldsymbol{j}\Delta\omega$ is a single complex pole and the cavity *detuning* $\Delta\omega = 2\pi\Delta f \equiv \omega_0 - \omega_g$ is the resonance frequency deviation from the RF carrier. Due to the Lorentz force (refer to chapter 2.5), the cavity detuning $\Delta\omega$ changes during a pulse and the maximum value can be comparable to the cavity half-bandwidth $\omega_{1/2}$ in the real operation condition.

Finally, the expression 2.3-5 for the *complex envelope* is written in *Laplace space* as follows:

$$\mathbf{s} \cdot \mathbf{V}(\mathbf{s}) = \mathbf{A}_e \cdot \mathbf{V}(\mathbf{s}) + \omega_0\rho \cdot \mathbf{I}(\mathbf{s}). \tag{2.3-7}$$

Moving to the *time domain* yields the *state space* equation with $\mathbf{v}(t)$ as a complex state variable of the cavity electrical model:

$$\frac{d}{dt}\mathbf{v}(t) = \mathbf{A}_e \cdot \mathbf{v}(t) + \omega_0\rho \cdot \mathbf{i}(t), \tag{2.3-8}$$

where $\mathbf{A}_e = -\omega_{1/2} + \boldsymbol{j}\Delta\omega$ is the state phasor and $\mathbf{i}(t) = \mathbf{i}_g(t) - \mathbf{i}_b(t)$ is a driving input.

According to the resultant *state space* equation 2.3-8 for the *complex envelope*, the cavity bandwidth and detuning are responsible for the cavity behavior and should be carefully

recognized (refer to chapter 6). The term $\omega_0\rho = 2\,\omega_{1/2}\,R_L = 1/C$ is a relatively stable and well-defined driving factor ($C \approx 0.235$ pF for TESLA cavity).

A general solution of equation 2.3-8 is

$$\mathbf{v}(t) = \mathbf{v}(0)\cdot\exp(\mathbf{A}_e t) + \omega_0\rho\int_0^t \exp\big(\mathbf{A}_e\cdot(t-\tau)\big)\cdot\mathbf{i}(\tau)d\tau\,. \qquad (2.3\text{-}9)$$

The *steady state* (for $t \to \infty$), as a particular solution of the equation 2.3-8, for $\mathbf{i}(t) = \mathbf{i}_0 = \mathbf{i}_g - \mathbf{i}_b$ = const. is given in the corresponding forms:

$$\mathbf{v}(\infty) = \mathbf{v}_c = -\frac{\omega_0\rho}{\mathbf{A}_e}\cdot\mathbf{i}_0 \;=\; \frac{2R_L}{1-\boldsymbol{j}\dfrac{\Delta\omega}{\omega_{1/2}}}\cdot\mathbf{i}_0 \;=\; 2R_L\cos\psi\cdot\exp(\boldsymbol{j}\psi)\cdot\mathbf{i}_0\,, \qquad (2.3\text{-}10)$$

where $\psi = \arctan\dfrac{\Delta\omega}{\omega_{1/2}}$ is called a tuning angle.

The transient solution for a homogeneous case with $\mathbf{i}(t) = 0$, and a certain initial value $\mathbf{v}(0) = \mathbf{v}_0$, is given by

$$\mathbf{v}(t) = \mathbf{v}_0\exp(\mathbf{A}_e t)\,. \qquad (2.3\text{-}11)$$

Finally, the step response as the general solution of the equation 2.3-8, with the initial value $\mathbf{v}(0) = \mathbf{v}_0$, and the final value $\mathbf{v}(\infty) = \mathbf{v}_c$ (refer to equation 2.3-10), for the current input step $\mathbf{i}(t) = \mathbf{i}_0\cdot\mathbf{1}(t)$ is as follows:

$$\mathbf{v}(t) = \mathbf{v}_c + (\mathbf{v}_0 - \mathbf{v}_c)\cdot\exp(\mathbf{A}_e t) \qquad (t \ge 0\,). \qquad (2.3\text{-}12)$$

A useful approximation with the error less than 1% for time $t < 15$ μs is given by

$$\mathbf{v}(t) \;\approx\; (1+\mathbf{A}_e t)\cdot\mathbf{v}_0 + \omega_0\rho\cdot t\cdot\mathbf{i}_0 \qquad \text{for } |\mathbf{A}_e t| << 1. \qquad (2.3\text{-}13)$$

An example of the phasor diagram for the steady state is presented in figure 2.3-3 for the cavity bandwidth $f_{1/2} = 217$ Hz (refer to equation 2.3-10). The step response of the cavity voltage is presented in figure 2.3-4 and 2.3-5 for a driving current of $\mathbf{i}_0 = \mathbf{i}_g = 16$ mA, and selected detuning (refer to equation 2.3-11 for $\mathbf{v}_0 = 0$).

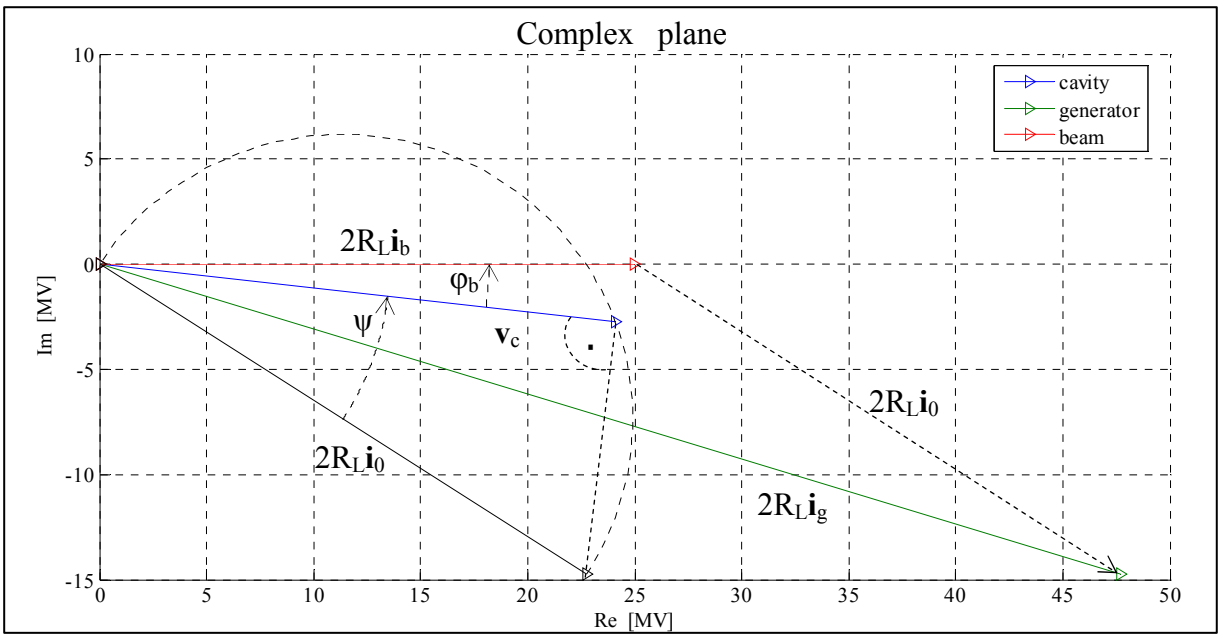


Fig. 2.3-3. The phasor diagram of the steady state solution for a driving current $\mathbf{i}_0 = \mathbf{i}_g - \mathbf{i}_b$ ($\mathbf{i}_g = 16e^{-i0.3}$ mA, $\mathbf{i}_b = 8$ mA, tg $\psi = 0.5$, beam phase $\varphi_b \approx 0.11$ rad.)

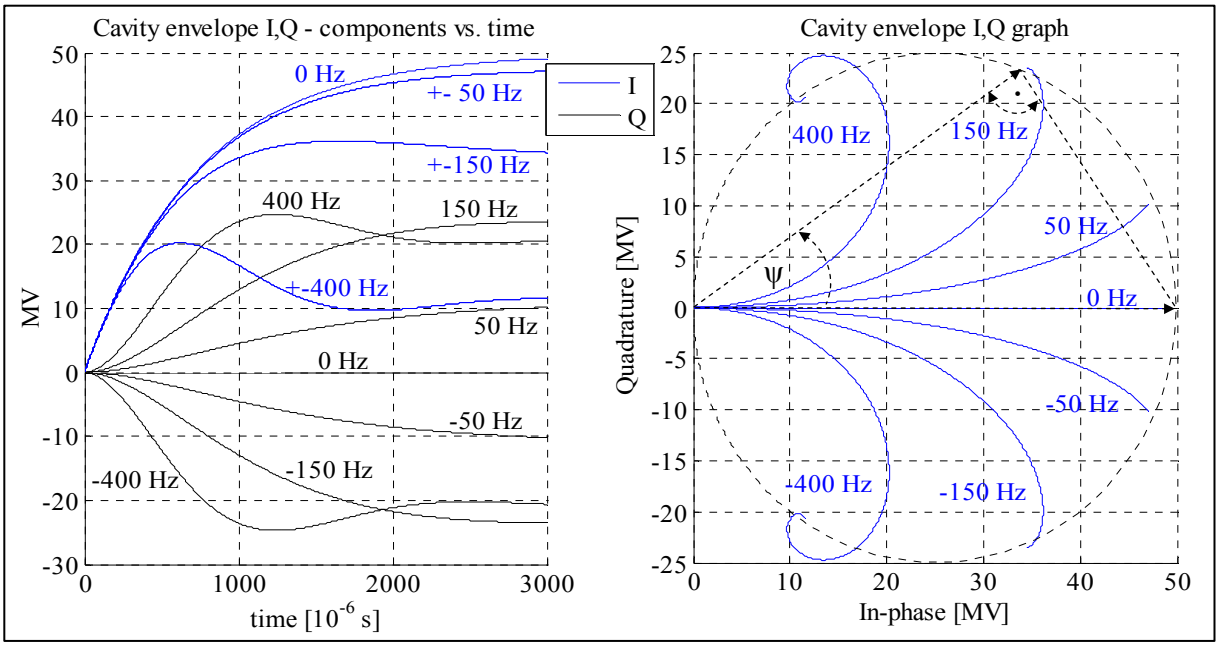


Fig. 2.3-4. Step response of the cavity voltage envelope represented by [I,Q] – components vs time for selected detuning and the corresponding envelope graph – trajectory of the [I, Q] phasor with the circle of the steady state placement; $\psi$ – tuning angle for $\Delta f = 150$ Hz.

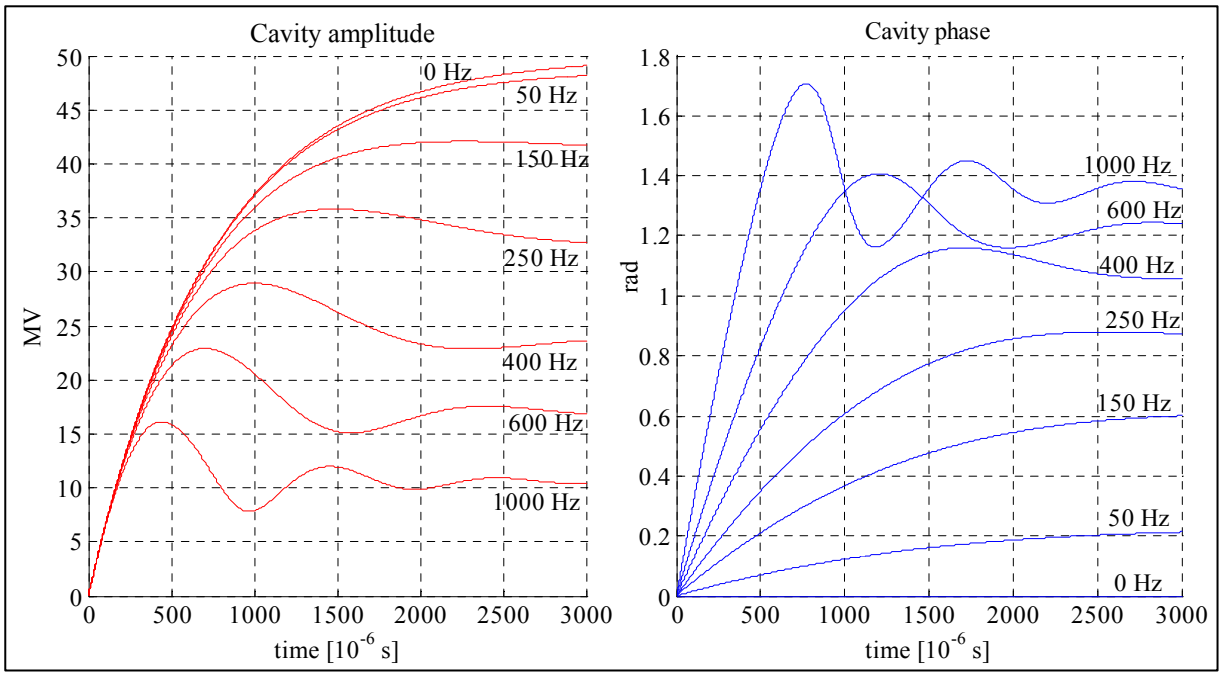


Fig. 2.3-5. Step response of the cavity voltage envelope for driving current of $\mathbf{i}_0$ = 16 mA represented by amplitude and phase for selected detuning.

***Time domain consideration***

Let us consider the second order differential equation with respect to the voltage v(t) for a parallel resonant circuit RLC driven with a current 2i(t) (refer to equation 2.2-4 and 2.2-2):

$$C \cdot v''(t) + \frac{1}{R_L} v'(t) + \frac{1}{L} v(t) = 2i'(t) .$$

The equivalent relation for the *analytic signal* is given by:

$$\breve{\mathbf{v}}'' + 2\omega_{1/2}\breve{\mathbf{v}}' + \omega_0^2\breve{\mathbf{v}} = 2\omega_0\rho\breve{\mathbf{i}}' .$$

Substituting: $\breve{\mathbf{v}}(t) = \mathbf{v}(t)\exp(\boldsymbol{j}\omega_g t)$ and $\breve{\mathbf{i}}(t) = \mathbf{i}(t)\exp(\boldsymbol{j}\omega_g t)$ for $\omega_g \approx \omega_0$ results in, after a few steps of conversion:

$$-\frac{1}{2}\boldsymbol{j}\mathbf{v}'' + (\omega_g - \boldsymbol{j}\omega_{1/2})\mathbf{v}' = \omega_g(-\omega_{1/2} + \boldsymbol{j}\Delta\omega)\mathbf{v} + \omega_0\rho(\omega_g\mathbf{i} - \boldsymbol{j}\cdot\mathbf{i}') .$$

Assuming: $\omega_{1/2} << \omega_g$, $|\mathbf{i}'| << \omega_g|\mathbf{i}|$ and $|\mathbf{v}''| << 2\omega_g|\mathbf{v}'|$, yields approximation 3.3-8. Taking into account the solution 2.3-11 or 2.3-12, provides $\frac{|\mathbf{v}''|}{2\omega_g|\mathbf{v}'|} = \frac{\sqrt{\omega_{1/2}^2 + \Delta\omega^2}}{2\omega_g} < \frac{1}{Q_L} << 1$, what confirms the last assumption.

### 2.4. Cavity power consideration

High energy requirements for a beam acceleration impose the power aspect as a significant one for the RF control system design (refer to equation 2.1-7). The objective of the accelerator system is to supply the power by the klystron to the cavity, and finally to the beam, with the best efficiency. The klystron forward power $P_f$, which is provided by the wave-guide, reflects partly due to the mismatched input coupler and dissipates in the circulator load as the reflected power $P_r$ (figure 2.2-1). The residual transmitted power $P_t$, supplies the cavity and the beam loading.

According to the RF signal modeling (chapter 2.3), the cavity voltage and current are represented by a relatively slow varying *complex envelope* $\mathbf{v}(t)$ and $\mathbf{i}(t)$, respectively. Thus, like for a *phasor* of harmonic signal, the real power specified in terms of complex voltage and complex conjugate current is given by

$$P = \tfrac{1}{2}\, Re\left\{\mathbf{v}\cdot\mathbf{i}^*\right\} = \tfrac{1}{2}\, v\cdot i\cdot\cos\angle\left\{\mathbf{v}\cdot\mathbf{i}^*\right\}. \qquad (2.4\text{-}1)$$

Taking into account the electrical circuit model (refer to chapter 2.2), the power distribution in the cavity setup is determined by the energy conservation law as follows:

$$P_f = P_r + P_t \qquad \text{and} \qquad P_t = P_d + \frac{dW}{dt} + P_b \qquad (2.4\text{-}2)$$

where subsequent components, given with a reasonable approximation for the coupling factor $\beta >> 1$, are determined by the related signals (refer to equations 2.2-3) :

- forward power $P_f = \tfrac{1}{2}\, Re\left\{\mathbf{v}_f\cdot\mathbf{i}_f^*\right\} = \tfrac{1}{2} Z_0 i_f^2 \approx \tfrac{1}{2} R_L i_g^2$

- reflected power $P_r = \tfrac{1}{2}\, Re\left\{\mathbf{v}_r\cdot\mathbf{i}_r^*\right\} = \dfrac{v_r^2}{2Z_0} \approx \dfrac{\left|\mathbf{v} - R_L\mathbf{i}_g\right|^2}{2R_L}$

- transmitted power $P_t = P_f - P_r = Re\left\{\mathbf{v}\cdot\mathbf{i}_g^*\right\} - \dfrac{v^2}{2R_L}$

- cavity dissipated power $P_d = \tfrac{1}{2}\, Re\left\{\mathbf{v}\cdot\mathbf{i}_c^*\right\} = \dfrac{v^2}{2R} \approx 0$

- electromagnetic energy stored in cavity $W = \dfrac{Q_0\cdot P_d}{\omega_0} = \dfrac{v^2}{2\omega_0\rho}$

- beam loading power $P_b = Re\left\{\mathbf{v}\cdot\mathbf{i}_b^*\right\} = v\cdot i_b\cdot\cos\varphi_b$.

The step response of the cavity power: forward, reflected and transmitted is presented in figure 2.4-1 for a constant driving current of $\mathbf{i}_g$ = 16 mA, $\mathbf{i}_b$ = 0, loaded quality factor $Q_L$ = $3 \cdot 10^6$ Hz, and selected detuning values (refer to equation 2.3-12 for $\mathbf{v}_0 = 0$).

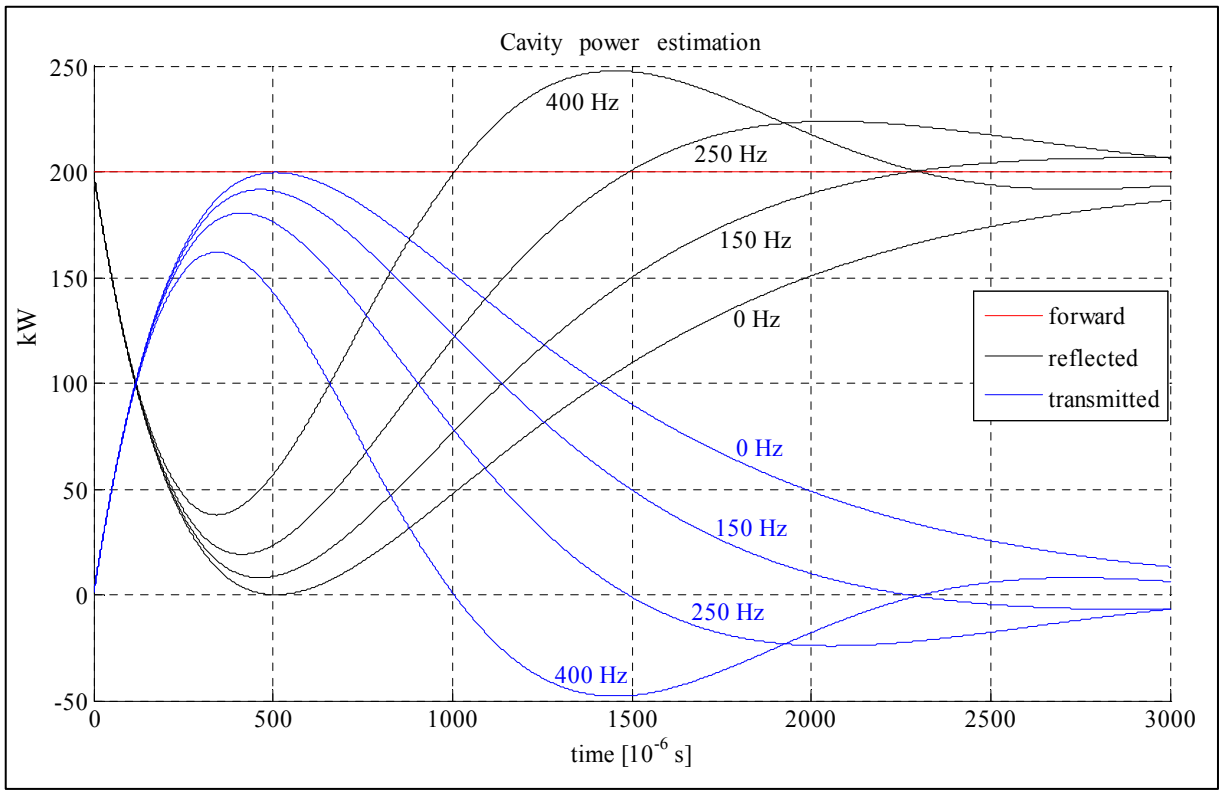


Fig. 2.4-1 Step response of the cavity power: forward, reflected and transmitted for selected detuning values (driving current is $\mathbf{i}_0$ = 16 mA)

The transmitted power fills up the cavity with electromagnetic energy and increases the voltage. The transmitted power rises from zero to the maximum value, contrary to the reflected one. The energy rising range is called *filling* of the cavities driven by pulsed mode, before a beam is injected.

A beam is injected at the end of the *filling* and the cavity field should be stabilized during a, so called, *flattop* range, for acceleration process. The transmitted power feeds the beam loading and an electromagnetic energy stored in the cavity is stable for stationary condition. The required forward power $P_f$ is estimated for a detuned cavity with a given constant voltage $\mathbf{v}_c$ and a beam current $\mathbf{i}_b$. The inverse solution of the *steady state* equation 2.3-10 for a desired RF generator current yields

$$\mathbf{i}_g = \mathbf{i}_b + \frac{\mathbf{v}_c}{2R_L}(1 - \boldsymbol{j}\tan\psi)\,. \qquad (2.4\text{-}3)$$

The requested generator power, for $P_b > 0$, is calculated as follows:

$$P_g = P_f = P_r + P_b = \tfrac{1}{2} R_L i_g^2 = \frac{(1+g)^2 + (\tan\psi - g\cdot\tan\varphi_b)^2}{4g}\cdot P_b, \quad \text{for } g = \frac{2R_L i_b \cos\varphi_b}{v_c}. \quad (2.4\text{-}4)$$

The required forward power as a function of relative detuning $\frac{\Delta\omega}{\omega_{1/2}} = \tan\psi$ is shown in figure 2.4-2, for the voltage absolute value of $v_c = 25$ MV, and for selected beam currents.

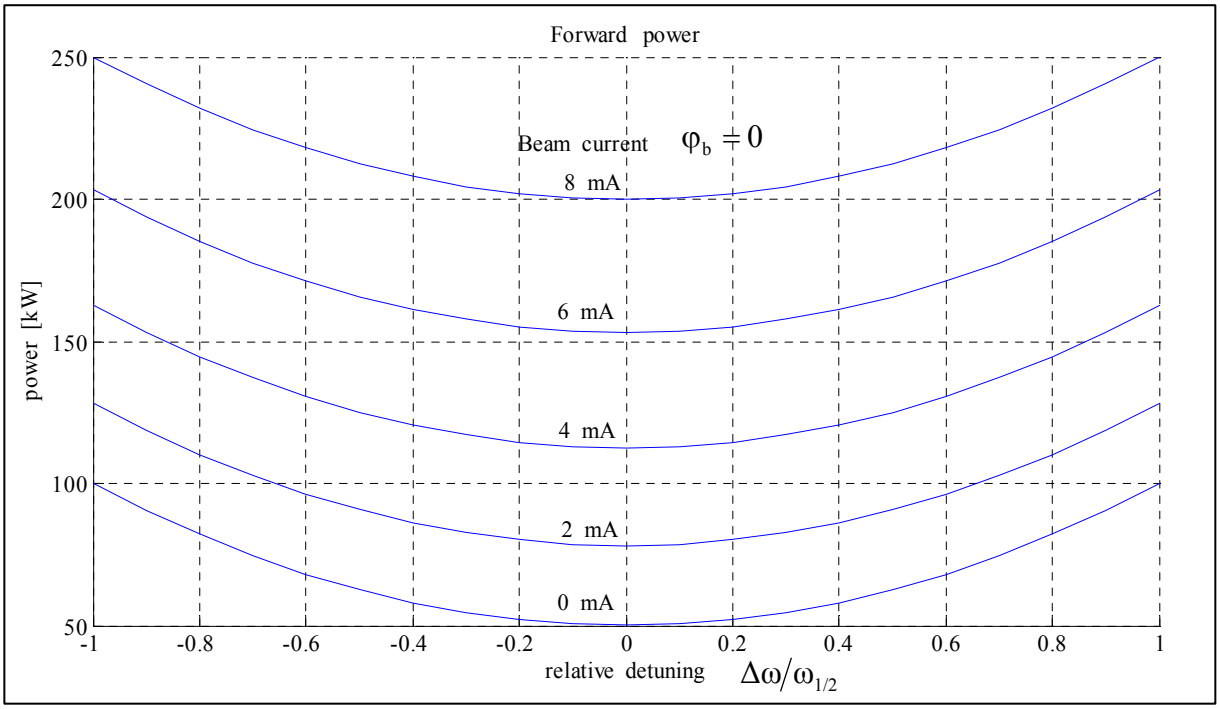


Fig. 2.4-2. Forward power as a function of detuning related to the half-bandwidth $\omega_{1/2} = 2\pi\cdot 217$ Hz for the voltage $v_c = 25$ MV and for different beam currents with $\varphi_b = 0$.

The estimated power can be minimized with respect to the shunt impedance $R_L$ and the tuning angle $\psi$ for a given beam loading power. The value of the optimal forward power equals to the beam loading power, under the following conditions:

$$P_f = P_b = v_c \cdot i_b \cos\varphi_b = 2\omega_{1/2} W \quad \Leftrightarrow \quad P_r = 0 \quad \Leftrightarrow \quad \mathbf{v}_c = R_L \mathbf{i}_g \quad \Leftrightarrow$$

$$\Leftrightarrow \quad \left( \psi = \varphi_b \quad \text{and} \quad g = 1 \quad \Rightarrow \quad R_L = \frac{v_c}{2 i_b \cos\varphi_b} \right). \quad (2.4\text{-}5)$$

In the case of TESLA cavity, for $v_c = 25$ MV, $i_b = 8$ mA, $\psi = \varphi_b = 0$, the beam loading power is $P_b = P_f = 200$ kW, and the optimum loaded $Q_L = R_L/\rho$ is in the order of $3\cdot 10^6$.

## 2.5. Cavity mechanical model

A strong electromagnetic field in an RF cavity (up to 25 MV/m) exerts a pressure on the cavity wall. The pressure P is a function of the surface electric E and magnetic H fields as shown below [13, 16]

$$P = \frac{1}{4}\left(\mu_0 H^2 - \varepsilon_0 E^2\right).$$

The radiation pressure due to the cavity electromagnetic field causes a small deformation of the cavity shape resulting in a decreasing of the cavity resonant frequency, so called Lorentz-force detuning. This effect can be especially detrimental for a pulsed operation, as it causes the cavity frequency change during the RF pulse.

In a steady state, the cavity detuning value $\Delta f$ is proportional to the square of the cavity accelerating field gradient $E_{acc}$, and consequently to the voltage $|\mathbf{v}|^2 = v^2$ [13, 17, 19, 20]:

$$\Delta f = -K \cdot E_{acc}^2 = -K \cdot \left(v/L\right)^2 = -k \cdot v^2 \qquad (2.5\text{-}1)$$

where K is the Lorentz force detuning constant, and $k = K/L^2$ is the substituted Lorentz force detuning constant related to the resultant cavity voltage $v$ for the total cavity length L. In the case of the TESLA cavity, K is in the order of 1 Hz/(MV/m)$^2$.

Any mechanical vibration outside the cryo-module can couple to the cavity exciting its mechanical resonances. Mechanical vibrations of the cavity walls modulate the cavity resonant frequency, which in turn translates in amplitude and phase modulation of the cavity field. This parasitic modulation is frequently called microphonic noise or simply microphonics [13, 18, 21].

The super-conducting resonator has an extremely high loaded quality factor $Q_L \sim 3 \cdot 10^6$ and the narrow bandwidth of about 430 Hz. Hence, the cavity is very sensitive to mechanical distortion caused by microphonics and the Lorentz force, changing the resonator's frequency $\omega_0 = 2\pi f_0 = 1/\sqrt{LC}$. The resonance frequency variation due to microphonics is in the order of 10 Hz. Therefore, the cavity electrical model (refer to equation 2.3-8) is a non-stationary one with the time varying *detuning* $\Delta\omega(t) = \omega_0(t) - \omega_g = 2\pi \cdot \Delta f(t)$, as the deviation from the generator nominal frequency $\omega_g$. This cavity parameter has two dominant deterministic components: the Lorentz force detuning and the initial *predetuning*. The mechanically biased *predetuning* attempts to compensate the EM forced detuning factor during the operational

condition of the cavity. The cavity detuning value can be comparable to the cavity bandwidth in the real operation condition.

The mechanical model of a super-conductive cavity has been proposed for the simulation purpose [13, 17, 19]. The dynamic model bases on the heuristic relationship for the independent mechanical modes of the cavity with the resonance angular frequency $\omega_m = 2\pi f_m$, the quality factor $q_m$ and the Lorentz force detuning constant $k_m$ for the given *m*-th mode. The time varying Lorentz force detuning of the *m*-th mode $\Delta\omega_m(t)$ is described by the second order differential equation driven with the square of the time varying amplitude of the cavity voltage $|\mathbf{v}(t)|^2 = v^2(t)$:

$$\frac{d^2}{dt^2}\Delta\omega_m(t) + \frac{\omega_m}{q_m}\cdot\frac{d}{dt}\Delta\omega_m(t) + \omega_m^2\cdot\Delta\omega_m(t) = -2\pi\cdot\omega_m^2\cdot k_m\cdot v^2(t). \qquad (2.5\text{-}2)$$

For the given *m*-th mode, the time-varying detuning, and its time derivative generate:

the *state vector* $\mathbf{w}_m(t) = \begin{bmatrix} \Delta\omega_m(t) \\ \frac{d}{dt}\Delta\omega_m(t) \end{bmatrix}$

of the *state space* equation $\frac{d}{dt}\mathbf{w}_m(t) = \mathbf{a}_m\cdot\mathbf{w}_m(t) + \mathbf{b}_m\cdot v^2(t)$,

described by the *system matrix* $\mathbf{a}_m = \begin{bmatrix} 0 & 1 \\ -\omega_m^2 & -\frac{\omega_m}{q_m} \end{bmatrix}$,

and the *input matrix* $\mathbf{b}_m = -2\pi\cdot\begin{bmatrix} 0 \\ \omega_m^2 k_m \end{bmatrix}$.

The dynamics of the cavity mechanical model, embracing M-modes, is described by the total *state space* equation

$$\frac{d}{dt}\mathbf{W}_M(t) = \mathbf{A}_M\cdot\mathbf{W}_M(t) + \mathbf{B}_M\cdot v^2(t), \qquad (2.5\text{-}3)$$

determined by the partial components within the matrix ranges: (2m-1:2m) for m = 1÷M, of the columns and rows, respectively, as follows:

partial *state vector* $\mathbf{W}_M^{(2m\text{-}1:2m)}(t) = \mathbf{w}_m(t)$,

partial *system matrix* $\mathbf{A}_M^{(2m\text{-}1:2m,\ 2m\text{-}1:2m)} = \mathbf{a}_m$, (other matrix elements are zero)

partial *input matrix* $\mathbf{B}_{M}^{(2m-1:2m)} = \mathbf{b}_{m}$.

The resulting cavity detuning is given by the superposition of all components:

$$\Delta\omega(t) = \sum_{m=1}^{M} \Delta\omega_{m}(t) + \Delta\omega_{0}, \tag{2.5-4}$$

where $\Delta\omega_0$ is the mechanically externally biased *predetuning*.

The resulting Lorentz force detuning constant k (refer to equation 2.5-1) is given by the superposition of all partial factors: $k = \sum_{m=1}^{M} k_{m}$.

The identification and verification of the proposed mechanical model, with so many degrees of freedom, is still under investigation [17, 19, 21]. However, the complexity and deviation from the real behavior of the plant do not favour to use the model for an efficient control purpose. The reliable estimation of the actual cavity detuning value bases on the identification of the electrical model, described by equation 2.3-8. The cavity detuning can be determined from the slope of the voltage phase during the *decay* range, according to the equation 2.3-11 (refer to chapter 6). The measurements show quasi instantaneous response of the cavity detuning for a fast change of the voltage slope (at the beginning and end of the *flattop* range) what disagrees with the inertial mechanical model. The alternative proposal is the modified model with the additional, dominant, no inertial mechanical *m*-th mode for m = M+1, described by the first order differential equation [13]:

$$\tau_{m} \frac{d}{dt} \Delta\omega_{m}(t) + \Delta\omega_{m}(t) = -2\pi \cdot k_{m} \cdot v^{2}(t), \tag{2.5-5}$$

where $\tau_m$ is the mechanical time constant. The additional, partial terms for the general *state space* model 2.5-3 are as follows: $\mathbf{W}_{M}^{(2M+1)}(t) = \mathbf{w}_{m}(t) = \Delta\omega_{m}(t)$, $\mathbf{A}_{M}^{(2M+1,\,2M+1)} = \mathbf{a}_{m} = -1/\tau_{m}$, $\mathbf{B}_{M}^{(2M+1)} = \mathbf{b}_{m} = -2\pi k_{m}/\tau_{m}$ for m = M+1.

Investigations of the mechanical properties are aimed mainly at an active cavity tuning. [20, 21, 22]. The cavity tuning is essential for the control purpose due to a critical limitation of the klystron power. The cavity should be operated as close to the resonance frequency as possible. The mechanical correction of the cavity features is performed additionally to the signal compensation executed by the main controller. The slow tuner, based on a stepping motor is used for a pre-tuning stage. The motor tuners are periodically adjusted based on information gathered by the LLRF system. The forward power expense depends on the cavity

operation condition: gradient and *pre-detuning* (refer to equation 2.4-4). The uniform power distribution during *flattop* range should be considered for the optimal cavity *predetuning* for the given gradient level. The fast frequency tuner realized as the Piezo Tuner System is dedicated for the Lorentz force compensation during a pulse. The autonomous controller driving the outer amplifier of the piezo-actuators is still under development [20, 21, 22].

### 2.6. Cavity electromechanical model

Coupling together the electrical and mechanical models (refer to equations 2.3-8, 2.5-3, 2.5-4, 2.5-5) creates a composed electromechanical representation of the cavity resonator, presented in fig. 2.6-1.

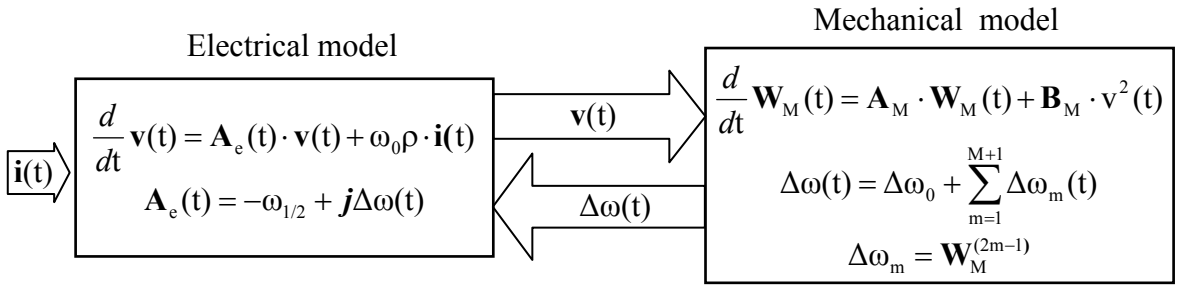


Fig. 2.6-1. The unified scheme of the cavity electromechanical model

The electrical model, characterized by the complex factor $\mathbf{A}_e$, is driven with the *complex envelope* of the current $\mathbf{i}(t)$ and yields the *complex envelope* of the cavity voltage $\mathbf{v}(t)$. The square of the amplitude of the cavity voltage $|\mathbf{v}(t)|^2 = v^2(t)$ drives the M-mode mechanical model, described by the matrices $\mathbf{A}_M$ and $\mathbf{B}_M$. The resultant cavity detuning $\Delta\omega(t)$, as the output of the mechanical model, modulates the factor $\mathbf{A}_e$ of the electrical model.

The discrete version of the cavity model, and its digital implementation, realized as the cavity simulator, are considered in the next chapter.

# 3. CAVITY SIMULATOR DESIGN

## 3.1 Discrete cavity model

***Electrical model***

Discrete processing of the cavity behavior has been developed for a digital implementation of the model [23]. The continuous model of the cavity (refer to equation 2.3-8) can be approximated by an iterative procedure in a finite number of N steps. Discrete samples of the input $\mathbf{i}(nT) = \mathbf{i}_g(nT) - \mathbf{i}_b(nT) = \mathbf{i}_n = \mathbf{i}_{g_n} - \mathbf{i}_{bn}$, assumed as constant values within the sampling interval of T for n = 1÷N, are considered for the discrete implementation of the cavity electrical model. The corresponding discrete samples of the output $\mathbf{v}(nT) = \mathbf{v}_n$, are determined as the step response solution, given by equation 2.3-12 for t = T and translated by the time value of nT. Consequently, the difference equation for successive n-th and (n+1)-th samples is as follows:

$$\mathbf{v}_{n+1} = \mathbf{v}_n \cdot \exp(\mathbf{A}_e T) + \omega_0 \rho \frac{\exp(\mathbf{A}_e T) - 1}{\mathbf{A}_e} \cdot \mathbf{i}_n \tag{3.1-1}$$

Applying the linear approximation: $\exp(\mathbf{A}_e \cdot T) \approx 1 + \mathbf{A}_e T$, for a small enough value of sampling time T ( $|\mathbf{A}_e T| << 1$ ) the discrete form of the *state space* equation 2.3-8 is given by (compare to equation 2.3-13):

$$\mathbf{v}_{n+1} = (1 + \mathbf{A}_e T) \cdot \mathbf{v}_n + \omega_0 \rho T \cdot \mathbf{i}_n \tag{3.1-2}$$

Introducing new symbols for the discrete model representation yields:

$$\mathbf{v}_{n+1} = \mathbf{A} \cdot \mathbf{v}_n + \mathbf{u}_n, \tag{3.1-3}$$

where the cavity *system phasor* is: $\mathbf{A} = 1 + \mathbf{A}_e T = (1 - \omega_{1/2} T) + \boldsymbol{j}\Delta\omega T$,

the unified samples of the input signals are: $\mathbf{u}_n = \omega_0 \rho T \cdot \mathbf{i}_n = \mathbf{u}_{g_n} - \mathbf{u}_{bn}$, where

$\mathbf{u}_{g_n} = \omega_0 \rho T \cdot \mathbf{i}_{g_n}$ for a generator, and $\mathbf{u}_{bn} = \omega_0 \rho T \cdot \mathbf{i}_{bn}$ for a beam loading.

The sampling time T = 1μs has been applied for the LLRF control system of the FLASH setup in DESY. So, $|\mathbf{A}_e T| \approx 1.4 \cdot 10^{-3} << 1$ for $\Delta\omega = 0$ and the stability condition is: $|\mathbf{A}| < 1$ if $\Delta\omega < 2\pi \cdot 8308\ \text{Hz}$.

The step response as the general solution of the equation 3.1-3, for the input step $\mathbf{u}_n = \mathbf{u}_0 \cdot \mathbf{1}(n)$ is as follows:

$$\mathbf{v}_n = \mathbf{v}_0 \cdot \mathbf{A}^n + \mathbf{u}_0 \cdot \frac{1 - \mathbf{A}^n}{1 - \mathbf{A}} \qquad (n \geq 0). \tag{3.1-4}$$

Comparing relatively the discrete solution 3.1-4 and the continuous one 2.3-12 for $\mathbf{v}_0 = 0$ and $t = nT$ yields the sequence that converges to 1:

$$\mathbf{r}_n = \frac{1 - (1 + \mathbf{A}_e T)^n}{1 - \exp(n \cdot \mathbf{A}_e T)} \xrightarrow[n \to \infty]{} 1. \tag{3.1-5}$$

The absolute value of the ratio 3.1-5 versus discrete time *n* is presented in figure 3.1-1 for selected relative detuning.

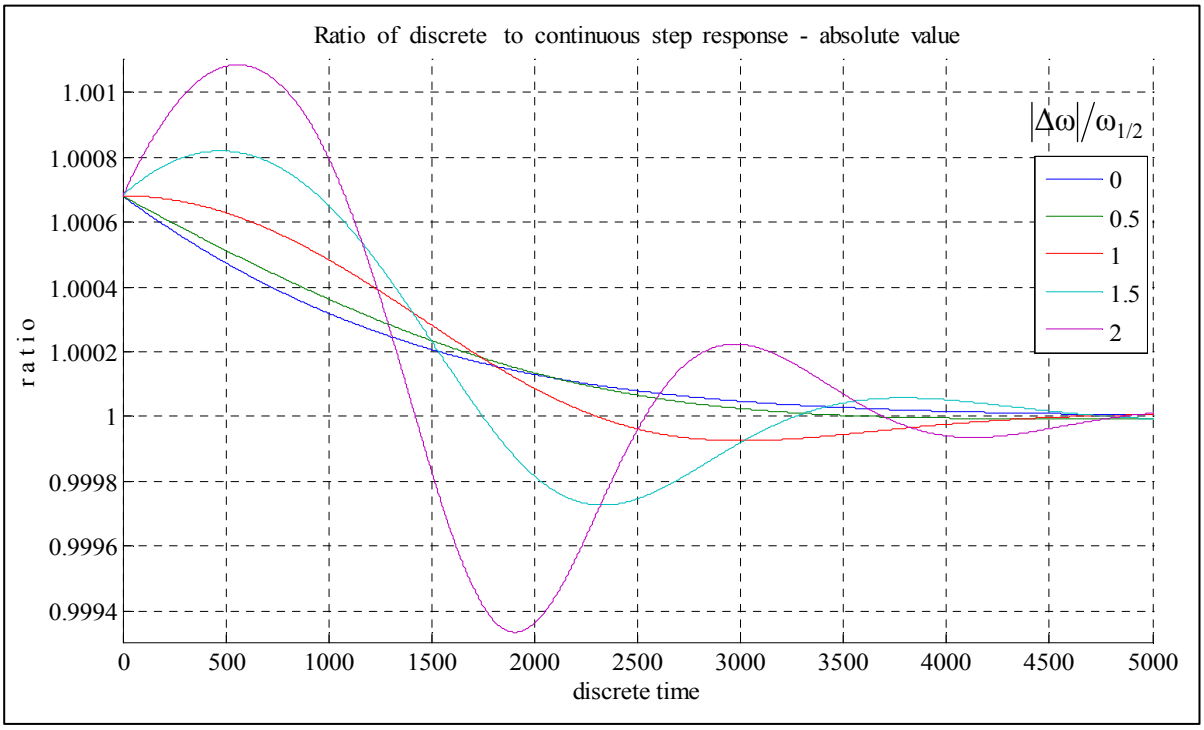


Fig. 3.1-1 Relative comparison of the step response for the discrete and continuous cavity model expressed by the absolute value of the sequence 3.1-5 as a function of discrete time for selected detuning $|\Delta\omega|$ related to the cavity half bandwidth $\omega_{1/2} = 2\pi \cdot 217$ Hz.

***Mechanical model***

The analogous procedure, like for the electrical model, has been performed for discrete processing of the mechanical model described by the *state space* equation 2.5-3. Applying directly the Euler approximation for the time derivative of the *state vector* $\frac{d\mathbf{W}_M}{dt} \approx \frac{(\mathbf{W}_M)_{n+1} - (\mathbf{W}_M)_n}{T}$ yields the following recursive equation for successive n-th and (n+1)-th samples:

$$\left(\mathbf{W}_M\right)_{n+1} = (\mathbf{1} + \mathbf{A}_M T) \cdot \left(\mathbf{W}_M\right)_n + \mathbf{B}_M T \cdot v_n^2 , \tag{3.1-6}$$

where **1** is the identity matrix.

Introducing new simplified symbols for the discrete model representation yields:

$$\mathbf{W}_{n+1} = \mathbf{C} \cdot \mathbf{W}_n + \mathbf{D} \cdot v_n^2 , \tag{3.1-7}$$

where discrete *state vector* is $\mathbf{W}_n = (\mathbf{W}_M)_n$, discrete *system matrix* is $\mathbf{C} = \mathbf{1} + \mathbf{A}_M T$, and discrete *input matrix* is $\mathbf{D} = \mathbf{B}_M T$.

***Electromechanical model***

Discrete representation of the composed electromechanical model of the cavity resonator is presented in figure 3.1-2.

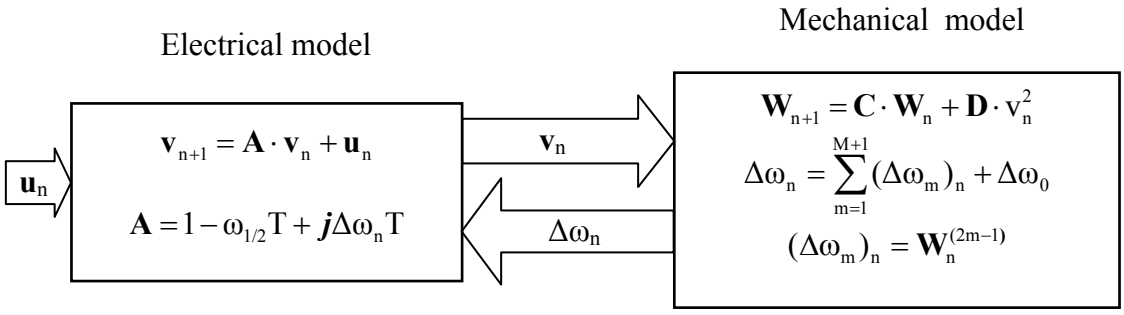


Fig. 3.1-2. A unified scheme of the cavity electromechanical discrete model

Iterative parallel processing, including electrical and mechanical model, has been implemented applying MATLAB code with time interval T = 1μs. Three resonance frequencies and the dominant, with no inertia mechanical mode is considered in the cavity model, and the superposition of all modes yields the resultant detuning. The main parameters of the cavity electromechanical model are combined for simulation examples in table 3.1-1.

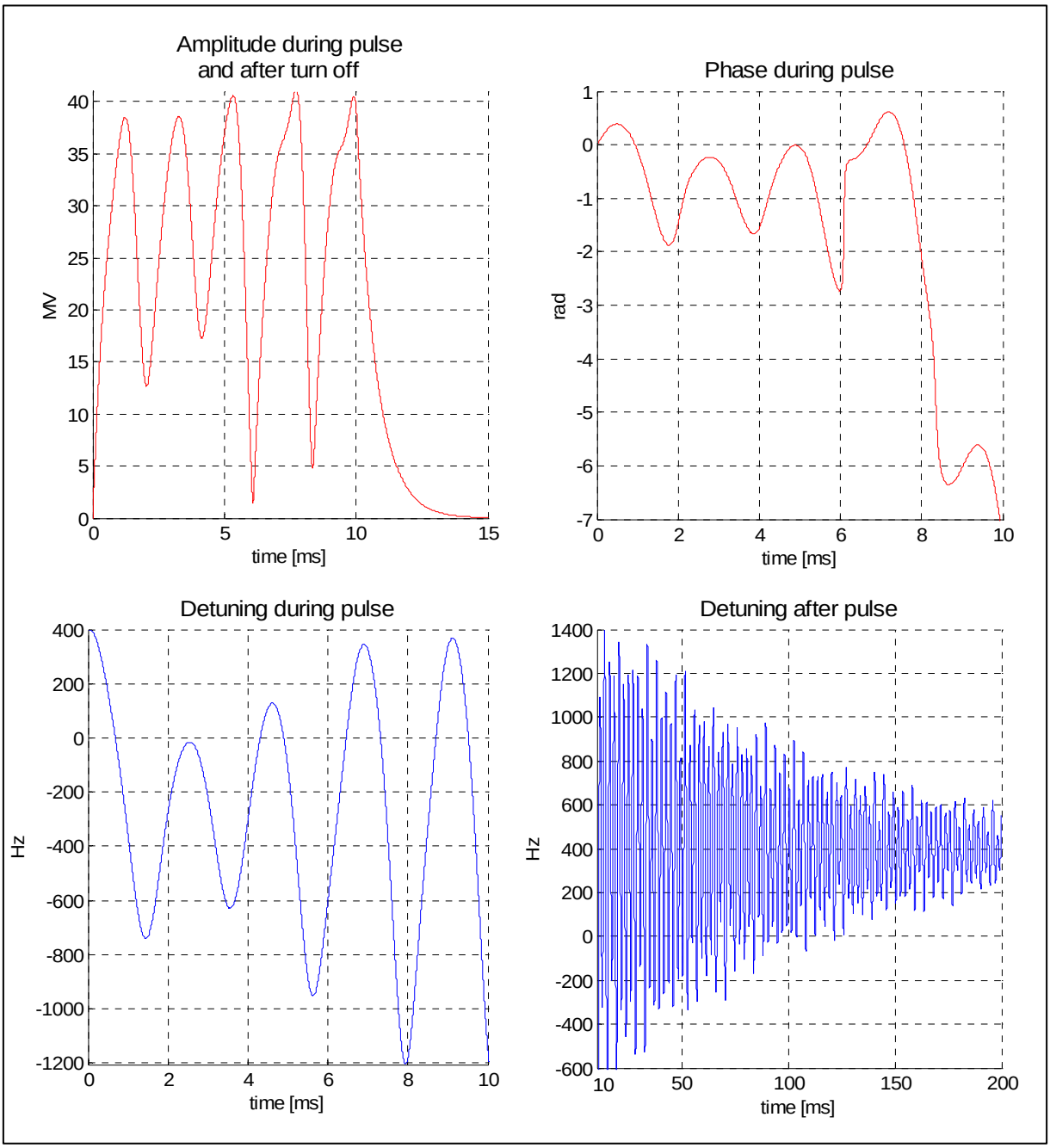


Fig. 3.1-3. Response of the electromechanical cavity model (according to the parameters from table 3.1-1) for 10 ms rectangle pulse of driving current **i** = 16 mA.

Table 3.1-1. Parameters of the cavity electromechanical model for simulation purpose

| ELECTRICAL parameters | MECHANICAL parameters |
|---|---|
| $f_0$ = 1.3 GHz……..resonance frequency<br>ρ = 520 Ω……..characteristic resistance<br>$Q_L = 3 \cdot 10^6$…….....loaded quality factor<br>$f_{1/2}$ = 217 Hz……half band-width<br>$\Delta f_0$ = 417 Hz ...predetuning (for 25 MV) | **f** = [235, 290, 450] Hz ..…… vector of resonance frequencies<br>**Q** = [100, 100, 100]…….vector of quality factors<br>τ = 0.1 ms…… time constant of the 4-th mode<br>**K** = [0.1, 0.1, 0.1, 0.5] Hz/(MV)$^2$…….vector of constants of Lorentz force detuning |

The response of the electromechanical model for 10 ms rectangle pulse of driving current **i** = 16 mA is presented in figure 3.1-3. The dominating oscillations are caused by the mechanical modes driven by the square of the cavity voltage amplitude. The mechanical model is weakly damped. But the dynamic *ponderomotive* instability [24] can be excited for the sufficiently high amplitude of the cavity voltage.

## 3.2 Digital simulator

Hardware implementation of the cavity model, called further in this work as a cavity simulator, has been performed for real time tests. The digital cavity model has been developed in MATLAB system as a reference for the hardware simulator based on the FPGA – Field Programmable Gate Array technology [23].

Digital implementation of the discrete cavity model requires numerical care due to the limited resolution of data for DSP - digital signal processing. Involved values with the given units span over the range up to seven decades (~$2^{23}$) for the cavity model. Normalization and scaling of the parameters and variables is an essential step in preparation for the DSP implementation with fixed point arithmetic. The optimal numerical accuracy for a linear arithmetic operation in the integer domain can be achieved by a preceding scaling (multiplication by power of two) and matching the real values within a given N-bit resolution range of $\pm 2^{N-1}$, common for all involved quantities. Consequently, the actual ranges of all parameters and variables have been established as an integer power of two for the assumed variety of operation. For a given absolute variable value x with the range of $2^r$, the required

scaling factor is $s = 2^{N-1-r}$. The main arithmetic processing, for each variable $x_i$, is a linear combination of the corresponding variables $x_k$ with the parameters $a_{ik}$ as follows: $x_i = \sum_k a_{ik} x_k$ . The equivalent DSP operation is: $X_i = \sum_k \frac{A_{ik} X_k}{S_{ik}}$, where the scaled values are: $X_i = s_i \cdot x_i$, $X_k = s_k \cdot x_k$, $A_{ik} = s_{ik} \cdot a_{ik}$ with the scaling factors: $s_i$, $s_k$, $s_{ik}$, respectively, and the resultant rescaling factor $S_{ik} = s_{ik} \cdot s_k / s_i$. So, concluding the DSP multiplication, the obtained product is rescaled by bit shifting (division by power of two) to preserve its normalization. The number of bits equals to $\log_2(S_{ik})$ for the rescaling shift after the multiplication.

The discrete cavity model (refer to 3.1-3 and 3.1-7), was adapted for the hardware implementation. A scaled model with integer-valued N-bit resolution was developed in the Matlab system as the pattern for the VHDL coding for the FPGA implementation. The numerical accuracy of the digital model was tested for different bit resolutions, and diverse scaling factors. The full bit resolution of the MATLAB cavity model, with normalized parameters and variables, was considered as a reference.

The step response of the digital N-bit resolution model has been compared to the reference with full resolution for a simulation time of 10 ms. The relative mean square error of the complex envelope Err(N) for N-bit resolution was calculated for 10000 steps according to the expression:

$$E_{rr}(N) = \frac{\sum_n \left| (\mathbf{v}_N)_n - (\mathbf{v}_{ref})_n \right|^2}{\sum_n \left| (\mathbf{v}_{ref})_n \right|^2}, \qquad \text{for } n = 1 \div 10000, \tag{3.2-1}$$

where $(\mathbf{v}_{ref})_n$ is a complex sample of the reference envelope for n-th step, $(\mathbf{v}_N)_n$ is complex sample of the N-bit resolution envelope for n-th step.

The results for different bit resolutions are presented in figure 3.2-1. However, for nonlinear systems, like this, they depend on detailed simulation conditions.

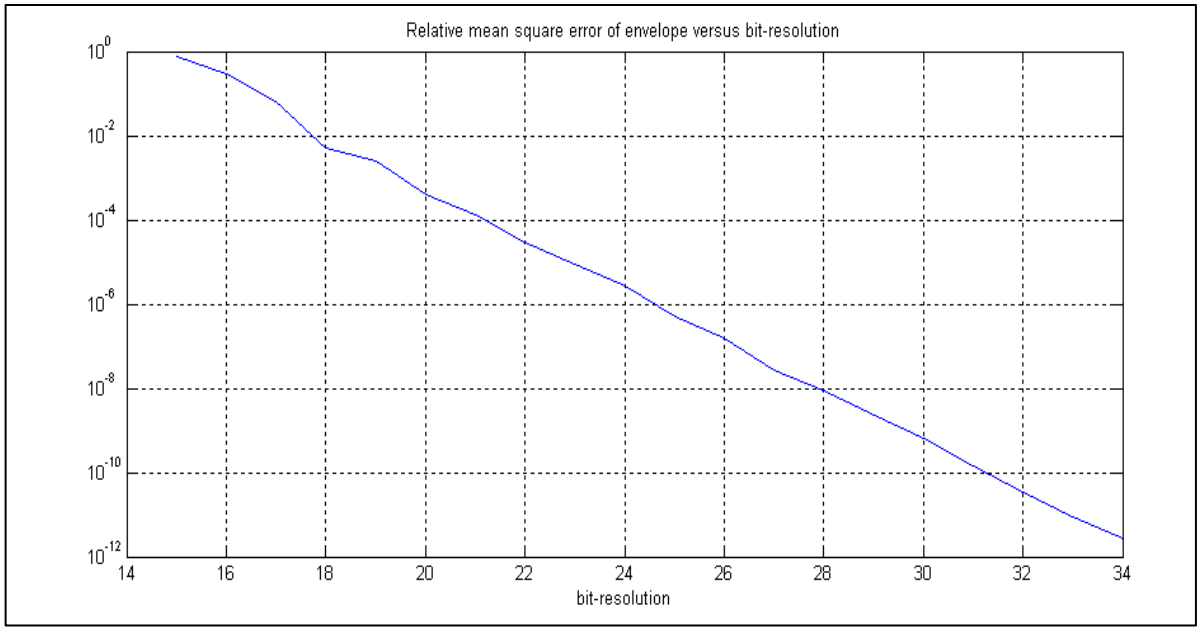


Fig. 3.2-1. Relative mean square error of complex envelope for different bit-resolution of cavity model (total time of the step response simulation - 10000 μs)

The 18-bit resolution was considered for the final hardware realization of the cavity model. The relative mean square error is Err(18) = 5.1e-3. The 18-bit resolution version of the FPGA cavity simulator is expected to be quite sufficient for this simulation. Limited validity of the heuristic mechanical model of the cavity and 14-bit resolution of the preferred analog-to-digital converter do not require a resolution of better quality.

A hardware layer of the cavity simulator and controller system (SIMCON) has been realized with the commercial development kit. The kit consists of the main board integrated with a daughter board (DB). The DB is realizing the hardware DSP algorithms. The DB possesses two fast 14-bit, 100 MHz ADC and DAC and a FPGA chip equipped with 18x18 bit multiplication circuits. The SIMCON card occupies two slots in the VME crate. The hardware realization is described in detail in [25, 26].

## 3.3 Cavity simulator control

The cavity simulator with controller has been coupled to the Matlab system via a communication interface. The Matlab system initiates the simulation process for given primary parameters of the cavity model according to table 3.1-1. Real time tests are carried out by iterative processing striving to achieve the required behavior of the cavity simulator. The control methods of the cavity model are described in chapter 5. A resulting example, for the simulation of a real operation condition, is presented in fig. 3.3-1.

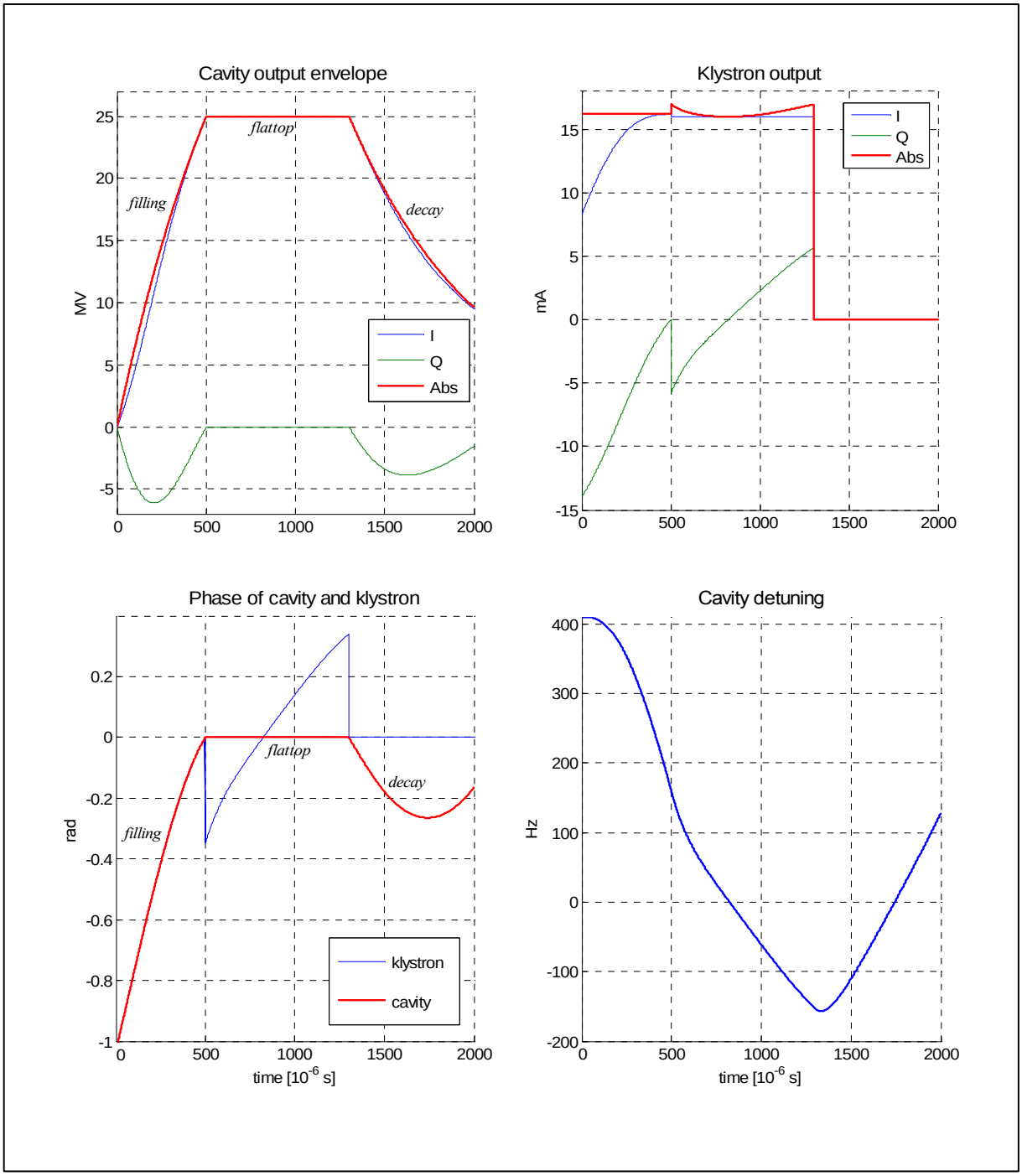


Fig. 3.3-1 Simulation results of the cavity real operation condition during *filling*, *flattop* and *decay* for a beam current of 8 mA.

The cavity is driven in a pulse mode forced by the klystron current. During the first stage of the operation (500 μs), the cavity is *filling* with a constant forward power, resulting in an exponential increase of the electromagnetic field under the resonant condition. When the cavity gradient reached the required final value, the beam current is injected. The klystron current is modulated, resulting in the steady-state *flattop* operation (800 μs). Turning off both, the generator and the beam current, yields an exponential *decay* of the cavity field.

# 4. CRITERIA OF CAVITY MODEL CONTROL

## 4.1. Electrical model control

According to the requirements for the LLRF system the cavity model is driven in a pulsed mode. The model is supplied by the input current **i**(t) and desired conditions for the cavity control are as follows:

1. During the first stage of operation, which is called *filling*, the cavity reaches the required final value of $\mathbf{v}(t_f) = \mathbf{v}_c$ at the limited time $t_f$. Filling the cavity with high power microwave energy is assumed to be done with an optimal energy efficiency.
2. During the second stage of the operation, which is called *flattop*, the beam current $\mathbf{i}_b$ is injected, and the cavity voltage is hold constant and stable with the value $\mathbf{v}_c$ and the phase matched to the beam.
3. During the third stage of the operation, which is called *decay*, the generator and beam currents are turned off yielding free expiration of the cavity field.

Control of electrical model of the cavity is considered separately for the three above stages of the LLRF system operation.

***Filling range***

The main purpose of the *filling* process is to obtain a required final state of a cavity voltage $\mathbf{v}_c$ at a given time $t_f$, taking into account the klystron power limitation. The *filling* energy efficiency $\eta_f$, defined below (refer to 2.4-2), is taken as the optimality criterion:

$$\eta_f = \frac{\text{stored energy}}{\text{expended energy}} = \frac{W(t_f)}{\int_0^{t_f} P_f(t)dt} = 2\omega_{1/2}\frac{\mathbf{v}_c \cdot \mathbf{v}_c^*}{\langle \mathbf{u}, \mathbf{u} \rangle}, \qquad (4.1\text{-}1)$$

where the unified input $\mathbf{u}(t) = \omega_0 \rho \cdot \mathbf{i}(t)$ is considered as an element of the function space $L^2\langle 0, t_f \rangle$, with the square of the norm value equal to $\|\mathbf{u}\|^2 = \int_0^{t_f} \mathbf{u} \cdot \mathbf{u}^* dt = \langle \mathbf{u}, \mathbf{u} \rangle$.

The solution $\mathbf{v}(t_f) = \mathbf{v}_c$ of the equation 2.3-8 for $\mathbf{v}(0) = 0$ is expressed as the inner product of two elements of the function space $L^2\langle 0, t_f \rangle$

$$\mathbf{v}_c = \int_0^{t_f} \mathbf{u}(t) \cdot \mathbf{\Phi}(t_f, t)dt = \langle \mathbf{u}, \mathbf{\Phi}^* \rangle, \qquad (4.1\text{-}2)$$

where for a non-stationary case, with the time varying detuning, the fundamental function is

$$\mathbf{\Phi}(t_f, t) = \exp\int_t^{t_f} \mathbf{A}_e(\tau)d\tau \quad \text{for} \quad \mathbf{A}_e(\tau) = -\omega_{1/2} + \boldsymbol{j}\Delta\omega(\tau).$$

As a consequence of the orthogonal projection statement [27], the optimal solution for **u,** with the minimal norm $\|\mathbf{u}\|$, lies in the subspace generated by the function **Φ*** and is given by

$$\mathbf{u} = \boldsymbol{\beta} \cdot \mathbf{\Phi}^*, \tag{4.1-3}$$

where the complex coefficient $\boldsymbol{\beta} = \dfrac{2\omega_{1/2} \cdot \mathbf{v}_c}{1 - \exp(-2\omega_{1/2} t_f)} = \mathbf{u}(t_f)$ satisfies the condition 4.1-2.

Consequently, the solutions for input **u**(t) and output **v**(t) voltages, respectively, are as follow:

$$\mathbf{u}(t) = \omega_{1/2}\mathbf{v}_c \cdot \frac{\exp(\omega_{1/2}t)}{\sinh(\omega_{1/2}t_f)} \cdot e^{-j\Delta\varphi(t_f,t)} = \omega_{1/2}\mathbf{v}_c \cdot \frac{\exp(\omega_{1/2}t)}{\sinh(\omega_{1/2}t_f)} \cdot e^{j\varphi(t)} \tag{4.1-4}$$

$$\text{for} \quad \Delta\varphi(t_f, t) = \int_t^{t_f} \Delta\omega(\tau)d\tau \quad \text{and phase} \quad \varphi(t) = \arg(\mathbf{v}_c) - \Delta\varphi(t_f, t), \text{ thus } \frac{d\varphi(t)}{dt} = \Delta\omega(t),$$

$$\mathbf{v}(t) = v_c \cdot \frac{\sinh(\omega_{1/2}t)}{\sinh(\omega_{1/2}t_f)} \cdot e^{j\varphi(t)} \tag{4.1-5}$$

The optimal factor $\eta_{fo}$ is given by

$$\eta_{fo} = 1 - \exp(-2\omega_{1/2}t_f). \tag{4.1-6}$$

Applying equations 4.1-4 and 4.1-5, the optimal input voltage **u**(t) can be determined as a direct feedback dependent on the output voltage **v**(t):

$$\mathbf{u}(t) = \frac{2\omega_{1/2}}{1 - \exp(-2\omega_{1/2}t)} \cdot \mathbf{v}(t) \qquad (t > 0). \tag{4.1-7}$$

The optimal control of the resonator, with respect to the energy for the *filling* range, can be provided alternatively, by the linear-quadratic regulator (LQR) via solving the Riccati equation [28]. The resulting algorithm, given by equation 4.1-7, is a kind of a self–tuning controller also known as a *self-exciting* loop (SEL) control.

The optimal energy efficiency $\eta_{fo}$, given by equation 4.1-6, depends on a *filling* time $t_f$, what is illustrated in fig.4.1-1 for a cavity half bandwidth $\omega_{1/2} = 2\pi\cdot 217$ Hz. Absolute values of the current input $|\mathbf{i}(t)| = |\mathbf{u}(t)|/\omega_0\rho$, voltage output $|\mathbf{v}(t)|$ and corresponding forward power $P_f(t)$ and reflected power $P_r(t)$ are presented in fig.4.1-2 for a typical value of *filling* time $t_f$ =500 μs and the final value of $v_c$ = 25 MV.

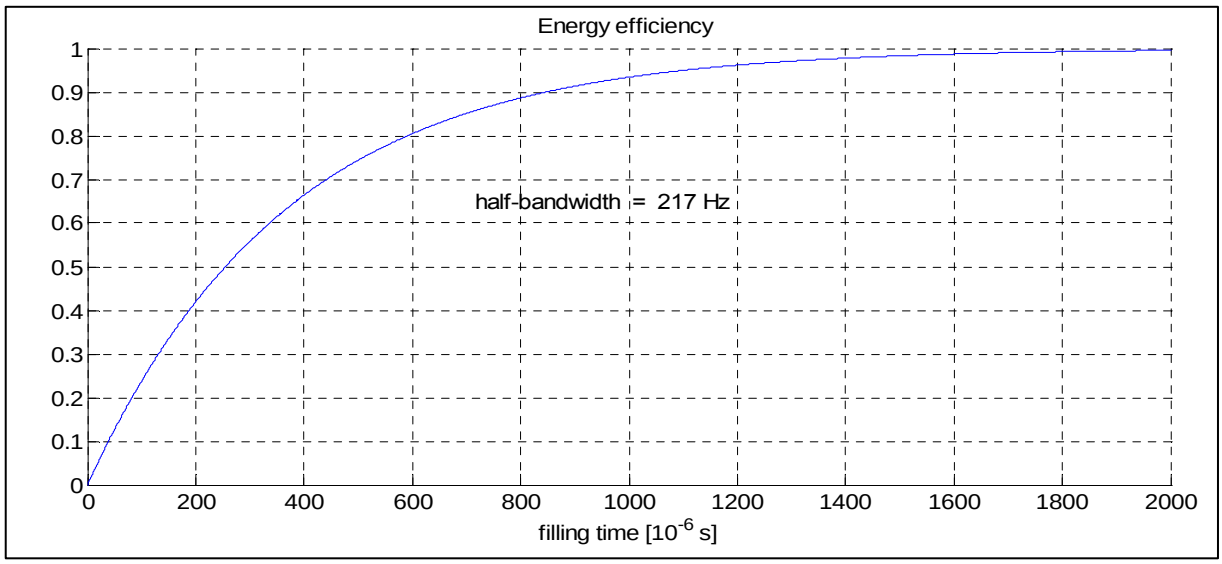


Fig. 4.1-1. The energy efficiency for the optimal control, given by equation 4.1-6, as a function of *filling* time, for a cavity half bandwidth $\omega_{1/2} = 2\pi\cdot 217$ Hz.

For the optimal *filling* process of a resonator, with respect to the energy, phase of the input signal $\angle\mathbf{u}(t)$ equals to the cavity phase $\angle\mathbf{v}(t) = \varphi(t)$. Moreover, the phase $\varphi(t)$ is modulated to compensate the cavity detuning $\Delta\omega(t)$, what is equivalent physically to the resonant condition. This general phase relation for the resonant condition, as a consequence of the cavity model 2.3-8, is unrelated to the absolute value $|\mathbf{v}(t)|$ and is stated as follows:

$$\angle\mathbf{u}(t) = \angle\mathbf{v}(t) = \varphi(t) \quad \Leftrightarrow \quad \frac{d}{dt}\varphi(t) = \Delta\omega(t)\,. \tag{4.1-8}$$

Consequently, the *state space* equation 2.3-8 of the cavity electrical model, under the resonant condition, is simplified to the scalar form for the absolute value of output $|\mathbf{v}(t)| = v(t)$ and input $|\mathbf{u}(t)| = u(t)$,

$$\frac{d}{dt}v(t) = -\omega_{1/2}v(t) + u(t)\,. \tag{4.1-9}$$

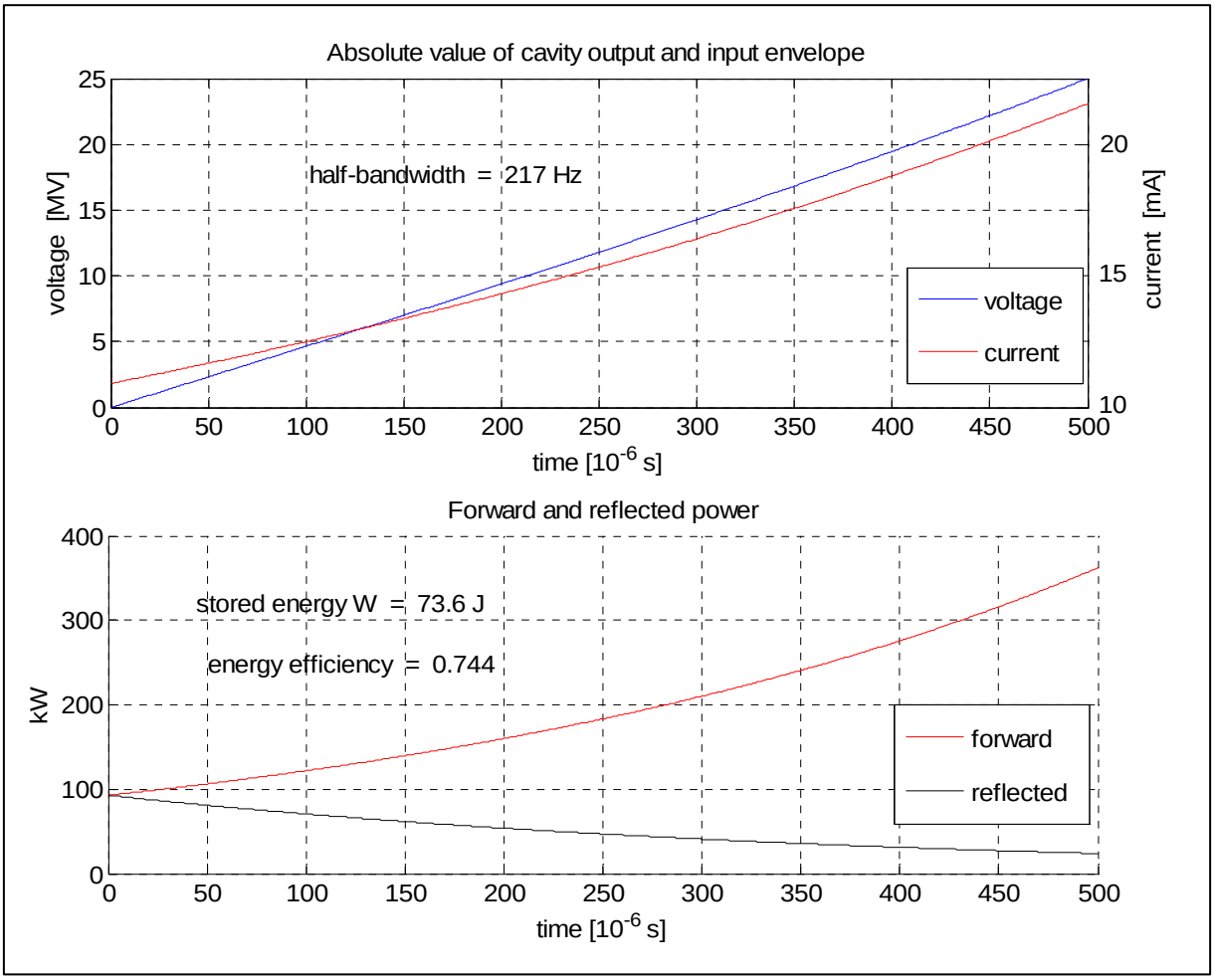


Fig. 4.1-2. The absolute value of current input, voltage output and corresponding forward and reflected power for optimal cavity driving for *filling* time $t_f$ = 500 μs and the final value of $v_c$ = 25 MV.

An implementation of the optimal control, given by equation 4.1-4, requires the knowledge of the cavity detuning $\Delta\omega(t)$ within the *filling* range to satisfy the relation 4.1-8 and drive a cavity in the resonant state. Therefore, it is useful for a repetitive, deterministic condition and actually can be apply iteratively for a cavity driven in a pulse mode (refer to chapter 4.3).

The optimal control realized as a *self-exciting* loop, given by equation 4.1-7, forces cavity itself to track its resonance frequency. But it is indeterminate for time t = 0, so it requires the initial driving according to the equation 4.1-4. The efficiency of SEL method is limited by a loop delay, as usually is the case for a feedback mode. However, it can be useful for the measurement purpose to estimate a cavity detuning.

Generally, the solution u(t) of equation 4.1-9 for any given output v(t) ≠ 0 can be expressed for the resonant condition as a *self-exciting* form:

$$u(t) = G(t)\cdot v(t) \quad \text{for a scalar value of feedback gain} \quad G(t) = \omega_{1/2} + \frac{d}{dt}v(t)\Big/v(t). \quad (4.1\text{-}10)$$

The optimal control, given by equation 4.1-4 or 4.1-7, should meet constrain of the klystron power rising at the end of *filling* range for high field gradient (> 20 MV/m). Therefore, alternative, modified, algorithms are also considered for a comparison.

Let us consider a cavity control under the resonant condition according to the phase relation 4.1-8 and given by the amplitude output-input relation:

$$u(t) = u_0 + (1-b)\omega_{1/2}v(t), \quad (4.1\text{-}11)$$

where $u_0$ and b are control parameters. The corresponding cavity model (ref. to 4.1-9) is given by:

$$\frac{d}{dt}v(t) = -b\omega_{1/2}v(t) + u_0 \quad (4.1\text{-}12)$$

and the parameter $u_0 = u(0) = \left(\frac{d}{dt}v(t)\right)_{t=0}$ satisfies the condition: $v(t_f) = v_c$ for a given value b.

The solution of equation 4.1-11 and 4.1-12 is as follows:

$$u(t) = \omega_{1/2}v_c \cdot \frac{1-(1-b)\cdot\exp(-b\omega_{1/2}t)}{1-\exp(-b\omega_{1/2}t_f)}, \quad v(t) = v_c \cdot \frac{1-\exp(-b\omega_{1/2}t)}{1-\exp(-b\omega_{1/2}t_f)} \quad \text{for} \quad b \neq 0 \quad (4.1\text{-}13)$$

$$u(t) = v_c \cdot \frac{1+\omega_{1/2}t}{t_f}, \quad v(t) = v_c \cdot \frac{t}{t_f} \quad \text{for} \quad b = 0 \quad (4.1\text{-}14)$$

The absolute value of current input $|\mathbf{i}(t)| = i(t) = u(t)/\omega_0\rho$, voltage output v(t) and corresponding forward power $P_f(t)$ and reflected power $P_r(t)$ are presented in figure 4.1-3 for a typical value of *filling* time $t_f$ = 500 μs and the final value of $v_c$ = 25 MV. Several charts for chosen control parameters b are compared with the previously derived optimal solution for a cavity half bandwidth $\omega_{1/2} = 2\pi\cdot 217$ Hz. The corresponding energy efficiency is presented in figure 4.1-4 as a function of *filling* time $t_f$ for chosen parameters b and in figure 4.1-5 (blue line) for *filling* time $t_f$ = 500 μs within the range of b = [-2 : 2]. The maximum energy efficiency $\eta_{fm} \approx 0.7436$ for the parameter b ≈ -0.32 is comparable to the optimal value $\eta_{fo} \approx 0.7437$.

The analogous deviation of the optimal solution 4.1-5, by introducing a factor b, is considered for the absolute value v(t) as follows:

$$v(t) = v_c \cdot \frac{\sinh(b\omega_{1/2}t)}{\sinh(b\omega_{1/2}t_f)} \quad \text{for } b \neq 0 \quad \text{and} \quad v(t) = v_c \cdot \frac{t}{t_f} \quad \text{for } b = 0 \qquad (4.1\text{-}15)$$

The corresponding energy efficiency $\eta_f$ for resonant condition for *filling* time $t_f = 500$ μs is presented at figure 4.1-5 (red line) within the range of the parameter b = [-2 : 2].

Let us consider a cavity control resulting in the equivalent set of solutions for amplitude v(t) given by 4.1-13 and 4.1-14, but not under the resonant condition. Thus, the cavity phase does not satisfy the relation 4.1-8 and it is assumed to be a constant value $\angle \mathbf{v} = \varphi$ during *filling* range. According to the cavity model 2.3-8, the required input **u**(t), for a given cavity detuning Δω, is as follows:

$$\mathbf{u}(t) = \frac{d}{dt}\mathbf{v}(t) + (\omega_{1/2} - \boldsymbol{j}\Delta\omega)\mathbf{v}(t) \quad \text{for} \quad \mathbf{v}(t) = v(t) \cdot \exp(\boldsymbol{j}\varphi) \qquad (4.1\text{-}16)$$

Consequently, substituting v(t) given by 4.1-13 and 4.1-14, yields:

$$\mathbf{u}(t) = \omega_{1/2} v_c \cdot \frac{1 - \boldsymbol{j}\frac{\Delta\omega}{\omega_{1/2}} - \left(1 - b - \boldsymbol{j}\frac{\Delta\omega}{\omega_{1/2}}\right) \cdot \exp(-b\omega_{1/2}t)}{1 - \exp(-b\omega_{1/2}t_f)} \cdot \exp(\boldsymbol{j}\varphi) \quad \text{for} \quad b \neq 0 \qquad (4.1\text{-}17)$$

$$\mathbf{u}(t) = v_c \cdot \frac{1 + \omega_{1/2}\left(1 - \boldsymbol{j}\frac{\Delta\omega}{\omega_{1/2}}\right)t}{t_f} \cdot \exp(\boldsymbol{j}\varphi) \quad \text{for} \quad b = 0\,. \qquad (4.1\text{-}18)$$

The corresponding energy efficiency $\eta_f$ (refer to 4.1-1) is presented in figure 4.1-5 within the range of the parameter b = [-2 : 2] for chosen detuning values related to the cavity half bandwidth $\omega_{1/2} = 2\pi \cdot 217$ Hz for *filling* time $t_f = 500$ μs.

A decrease in the energy efficiency with a cavity detuning is associated with undesirable increase of the peak forward power. In conclusion, cavity driving under the resonant condition is desired. A variation of the energy efficiency is relatively small, within a wide range of control parameter b. Thus, the cases with a smaller peak forward power can be considered as a reasonable choice for a cavity control during *filling* range. For example, a constant driving, according to 4.1-13 for b = 1, or a linear driving, according to 4.1-14 for b = 0, are practically applied for a cavity *filling*. Moreover, a longer *filling* time significantly increases the energy efficiency and decreases a peak forward power.

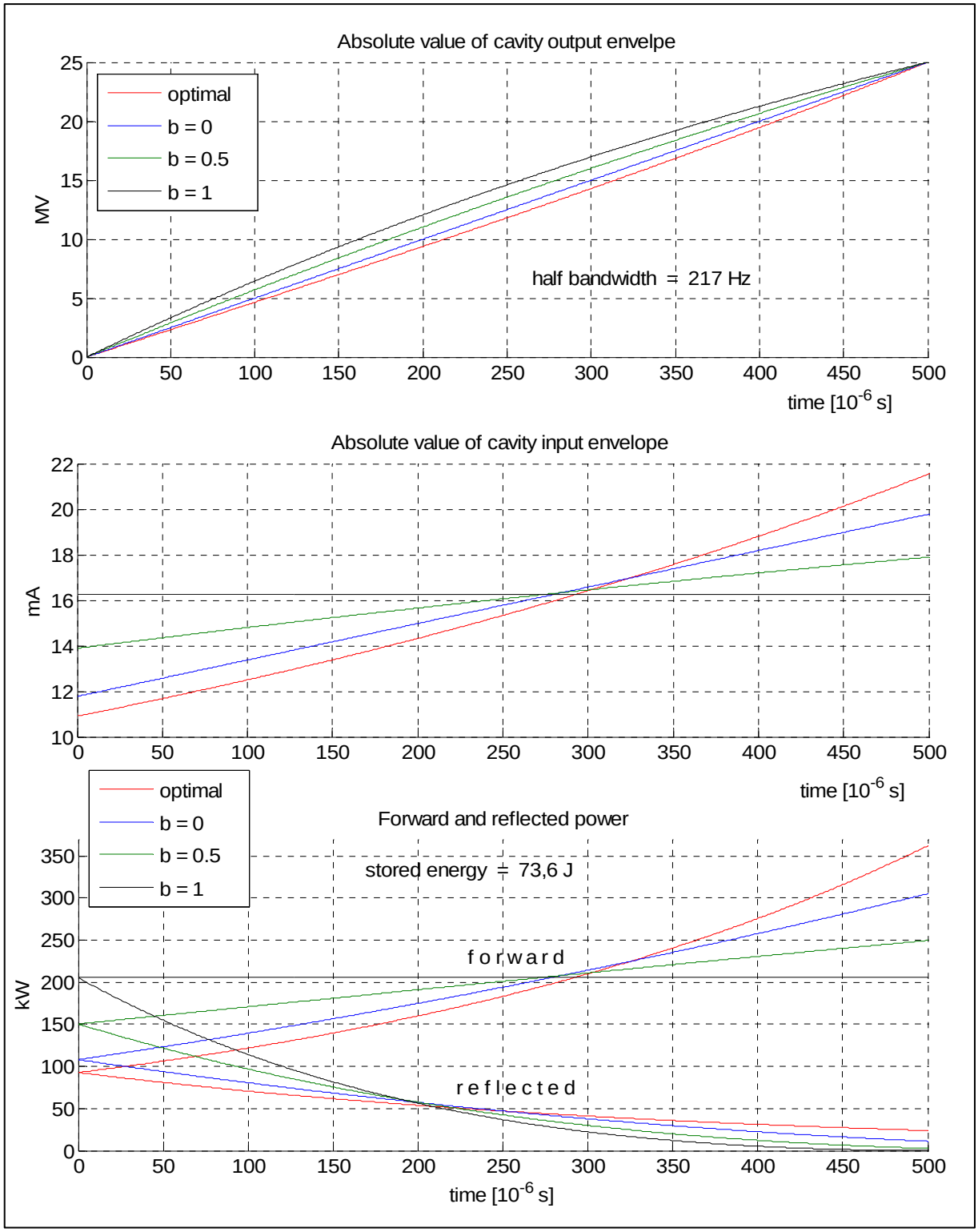


Fig. 4.1-3. The absolute value of current input envelope, voltage output envelope according to the control algorithm 4.1-11 and corresponding forward and reflected power versus time for *filling* time $t_f$ = 500 μs and the final value of $v_c$ = 25 MV. Charts for three chosen values of control parameter b are presented jointly with the optimal solution for a cavity half bandwidth $\omega_{1/2} = 2\pi \cdot 217$ Hz.

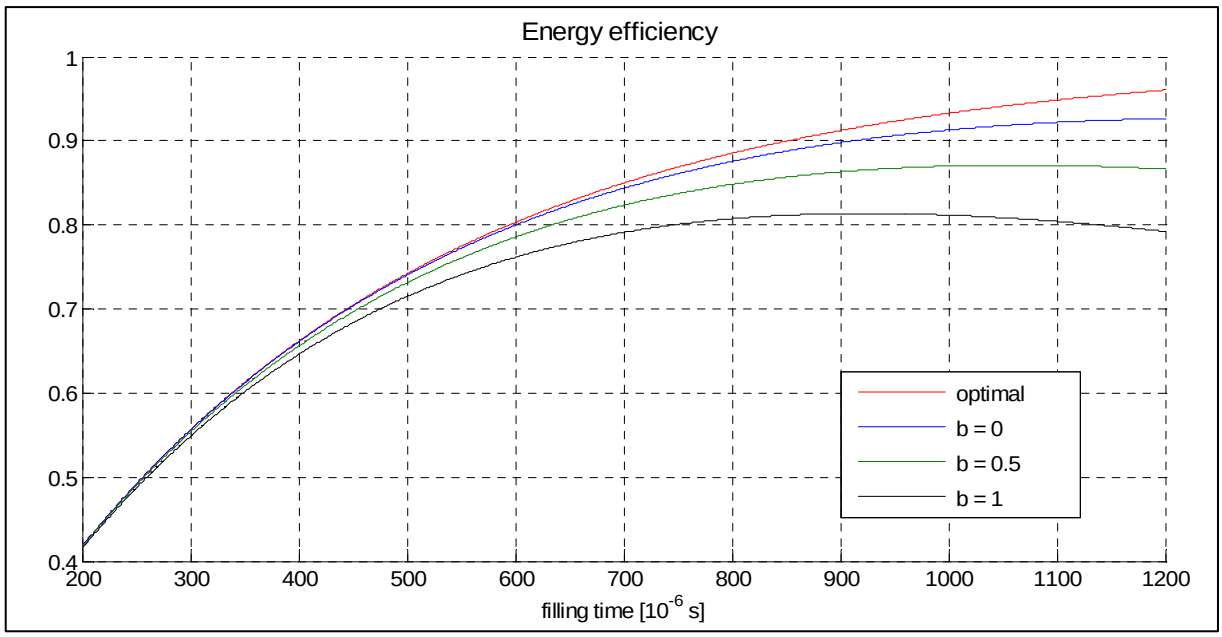


Fig. 4.1-4. The energy efficiency according to the control algorithm 4.1-11, as a function of *filling* time. Charts for three selected values of control parameter b are presented jointly with the optimal solution for a cavity half bandwidth $\omega_{1/2} = 2\pi \cdot 217$ Hz.

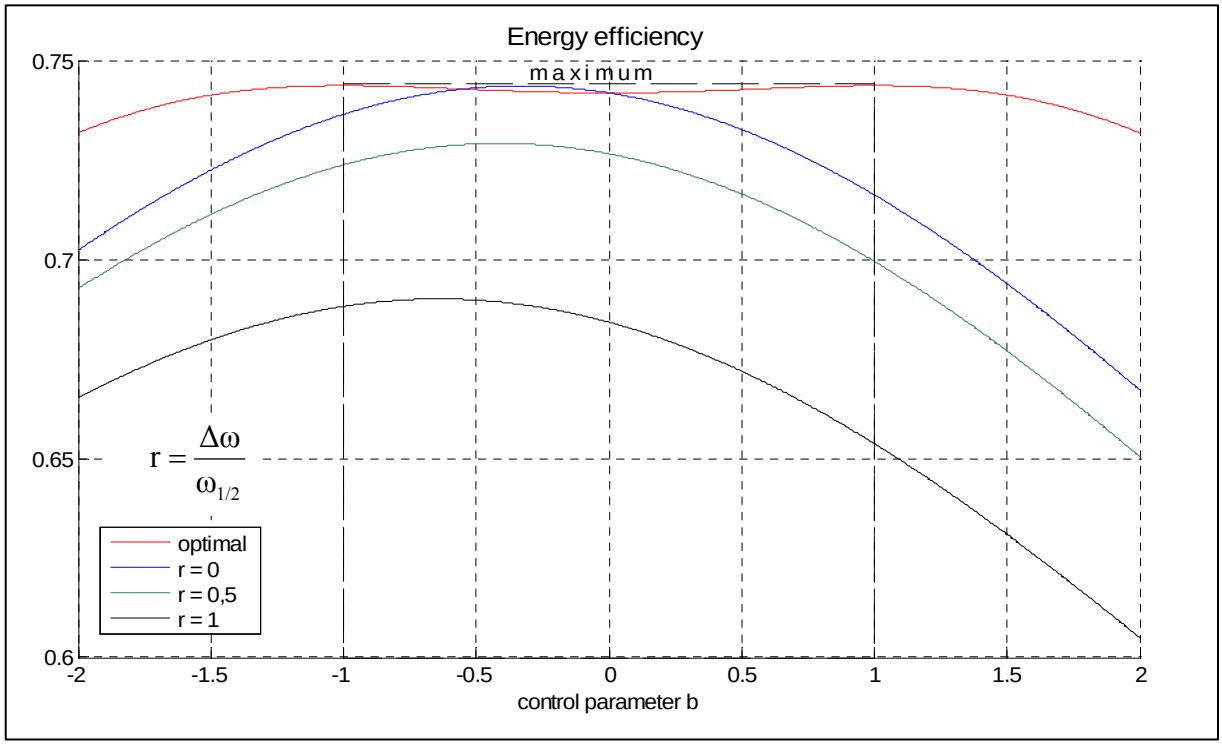


Fig. 4.1-5. The energy efficiency according to the control algorithm 4.1-11, as a function of control parameter b for *filling* time $t_f = 500$ µs and cavity half bandwidth $\omega_{1/2} = 2\pi \cdot 217$ Hz. Charts for three selected values of relative detuning $r = \Delta\omega/\omega_{1/2}$ are presented jointly with the optimal modified solution given by 4.1-15.

***Flattop range***

The main purpose of the cavity control is to keep a stable and specified value $\mathbf{v}_c$ = const. of a cavity voltage to assure the unique condition of beam acceleration during *flattop* range. The required cavity phase $\angle\mathbf{v}_c = \varphi_c = \angle\mathbf{i}_b - \varphi_b$ is matched to the desired relative beam phase $\varphi_b$ for a given beam loading $\mathbf{i}_b$. According to the cavity model 2.3-8, the required unified input $\mathbf{u}_g = \omega_0\rho\cdot\mathbf{i}_g$ for a specified unified beam loading $\mathbf{u}_b = \omega_0\rho\cdot\mathbf{i}_b$, is as follows (compare to equation 2.4-3):

$$\mathbf{u}_g = \mathbf{u}_b - \mathbf{A}_e\cdot\mathbf{v}_c\,. \tag{4.1-19}$$

So, the cavity input requires additional component to compensate the beam loading value $\mathbf{u}_b$. Moreover, the cavity input $\mathbf{u}_g(t)$ is modulated to compensate a time varying factor $\mathbf{A}_e(t) = -\omega_{1/2} + \boldsymbol{j}\Delta\omega(t)$, with time varying cavity detuning $\Delta\omega(t)$.

The *flattop* energy efficiency $\eta_b$ is introduced for the *flattop* range $t_b$, as follows (refer to equation 2.4-4):

$$\eta_b = \frac{\text{beam energy gain}}{\text{expended energy}} = \frac{\int_0^{t_b} P_b(t)dt}{\int_0^{t_b} P_f(t)dt} = \frac{4g}{(1+g)^2 + \frac{1}{t_b}\cdot\int_0^{t_b}\left(\frac{\Delta\omega(t)}{\omega_{1/2}} - g\cdot\tan\varphi_b\right)^2 dt} \tag{4.1-20}$$

for factor $g = \frac{u_b\cos\varphi_b}{\omega_{1/2}v_c}$, with a constant value of beam loading $u_b$.

The required forward power during *flattop* range depends on the cavity detuning which is externally biased by the *predetuning* $\Delta\omega_0$ to minimize the expended energy. The energy efficiency $\eta_b$ is maximized with respect to the factor g for the minimal value of the integral component in the denominator. The minimum of the detuning dependent component equals to the variance of the relative detuning: $\left(\frac{\Delta\omega_b}{\omega_{1/2}}\right)^2 = \frac{1}{t_b}\int_0^{t_b}\left(\frac{\Delta\omega(t)}{\omega_{1/2}} - \frac{1}{t_b}\int_0^{t_b}\frac{\Delta\omega(t)}{\omega_{1/2}}dt\right)^2 dt$ within the *flattop* range. Consequently, the optimal values $\eta_{bo}$ and $g_{bo}$ fulfill the relation:

$$\eta_{bo} = \frac{2}{1+g_{bo}} \quad\Leftrightarrow\quad \left(g_{bo}^2 = 1 + \left(\frac{\Delta\omega_b}{\omega_{1/2}}\right)^2 \quad\text{and}\quad \frac{1}{t_b}\int_0^{t_b}\frac{\Delta\omega(t)}{\omega_{1/2}}dt = g_{bo}\tan\varphi_b\right). \tag{4.1-21}$$

The optimal condition for the *flattop* energy efficiency for the *flattop* range $t_b$ = 800 μs are presented in figure 4.2-3, as a function of the cavity *flattop* voltage $v_c$. The factor $\eta_b$, as a function of the beam current, is presented in figure 4.2-5 for the electromechanical model control described in chapter 4.2. The simulation procedure has been performed for the cavity discrete model according to fig.3.1-2 defined by the parameters from table 3.1-1.

***Decay range***

During the third stage of the operation called *decay*, the generator and beam current are turned off yielding freely expiring of the cavity field. The homogeneous solution of equation 2.3-8 for no stationary case is given by**:**

$$\mathbf{v}(t) = \mathbf{v}_c \cdot \exp\int_0^t \mathbf{A}_e(\tau)d\tau = v(t) \cdot e^{j\varphi(t)}, \qquad (4.1\text{-}22)$$

where, amplitude $v(t) = v_c \cdot \exp(-\omega_{1/2}t)$ and phase $\varphi(t) = \varphi_c + \int_0^t \Delta\omega(\tau)d\tau$. The cavity parameters: half-bandwidth $\omega_{1/2}$ and detuning $\Delta\omega(t)$, fulfill the relations:

$$\omega_{1/2} = -\frac{\frac{d}{dt}v(t)}{v(t)} \qquad \text{and} \qquad \Delta\omega(t) = \frac{d}{dt}\varphi(t). \qquad (4.1\text{-}23)$$

## 4.2. Electromechanical model control

The electromechanical model of the cavity, presented by the scheme of figure 2.6-1, is employed for the implementation of the steering methods considered in chapter 4.1. The input and output condition of the cavity model control are summarized in table 4.2-1 for three separated ranges of the cavity operation: *filling*, *flattop* and *decay*.

The cavity model is driven with the unified input $\mathbf{u}(t) = \omega_0\rho \cdot \mathbf{i}(t) = \mathbf{u}_g(t) - \mathbf{u}_b(t)$ according to the general formula given by the electrical inverse model of the cavity:

$$\mathbf{u}(t) = \frac{d}{dt}\mathbf{v}(t) - \mathbf{A}_e(t) \cdot \mathbf{v}(t) \qquad (4.2\text{-}1)$$

for the required output **v**(t) and for the recognized factor $\mathbf{A}_e(t) = -\omega_{1/2} + \boldsymbol{j}\Delta\omega(t)$.

Table 4.2-1. The input – output condition of the cavity model control

| *Range* | | filling | flattop | decay |
|---|---|---|---|---|
| Output **v**(t) | $\lvert\mathbf{v}(t)\rvert$ | $v(t):\langle v(0)=0;\ v(t_f)=v_c\rangle$ | $v_c = \text{const.}$ | $v_c \cdot \exp(-\omega_{1/2}t)$ |
| | $\angle\mathbf{v}(t)$ | $\varphi_c - \int_t^{t_f} \Delta\omega(\tau)d\tau$ | $\varphi_c = \text{const.}$ | $\varphi_c + \int_0^t \Delta\omega(\tau)d\tau$ |
| Input **u**(t) | $\lvert\mathbf{u}(t)\rvert$ | $\frac{d}{dt}v(t) + \omega_{1/2}v(t)$ | $(\omega_{1/2} - \boldsymbol{j}\Delta\omega(t))\cdot\mathbf{v}_c$ | **0** |
| | $\angle\mathbf{u}(t)$ | $\angle\mathbf{v}(t)$ | | |

The absolute value $|\mathbf{v}(t)| = v(t)$ is established uniquely by the desired operation condition of the cavity electrical model within all ranges. For the *filling* range, a rising function v(t) is selected according to the considerations in chapter 4.1. Moreover, the absolute value v(t), as the input of the mechanical part of the model, determines uniquely the cavity detuning $\Delta\omega(t)$ within all ranges for a given *predetuning* $\Delta\omega_0$. Thus, the required control **u**(t) is estimated definitely for a desired output **v**(t) of the cavity model. A simplified scheme of the procedure is depicted in figure 4.2-1. The cavity detuning is estimated iteratively by the output of the mechanical discrete model (refer to figure 3.1-2) for a given series $v_n = v(nT)$ and *predetuning* value $\Delta\omega_0$.

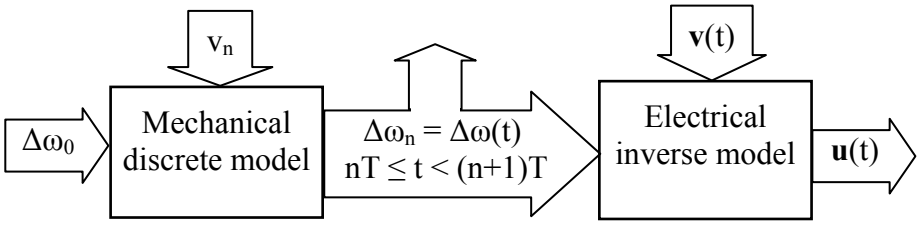


Fig. 4.2-1. The scheme of estimation procedure for required control **u**(t) of the cavity model with the required output **v**(t).

The simulation procedure has been performed for the cavity discrete model according to fig. 3.1-2 defined by parameters from table 3.1-1. Simulation results are presented in fig. 4.2-2 for timing pulse parameters: *filling* $t_f$ = 500 μs and *flattop* $t_b$ = 800 μs. The cavity model is driven with the unified input current $\mathbf{i}(t) = \mathbf{u}(t)/\omega_0\rho = \mathbf{i}_g(t) - \mathbf{i}_b(t)$ for three values of the cavity *flattop* level $v_c$: 15 MV, 20 MV, 25 MV with cavity phase $\varphi_c = 0$ and beam phase $\varphi_b = 0$.

The optimal control given by equation 4.1-4 has been chosen for the *filling* range. The value of *predetuning* $\Delta\omega_0$ has been selected according to the energy criterion described below.

The pulse energy efficiency $\eta_p$ is introduced for pulse range: $t_p = t_f + t_b$, as follows (refer to equations 4.1-1 and 4.1-20):

$$\eta_p = \frac{\text{beam energy gain}}{\text{pulse expended energy}} = \frac{\int_0^{t_p} P_b(t)dt}{\int_0^{t_p} P_f(t)dt} = \frac{P_b \cdot t_b}{\frac{W(t_f)}{\eta_f} + \frac{P_b \cdot t_b}{\eta_b}} =$$

$$= \frac{4g}{\frac{2}{\omega_{1/2} t_b \eta_f} + (1+g)^2 + \frac{1}{t_b} \cdot \int_{t_f}^{t_p} \left( \frac{\Delta\omega(t)}{\omega_{1/2}} - g \cdot \tan\varphi_b \right)^2 dt}, \qquad (4.2\text{-}2)$$

where the beam loading power $P_b$ is assumed as a constant value during flattop time $t_b$.

The efficiency of pulse energy $\eta_p$ is maximized with respect to the factor $g = \frac{u_b \cos\varphi_b}{\omega_{1/2} v_c}$ for the minimal value of the integral component in denominator, analogously to equation 4.1-20. The minimum of this component equals to the variance of relative detuning: $\left( \frac{\Delta\omega_b}{\omega_{1/2}} \right)^2 = \frac{1}{t_b} \int_0^{t_b} \left( \frac{\Delta\omega(t)}{\omega_{1/2}} - \frac{1}{t_b} \int_0^{t_b} \frac{\Delta\omega(t)}{\omega_{1/2}} dt \right)^2 dt$. Due to the model linearity it does not depend on the cavity *predetuning* $\Delta\omega_0$, which modifies a mean value only without change of a detuning shape. Consequently, the optimal values $\eta_{po}$ and $g_{po}$ fulfill the relation:

$$\eta_{po} = \frac{2}{1+g_{po}} \Leftrightarrow \left( g_{po}^2 = 1 + \left( \frac{\Delta\omega_b}{\omega_{1/2}} \right)^2 + \frac{2}{\omega_{1/2} t_b \eta_f} \quad \text{and} \quad \frac{1}{t_b} \int_{t_f}^{t_p} \frac{\Delta\omega(t)}{\omega_{1/2}} dt = g_{po} \tan\varphi_b \right). \qquad (4.2\text{-}3)$$

The optimal *predetuning* $\Delta\omega_0$ meets the above requirement for mean value of the relative detuning and it is calculated by mean value of all residual detuning components without *predetuning,* as follows:

$$\Delta\omega_0 = \omega_{1/2} g_{po} \tan\varphi_b - \frac{1}{t_b} \int_{t_f}^{t_p} \Delta\omega(t)\big|_{\Delta\omega_0 = 0} dt \,. \qquad (4.2\text{-}4)$$

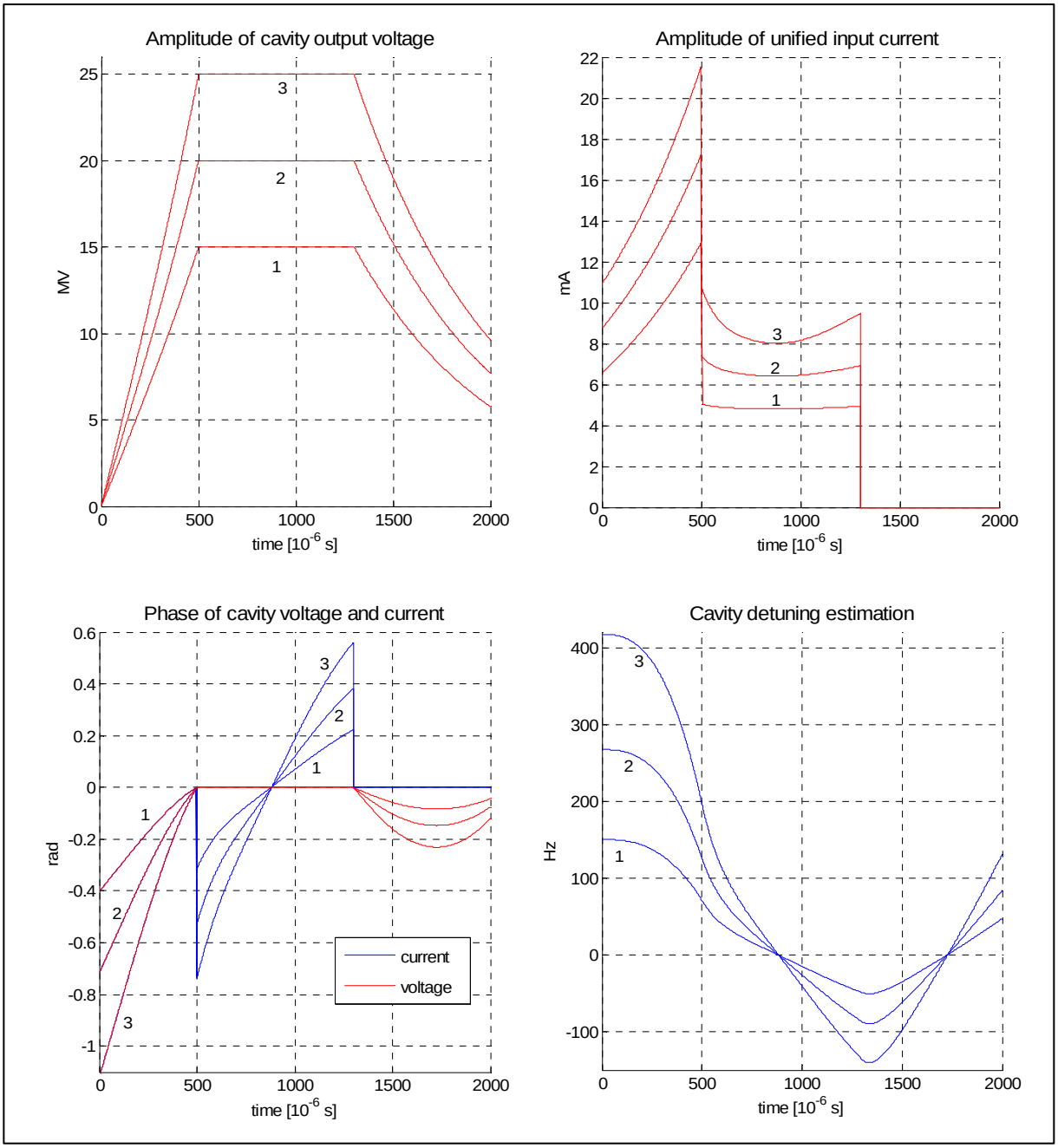


Fig. 4.2-2. Simulation results of the cavity model control for three values of the voltage $v_c$: 1 - 15 MV, 2 - 20 MV, 3 - 25 MV and for cavity phase $\varphi_c = 0$.

The factor $\eta_{po}$ is weakly dependent on the *filling* time within the range of $t_f = (300:600)$ μs and it varies between 0.67 to 0.7 for typical pulse time $t_p = 1300$ μs. The optimal energy efficiency $\eta_{fo}(t_f)$ expressed by equation 4.1-6 for *filling* time $t_f = 500$ μs has been chosen for the simulation performance. The factor $\eta_{po}$ for pulse range $t_p = t_f + t_b = 500$ μs + 800 μs =1300 μs is compared to the factor $\eta_{bo}$ for the *flattop* range $t_b = 800$ μs (refer to equation 4.1-21) in

figure 4.2-3, as a function of the cavity *flattop* voltage $v_c$. The required optimal *predetuning* and the beam current are also presented in figure for the beam phase $\varphi_b = 0$. The beam, forward and reflected power estimations, corresponding to figure 4.2-2, for the optimal pulse energy efficiency $\eta_{po}$ are depicted in figure 4.2-4 for three values of the cavity voltage $v_c$: 15 MV, 20 MV and 25 MV. Due to an actual klystron power limitation, diverse values of the beam current are also considered for the simulation procedure. The *flattop* energy efficiency $\eta_b$ is compared to the pulse energy efficiency $\eta_b$, (refer to equation 4.1-20 and 4.2-2), as a function of beam current in figure 4.2-5 for three values of the cavity voltage $v_c$: 15 MV, 20 MV and 25 MV.

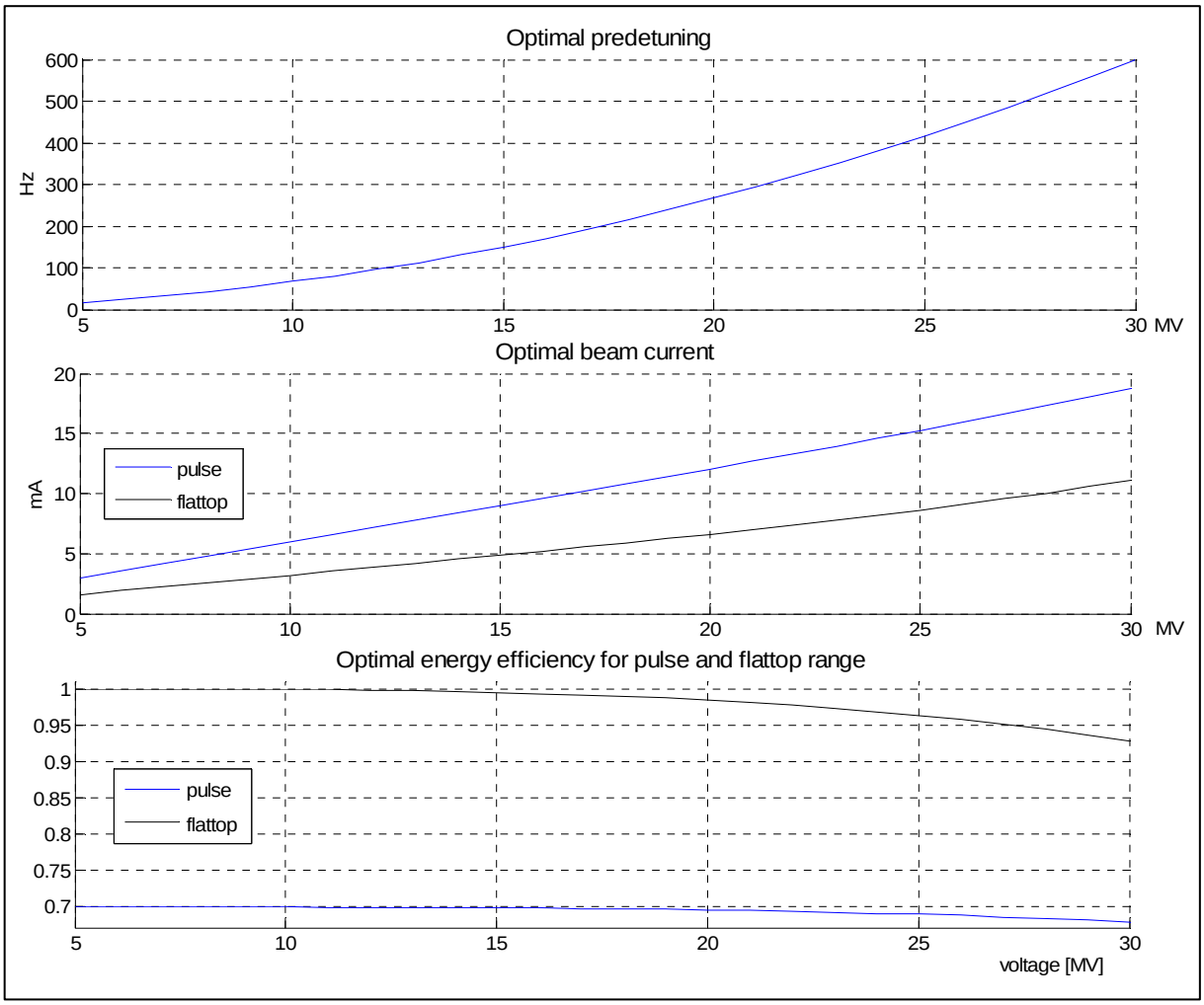


Fig. 4.2-3. The optimal condition for the pulse energy efficiency $\eta_{po}$ ($t_p$ = 1300 μs) and for *flattop* energy efficiency $\eta_{bo}$ ($t_b$ = 800 μs), as a function of the cavity *flattop* voltage $v_c$ for the beam phase $\varphi_b = 0$. The required *predetuning* is the same for the pulse and *flattop* cases.

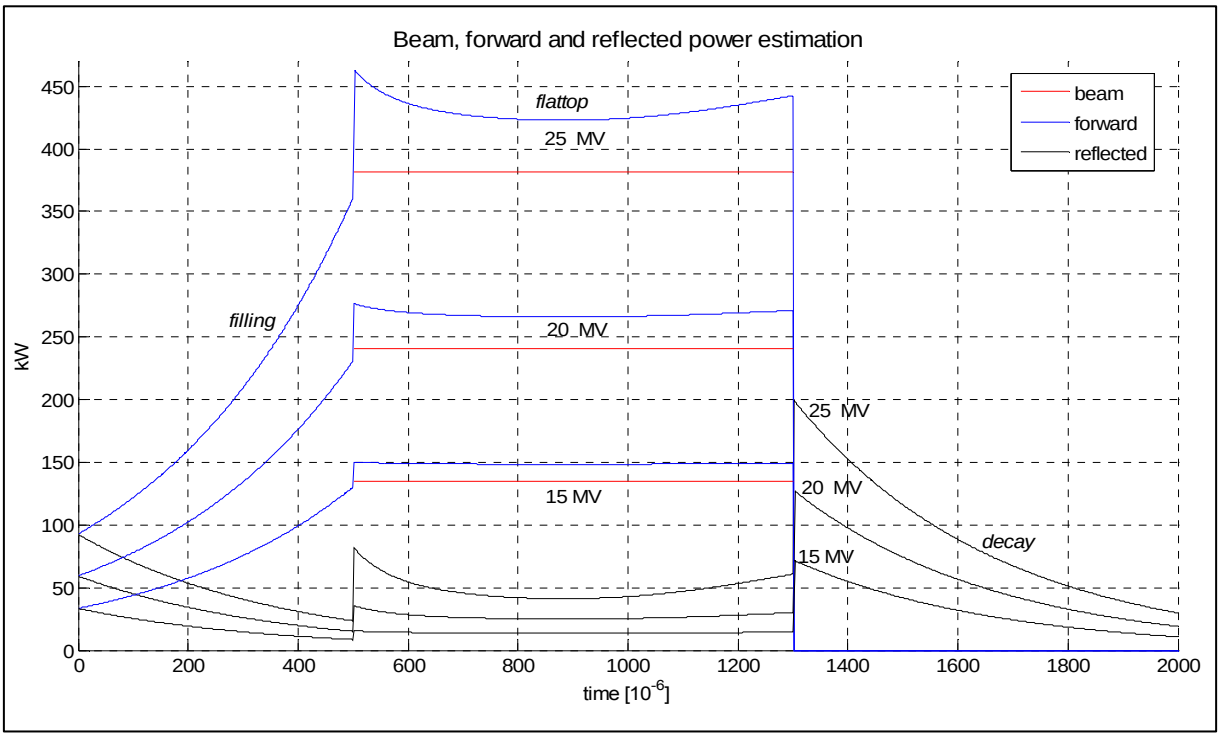


Fig. 4.2-4. The estimation of beam, forward and reflected power, corresponding to figure 4.2-2, for the optimal pulse energy efficiency $\eta_{po}$ for three values of the cavity voltage $v_c$: 15 MV, 20 MV and 25 MV.

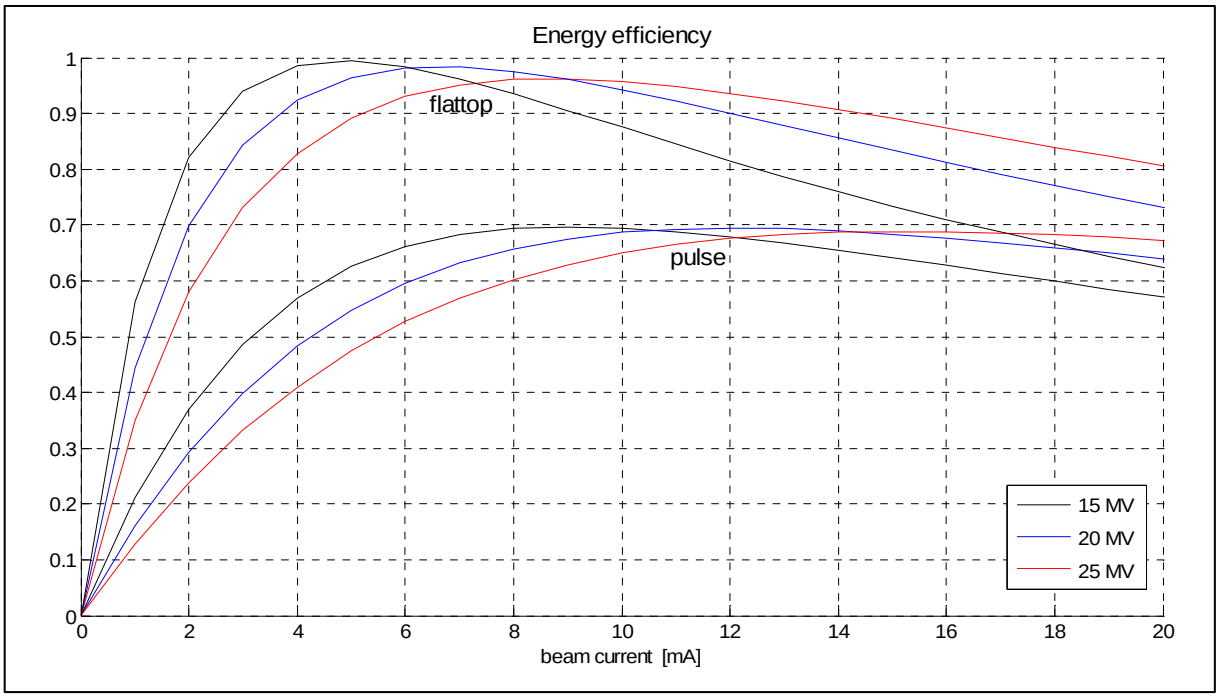


Fig. 4.2-5. The *flattop* energy efficiency $\eta_b$ and the pulse energy efficiency $\eta_b$, (refer to equation 4.1-20 and 4.2-2), as a function of beam current, (beam phase $\varphi_b = 0$) for three values of the cavity voltage $v_c$: 15 MV, 20 MV, 25 MV.

# 5. ALGORITHMS OF CAVITY CONTROL

## 5.1 Adaptive Feed-Forward by direct inverse control

A general formula of the cavity control, given by the inverse electrical model (refer to equation 4.2-1), requires a recognition of the factor $\mathbf{A}_e(t) = -\omega_{1/2} + \boldsymbol{j}\Delta\omega(t)$, for a desired output $\mathbf{v}^{\bullet}(t)$. In previous chapter, the cavity detuning is prearranged by the output of the mechanical model $\Delta\omega(t)$ for a given input $v^2(t)$ and for a *predetuning* value $\Delta\omega_0$. If the mechanical model is inaccessible, what is a practical case, the cavity detuning is unforeseen. The cavity control with an inaccessible internal input of the mechanical model, but with a recognized output after a pulse, is considered in this chapter. The arrangement of the cavity model control, based on the inverse electrical model, which applies the cavity detuning after a pulse, is presented in fig. 5.1-1.

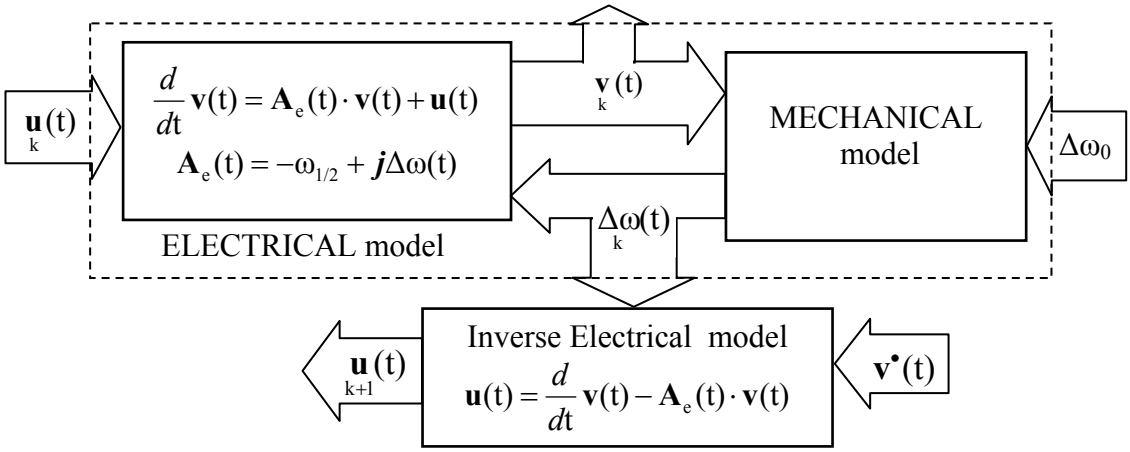


Fig. 5.1-1. A diagram of the adaptive feed-forward control for the cavity model with an inaccessible internal input but with a recognized output of the mechanical model.

The proposed adaptive feed-forward algorithm for a repetitive process assumes that the following operation: $\mathbf{u}_k(t) \mapsto \mathbf{u}_{k+1}(t)$ is a contractive mapping for successive pulses k, k+1. The function $\mathbf{u}(t)$ is considered as an element of a complete metric space. According to the fixed point theorem [29], a sequence of iterative operations converges to a unique solution: $\mathbf{u}_{k\to\infty}(t) \mapsto \mathbf{u}^{\bullet}(t)$. Consequently, the following relations are true for the cavity detuning $\Delta\omega_{k\to\infty}(t) \mapsto \Delta\omega^{\bullet}(t)$ and for the cavity output $\mathbf{v}_{k\to\infty}(t) \mapsto \mathbf{v}^{\bullet}(t)$. The cavity model control is carried on iteratively by using a recognized detuning $\Delta\omega_k(t)$ from previous k-th pulse to estimate the cavity control $\mathbf{u}_{k+1}(t)$ for a next (k+1)-th pulse and for the required trajectory $\mathbf{v}^{\bullet}(t)$, according

to fig. 5.1-1 [30]. The prearranged cavity *predetuning* $\Delta\omega_0$ is stable, for a given iterative process, and can be adjusted in the next iterative process according to equation 4.2-4.

For the *filling* range, the iterative process to attain the final state of the cavity $\mathbf{v}_c^{\bullet}$ = 25 MV, at the time $t_f$ = 500 μs, is considered for the required amplitude linear trajectory $v^{\bullet}(t) = v_c^{\bullet} \cdot \frac{t}{t_f}$, according to equation 4.1-14. The initial input $\underset{1}{\mathbf{u}}(t)$ of the cavity model has been set for the arbitrary detuning value $\underset{0}{\Delta\omega}(t) \equiv 0$. According to the input-output relation from table 4.2-1, the adaptive feed-forward control for a k-th pulse of the *filling* range is given by

$$\underset{k}{\mathbf{u}}(t) = u(t) \cdot \exp \boldsymbol{j} \underset{k}{\varphi}(t) \quad \text{for} \quad u^{\bullet}(t) = v_c^{\bullet} \frac{1 + \omega_{1/2} t}{t_f} \quad \text{and} \quad \underset{k}{\varphi}(t) = \varphi_c^{\bullet} - \int_t^{t_f} \underset{k-1}{\Delta\omega}(\tau) d\tau \tag{5.1-1}$$

The corresponding output $\underset{k}{\mathbf{v}}(t)$ is as follows (refer to equation 4.1-2):

$$\underset{k}{\mathbf{v}}(t) = \int_0^t \left( u^{\bullet}(\tau) \cdot e^{-\omega_{1/2}(t-\tau)} \cdot \exp \boldsymbol{j} \, \underset{k}{d\varphi}(t,\tau) \right) d\tau \cdot \exp \boldsymbol{j} \underset{k}{\varphi}(t) \tag{5.1-2}$$

for $\underset{k}{d\varphi}(t,\tau) = \int_{\tau}^{t} \left( \underset{k}{\Delta\omega}(\eta) - \underset{k-1}{\Delta\omega}(\eta) \right) d\eta$. The function series $\left| \underset{k}{\mathbf{v}}(t) \right|$, of the cavity output, is limited by the final amplitude trajectory $v^{\bullet}(t) = \int_0^t u^{\bullet}(\tau) \cdot e^{-\omega_{1/2}(t-\tau)} d\tau \le \left| \underset{k}{\mathbf{v}}(t) \right|$, and the series $\underset{k}{\mathbf{v}}(t)$ converges to the following limit $\mathbf{v}^{\bullet}(t) = v^{\bullet}(t) \cdot \exp \boldsymbol{j} \varphi^{\bullet}(t)$ for $\varphi^{\bullet}(t) = \varphi_c^{\bullet} - \int_t^{t_f} \Delta\omega^{\bullet}(\tau) d\tau$, if $\underset{k \to \infty}{d\varphi}(t,\tau) = 0$.

For the *flattop* range, the contractive condition of the iterative control $\underset{k}{\mathbf{u}}(t) = \left( \omega_{1/2} - \boldsymbol{j} \, \underset{k-1}{\Delta\omega}(t) \right) \cdot \mathbf{v}_c^{\bullet}$ is estimated by the functions norms, as follows:

$$\left\| \underset{k+1}{\Delta\omega}(t) - \underset{k}{\Delta\omega}(t) \right\| < \left\| \underset{k}{\Delta\omega}(t) - \underset{k-1}{\Delta\omega}(t) \right\| = \frac{1}{v_c^{\bullet}} \left\| \underset{k+1}{\mathbf{u}}(t) - \underset{k}{\mathbf{u}}(t) \right\|. \tag{5.1-3}$$

The required *flattop* value of $\mathbf{v}_c^{\bullet}$ = 25 MV is small enough for the fast convergence of the adaptive process.

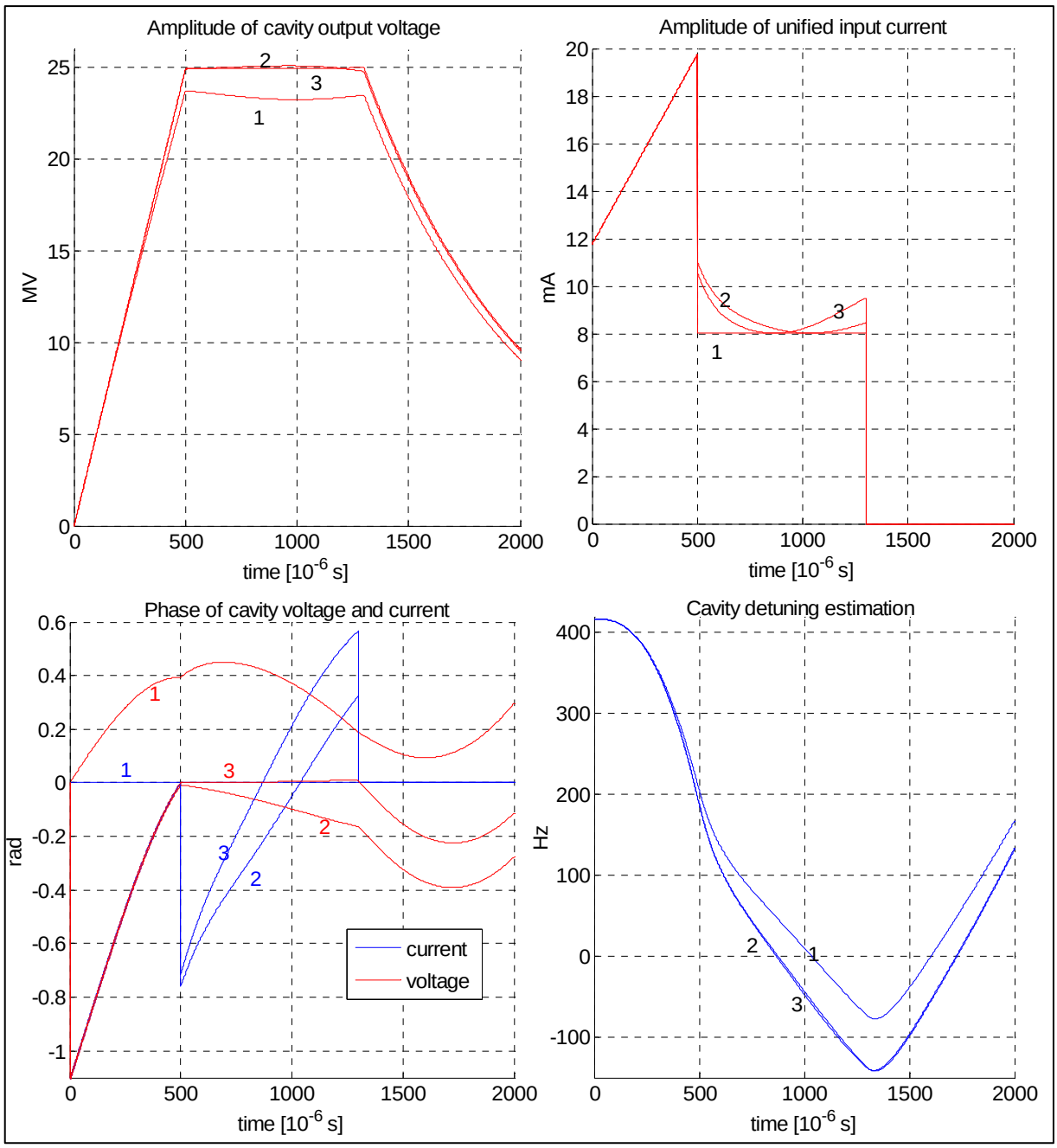


Fig. 5.1-2. Simulation results of the adaptive feed-forward by direct inverse control of the cavity model for three steps of iteration.

The simulation results of the adaptive feed-forward control of the cavity model, for the first three steps of iteration, are presented in fig. 5.1-2. The discrete model of cavity is defined by the parameters from table 3.1-1. The linear driving of cavity has been chosen for the *filling* range of $t_f = 500$ μs, according to equation 4.1-14.

Actually, the adaptive feed-forward by direct inverse control, as a repetitive process, is useful in a practical implementation when a mechanical model is fully inaccessible for a real cavity control. A reasonable estimation of the cavity detuning is performed by stochastic methods between pulses. The input-output relation of the electrical model is applied for the parameters identification of a real cavity (refer to chapter 6.2). But, an efficiency of the cavity control is strongly limited by an accuracy of the parameters estimation. The relative mean error $\overline{\frac{\Delta v_c}{v_c^\bullet}}$ of *flattop*, as the mean of the absolute error $\Delta v_c = \left| \mathbf{v}_c^\bullet - \mathbf{v}_c \right|$, related to the absolute value of set-point $v_c^\bullet = \left| \mathbf{v}_c^\bullet \right|$ for the *flattop* range, is presented in figure 5.1-3, as a function of the pulse number of the adaptive control process. The two adaptive processes, by direct inverse control, are considered: 1 – with known, actual cavity model parameters, 2 – with unknown but estimated cavity model parameters.

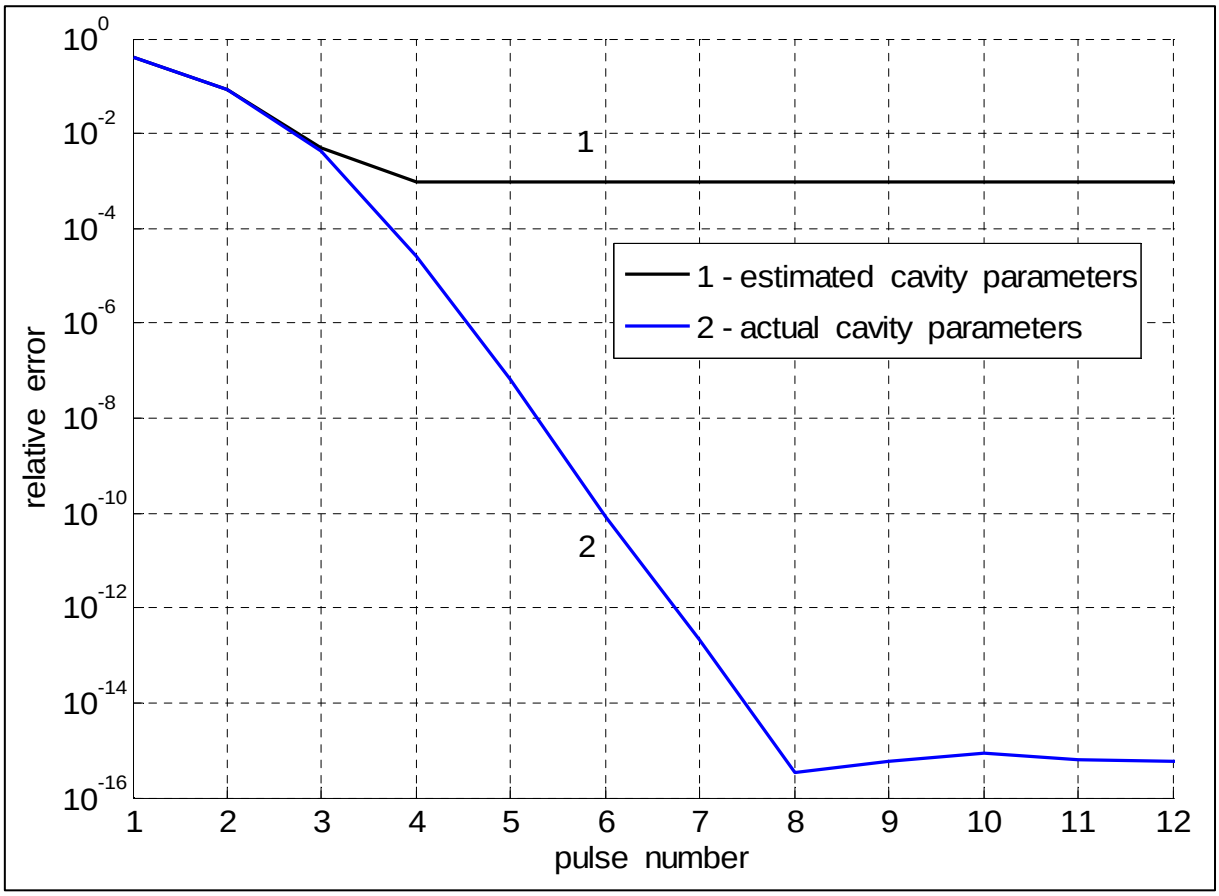


Fig. 5.1-3. The relative mean error of the *flattop*, as a function of pulse number of the adaptive feed-forward by a direct inverse control of the cavity model for two processes: 1 – with known, actual cavity model parameters, 2 – with unknown but estimated cavity model parameters.

The adaptive feed-forward control, treated as a "slow feedback", is especially effective for the *filling* range. Driving under the resonance condition, to achieve a desired state of the cavity, requires a recognition of detuning in advance within the full *filling* range, and can be done iteratively from a pulse to a pulse. However, the adaptive feed-forward control can be modified as a "fast feedback", when executed during a pulse for the *flattop* range. The current detuning of cavity model is applied, for the inverse electrical model, to estimate *on line* the required control for the *flattop* range.

In a more general overview, the adaptive feed-forward algorithm, based on a direct inverse control, can be expressed by a series of linear operations $\underset{k}{P}$ and $\underset{k}{P^{-1}}$ for successive pulses k and k+1 as follows:

$$\underset{k}{\mathbf{v}} = \underset{k}{P}(\underset{k}{\mathbf{u}}) \quad \Rightarrow \quad \underset{k+1}{\mathbf{u}} = \underset{k}{P^{-1}}(\mathbf{v}^{\bullet}) \quad \Rightarrow \quad \underset{k+1}{\mathbf{v}} = \underset{k+1}{P}\left(\underset{k}{P^{-1}}(\mathbf{v}^{\bullet})\right). \tag{5.1-4}$$

The cavity process is represented by a linear and reversible operator $\underset{k}{P}$ in *k*-th pulse for the input $\underset{k}{\mathbf{u}}$ and output $\underset{k}{\mathbf{v}}$. The input $\underset{k+1}{\mathbf{u}}$ for the next (*k*+1)-th pulse is determined by the inverse operator $\underset{k}{P^{-1}}$ for the required output $\mathbf{v} = \mathbf{v}^{\bullet}$. Parameters of the operator $\underset{k}{P}$ depend on the cavity state, and are recognized after *k*-th pulse. Initial parameters are taken arbitrarily for the first pulse. The convergence conditions are set as follows:

$$\lim_{k\to\infty} \underset{k}{P} = P, \qquad \lim_{k\to\infty} \underset{k}{\mathbf{u}} = \mathbf{u} = P^{-1}(\mathbf{v}^{\bullet}), \qquad \lim_{k\to\infty} \underset{k}{\mathbf{v}} = \mathbf{v} = P(\mathbf{u}). \tag{5.1-5}$$

Signals **u** and **v** are vector representations for discrete time. Discrete model of the cavity defines an operation P(**u**) = **v**, which is expressed recursively for successive steps *n* and *n*+1 for any pulse, as follows (ref. to equation 3.1.3)

$$\mathbf{v}_{n+1} = \mathbf{A}_n \cdot \mathbf{v}_n + \mathbf{u}_n \quad \text{for the initial value of } \mathbf{v}_0 = \mathbf{0}, \tag{5.1-6}$$

where the time-varying *system phasor* is: $\mathbf{A}_n = (1 - \omega_{1/2}T) + \boldsymbol{j}\Delta\omega_n T$.

Inverse model of the cavity defines the inverse operation $P^{-1}(\mathbf{v}) = \mathbf{u}$ expressed recursively as

$$\mathbf{u}_n = \mathbf{v}_{n+1} - \mathbf{A}_n \cdot \mathbf{v}_n. \tag{5.1-7}$$

The inverse operation is performed o*ffline* between the pulses without regard to causality.

The adaptive feed-forward algorithm, by direct inverse control, determines the unified input $\mathbf{u} = \mathbf{u}_g - \mathbf{u}_b$, including a generator $\mathbf{u}_g$ and a beam loading $\mathbf{u}_b$ signals. But, a beam loading

and all additive disturbances are generally unknown. Moreover, a discrepancy of the cavity model and output disturbance causes a mismatch $\Delta\mathbf{v} = \mathbf{v}^{\bullet} - \mathbf{v}$ between the achieved output $\mathbf{v}$ and the required output $\mathbf{v}^{\bullet}$ for the real plant. The following modification of the feed-forward algorithm leads to cancelling of plant disturbances. Disturbance cancelation includes unidentified but repetitive beam loading and mismatch of the cavity model.

## 5.2 Adaptive Feed-Forward by differential inverse control

Let us consider a more general cavity process, represented by a linear operator $\underset{k}{\mathrm{P}}$, for a *k*-th pulse (fig. 5.2-1), given by

$$\underset{k}{\mathbf{v}} = \underset{k}{\mathrm{P}}(\underset{k}{\mathbf{u}}) + \underset{k}{\mathbf{w}} \quad \text{for} \qquad \underset{k}{\mathbf{u}} = \underset{k}{\mathbf{u}_g} - \mathbf{u}_b \tag{5.2-1}$$

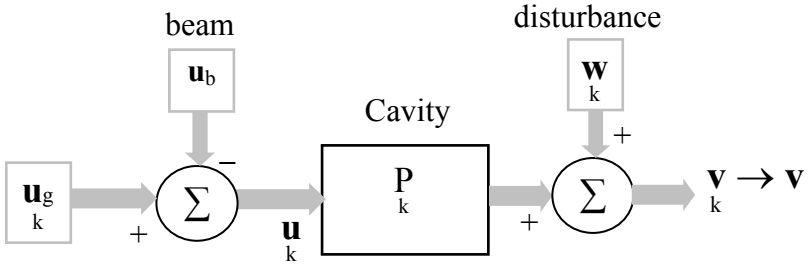


Fig. 5.2-1. The cavity process represented by a linear operator $\underset{k}{\mathrm{P}}$ for a *k*-th pulse, the input component of a beam loading $\mathbf{u}_b$ and the output deterministic disturbance $\underset{k}{\mathbf{w}}$.

The cavity is driven with a resultant input $\underset{k}{\mathbf{u}}$ including the generator output $\underset{k}{\mathbf{u}_g}$ and a repetitive beam loading $\mathbf{u}_b$. The external output $\underset{k}{\mathbf{v}}$ includes a deterministic disturbance $\underset{k}{\mathbf{w}}$, which comprises a mismatch of the cavity model to the real plant. The required cavity output is $\mathbf{v}^{\bullet}$. The desired condition for the input $\underset{k+1}{\mathbf{u}}$, in the next (*k*+1)-th pulse, takes operator parameters and disturbance values from *k*-th pulse, and is stated as follows:

$$\mathbf{v}^{\bullet} = \underset{k}{\mathrm{P}}(\underset{k+1}{\mathbf{u}}) + \underset{k}{\mathbf{w}} \quad \text{for} \qquad \underset{k+1}{\mathbf{u}} = \underset{k+1}{\mathbf{u}_g} - \mathbf{u}_b \tag{5.2-2}$$

Consequently, subtracting equation 5.2-1 from 5.2-2, a disturbance $\underset{k}{\mathbf{w}}$ and a beam component $\mathbf{u}_b$ are cancelled, and the recursive solution for a next (*k*+1)-th input is given by

$$\underset{k+1}{\mathbf{u}_g} = \underset{k}{\mathbf{u}_g} + \underset{k}{\mathrm{P}}^{-1}(\mathbf{v}^{\bullet} - \underset{k}{\mathbf{v}}) \qquad \text{or in differential form} \qquad \underset{k+1}{\Delta\mathbf{u}_g} = \underset{k}{\mathrm{P}}^{-1}(\underset{k}{\Delta\mathbf{v}}). \tag{5.2-3}$$

The parameters of the reversible operator $\underset{k}{P}$ depend on the output $\underset{k}{\mathbf{v}}$ and are recognized after a pulse. The unknown parameters can be estimated *offline* by the *least squares* method regarding the measured input and output data for a given model structure (ref. to chapter 6.2). The internal input $\underset{k}{\mathbf{u}}$ and the external output $\underset{k}{\mathbf{v}}$ are considered for parameters identification according to the given input – output relation: $(\underset{k}{\mathbf{u}}, \underset{k}{\mathbf{v}}) \Rightarrow \underset{k}{P}$. But, for an unforeseen beam component $\mathbf{u}_b$, the cavity should be recognized in advance, for a required state, without a beam loading, so $\mathbf{u}_b = \mathbf{0}$ and $\underset{k}{\mathbf{u}} = \underset{k}{\mathbf{u}_g}$.

The convergence conditions are stated as follows:

$$\lim_{k\to\infty} P_k = P, \quad \lim_{k\to\infty} \mathbf{u}_k = \mathbf{u} = \mathbf{u}_g, \quad \lim_{k\to\infty} \mathbf{w}_k = \mathbf{w}, \quad \lim_{k\to\infty} \mathbf{v}_k = \mathbf{v} = P(\mathbf{u}) + \mathbf{w}. \tag{5.2-4}$$

Actually, the cavity control process quickly converges to the final state, similarly to the adaptive feed-forward driving presented in figure 5.1-2.

The simulation procedure has been carried out for the cavity model defined by parameters from table 3.1-1. Constant cavity driving has been chosen for the *filling* range (500 μs), according to equation 4.1-13, for parameter b = 1. All initial data: input $\underset{0}{\mathbf{u}}$, output $\underset{0}{\mathbf{v}}$ and the cavity detuning $\underset{0}{\Delta\omega}$ are set to zero. The relative mean error $\dfrac{\overline{\Delta v_c}}{v_c^{\bullet}}$ of *flattop*, as the mean of the absolute error $\Delta v_c = \left|\mathbf{v}_c^{\bullet} - \mathbf{v}_c\right|$, related to the absolute value of set-point $v_c^{\bullet} = \left|\mathbf{v}_c^{\bullet}\right|$ for the *flattop* range, is presented in fig. 5.2-2, as a function of the pulse number of the adaptive control process. The following two adaptive processes, by differential inverse control, without a beam, are considered:

1 – with known, actual cavity model parameters, 2 – with unknown, but estimated, cavity model parameters.

The adaptive feed-forward control is quite immune from a disparity of the cavity model. This is due to disturbance cancelling, which is inherent in the differential formula (5.2-3). Simulation results confirm, that for ±10% of mismatch of the cavity parameters, practically, the perturbation of a final *flattop* stabilization is not observed after several cycles of the transient state. So, the cavity parameters estimation is not a critical issue for the *flattop* stabilization. However, the real cavity detuning determines the optimal energy conditions required for *filling* and *flattop* ranges (ref. to formula 4.1-8, 4.1-21 and 4.2-3).

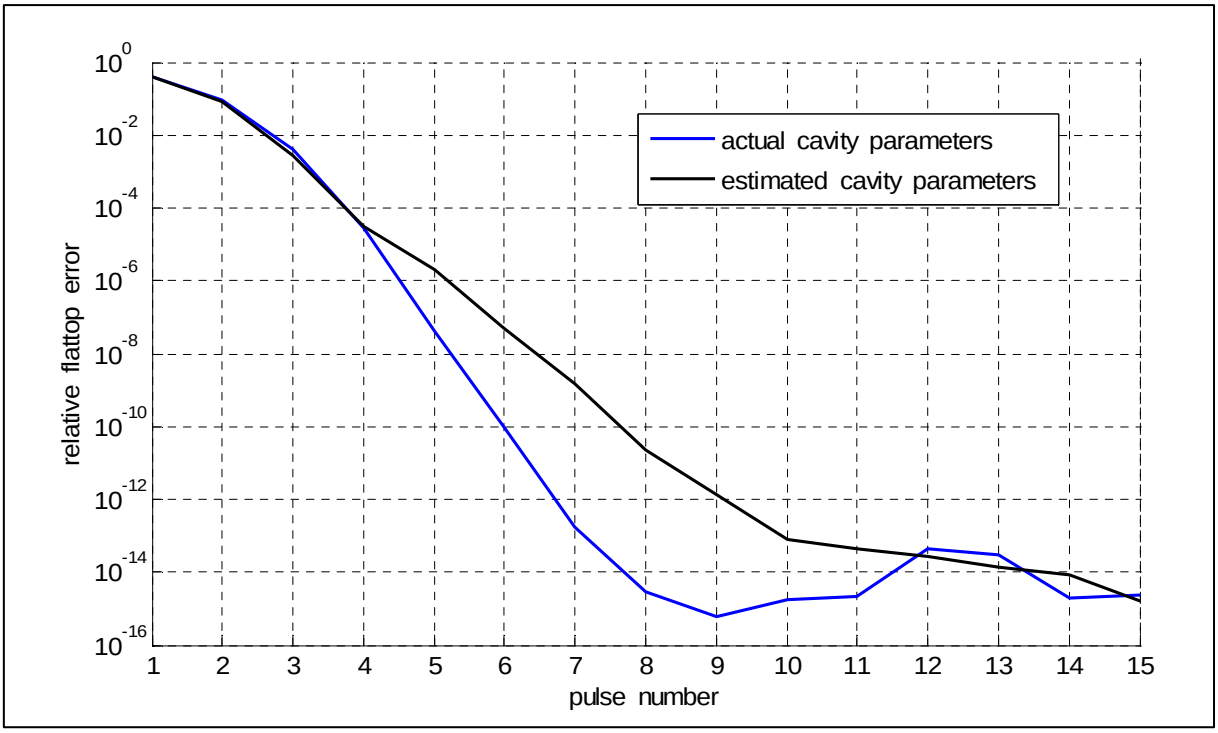


Fig. 5.2-2. The relative mean error of *flattop*, as a function of pulse number of the adaptive feed-forward, by differential inverse control of the cavity model, without a beam, for the following two processes: 1 – with known, actual cavity model parameters, 2 – with unknown but estimated cavity model parameters

***Detuning adjustment***

The optimization of energy efficiency, with respect to *predetuning* value $\Delta\omega_0$, can be done after a recognition of the cavity detuning for the desired output $\mathbf{v}^\bullet$. The actual mean value $\overline{\Delta\omega_b} = \frac{1}{t_b}\int_0^{t_b} \Delta\omega(t)dt$ of *flattop* detuning can be adjusted by the correction value of *predetuning* $d(\Delta\omega_0)$, given by (ref. to 4.2-4)

$$d(\Delta\omega_0) = \omega_{1/2} g_o \tan\varphi_b - \overline{\Delta\omega_b}\,, \tag{5.2-5}$$

where $g_0$ is the optimal factor according to 4.1-21, for the *flattop* energy efficiency, or according to 4.2-3, for the pulse energy efficiency. Resultant change of the cavity detuning requires again an iterative control process expressed by equation 5.2-3. Consequently, a modified input **u** satisfies again the ultimate equations 5.2-4. The simulation results of the cavity model control are presented in figure 5.2-3. The cavity model is defined by the parameters from table 3.1-1. The constant cavity driving has been chosen for the *filling* range (500 μs), according to equation 4.1-13, for the parameter b = 1. Three values of the cavity

*predetuning* are considered: optimal – 0: $\Delta\omega_0 = 430$ Hz, over tuned – 1: $\Delta\omega_0 = 530$ Hz, under tuned – 2: $\Delta\omega_0 = 330$. For all cases, the cavity has reached the same required state for the *flattop* value of $\mathbf{v}_c = 25$ MV, without a beam.

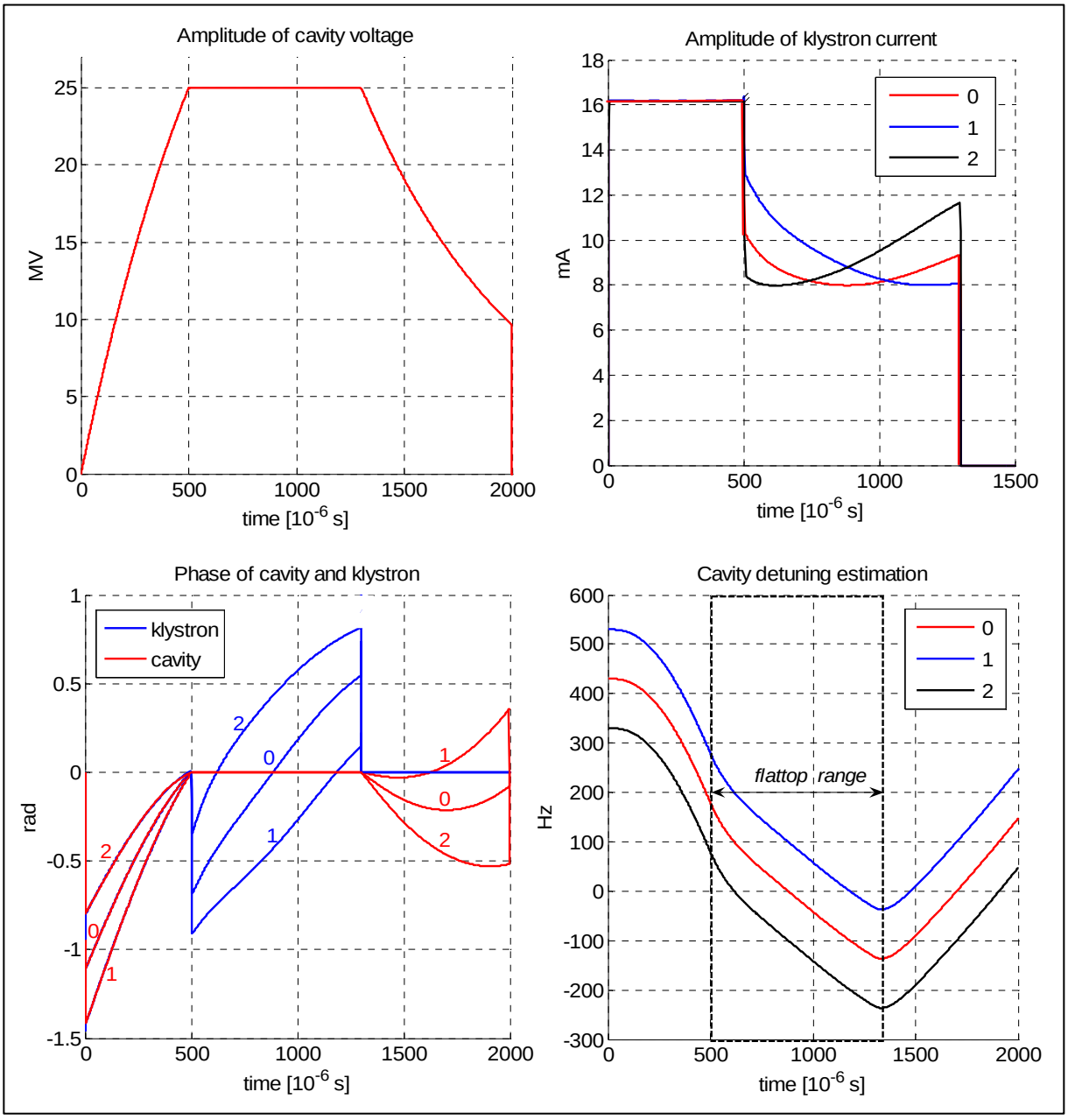


Fig. 5.2-3. The results of differential inverse control for three values of *predetuning*: optimal – 0: $\Delta\omega_0 = 430$ Hz, over tuned – 1: $\Delta\omega_0 = 530$ Hz, under tuned – 2: $\Delta\omega_0 = 330$.

***Beam loading compensation***

The beam can be injected in the beginning of the *flattop* range, after achieving the required final state of the cavity, according to relation 5.2-4. The estimated, ultimate parameters of the operator P, before beam injection, are saved and used for the general control algorithm 5.2-3. The uncompensated beam loading changes the cavity state during the first pulse. In spite of a temporary model mismatch with the real plant during *flattop* range, the previous ultimate state of the cavity can be recovered, after several pulses of the transient condition. Then, the relation 5.2-4 is valid again, for the same value of internal input **u**, but with new components given by

$$\mathbf{u} = (\mathbf{u}_g + \Delta\mathbf{u}_g) - \mathbf{u}_b . \tag{5.2-6}$$

An additional component of the generator signal $\Delta\mathbf{u}_g$ compensates the beam loading, according to equation 5.2-6. So, the beam component is recognized as follows

$$\mathbf{u}_b = \Delta\mathbf{u}_g . \tag{5.2-7}$$

Now, the cavity phase $\angle\mathbf{v}_c = \varphi_c$, for the *flattop* set-point, can be adjusted to meet requirements for the relative beam phase $\varphi_b$ as follows

$$\varphi_c = \angle\mathbf{u}_b - \varphi_b . \tag{5.2-8}$$

Change of the required cavity *flattop* phase $\angle\mathbf{v}_c$ requires again an iterative control process, which is expressed by equation 5.2-3, but without a change of the operator P parameters. Consequently, modified inputs **u** and $\mathbf{u}_g$ satisfy again the ultimate equations 5.2-4 and 5.2-6.

Simulation results of the adaptive feed-forward, by differential inverse control, of the cavity model, with a beam, are presented in fig. 5.2-4. The cavity model is defined by the parameters from table 3.1-1. The constant cavity driving has been chosen for the *filling* range (500 μs), according to equation 4.1-13, for the parameter b = 1. The beam value is $\mathbf{i}_b$ = 8 mA and the beam phase is $\varphi_b$ = 0 during *flattop* range (800 μs). The first two pulses of the transient state are selected in figure 5.2-4. The fifth pulse practically recovers the cavity previous condition, before the beam injection, in the " zero pulse", according to relation 5.2-4.

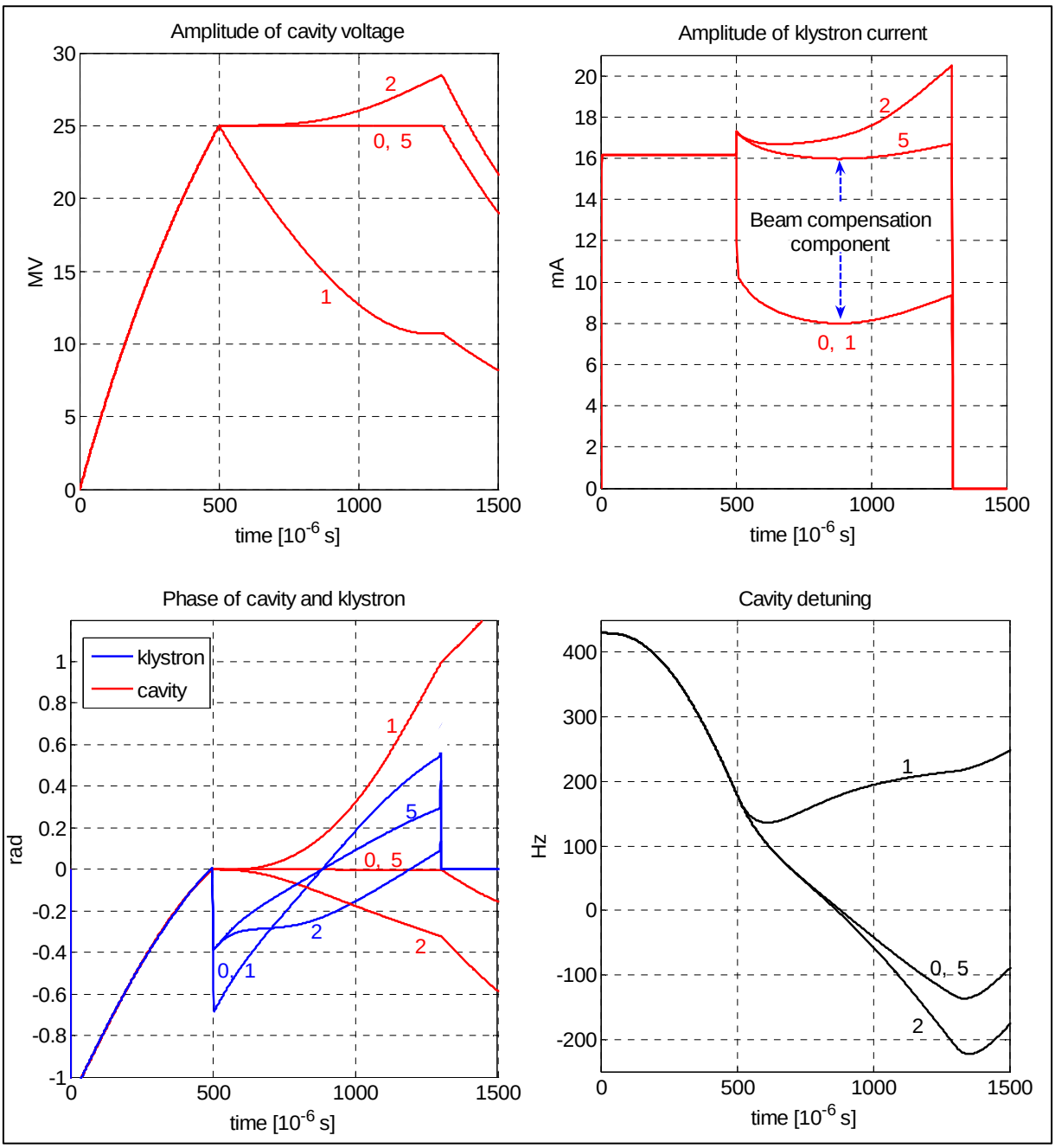


Fig. 5.2-4. The results of differential inverse control of the cavity with a beam for four pulses: 0 – pulse without beam, 1,2, 5 – pulse number, with the beam, ( $\mathbf{i}_b = 8$ mA , $\varphi_b = 0$).

The relative mean error $\frac{\overline{\Delta v_c}}{v_c^{\bullet}}$ of *flattop*, as the mean of the absolute error $\Delta v_c = \left|\mathbf{v}_c^{\bullet} - \mathbf{v}_c\right|$, related to the absolute value of set-point $v_c^{\bullet} = \left|\mathbf{v}_c^{\bullet}\right|$ for the *flattop* range, is presented in figure 5.2-5, as a function of the pulse number of the adaptive control process. The following three adaptive feed-forward processes, by differential inverse control of the estimated cavity model, are considered: 1 – before beam injection with initial estimation of

the cavity model parameters, 2 – after beam injection with fixed, estimated before, parameters of the cavity model, 3 – after beam stop with fixed parameters of the cavity model.

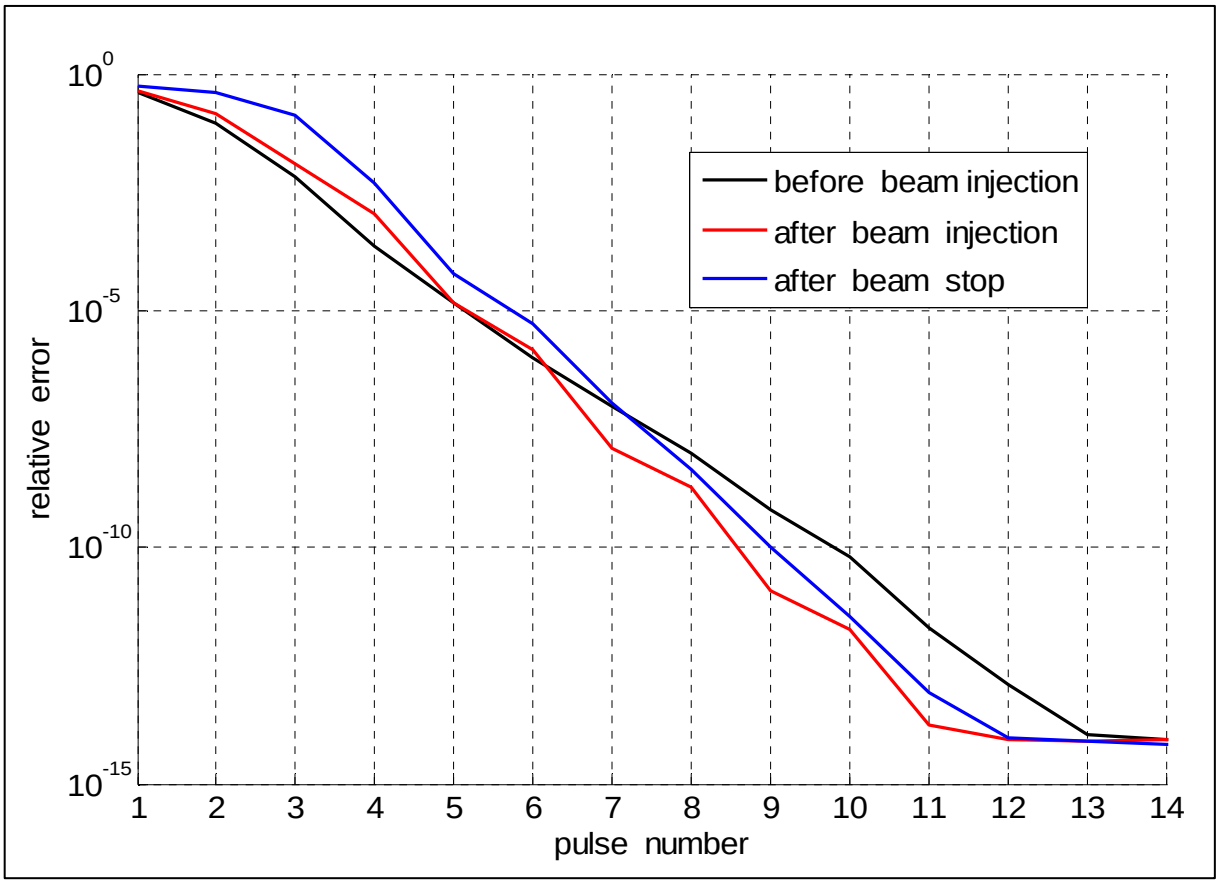


Fig. 5.2-5. The relative mean error, as a function of pulse number of the adaptive feed-forward, by differential inverse control of the estimated cavity model, for three processes: 1 – before beam injection (starting from "zero"), 2 – after beam injection, 3 – after beam stop.

The flowchart of the adaptive processes of the cavity control is outlined in figure 5.2-6, where *s* is the decisive control parameter. The procedure begins for pulse k = 0. The initial data is given arbitrarily or is loaded from a memory. The primary adaptive control process, without beam, includes the cavity parameters estimation for s = 0. The data of ultimate process is saved after a convergence. The adaptive process can start again for the detuning adjustment (s = 1). Then, the beam compensation (s = 2), and next, the beam estimation, or cavity phase adjustment (s = 3) can be adaptively performed, but without the cavity parameters estimation.

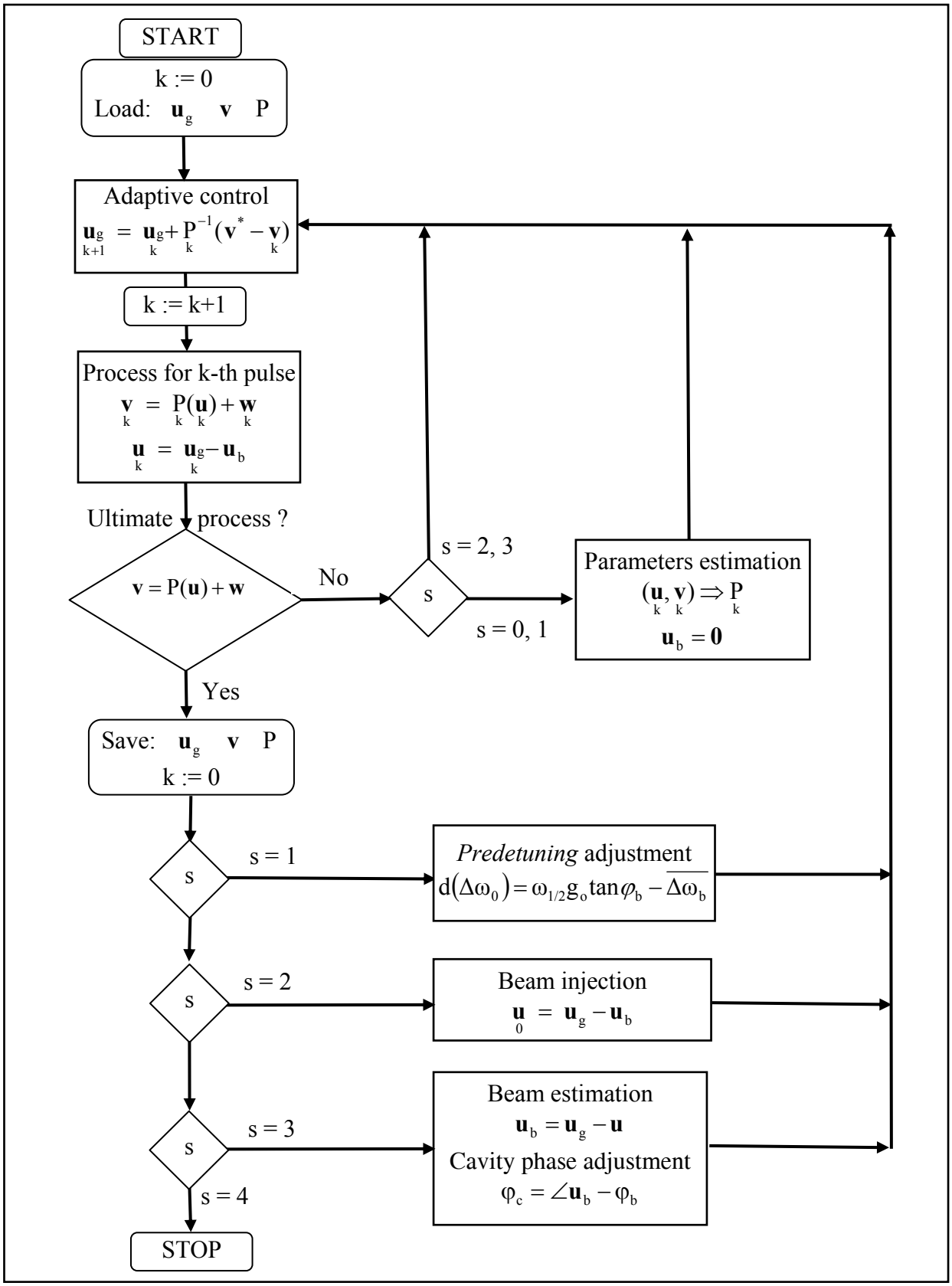


Fig. 5.2-6. Outline of the adaptive feed-forward processes by differential inverse control dependent on the control parameter s = 0, 1, 2, 3, 4.

Simulation results confirm practically the ideal control of the cavity deterministic model for *filling* and *flattop* ranges, applying the adaptive feed-forward, by differential inverse control. The achieved relative mean error of *flattop* is $\frac{\overline{\Delta v_c}}{v_c^\bullet} \sim 10^{-14}$ without and with a beam alike. The actual parameters of the cavity and beam remain unknown for the algorithm procedure, but are estimated respectively.

### 5.3 Adaptive feedback by differential inverse control

Let us consider the cavity process given by 5.2-1, represented by a linear and reversible operator P, for any pulse, with omitted index *k*, as follows

$$\mathbf{v} = \mathrm{P}(\mathbf{u}) + \mathbf{w} \quad \Leftrightarrow \quad \mathbf{u} = \mathbf{P}^{-1}(\mathbf{v} - \mathbf{w}) \quad \text{for} \quad \mathbf{u} = \mathbf{u}_g - \mathbf{u}_b, \tag{5.3-1}$$

where, **u** is internal input, **v** is external output and **w** is output disturbance.

The required condition for the cavity process is stated as follows

$$\mathbf{v}^\bullet = \mathrm{P}(\mathbf{u}^\bullet) + \mathbf{w} \quad \text{for} \quad \mathbf{u}^\bullet = \mathbf{u}_g^\bullet - \mathbf{u}_b, \tag{5.3-2}$$

where $\mathbf{u}_g^\bullet$ is a desired cavity input for the required cavity output $\mathbf{v}^\bullet$.

Analogous reasoning, like for the feed-forward *offline* differential inverse control, leads to the feedback *online* control, within a pulse, which is expressed in the related form

$$\mathbf{u}_g^\bullet = \mathbf{u}_g + \mathrm{P}^{-1}(\mathbf{v}^\bullet - \mathbf{v}) \quad \text{or in differential form} \quad \Delta\mathbf{u} = \mathrm{P}^{-1}(\Delta\mathbf{v}), \tag{5.3-3}$$

for $\Delta\mathbf{u} = \mathbf{u}_g^\bullet - \mathbf{u}_g$, $\Delta\mathbf{v} = \mathbf{v}^\bullet - \mathbf{v}$.

The desired cavity input $\mathbf{u}_g^\bullet$ is a response based on the previous input value $\mathbf{u}_g$. Due to the stability reason, it is synchronized with an actual internal cavity input delayed by the time *d*, so $\mathbf{u}_g = \mathbf{u}_{g(-d)}^\bullet$ or $\mathbf{u}_g^\bullet = \mathbf{u}_{g(+d)}$. The indices *–d* and *+d* denote time delay and time advance respectively.

The operator P does not include a delay and the total latency *d* of the cavity system has been separated. The parameters of the operator P are recognized *offline* between the pulses and are adaptively estimated until the process reaches the ultimate state, without a beam.

The feedback algorithm, by differential inverse control, can be implemented *online*, in several equivalent configurations, acquired by algebraic transformations of the primary expression 5.3-3. The following three versions are presented below.

1. Direct primary form related to fig. 5.3-1:

$$\mathbf{u}_g^{\bullet} = \mathbf{u}_g + \mathrm{P}^{-1}(\mathbf{v}^{\bullet} - \mathbf{v}). \tag{5.3-4}$$

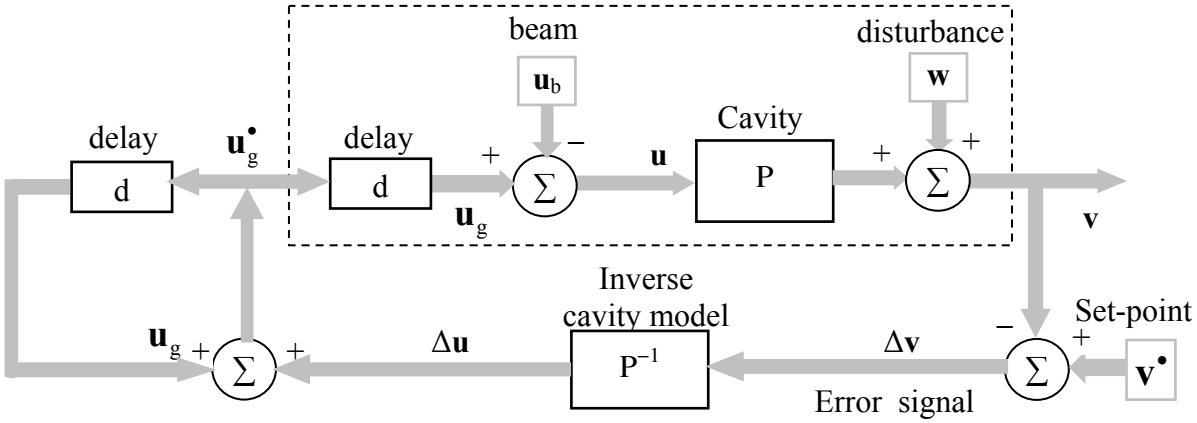


Fig. 5.3-1. Feedback algorithm by differential inverse control according to 5.3-4.

2. Adaptive inverse control with disturbance canceling related to fig. 5.3-2 (B. Widrow [31]).

$$\mathbf{u}_g^{\bullet} = \mathrm{P}^{-1}(\mathbf{v}^{\bullet}) + \mathrm{P}^{-1}\big(\mathrm{P}(\mathbf{u}_g) - \mathbf{v}\big). \tag{5.3-5}$$

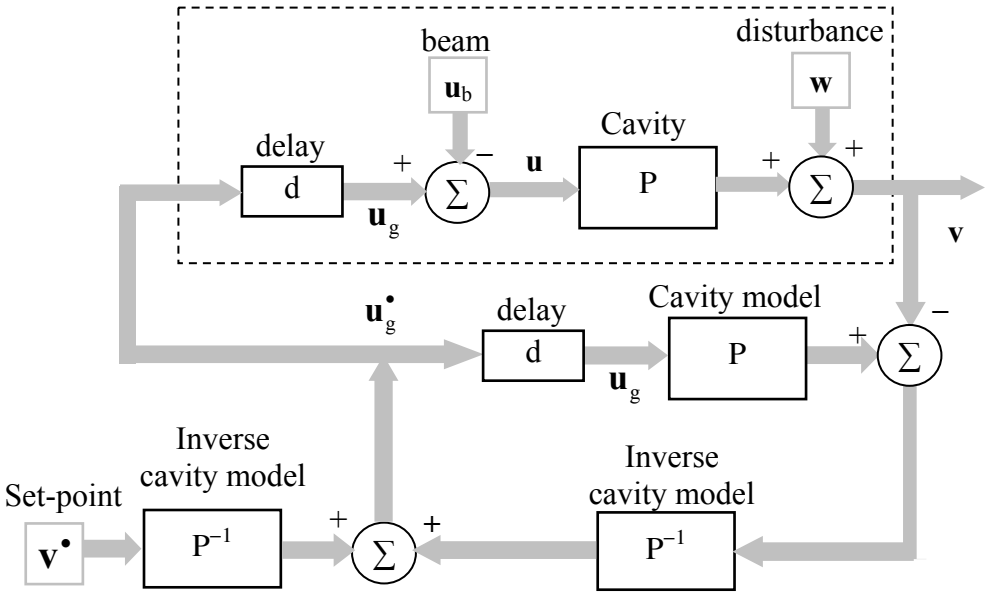


Fig. 5.3-2. Adaptive inverse control with disturbance canceling by Widrow [31] according to 5.3-5.

3. Unified structure related to fig. 5.3-3:

$$\mathbf{u}_g^{\bullet} = \mathrm{P}^{-1}\left(\mathrm{P}(\mathbf{u}_g) + \mathbf{v}^{\bullet} - \mathbf{v}\right). \tag{5.3-6}$$

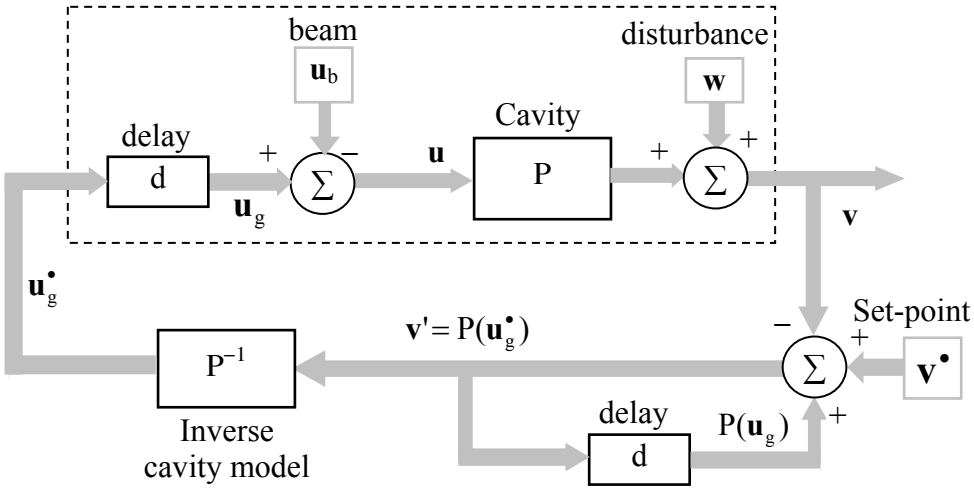


Fig. 5.3-3. Feedback algorithm by differential inverse control according to 5.3-6.

The unified structure with a single summing junction, showed in figure 5.3-3, is considered for the simplified analysis. The block diagram can be reduced to the scheme a) and finally to the scheme b) of fig. 5.3-4.

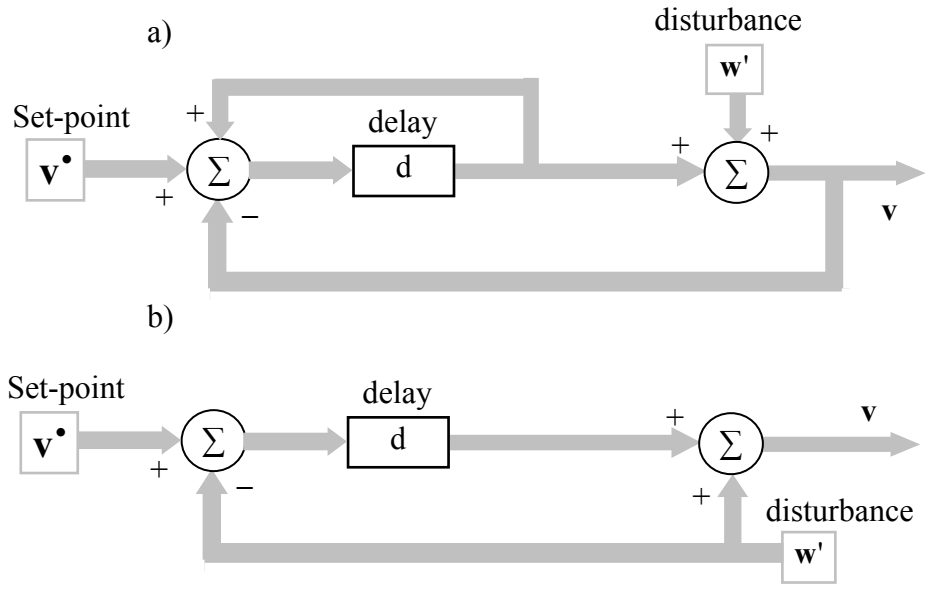


Fig. 5.3-4. The last two stages of the system reduction: a) and b) for the analysis of the feedback algorithm by differential inverse control.

The beam loading component has been moved to the cavity output, so the substituted output disturbance is $\mathbf{w}' = \mathbf{w} - \mathrm{P}(\mathbf{u}_b)$. The cavity model and the inverse cavity model cancel themselves mutually. The delayed feedback signal tries to cancel out its own disturbance. Substituted delay *d* is a common one for the plant and the controller. Consequently, the solution for output **v** is a delayed version of the set-point $\mathbf{v}^{\bullet}_{-d}$ perturbed by a residual difference caused by a delayed feedback disturbance $\mathbf{w}'_{-d}$ as follows

$$\mathbf{v} = \mathbf{v}^{\bullet}_{-d} + \Delta\mathbf{w}'_{-d} \qquad \text{for} \qquad \Delta\mathbf{w}'_{-d} = \mathbf{w}' - \mathbf{w}'_{-d}. \tag{5.3-7}$$

A remaining difference $\Delta\mathbf{w}'_{-d}$ depends on the deviation of a disturbance $\mathbf{w}'$ within a delay time *d*. So, the output **v** requires filtering for a high frequency noise. Moreover, the disturbance component $\mathrm{P}(\mathbf{u}_b)$, caused by a steady beam loading $\mathbf{u}_b$, is time-varying, due to the time-varying parameters of the operator P (cavity detuning).

The discrete cavity process, described by 5.1-6 and 5.1-7, defines the inverse operator $\mathrm{P}^{-1}$, implemented recursively with regard to causality for feedback algorithm configuration, according to fig. 5.3-3 as follows ( the step index has been omitted)

$$\mathbf{u}^{\bullet}_{g} = \mathbf{v}' - \mathbf{A}_{(-1)} \cdot \mathbf{v}'_{(-1)}. \tag{5.3-8}$$

The simulation results of the feedback algorithm, by differential inverse control of the cavity model, are presented in fig. 5.3-5 for the ultimate state with a beam. The unified structure, with a single summing junction, has been chosen for a digital implementation, due to a better numerical performance. The cavity model is defined by the parameters from table 3.1-1. The constant cavity driving has been chosen for the *filling* range (500 μs), according to equation 4.1-13, for the parameter b = 1. The beam value is $\mathbf{i}_b$ = 8 mA and the beam phase is $\varphi_b$ = 0 during *flattop* range (800 μs). The discrete delay time is d = 1 μs. After a fast convergence to the ultimate state without a beam, the cavity parameters have been established and fixed. The new ultimate condition, with a beam, has been settled at once, within a pulse. After turning off the beam, the previous state of the cavity is recovered at once, within a pulse again.

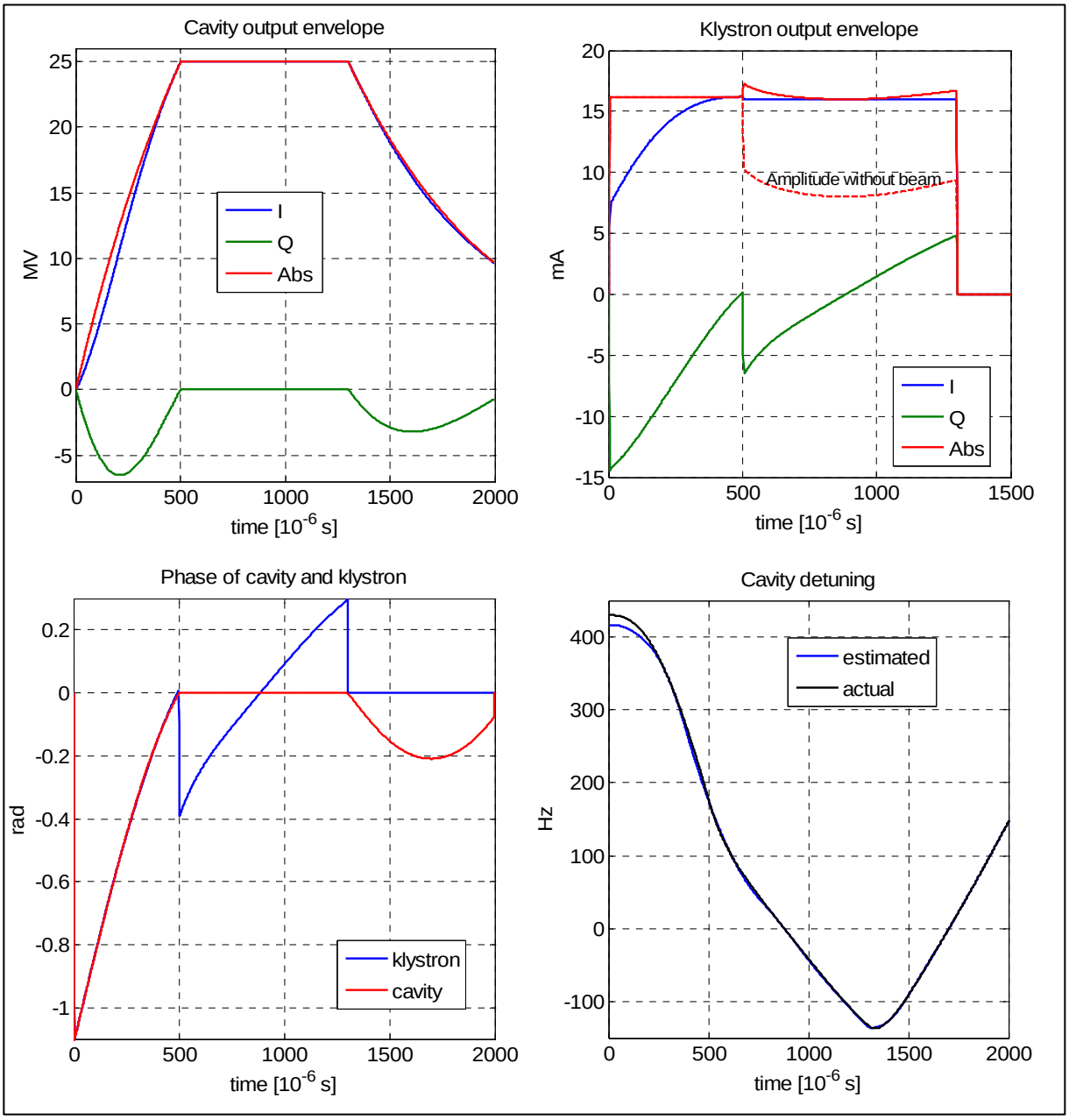


Figure 5.3-5. The simulation results of the feedback algorithm, by differential inverse control of the cavity model, with the beam $\mathbf{i}_b = 8$ mA and the beam phase $\varphi_b = 0$

The relative mean error $\frac{\overline{\Delta v_c}}{v_c^{\bullet}}$ of *flattop*, is presented in figure 5.3-6, as a function of the pulse number of the adaptive feedback control process. The following three feedback processes, by differential inverse control, are considered:

1 – before beam injection with estimation of the cavity model parameters from "zero"

2 – after beam injection with fixed, estimated before, parameters of the cavity model

3 – after beam stop, with fixed parameters of the cavity model.

The diagrams are separated for the two cases:

1 – for the known, actual parameters of the cavity model

2 – for the unknown, but estimated, parameters of the cavity model.

The achieved accuracy of the feedback, by differential inverse control, is $\frac{\overline{\Delta v_c}}{v_c^{\bullet}} \sim 10^{-5}$ without a beam and it is $\sim 10^{-3}$ with a beam, for the estimated cavity model parameters. So, it is limited mainly by the time-varying disturbance **w**' of the estimated cavity model (refer to 5.3-7).

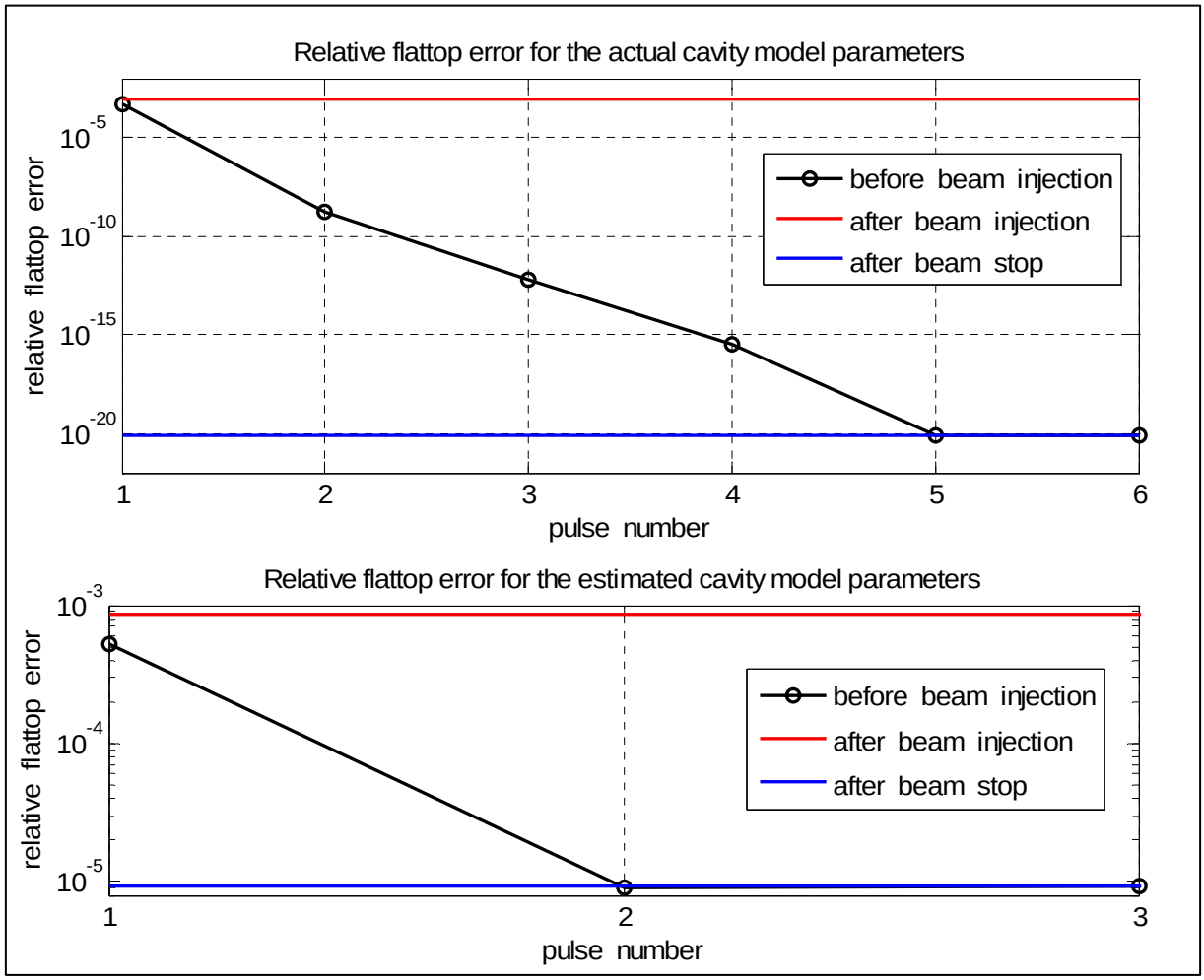


Fig. 5.3-6. The relative *flattop* error, as a function of pulse number of the adaptive feedback by differential inverse control of the cavity model for the three processes: 1 – before beam injection (starting from "zero"), 2 – after beam injection, 3 – after beam stop. The diagrams are separated for the two cases: 1 – for the known, actual cavity model parameters, 2 – for the unknown, but estimated, cavity model parameters.

## 5.4 Complex differential inverse control

The advantages of the differential inverse control are significantly enhanced by simultaneous superposition of the feed-forward and feedback driving (fig. 5.4-1). The cavity is driven with a feed-forward signal $\mathbf{u}_{ff}$, which is based on the previous pulse, and is supported *online* by a feedback signal $\mathbf{u}_{fb}$, so the resultant input is

$$\mathbf{u}_g^{\bullet} = \mathbf{u}_{ff} + \mathbf{u}_{fb}\,. \tag{5.4-1}$$

The feed-forward signal $\mathbf{u}_{ff}$ takes over the cavity control and determines the output component $\mathbf{w}'' = \mathbf{v}_{-d}^{\bullet}$, as delayed version of *Set-point*. Consequently, the reference signal for the feed-back control is also delayed, so the actual *Set-point* = $\mathbf{v}_{-d}^{\bullet}$. Making use of (5.3-7), for a substituted output "disturbance" $\mathbf{w}'' = \mathbf{v}_{-d}^{\bullet}$, the resultant output becomes

$$\mathbf{v} = \mathbf{v}_{-2d}^{\bullet} + \Delta\mathbf{w}''_{-d} = \mathbf{v}_{-2d}^{\bullet} + \mathbf{v}_{-d}^{\bullet} - \mathbf{v}_{-2d}^{\bullet} = \mathbf{v}_{-d}^{\bullet}\,. \tag{5.4-2}$$

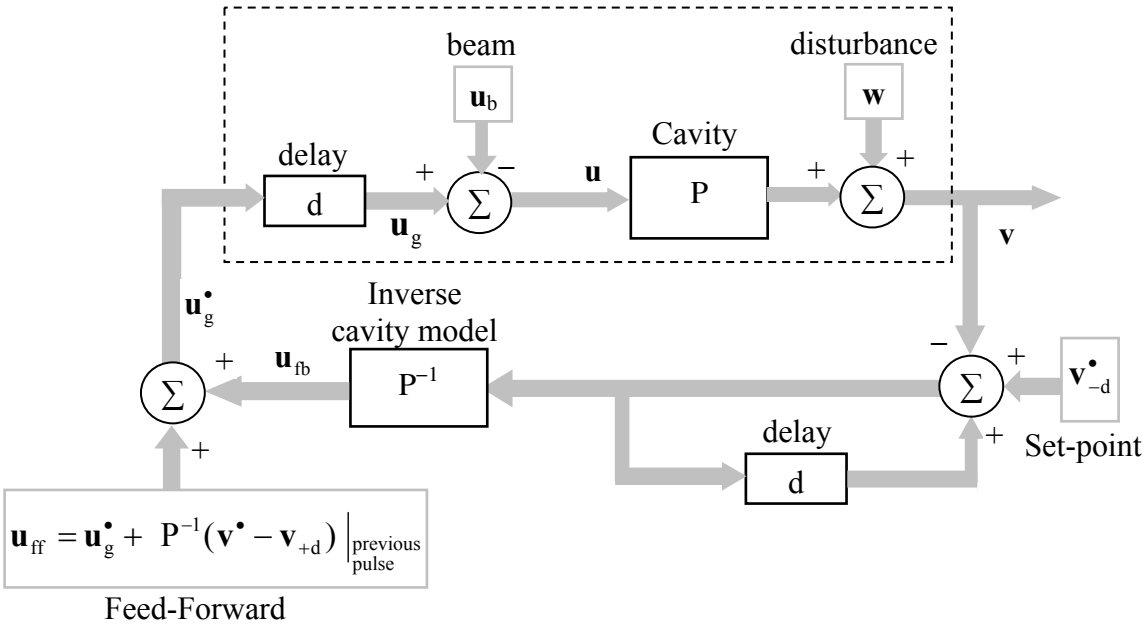


Figure 5.4-1. The complex differential inverse control using feed-forward supported by feedback driving. The indices *–d* and *+d* denote time delay and time advance respectively.

The simulation procedure, analogous to the previous one, has been carried out for the complex differential inverse control of the cavity model using feed-forward supported by feedback driving. The relative mean error $\dfrac{\overline{\Delta v_c}}{v_c^{\bullet}}$ of *flattop*, is presented in figure 5.4-2, as a function of the pulse number of the adaptive control process. The following three adaptive

processes of the complex differential inverse control of the estimated cavity model are considered:

1 – before beam injection, with estimation of the cavity model parameters from "zero"

2 – after beam injection, with fixed, estimated before, parameters of the cavity model

3 – after beam stop, with the established parameters of the cavity model

The simulation results verify a significant improvement of the cavity model driving for *filling* and *flattop* ranges by the complex differential inverse control. The achieved accuracy is $\frac{\overline{\Delta v_c}}{v_c^{\bullet}} \sim 10^{-17}$ for the *flattop* range, without and with a beam. The actual cavity parameters and the actual beam remain unknown for the algorithm procedure, but are estimated respectively.

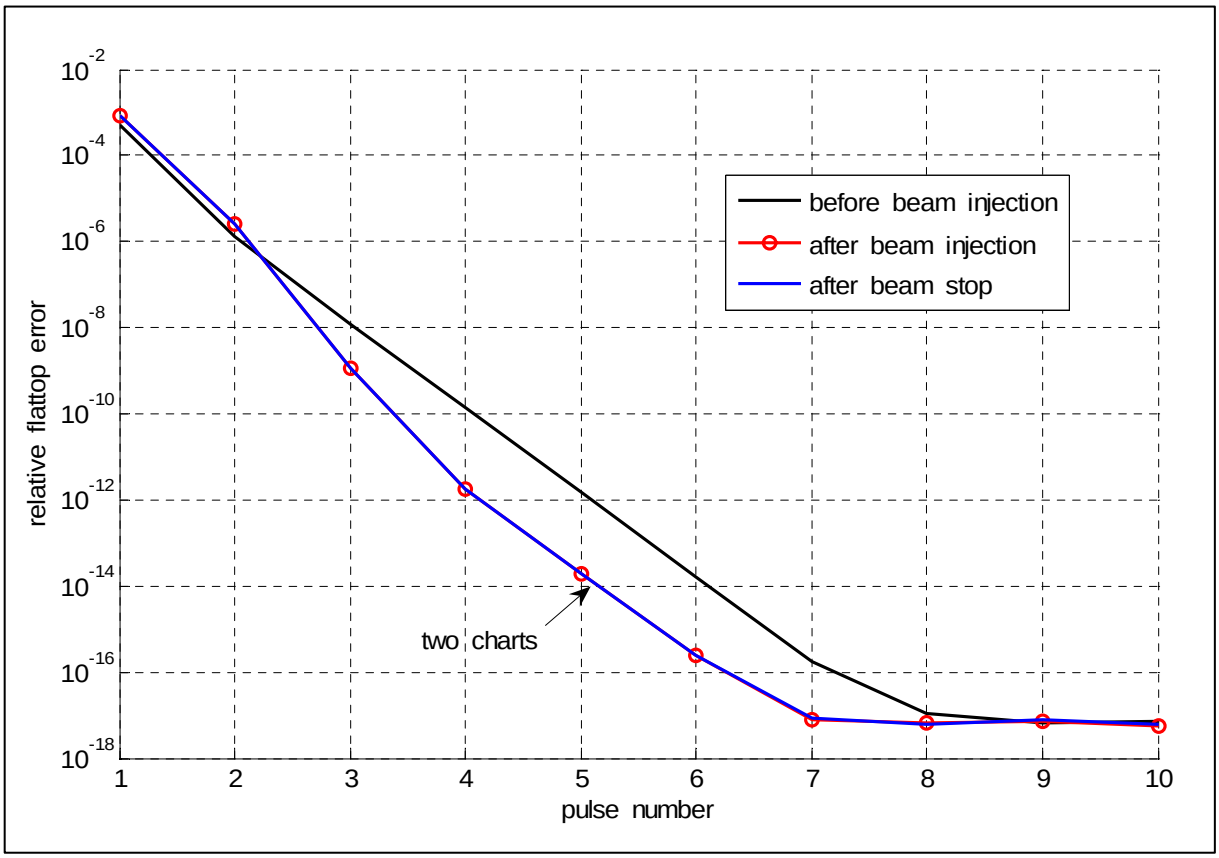


Fig. 5.4-2. The relative *flattop* mean error, as a function of pulse number of the adaptive algorithm by the complex differential inverse control of the estimated cavity model for the three processes: 1 – before beam injection (starting from "zero"), 2 – after beam injection, 3 – after beam stop.

The algorithm of the feed-forward control, supported by feedback driving, can be efficiently simplified applying the *offline* filtered input signal $\mathbf{u}_g^{\bullet}$ from the previous pulse, so

$$\mathbf{u}_{ff} = \mathbf{u}_g^{\bullet}\Big|_{\substack{\text{previous}\\ \text{pulse}}} \quad \text{(refer to the chapter 5.5).} \tag{5.4-2}$$

Finally, the feed-forward signal can be kept stable from a pulse to a pulse as the deterministic control component for the repetitive condition. So, the feedback signal compensates stochastic disturbances only.

A practical implementation of the complex differential inverse control (ref. to chapter 7) requires a filtering of high frequency noise: *online* for the cavity output **v** and *offline* for the feed-forward input $\mathbf{u}_{ff}$. Moreover, the feedback formula (5.3-3) can be modified as follows

$$\Delta\mathbf{u} = \mathrm{P}^{-1}(\alpha\cdot\Delta\mathbf{v}) = \alpha\cdot\mathrm{P}^{-1}(\Delta\mathbf{v}) \quad \text{for} \quad \alpha \le 1 \tag{5.4-3}$$

So, the error signal is attenuated to keep stability, in expense of an accuracy and a rate of convergence, in a case of time delay mismatch between the plant and the controller.

## 5.5 Conventional feedback supported by feed-forward control

An open loop control, by deterministic feed-forward driving, requires recognition of the cavity model. Due to stochastic disturbances and discrepancy of the parameters, the feedback driving by closed loop is a necessary support of the real cavity control. The complex control by the conventional feedback, supported by the feed-forward driving, of the cavity model is considered, according to the scheme presented in fig. 5.5-1.

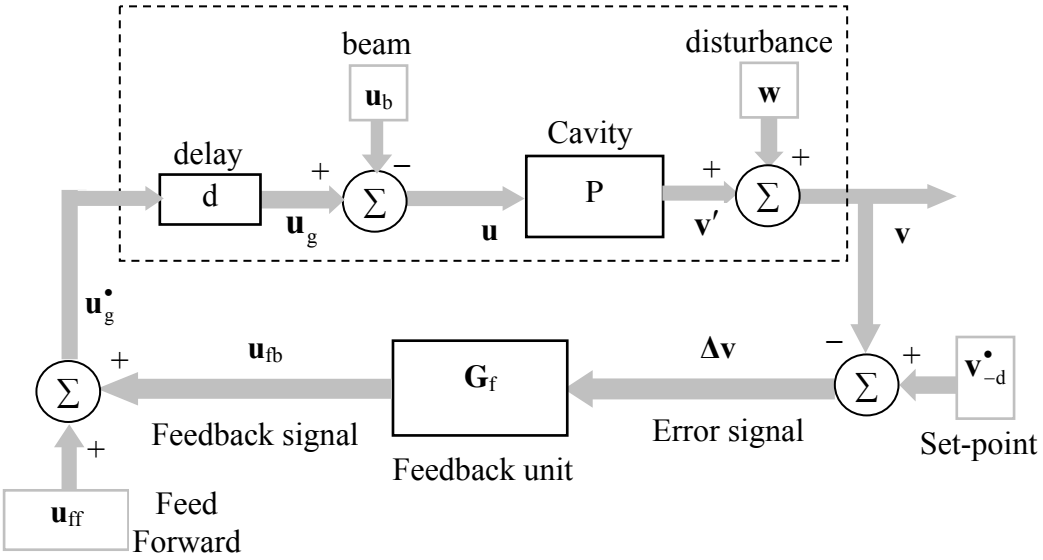


Fig. 5.5-1. The conventional feedback control supported by the feed-forward driving of the cavity model represented by the operator P.

The cavity model, represented by the operator P and the separated delay *d*, is driven by the generator signal $\mathbf{u}_g$, which is a delayed superposition $\mathbf{u}_g^{\bullet}$ of the feed-forward $\mathbf{u}_{ff}$ and the feedback $\mathbf{u}_{fb}$ signals. The output signal $\mathbf{v}$ of the cavity model is compared to the reference signal $\mathbf{v}^{\bullet}$ given by the set-point unit. The proportional feedback unit, modeled by the complex factor $\mathbf{G}_f$, which is the feedback gain, converts the error signal $\Delta\mathbf{v} = \mathbf{v}^{\bullet} - \mathbf{v}$ to the feedback signal.

The discrete cavity model defines the operator $\mathrm{P}(\mathbf{u}) = \mathbf{v}'$, which is expressed recursively as follows (step index has been omitted)

$$\mathbf{v}' = \mathbf{A} \cdot \mathbf{v}'_{(-1)} + \mathbf{u} \qquad \text{for} \qquad \mathbf{A} = (1 - \omega_{1/2}\mathrm{T}) + \boldsymbol{j}\Delta\omega\mathrm{T} \qquad (5.5\text{-}1)$$

***Stability condition***

The resultant dynamics of the cavity control system is described by a difference equation and the homogenous part, responsible for the system stability, is

$$-\mathbf{v} + \mathbf{A} \cdot \mathbf{v}_{(-1)} - \mathbf{G}_f \cdot \mathbf{v}_{(-d)} = 0 \qquad \text{for} \quad d \in \mathrm{N}\,. \qquad (5.5\text{-}2)$$

The stability condition, dependent on the parameters $\mathbf{A}$, $\mathbf{G}_f$, d, is considered by investigation of the characteristic polynomial of a complex variable $\mathbf{z}$, obtained by the *z*-transform and introduced in a convenient form

$$g(\mathbf{z}) = f(\mathbf{z}) - \mathbf{G}_f \quad \text{for} \quad f(\mathbf{z}) = \mathbf{z}^{d-1}(\mathbf{A} - \mathbf{z})\,. \qquad (5.5\text{-}3)$$

For a stability of a discrete system, all the roots of the characteristic polynomial g($\mathbf{z}$) must be included inside the circle $|\mathbf{z}| = 1$. The closed curve f($\mathbf{z}$) = g($\mathbf{z}$) + $\mathbf{G}_f$ for $|\mathbf{z}| = 1$ is considered in the complex plane. As a consequence of the *argument principle*, the factor $\mathbf{G}_f$ lies in the stability area only, if the winding number of the closed curve f($\mathbf{z}$) for $|\mathbf{z}| = 1$ around that area is equal to the degree *d* of the characteristic polynomial. The complex plane with the closed curve f($\mathbf{z}$) for $|\mathbf{z}| = 1$ and the stability area of the factor $\mathbf{G}_f$ is presented in fig. 5.5-2 for the time delay d = 2, as an example. The parameters of the factor $\mathbf{A}$ are taken as follows: T = 1 μs, $\omega_{1/2} = 2\pi \cdot 217$ Hz, $\Delta\omega = 0$ Hz. The absolute value of the factor $\mathbf{A}$ is $|\mathbf{A}| \approx 0.9986$ and slightly depends on the cavity detuning Δω for the given simulation system.

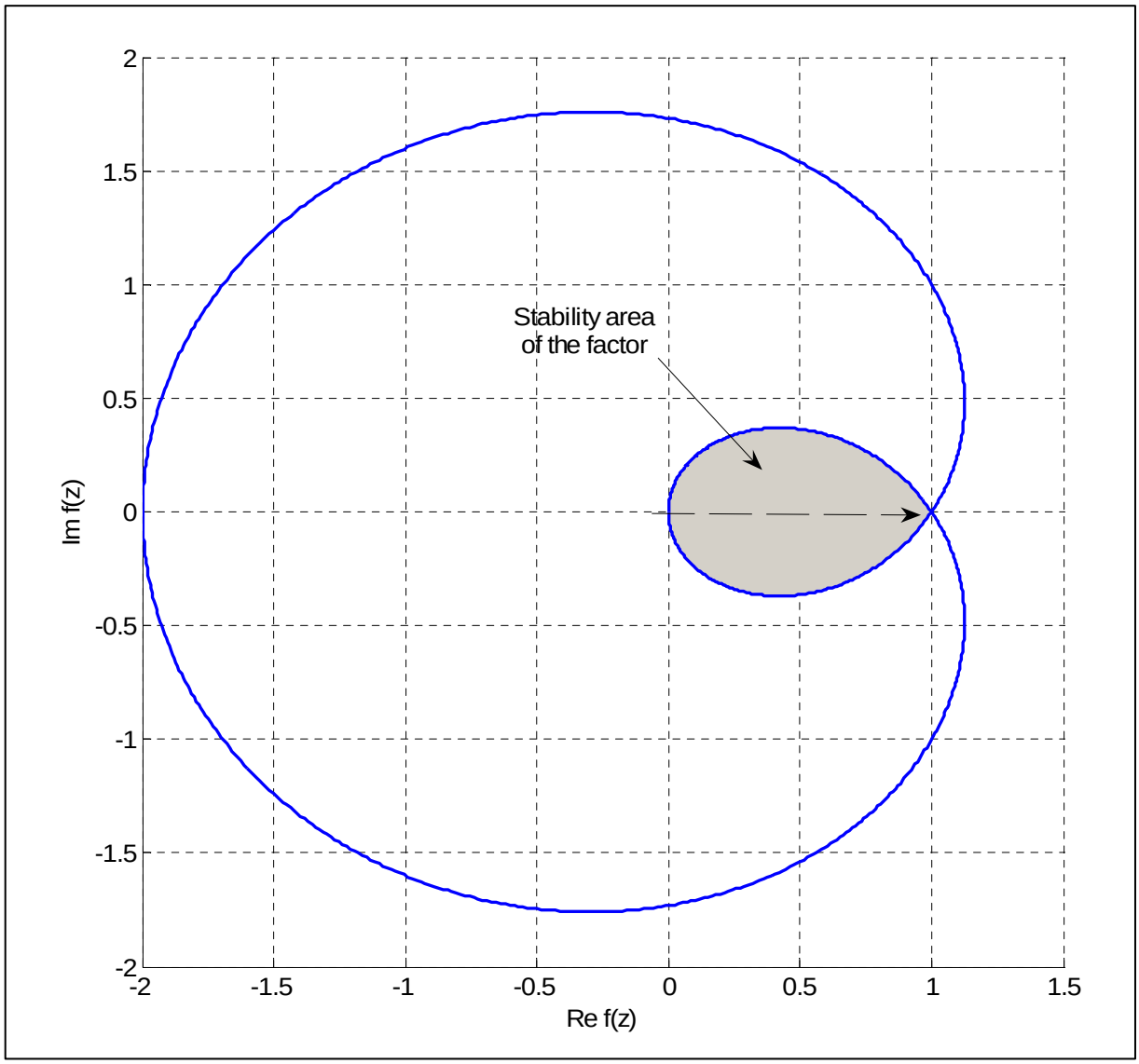


Fig. 5.5-2. The complex plane with the closed curve f(**z**) for $|\mathbf{z}| = 1$ and the stability area of the feedback gain $\mathbf{G}_f$ for the discrete time delay d = 2. Sampling time is T = 1μs.

The stability area of the feedback gain $\mathbf{G}_f$ is presented in figure 5.5-3 as the interior of the closed curves for different values of the time delay *d*, but with the stated above parameters of the factor **A**. The best stability margin is achieved for the real value of the feedback gain $\mathbf{G}_f$. The stability limit of that real value $G_{fd}$, for the respective delay *d*, is efficiently estimated by solving equation f(**z**) = $G_{fd}$ for $|\mathbf{z}| = 1$, under the simplified assumption **A** = 1. The result of this estimation is

$$G_{fd} \approx 2\sin\frac{\pi}{2(2d-1)}. \qquad (5.5\text{-}4)$$

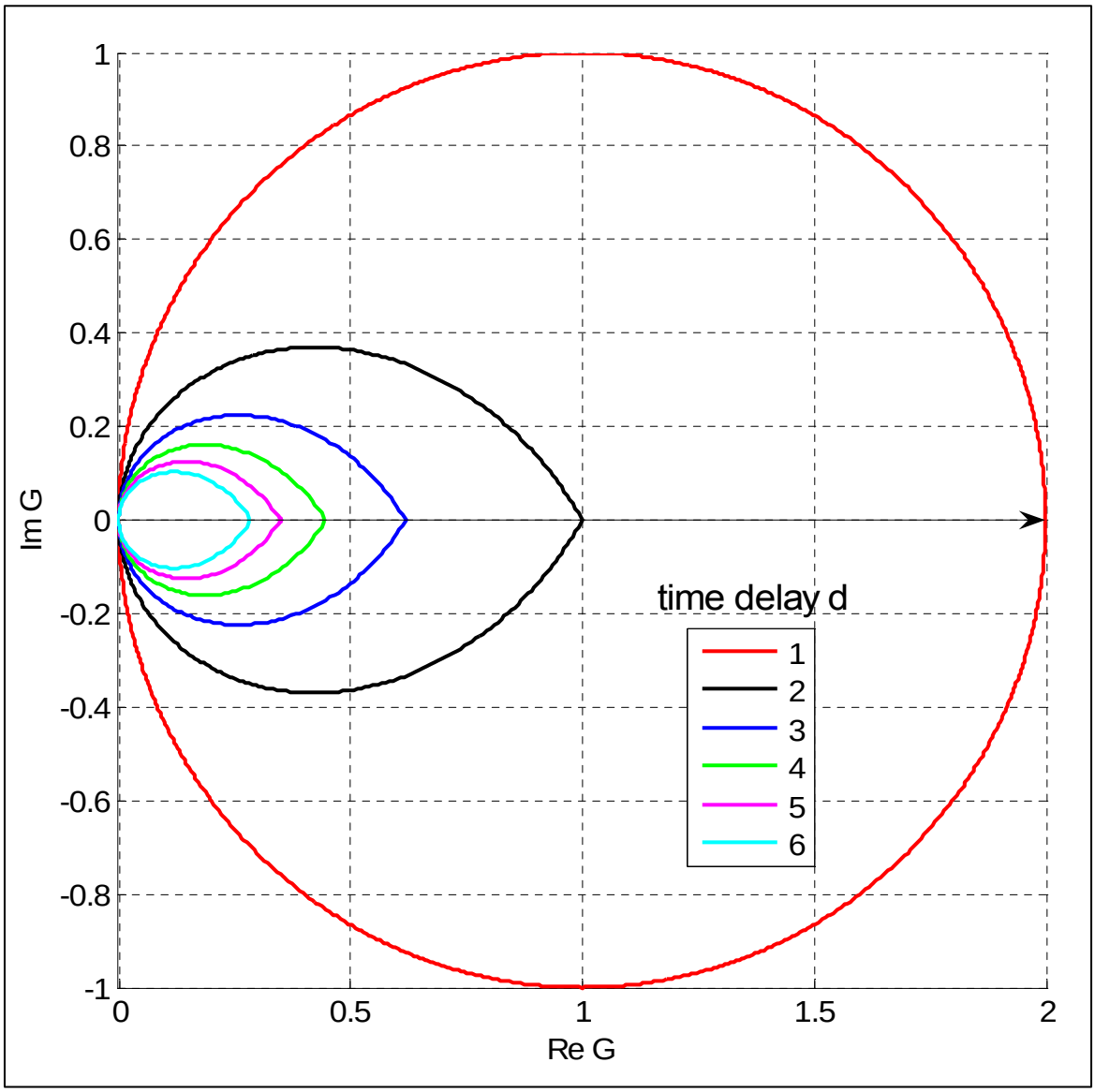


Fig. 5.5-3. The complex plane with the stability area of the feedback gain $\mathbf{G}_f$ for different values of the discrete time delay *d*. Sampling time T = 1μs.

***Steady state condition***

The steady state for the achieved *flattop* value $\mathbf{v}_c$ can be expressed by (any delay has been neglected)

$$\mathbf{v}_c = \mathbf{G}_L \cdot \left( \Delta\mathbf{v}_c + \frac{\mathbf{u}_{ff} - \mathbf{u}_b}{\mathbf{G}_f} \right) + \mathbf{w} \qquad (5.5\text{-}5)$$

where, $\mathbf{G}_L = \dfrac{\mathbf{G}_f}{1-\mathbf{A}} = \dfrac{\mathbf{G}_f}{\omega_{1/2}T - \boldsymbol{j}\Delta\omega T}$ is the loop gain and $\Delta\mathbf{v}_c = \mathbf{v}_c^{\bullet} - \mathbf{v}_c$ is the *flattop* error.

Additionally, the resonant loop gain $\mathbf{G}_{L0}$ is introduced as the reference gain value, defined for the cavity detuning $\Delta\omega = 0$, as follows

$$\mathbf{G}_{L0} = \frac{\mathbf{G}_f}{\omega_{1/2} T}. \tag{5.5-6}$$

Another, useful form for the steady state is given by

$$\mathbf{v}_c = \mathbf{G}_s \cdot \left( \mathbf{v}_c^{\bullet} + \frac{\mathbf{u}_{ff} - \mathbf{u}_b}{\mathbf{G}_f} \right) + \mathbf{w} \cdot (1 - \mathbf{G}_s) \tag{5.5-7}$$

where, $\mathbf{G}_s = \dfrac{\mathbf{G}_f}{1 - \mathbf{A} + \mathbf{G}_f} = \dfrac{\mathbf{G}_L}{1 + \mathbf{G}_L}$ is the static gain.

The *flattop* relative error is $\dfrac{\Delta \mathbf{v}_c}{\mathbf{v}_c^{\bullet}} = \dfrac{\mathbf{G}_s}{\mathbf{G}_L} = \dfrac{1}{1 + \mathbf{G}_L}$ for the feedback control alone. without feed-forward support, and without a beam, and output disturbance. The efficiency of the feedback control alone, is considered by the simulation procedure under the analogous condition to the previous one in this chapter. The *flattop* relative mean error $\dfrac{\overline{\Delta v_c}}{v_c^{\bullet}}$ of the feedback control for $\mathbf{v}_c^{\bullet}$ = 25 MV is presented in figure 5.5-4, as a function of the resonant loop gain $\mathbf{G}_{L0}$. The charts for the processes, without and with the beam of 8 mA, are plotted with the logarithmic scale. The time delay is d = 1. The stability limit of the resonant loop gain is $\mathbf{G}_{L0} \approx 1470$.

***Complex control***

The efficiency of the conventional feedback is significantly enhanced by the simultaneous support of feed-forward control (refer to fig. 5.5-1). Actually, the feed-forward signal takes over the cavity control so, the feedback signal compensates only the stochastic disturbances.

The simulation procedure has been carried out for the adaptive feed-forward, by differential inverse control of the cavity model, supported by the conventional feedback driving. The simulation condition are analogous to that of the complex control in the chapter 5.4. The *flattop* relative mean error $\dfrac{\overline{\Delta v_c}}{v_c^{\bullet}}$ is presented in fig. 5.5-5, as a function of the pulse number of the adaptive control process. The time delay is d = 1.

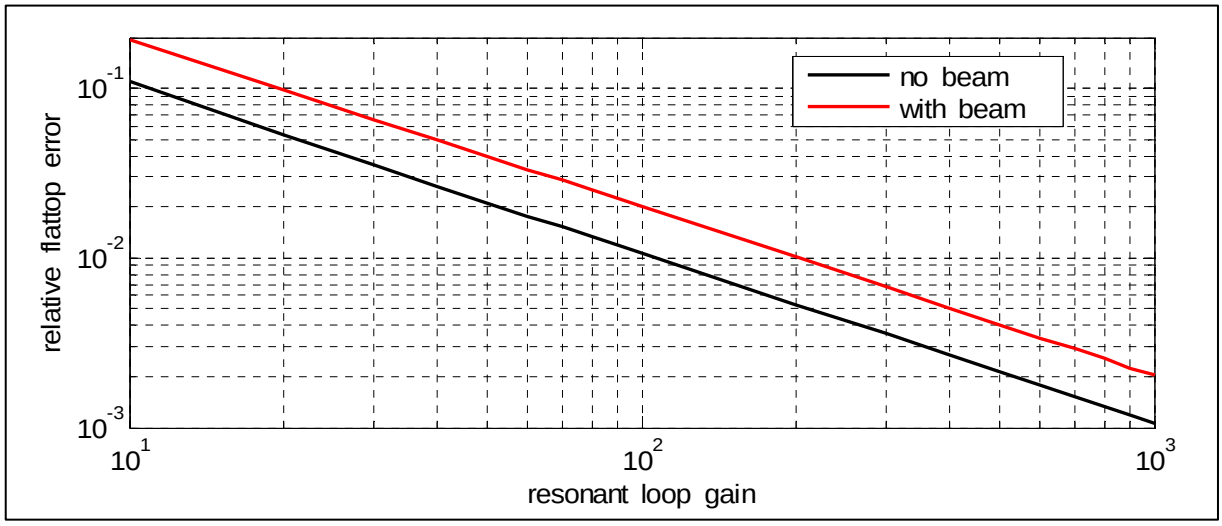


Fig. 5.5-4. The relative *flattop* mean error of the feedback control alone for $\mathbf{v}_c^{\bullet}$ = 25 MV, as a function of the resonant loop gain. The charts for the processes without and with the beam of 8 mA are plotted with the logarithmic scale.

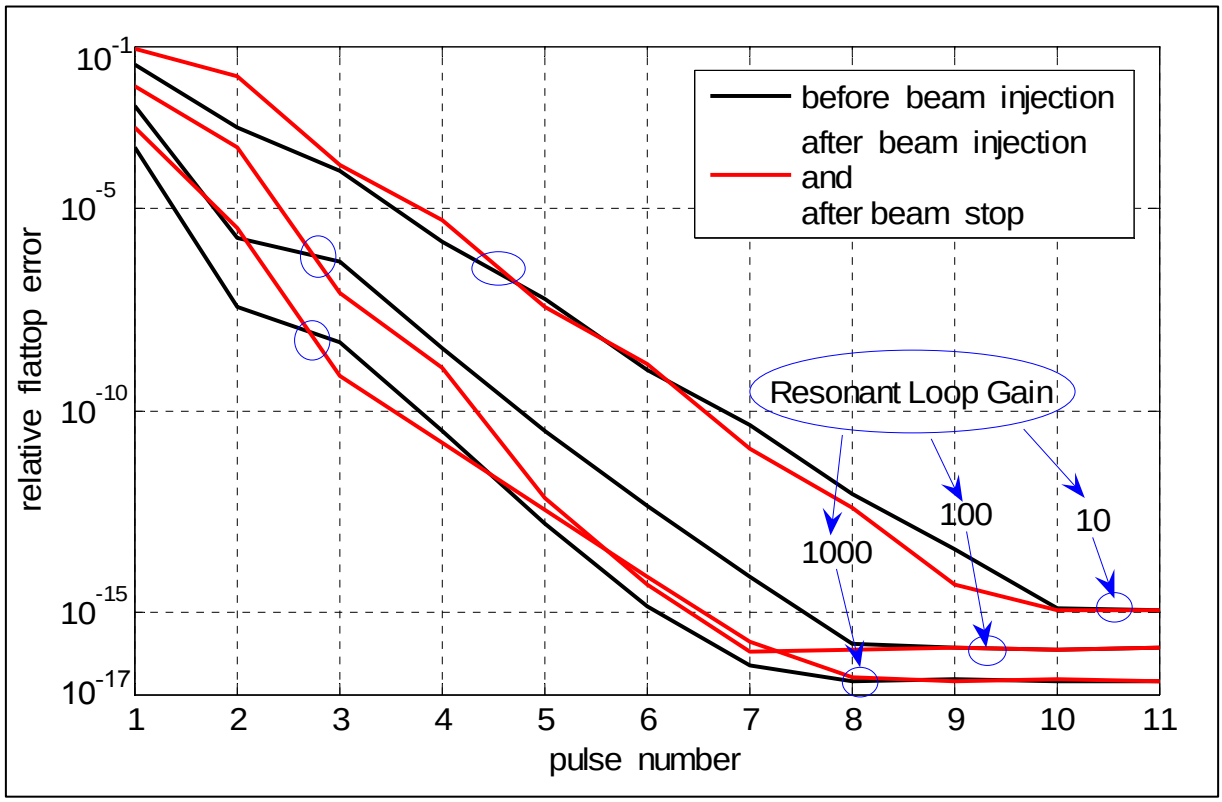


Fig. 5.5-5. The *flattop* relative mean error, as a function of pulse number of the adaptive feed-forward, by differential inverse control, supported by the conventional feedback, with different values of the resonant loop gain. The three adaptive control processes for the estimated cavity model are considered: 1 – before beam injection (starting from "zero"), 2 – after beam injection, 3 – after beam stop.

The simulation series for different values of the resonant loop gain have been completed. The following three adaptive control processes for the estimated cavity model are considered:

1 – before beam injection, with estimation of the cavity model parameters from "zero"

2 – after beam injection, with fixed, estimated before, parameters of the cavity model

3 – after beam stop, with the established parameters of the cavity model.

***Adaptive feed-forward based on feedback control***

The complex control with the conventional feedback can be efficiently simplified, without recognition of the cavity model, if the feed-forward signal $\underset{k}{\mathbf{u}}_{ff}$, in the current pulse *k*, is based on the resultant generator output $\underset{k-1}{\mathbf{u}}^{\bullet}_{g}$ from the previous pulse k−1 (refer to fig. 5.5-1), so

$$\underset{k}{\mathbf{u}}_{ff} = \underset{k-1}{\mathbf{u}}^{\bullet}_{g} . \tag{5.5-8}$$

The feedback signal tries to compensate a feed-forward mismatch to the inverse model. So, the resultant generator output is a better approximation of the required feed-forward which can be iteratively improved. Consequently, the iterative process of a successive control is stated as follows

$$\underset{k}{\mathbf{u}}^{\bullet}_{g} = \underset{k-1}{\mathbf{u}}^{\bullet}_{g} + \mathbf{G}_{f} \cdot \underset{k}{\Delta\mathbf{v}} \qquad \text{for} \qquad \underset{k}{\Delta\mathbf{v}} = \mathbf{v}^{\bullet} - \underset{k}{\mathbf{v}} \tag{5.5-9}$$

Supposing a delay time *d* to both sides of the above equation, yields

$$\underset{k}{\mathbf{u}}_{g} = \underset{k-1}{\mathbf{u}}_{g} + \mathbf{G}_{f} \cdot \underset{k}{\Delta\mathbf{v}}_{(-d)} \tag{5.5-10}$$

The cavity process, for a pulse k, is expressed as

$$\underset{k}{\mathbf{v}} = \mathrm{P}(\underset{k}{\mathbf{u}}) + \mathbf{w} \quad \text{for} \quad \underset{k}{\mathbf{u}} = \underset{k}{\mathbf{u}_{g}} - \mathbf{u}_{b} \tag{5.5-11}$$

Transforming the both sides of equation (5.5-10) to the form of (5.5-11) for pulses, *k* and *k-1*, we obtain

$$\underset{k}{\mathbf{v}} = \underset{k-1}{\mathbf{v}} + \mathbf{G}_{f} \cdot \mathrm{P}(\underset{k}{\Delta\mathbf{v}}_{(-d)}) \qquad \text{or} \qquad \underset{k}{\Delta\mathbf{v}} + \mathbf{G}_{f} \cdot \mathrm{P}(\underset{k}{\Delta\mathbf{v}}_{(-d)}) = \underset{k-1}{\Delta\mathbf{v}} \tag{5.5-12}$$

The discrete time operator P can be conveyed to the transfer function in the *z*-space, for the given factor **A** (refer to 5.5-1). Consequently, making use of the *z*-transform, we have

$$P \leftrightarrow P(z) = \frac{1}{1 - Az^{-1}} \qquad \text{and} \qquad \Delta v \leftrightarrow \Delta V(z) \tag{5.5-13}$$

Therefore, the solution of (5.5-12) in the $z$-space, for the error transformation, is given by

$$\underset{k}{\Delta V}(z) = \Gamma(z) \cdot \underset{k-1}{\Delta V}(z) \tag{5.5-14}$$

where, $\Gamma(z) = \dfrac{1}{1 + G_f P(z) z^{-d}} = \dfrac{f(z)}{g(z)}$ (refer to 5.5-3).

The single transformation $\Gamma(z)$ is stable for a stable feedback system. For a convergence of the error series, the operation $\Gamma(z)$ should be a contractive mapping. The convergence condition is considered in the frequency ω domain for the sampling time T and is stated as follows

$$|\Gamma(z)| < 1 \quad \text{for} \quad z = e^{j\omega T},\ \omega = 2\pi f\ . \tag{5.5-15}$$

The factor $|\Gamma(e^{j\omega T})|$, versus frequency $f$, is presented in fig. 5.5-6, for the selected values of delay $d$, and the feedback gain $G_f = 0.5\ G_{fd}$, for the respective delay $d$.

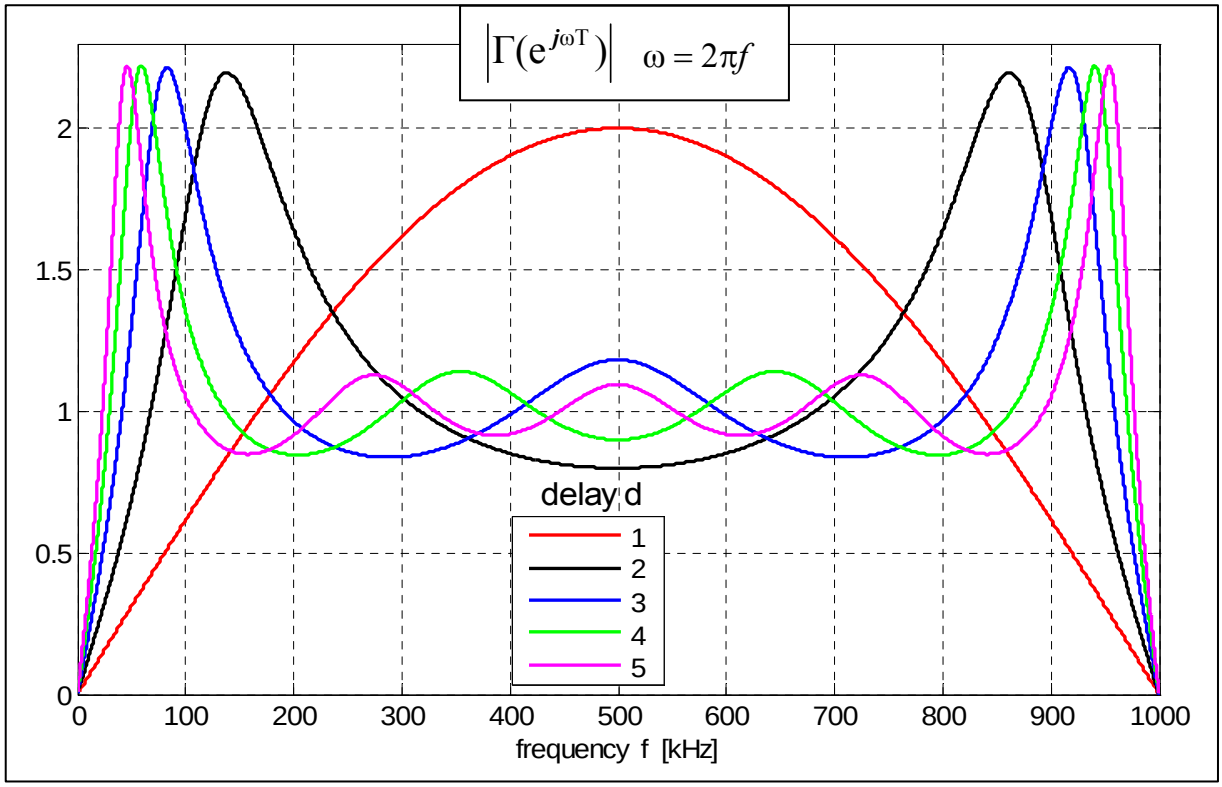


Fig. 5.5-6. The factor $|\Gamma(e^{j\omega T})|$ versus frequency, for the selected values of delay $d$, and the feedback gain $G_f = 0.5\ G_{fd}$, for the respective delay $d$. Sampling time is T = 1μs.

The factor $\left|\Gamma(e^{j\omega T})\right|$ exceeds the value of one for any time delay d > 0, for high enough frequencies, what causes instabilities. The convergence limit of the frequency *f*, versus real resonant loop gain, is presented in fig. 5.5-7, for the selected values of delay *d*. The required feedback gain $G_f$, for the respective frequency limit *f*, is given by

$$G_f = 2\mathrm{Re}\,f(e^{j2\pi fT}) \approx 4\sin\pi fT\,\sin(2d-1)\pi fT\,. \qquad (5.5\text{-}16)$$

The range of the resonant loop gain is limited by the stability area of the feedback gain $G_{fd}$, for the respective delay *d* (refer to 5.5-4).

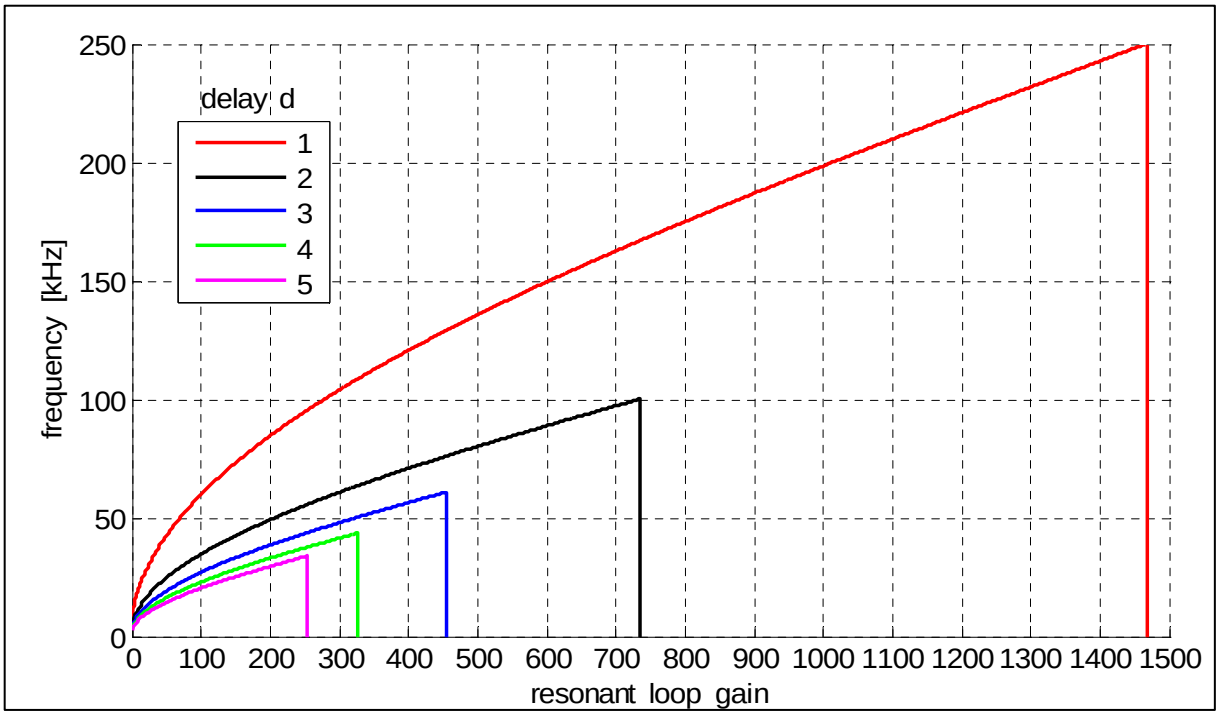


Fig. 5.5-7. The convergence limit of the frequency *f*, versus resonant loop gain $G_{L0}$, for the selected values of delay *d*. Sampling time is T = 1μs.

The sufficiently high frequencies, transferred by the feed-forward, are amplified from a pulse to a pulse, causing a divergence of the error signal. Therefore, all the frequencies exceeding the convergence limit, for a given resonant loop gain and time delay, should be filtered effectively out. The *offline* smoothing of the feed-forward signal, between pulses, without regard to causality and without any delay, is a quite sufficient solution for the adaptive feed-forward, based on the feedback control [32].

The simulation procedure has been carried out for the adaptive feed-forward based on the conventional feedback control of the cavity model. The polynomial *spline* function has been applied, for the *offline* smoothing of the feed-forward signal (ref. to Appendix).

The simulation conditions are analogous to the previous ones of the complex control in this chapter. The time delay is d = 1. The *flattop* relative mean error $\frac{\overline{\Delta v_c}}{v_c^{\bullet}}$ is presented in fig. 5.5-8, as a function of the pulse number of the adaptive control process. The simulation series for different values of the resonant loop gain has been performed. The following three adaptive control processes for the estimated cavity model are considered:

1 – before beam injection, with estimation of the cavity model parameters from "zero"

2 – after beam injection, with fixed, estimated before, parameters of the cavity model

3 – after beam stop, with the established parameters of the cavity model

The cavity parameters estimation is required, for the control *set-point* optimization, during the *filling* range (refer to chapter 4.1).

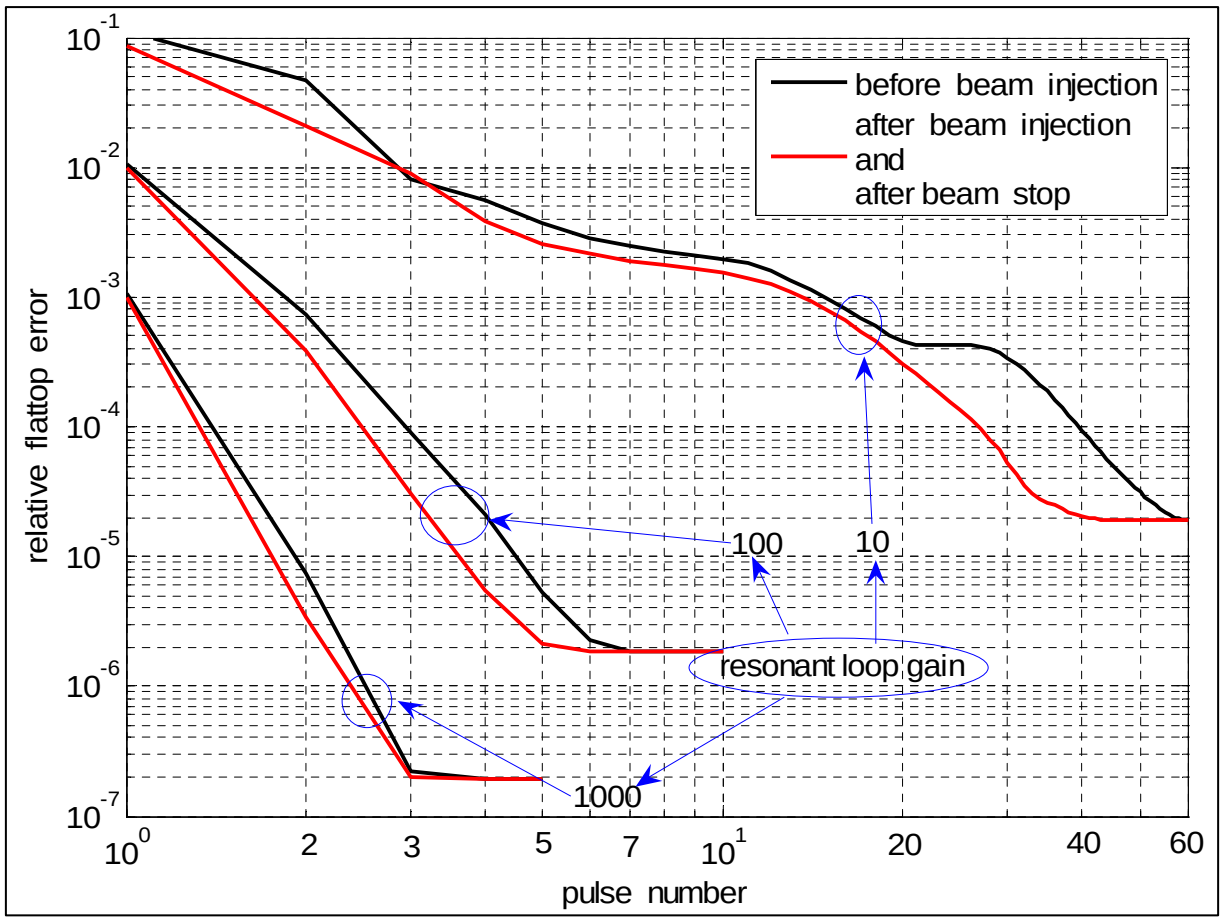


Fig. 5.5-8. The *flattop* relative mean error, as a function of pulse number of the adaptive feed-forward based on the conventional feedback control, with different values of the resonant loop gain The three adaptive control processes, for the estimated cavity model, are considered: 1 – before beam injection (starting from "zero"), 2 – after beam injection, 3 – after beam stop. The charts are plotted with the logarithmic scale.

# 6. MULTI-CAVITY MODELING AND CONTROL

## 6.1. The real plant system modeling

The Low Level RF control system applied in the FLASH linear accelerator is shortly introduced in chapter 1.4. The structure of the plant system is schematically repeated in fig. 6.1-1 (ref. to fig. 1.4-1). The real plant to be controlled consists of RF system and FPGA based DSP part. The analog and digital parts are linked by DAC and ADC converters. In a practical application of a linear accelerator one klystron drives many cavities in a single crio-module. Therefore, a multi-channel system, driven with a common klystron, for vector sum control is considered.

The digital controller output **x** determines the actual plant input. The digital plant output **v**, which is the *vector sum*, determines the actual controller input. The digital signal **y** is considered, additionally, as the klystron output. All signals are represented by *complex envelopes*, called also the *phasors*.

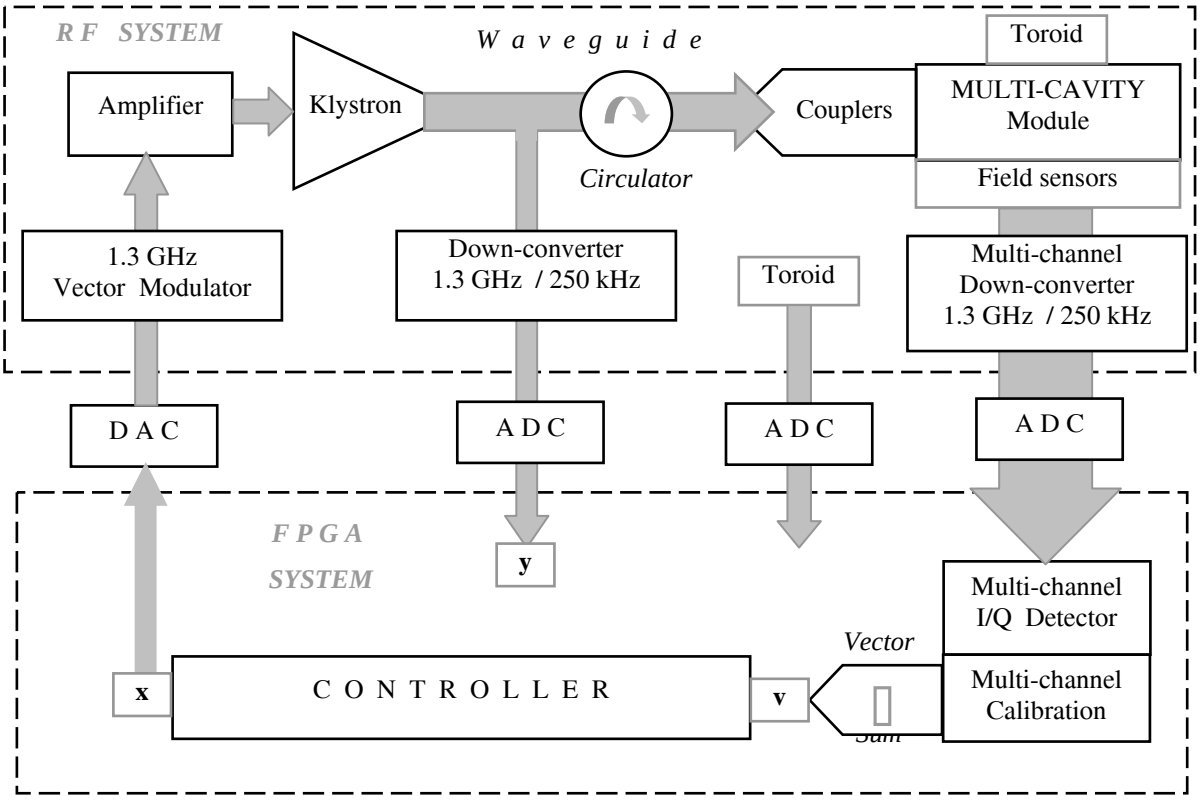


Fig. 6.1-1. The functional block diagram of the multi-cavity plant system

A discrete-time model in the complex domain is introduced to analyze the multi-cavity plant system (fig. 6.1-2). The system is decomposed to several consistent parts. The distinguished modules of the system form complex signals according to their characteristics described by complex factors [23, 33, 34].

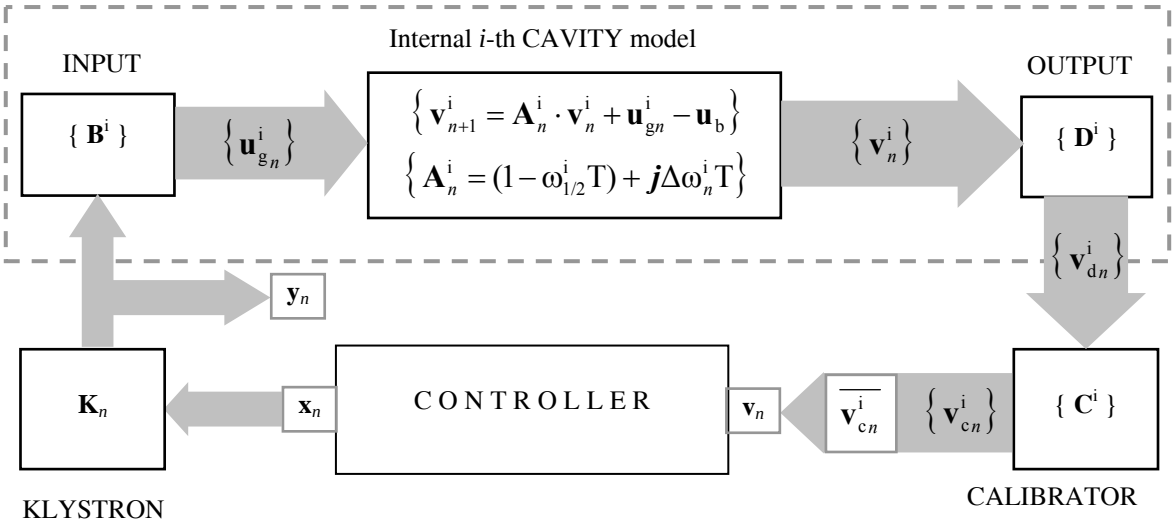


Fig. 6.1-2. Algebraic model of the multi-cavity plant system.

The electrical model of a single cavity is assumed as the only dynamic part (inertial) of the *i*-th channel. All others units are relatively fast, and sufficiently to be considered as static ones (inertialess). The discrete internal model of the single cavity is based on a difference equation of first order for the output *phasor* $\mathbf{v}^{\mathrm{i}}$, driven with the input *phasor* $\mathbf{u}_{\mathrm{g}}^{\mathrm{i}}$ for *i*-th channel. The recursive equation of the *i*-th cavity model, with the sampling interval T, is expressed by a complex form, for a step *n* (ref. to equation 3.1.3)

$$\mathbf{v}_{n+1}^{\mathrm{i}} = \mathbf{A}_n^{\mathrm{i}} \cdot \mathbf{v}_n^{\mathrm{i}} + \mathbf{u}_{\mathrm{g}_n}^{\mathrm{i}} - \mathbf{u}_{\mathrm{b}} \tag{6.1-1}$$

where cavity dynamics is described by the time-varying factor $\mathbf{A}_n^{\mathrm{i}} = (1 - \omega_{1/2}^{\mathrm{i}}\mathrm{T}) + \boldsymbol{j}\Delta\omega_n^{\mathrm{i}}\mathrm{T}$ with *i*-th cavity parameters: constant half-bandwidth $\omega_{1/2}^{\mathrm{i}}$ and time varying detuning $\Delta\omega^{\mathrm{i}}{}_n$. A beam component $\mathbf{u}_{\mathrm{b}}$ is a common one, for the set of serial cavities.

The inputs and outputs of the internal cavities are directly inaccessible for the control purpose and are coupled with the multi-channels Input and Output units respectively. The linear Input unit, described by the constant factors $\{\mathbf{B}^{\mathrm{i}}\}$, comprises waveguides with circulators and couplers. The potential signal delay can be considered here. Three-stub tuners and high-power couplers are responsible for power distribution and phase alignment of the

cavities (ref. to input calibration in 6.3). The klystron forward signal $\mathbf{y}_n$, common one for all cavities, is distributed by the multi-channel Input unit according to the relation, for *i*-th channel:

$$\mathbf{u}^{\mathrm{i}}_{\mathrm{g}_n} = \mathbf{B}^{\mathrm{i}}\mathbf{y}_n \,. \tag{6.1-2}$$

The static (inertialess) but nonlinear Klystron unit, driven with the controller output $\mathbf{x}_n$, is modeled by the time varying factor $\mathbf{K}_{\mathrm{n}}$, for a repetitive pulse mode of operation. This module includes digital-to-analog converters, vector modulator, amplifier and actual power amplifier, which is the klystron with dominating nonlinear characteristics. Moreover, the Input and Klystron units contain a common measurement channel (down-converter, ADC and I/Q detector), which provides an access to the klystron forward signal, represented by the *phasor* $\mathbf{y}_n$. Consequently, the input – output relations for Klystron unit is given by

$$\mathbf{y}_n = \mathbf{K}_n\mathbf{x}_n \,. \tag{6.1-3}$$

Making use of (6.1-1), (6.1-2) and (6.1-3), the static, but nonlinear gain (or time varying) from the controller output to the *i*-th cavity output without a beam, is introduced for the steady state

$$\mathbf{g}^{\mathrm{i}}_n = \frac{\mathbf{B}^{\mathrm{i}}\mathbf{K}_n}{1-\mathbf{A}^{\mathrm{i}}_n} \,. \tag{6.1-4}$$

The factor $\mathbf{B}^{\mathrm{i}}\mathbf{K}_n$, as characteristics of *i*-th actuator transducer, determines the actual operating range of the respective cavity output for a given range of the digital controller output.

The linear Output unit, described by the constant factors $\{\mathbf{D}^{\mathrm{i}}\}$, includes field sensors, down-converters, analog-to-digital converters and I/Q detectors. The output measurement channels are assumed to cause diverse but linear distortion resulting in a set of inconsistent signals

$$\{\, \mathbf{v}^{\mathrm{i}}_{\mathrm{d}n} = \mathbf{D}^{\mathrm{i}}\mathbf{v}^{\mathrm{i}}_n \,\} \,. \tag{6.1-5}$$

The final restoring correction is accomplished by the Calibrator unit, described by the constant factors $\{\mathbf{C}^{\mathrm{i}}\}$, which results in a set of calibrated signals

$$\{\, \mathbf{v}^{\mathrm{i}}_{\mathrm{c}n} = \mathbf{C}^{\mathrm{i}}\mathbf{v}^{\mathrm{i}}_{\mathrm{d}n} = \mathbf{C}^{\mathrm{i}}\mathbf{D}^{\mathrm{i}}\mathbf{v}^{\mathrm{i}}_n \,\} \,. \tag{6.1-6}$$

The resultant factor $\mathbf{C}^{\mathrm{i}}\mathbf{D}^{\mathrm{i}}$ is a characteristic of the measuring transducer linking the physical and numerical domains for *i*-th channel. All of the signals, involved in the modeling

process and accessible for the control purpose in the digital part of the system, are expressed by digits within the given range. The 18-bit resolution, corresponding to the digital range: $-2^{17} \div 2^{17}-1$ , has been applied for the final hardware realization of the FPGA based digital controller (ref. to chapter 7).

The resultant calibration restores original signals, if $\{\mathbf{C}^{\mathrm{i}}\cdot\mathbf{D}^{\mathrm{i}} = \mathbf{C} = \text{const.}\}$ for all channels, so $\mathbf{v}^{\mathrm{i}}_{\mathrm{c}n} = \mathbf{C}\mathbf{v}^{\mathrm{i}}_{n}$ , for *i*-th channel. The absolute value of the factor **C**, common one for all channels, is determined as a scaling coefficient, given by

$$\mathrm{C} = |\mathbf{C}| = \frac{\mathrm{R_d}}{\mathrm{R_a}}, \tag{6.1-7}$$

where $R_a$ is the measured size of the actual (analog) range of the signal in the physical units (e.g. $R_a$ = 64 MV for the range: -32 MV ÷ 32 MV), $R_d$ is the corresponding size of the digital range (e.g. $R_d = 2^{18}$). The relative phasing of the factor **C** is determined by the phases requirements of the beam and the *flattop* set-point (ref. to chapter 6.3).

Multiplying both sides of equation (6.1-1) by the factor $\mathbf{C}^{\mathrm{i}}\cdot\mathbf{D}^{\mathrm{i}} = \mathbf{C}$**,** and using (6.1-2) and (6.1-6), the recursive relation between klystron *phasor* $\mathbf{y}_n$ and output *phasor* $\mathbf{v}^{\mathrm{i}}_{\mathrm{c}n}$, for calibrated *i*-th channel, is expressed as

$$\mathbf{v}^{\mathrm{i}}_{\mathrm{c}n+1} = \mathbf{A}^{\mathrm{i}}_{n}\mathbf{v}^{\mathrm{i}}_{\mathrm{c}n} + \mathbf{C}\mathbf{B}^{\mathrm{i}}\mathbf{y}_{n} - \mathbf{C}\mathbf{u}_{\mathrm{b}}. \tag{6.1-8}$$

The resultant response of the multi-cavity plant to be controlled is represented by the calibrated *vector sum* $\sum_{\mathrm{i}} \mathbf{v}^{\mathrm{i}}_{\mathrm{c}n}$, or by the calibrated mean value, over all channels, $\mathbf{v}_n = \overline{\mathbf{v}^{\mathrm{i}}_{\mathrm{c}n}} = \mathbf{C}\overline{\mathbf{v}^{\mathrm{i}}_{n}}$ .

Taking mean value of both sides of equation (6.1-8), over all channels, and introducing new factors $\mathbf{A}_n$ and **B** yields

$$\mathbf{v}_{n+1} = \mathbf{A}_{n}\mathbf{v}_{n} + \mathbf{B}\mathbf{y}_{n} - \mathbf{C}\mathbf{u}_{\mathrm{b}}, \tag{6.1-9}$$

where the resultant system factor is defined as the weighted mean value, over all channels, $\mathbf{A}_n = \dfrac{\overline{\mathbf{A}^{\mathrm{i}}_{n}\mathbf{v}^{\mathrm{i}}_{n}}}{\overline{\mathbf{v}^{\mathrm{i}}_{n}}}$, and the resultant input factor is $\mathbf{B} = \mathbf{C}\overline{\mathbf{B}^{\mathrm{i}}}$ .

The resulting, multi-cavity system model, introduced by equation (6.1-9), has the same structure like a single channel model (6.1-8), but with different parameters, in a case of

diverse operating condition for cavities. Therefore, the system *phasor* is analogously decomposed to the real and imaginary parts:

$$\mathbf{A}_n = (1 - \omega_{1/2}\mathrm{T}) + \boldsymbol{j}\Delta\omega_n\mathrm{T} \tag{6.1-10}$$

with substituted half-bandwidth = $\omega_{1/2}$ and substituted detuning = $\Delta\omega_n$.

The experimental results confirm, that a multi-cavity setup arranged in series behaves like a single cavity.

Finally, the reduced model of the multi-cavity plant system, functional for the control purpose, is presented in fig. 6.1-3. The following two, no stationary parts have been selected: the *Multi-cavity* as a dynamic one and the *Klystron* as a static one.

Including the Klystron unit to the multi-cavity system, the ultimate model, driven with the controller output $\mathbf{x}_n$, is given by

$$\mathbf{v}_{n+1} = \mathbf{A}_n\mathbf{v}_n + \mathbf{F}_n\mathbf{x}_n - \mathbf{C}\mathbf{u}_\mathrm{b}\,, \tag{6.1-11}$$

with the resultant factor $\mathbf{F}_n = \mathbf{B}\cdot\mathbf{K}_n$.

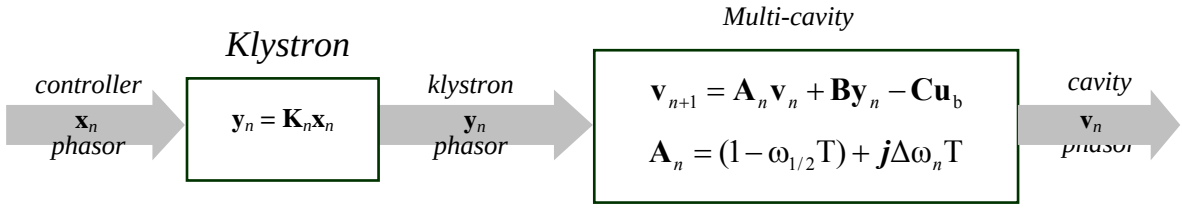


Fig. 6.1-3. Reduced model of the multi-cavity plant system.

*Signals rescaling with respect to the physical quantities*

The measured digital signals represent respective physical quantities. The original magnitudes can be restored as a result of rescaling (6.1-8) or (6.1-9), by the coefficient C, but preserving measured phase relation (refer to the primary cavity model 3.1-3 and 6.1-1).

Consequently, the basic physical quantities, with the respective units, for *i*-th cavity, are estimated as follow (ref. to chapters 2.2, 2.4, 3.1)

- $\mathbf{v}_n^\mathrm{i}\,[\mathrm{MV}] = \mathbf{v}_{cn}^\mathrm{i} \big/ \mathrm{C}$ for cavity voltage (6.1-12)

- $\mathbf{i}_{g_n}^\mathrm{i}\,[\mathrm{mA}] = \dfrac{\mathbf{C}\mathbf{B}^\mathrm{i}\mathbf{y}_n}{\omega_0\rho\mathrm{T}} \Big/ \mathrm{C}$ for generator current (klystron forward)

- $\mathbf{i}_b^i\,[\mathrm{mA}] = \dfrac{\mathbf{C}\mathbf{u}_b}{\omega_0 \rho \mathrm{T}} \Big/ \mathrm{C}$ for beam current

- $P_{f\,n}^i\,[\mathrm{kW}] = \dfrac{\omega_0 \rho}{4\omega_{1/2}} \left|\mathbf{i}_{g_n}^i\right|^2$ for forward power.

## 6.2. The system model identification

The control algorithms, based on the cavity model, require identification of the process parameters. Assuming a repetitive condition for the pulse mode of operation, the cavity parameters can be recognized *offline* between pulses. The *least square* (LS) method is proposed for the parameters estimation under a noisy and no stationary condition [ 35, 36].

The two complex, time varying, factors $\mathbf{A}_n$ and $\mathbf{F}_n$ should be recognized in the ultimate model (6.1-11) of the multi-cavity system. A recognition of a beam component $\mathbf{C}\mathbf{u}_b$ is necessary for a beam based vector sum calibration and to meet the requirement for the relative beam phase (ref. to 6.3). The procedure of parameters estimation is performed in accordance with the reduced model of the multi-cavity plant system presented in fig. 6.1-3. Three stages of the identification process are considered for the following issues: *Multi-cavity* as a dynamic module, *Klystron* as a static module and *Beam* as a disturbance component.

***Multi-cavity module recognition***

The Multi-cavity system model, introduced by equation (6.1-9), has the same structure like a single channel model (6.1-8), so the identification methods presented below are common for both cases.

The ultimate state of the cavity does not depend on a beam loading, if it is compensated by the generator signal. So, the cavity is recognized in advance, for a required state, without an unforeseen beam component $\mathbf{u}_b$.

*Real domain solution*

The two complex factors: $\mathbf{A}_n = (1 - \omega_{1/2}\mathrm{T}) + \boldsymbol{j}\Delta\omega_n\mathrm{T}$, and $\mathbf{B} = \mathrm{B_r} + \boldsymbol{j}\mathrm{B_i}$, in the multi-cavity model (6.1-9), include three constant parameters: half-bandwidth $\omega_{1/2}$, real component $\mathrm{B_r}$, imaginary component $\mathrm{B_i}$, and time varying detuning $\Delta\omega_n$. These unknown parameters should be estimated for the process, involving measured input and output data, described by equation (6.1-9) for $\mathbf{u}_b = 0$.

The time varying detuning $\Delta\omega_n$ can be modeled by L-order series of chosen base functions $\{w_j(n)\}$ with unknown, but constant coefficients $\alpha_j$, as follows:

$$\Delta\omega_n T = \sum_{j=1}^{L} \alpha_j w_j(n) = \mathbf{w}_n \cdot \boldsymbol{\alpha}\,, \tag{6.2-1}$$

where $\boldsymbol{\alpha}$ is a column vector of L coefficients, $\mathbf{w}_n$ is a row vector of L values of base functions for the *n*-th step. The polynomial *spline* functions have been applied for the linear decomposition of the time varying detuning (ref. to the Appendix). Substituting (6.2-1) to (6.1-10), all unknowns of equation (6.1-9) are extracted to the vector form as follows:

$$\mathbf{v}_{n+1} = \mathbf{h}_n \cdot \mathbf{p}, \tag{6.2-2}$$

where

$\mathbf{p} = [(1 - T\omega_{1/2}); \boldsymbol{\alpha}; B_r; B_i]$ is the resultant column vector of unknown L+3 real values,

$\mathbf{h}_n = [\mathbf{v}_n, j\mathbf{v}_n\mathbf{w}_n, \mathbf{y}_n, j\mathbf{y}_n]$ is the row vector of a given model structure for the step *n*.

Taking into account N steps of the process range, the vector form (6.2-2) is expanded to the corresponding matrix form

$$\mathbf{v} = \mathbf{h} \cdot \mathbf{p}. \tag{6.2-3}$$

Moving to the real domain yields

$$\mathbf{V} = \mathbf{H} \cdot \mathbf{p}, \tag{6.2-4}$$

where $\mathbf{V} = \begin{bmatrix} re(\mathbf{v}) \\ im(\mathbf{v}) \end{bmatrix}$ is the column vector [2N x 1], $\mathbf{H} = \begin{bmatrix} re(\mathbf{h}) \\ im(\mathbf{h}) \end{bmatrix}$ is the matrix [2N x L+3].

Taking into consideration perturbed, measured data **V** and **H**, the optimal solution for **p,** with the minimal norm $\|\mathbf{V} - \mathbf{H}\mathbf{p}\|$, satisfies the orthogonal condition expressed by the scalar product:

$$(\mathbf{H}\mathbf{p})^T \cdot (\mathbf{V} - \mathbf{H}\mathbf{p}) = 0\,, \tag{6.2-5}$$

where index "T" means, generally, the complex conjugate transpose. Excluding a condition **p** = **0**, the solution is given by

$$\mathbf{p} = (\mathbf{H}^T\mathbf{H})^{-1}\mathbf{H}^T\mathbf{V}\,. \tag{6.2-6}$$

According to the LS method, it is a unique solution for the over-determined set of equations (6.2-4), where, in a practical application, 2N>>L+3.

*Complex domain solution*

The two complex factors: $\mathbf{A}_n$ and $\mathbf{B}$, in the multi-cavity model (6.1-9) for $\mathbf{u}_b = 0$, can be estimated directly in the complex domain. The time varying factor $\mathbf{A}_n$ is modeled by L-order series of chosen real base functions $\{w_j(n)\}$ with unknown, complex coefficients $\boldsymbol{\alpha}_j$, as follows:

$$\mathbf{A}_n = \sum_{j=1}^{L} \boldsymbol{\alpha}_j w_j(n) = \mathbf{w}_n \cdot \boldsymbol{\alpha}, \tag{6.2-7}$$

where $\boldsymbol{\alpha}$ is a column vector of L coefficients, $\mathbf{w}_n$ is a row vector of L values of base functions for the *n*-th step. But in this case, the real component, including the substituted half-bandwidth $\omega_{1/2}$, and imaginary component, including the substituted detuning $\Delta\omega$, are both assumed as time-varying values.

Substituting (6.2-7) to equation (6.1-9), all unknowns are extracted to the vector form as follows:

$$\mathbf{v}_{n+1} = \mathbf{h}_n \cdot \mathbf{p}, \tag{6.2-8}$$

where $\mathbf{p} = [\boldsymbol{\alpha}; \mathbf{B}]$ is the resultant column vector of unknown L+1 complex values,

$\mathbf{h}_n = [\mathbf{v}_n \mathbf{w}_n, \mathbf{y}_n]$ is the row vector of given model structure for the step *n*.

Taking into account N steps of the process range, the vector form (6.2-8) is expanded to the matrix form

$$\mathbf{V} = \mathbf{H} \cdot \mathbf{p}, \tag{6.2-9}$$

where $\mathbf{V}$ is the column vector [N x 1], $\mathbf{H}$ is the matrix [N x L+1].

Analogously, like for the real domain, the optimal solution for the complex vector $\mathbf{p}$ is given by (6.2-6).

*Decay range solution*

The homogeneous solution of equation (2.3-8) or (6.1-9), with $\mathbf{y}_n = 0$ and $\mathbf{u}_b = 0$, for the *decay* range only, can be used for estimation of the constant half-bandwidth $\omega_{1/2}$ and the time varying detuning $\Delta\omega_n$.

Applying the continuous results (ref. to 4.1-22 and 4.1-23), the set of linear equations for discrete times nT, with the unknown half-bandwidth $\omega_{1/2}$, is established in the matrix form as (6.2-10)

$$\left\{ \ln v(nT) = \ln v_0 - nT\omega_{1/2} \quad \Rightarrow \quad \ln v_n = [1, -n] \cdot \begin{bmatrix} \ln v_0 \\ \omega_{1/2} T \end{bmatrix} \quad \Rightarrow \quad \mathbf{V}_k = \mathbf{H}_k \cdot \mathbf{p} \right\} \quad \Rightarrow \quad \mathbf{V} = \mathbf{H} \cdot \mathbf{p} ,$$

where $v(nT) = v_n$ is a measured absolute value of the output *phasor* at the instant nT, $v_0$ is an initial value, assumed as an unknown parameter, $k$ is a number of the respective equation.

The LS solution for the column vector **p** is given by

$$\mathbf{p} = \left(\mathbf{H}^T \mathbf{H}\right)^{-1} \mathbf{H}^T \mathbf{V} \qquad \text{and} \qquad \omega_{1/2} T = \mathbf{p}(2) = \mathbf{p}_2 . \tag{6.2-11}$$

The time varying detuning, within the *decay* range, is a time derivative of the output phase. Again, the time varying detuning can be modeled by a series of the given base functions. The set of polynomial *spline* functions have been applied for the linear decomposition of the time varying phase derivative (ref. to Appendix).

***Klystron module recognition***

Due to a nonlinearity of the high power klystron device, modeled as a time varying unit, the Klystron module recognition has been considered separately for the control purpose. The characteristics $\mathbf{K}_n$ of this static module is identified directly from the input-output relation (6.1-3):

$$\mathbf{K}_n = \frac{\mathbf{y}_n}{\mathbf{x}_n} . \tag{6.2-10}$$

In a noisy condition, the time varying factor $\mathbf{K}_n$ can be estimated by L-order series of chosen base functions $\{w_j(n)\}$ with unknown, complex coefficients $\boldsymbol{\alpha}_j$, as follows:

$$\mathbf{K}_n = \sum_{j=1}^{L} \boldsymbol{\alpha}_j w_j(n) = \mathbf{w}_n \cdot \boldsymbol{\alpha} , \tag{6.2-11}$$

where $\boldsymbol{\alpha}$ is a column vector of L coefficients, $\mathbf{w}_n$ is a row vector of L values of base functions for the *n*-th step.

Taking into account N steps of the process range, the relation (6.1-3) is expanded to the matrix form: $\mathbf{y} = \mathbf{H} \cdot \boldsymbol{\alpha}$, where **H** is a matrix [N x L] and $\mathbf{H}_n = \mathbf{x}_n \mathbf{w}_n$ is the *n*-th row vector.

The optimal solution for the complex vector $\boldsymbol{\alpha}$, analogously like for the *Multi-cavity* module, is given by

$$\boldsymbol{\alpha} = \left(\mathbf{H}^T \mathbf{H}\right)^{-1} \mathbf{H}^T \mathbf{y} . \tag{6.2-12}$$

***Experimental results of real system identification***

The experimental studies have been carried out using the superconducting 8 cavities setup from the first module ACC1 of the FLASH laser machine in DESY. Representative results of the experiments are presented below for a typical operating condition.

The basic characteristics of the multi-cavity setup are presented in fig. 6.2-1 and 6.2-2. The multi-cavity module is activated, by feed-forward driving, with a pulse of 1.2 ms duration and repetition of 10 Hz. During the first stage of the operation (~0.5 ms), the cavities are *filling* with constant forward power resulting in exponential increase of the field in the resonance condition. When the vector sum, or mean *phasor*, has reached the required final value, the steady state is forced during *flattop* range (~0.7 ms). The first four cavities in ACC1 module have significantly lower gradient, due to the requirements for a moderate acceleration of the beam. The initial *predetuning* attempts to compensate the Lorentz force detuning and balances the required power consumption during pulse operation of the cavities. However, the cavity no. 1 is rather over-tuned. Switching off the klystron power yields an exponential *decay* of the cavities field. Figure 6.2-1 presents amplitudes and phases of respective 8 cavities and the stabilized mean value (14 MV, 0 rad), designated by "0" (red line). Moreover, the forward power, time varying detuning and constant half-bandwidth are identified for all cavities, as well the substituted values respectively are estimated for the resultant multi-cavity module.

In fig. 6.2-2, the amplitude and phase of the measured mean *phasor* are compared with the corresponding values of the multi-cavity model obtained by the complex domain solution. The klystron output envelope is presented. The substituted half-bandwidth and detuning of the multi-cavity module are evaluated using three identification methods.

A single cavity control by feed-forward driving, excluding others from the vector sum, is presented in fig. 6.2-3. The cavity no.8 is initially activated with pulse 1.3 ms for the *flattop* range 0.8 ms. The basic following characteristics are showed for this condition: cavity output envelope (amplitude and I,Q–components), power (forward and reflected), klystron normalized characteristics (phase and absolute value), time-varying half-bandwidth and cavity detuning. Additionally, the cavity detuning has been estimated separately for different *decay* ranges (as a phase derivative) and compared with the respective complex domain solution for the total range. The pulse has been reduced from 1.3 m, successively with the step of 0.1 ms, up to 0.3 ms duration.

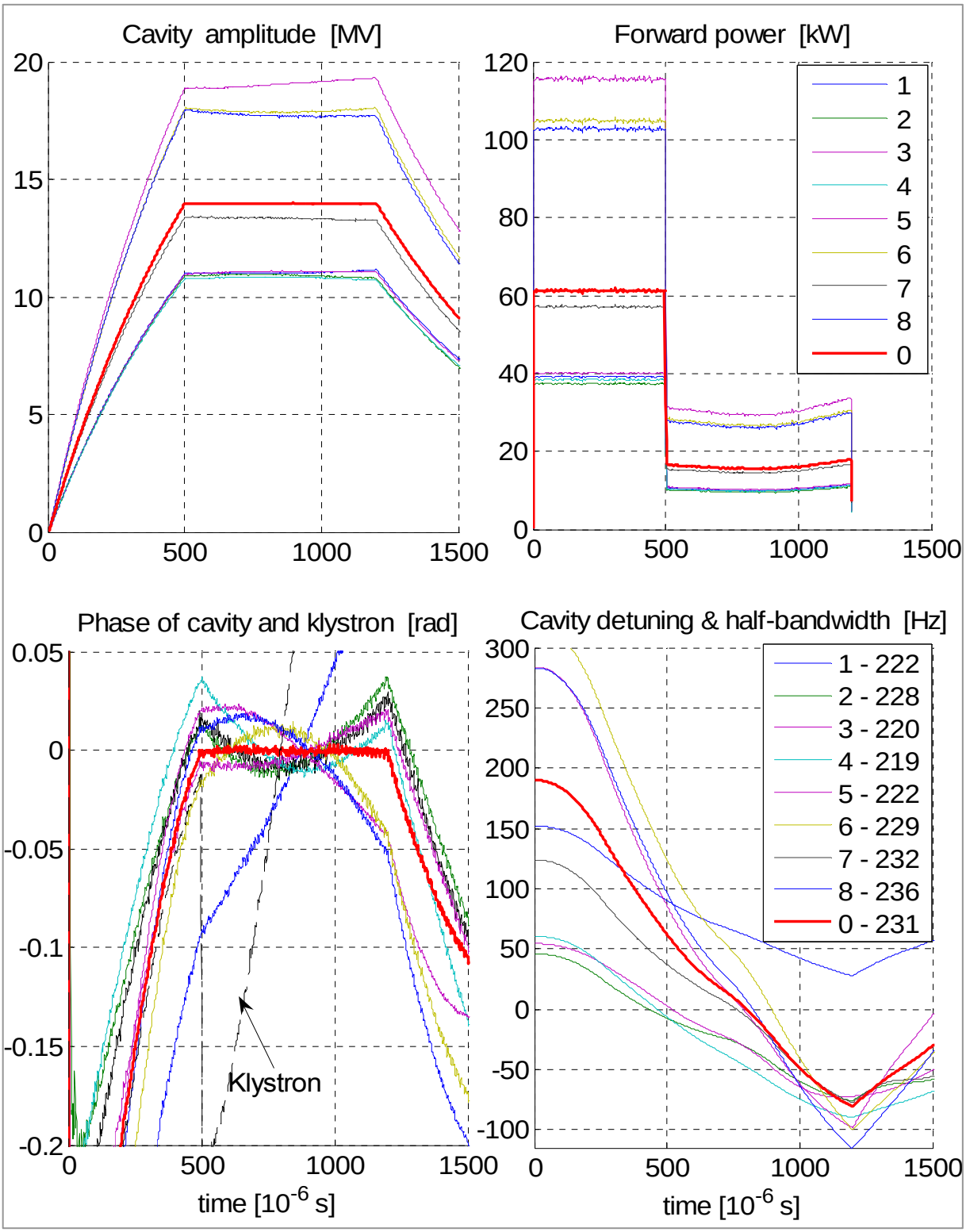


Fig. 6.2-1. Vector sum control of 8 cavities by feed-forward driving. The basic characteristics: amplitudes, phases, forward power, time varying detuning and constant half-bandwidth, are monitored for all cavities. The substituted mean value for the resultant multi-cavity is designated by "0" (red line).

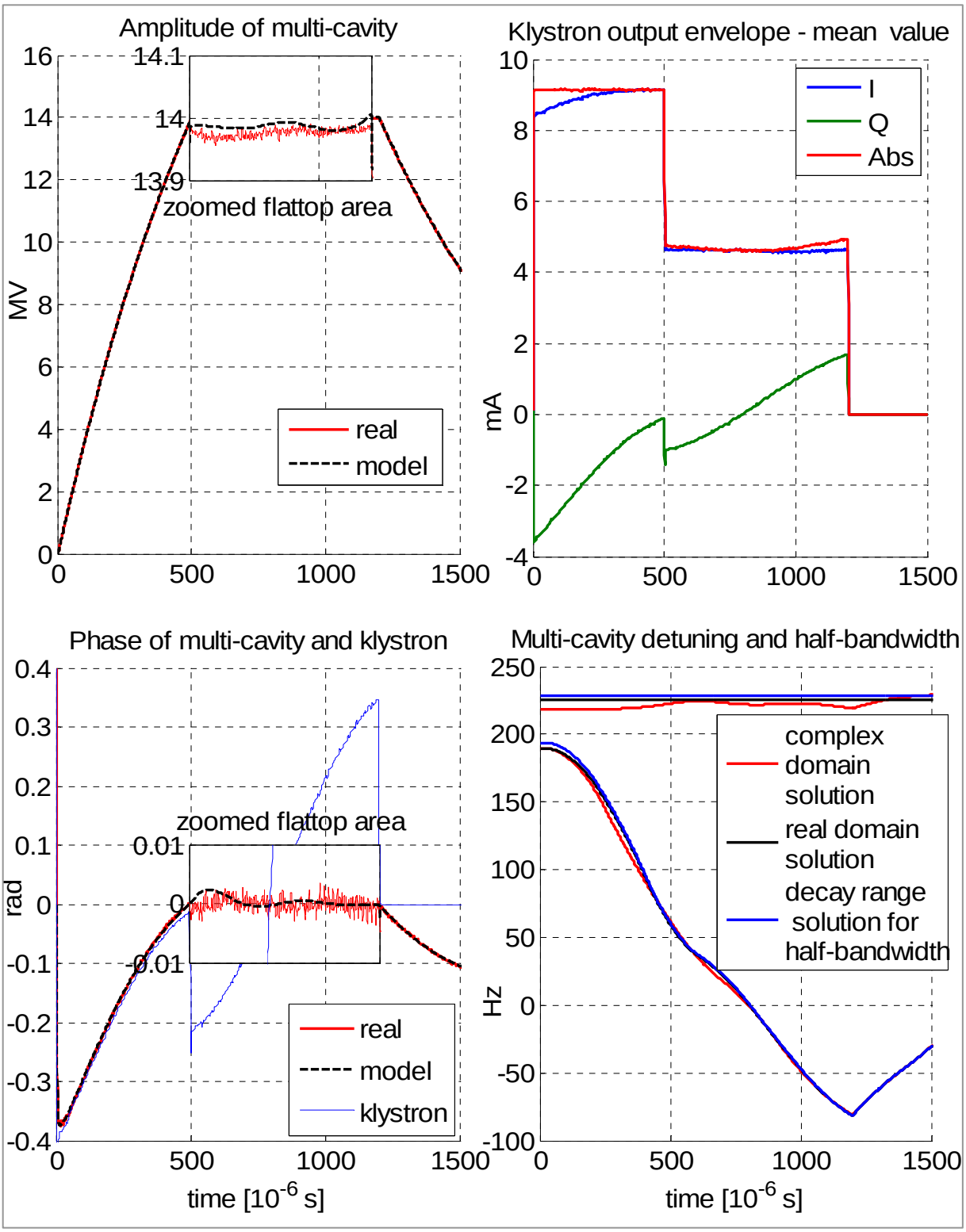


Fig. 6.2-2. Vector sum control of 8 cavities by feed-forward driving. The amplitude and phase of the measured mean *phasor* are compared with the multi-cavity model. The klystron output envelope (mean value over channels) is estimated (I, Q - components and absolute value – Abs). The results of three identification methods are compared for substituted half-bandwidth and detuning of the multi-cavity module.

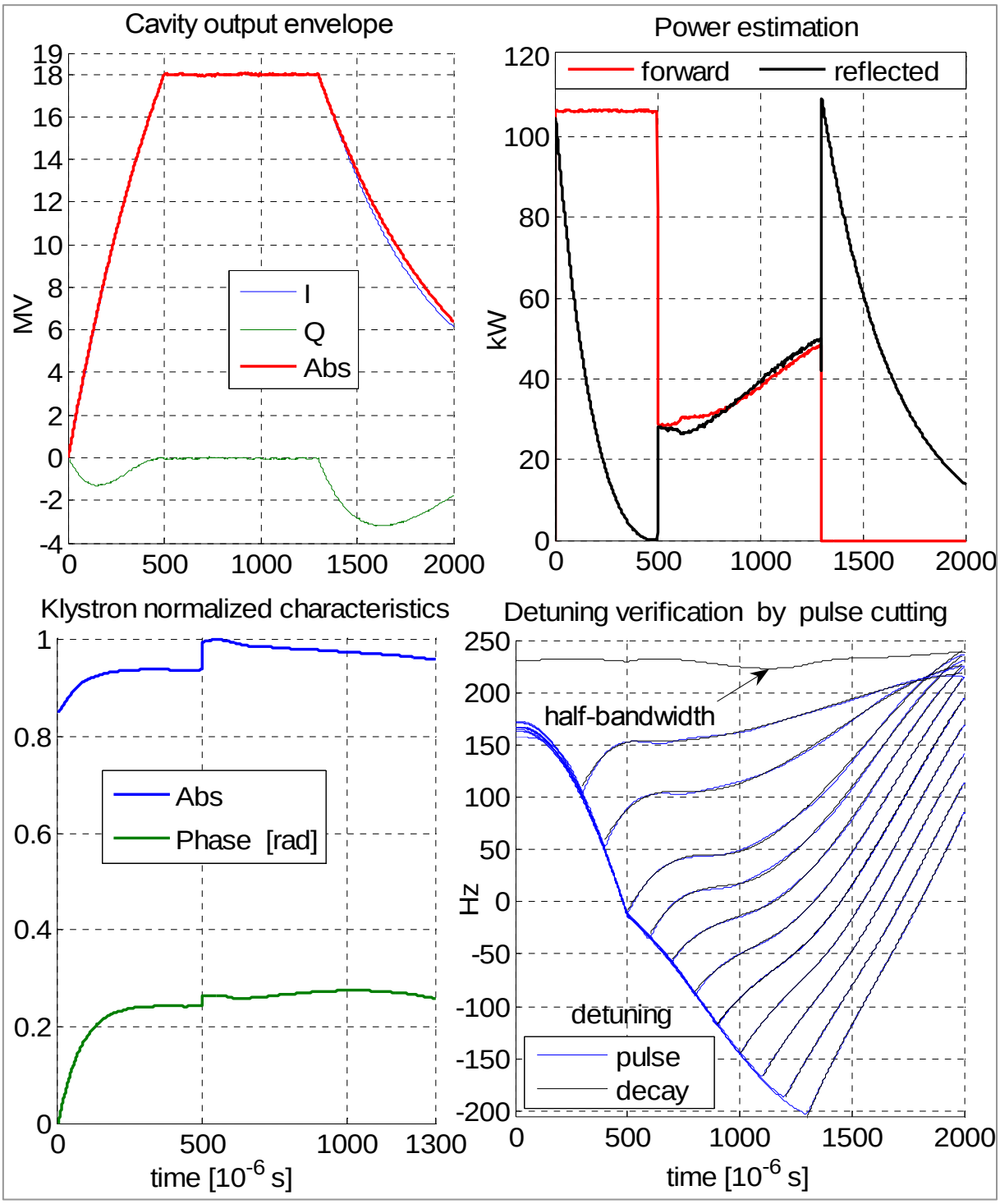


Fig. 6.2-3. Single cavity control by feed-forward driving. The basic characteristics are presented: cavity output envelope (amplitude – Abs, and I,Q–components), power (forward and reflected), klystron normalized characteristics (phase and absolute value), time-varying half-bandwidth and cavity detuning. The cavity detuning has been estimated separately for different *decay* ranges (as a phase derivative) and compared with the respective complex domain solution for the total range (pulse).

***Beam loading recognition***

The output calibration of the measurement channels and phase adjustment regarding the beam requires recognition of beam component for the respective cavities (ref. to 6.3). The beam component $\mathbf{C}^{\mathrm{i}}\mathbf{D}^{\mathrm{i}}\mathbf{u}_{\mathrm{b}}$, related to the single cavity model (6.1-8), is relatively diverse $\{\mathbf{C}^{\mathrm{i}}\mathbf{D}^{\mathrm{i}} \neq \text{const.}\}$, before the calibration of all channels. The single cavity is controlled separately, excluding the others from the vector sum, by setting $\mathbf{C}^{\mathrm{j}\neq\mathrm{i}} = \mathbf{0}$, for *i*-th channel. In this case, equation (6.1-8) is equivalent to (6.1-9) and is repeated in the convenient form, for *i*-th channel:

$$\mathbf{v}_{n+1} = \mathbf{A}_n^{\mathrm{i}}\mathbf{v}_n + \mathbf{C}^{\mathrm{i}}\mathbf{D}^{\mathrm{i}}\mathbf{B}^{\mathrm{i}}(\mathbf{y}_n + \Delta\mathbf{y}) - \mathbf{C}^{\mathrm{i}}\mathbf{D}^{\mathrm{i}}\mathbf{u}_{\mathrm{b}}, \tag{6.2-13}$$

where $\mathbf{v}_n = \mathbf{v}_{cn}^{\mathrm{i}} = \mathbf{C}^{\mathrm{i}}\mathbf{D}^{\mathrm{i}}\mathbf{v}_n^{\mathrm{i}}$, $\mathbf{y}_n$ is a klystron *phasor* before beam injection and $\Delta\mathbf{y}$ is an additional component of the klystron *phasor*, compensating the beam loading $\mathbf{C}^{\mathrm{i}}\mathbf{D}^{\mathrm{i}}\mathbf{u}_{\mathrm{b}}$, after beam injection. The beam component $\mathbf{C}^{\mathrm{i}}\mathbf{D}^{\mathrm{i}}\mathbf{u}_{\mathrm{b}}$, in equation (6.2-13), is estimated on condition, that the cavity has reached the same state, like before a beam injection. The control methods of a beam loading compensation are described in chapter 5.2. For the same output value $\mathbf{v}_n$, before a beam injection ($\mathbf{u}_{\mathrm{b}} = \mathbf{0}$), we have the unified input $\mathbf{u}_n = \mathbf{C}^{\mathrm{i}}\mathbf{D}^{\mathrm{i}}\mathbf{B}^{\mathrm{i}}\mathbf{y}_n$, and the same value $\mathbf{u}_n = \mathbf{C}^{\mathrm{i}}\mathbf{D}^{\mathrm{i}}\mathbf{B}^{\mathrm{i}}(\mathbf{y}_n + \Delta\mathbf{y}) - \mathbf{C}^{\mathrm{i}}\mathbf{D}^{\mathrm{i}}\mathbf{u}_{\mathrm{b}}$, after a beam injection. Therefore, the beam component is estimated for *i*-th channel as

$$\mathbf{C}^{\mathrm{i}}\mathbf{D}^{\mathrm{i}}\mathbf{u}_{\mathrm{b}} = \mathbf{B}\Delta\mathbf{y}, \tag{6.2-14}$$

where a factor $\mathbf{B} = \mathbf{C}^{\mathrm{i}}\mathbf{D}^{\mathrm{i}}\mathbf{B}^{\mathrm{i}}$ has been recognized before a beam injection.

An analogous reasoning is applied for a beam component recognition related to the multi-cavity system. Consequently, the beam component $\mathbf{C}\mathbf{u}_{\mathrm{b}}$ in (6.1-9) is estimated as

$$\mathbf{C}\mathbf{u}_{\mathrm{b}} = \mathbf{B}\Delta\mathbf{y}. \tag{6.2-15}$$

The proposed method of the beam recognition assumes a multi-bunch beam loading, sufficient for a reliable detection of the compensating klystron signal in the DSP part of the system. An additional component of the klystron *phasor*, compensating the beam loading is estimated within a selected time window, detected by a beam induced *toroid* signal.

A transient measurement technique, analyzing the RF signal, allows to evaluate small beam currents [37].

## 6.3. Vector sum calibration

***Output calibration of the measurement channels***

The main purpose of the output (low power) calibration is a correction of the measurement paths, necessary for a reliable vector sum control. The required calibration restores original signals information, if the resultant output factor is $\mathbf{C}^{\mathrm{i}}\cdot\mathbf{D}^{\mathrm{i}} = \mathbf{C} = \text{const.}$, for all channels, by proper scaling and phasing. So, the calibrated output is $\mathbf{v}_n = \mathbf{C}\mathbf{v}_n^{\mathrm{i}}$, for *i*-th channel, and the beam loading component $\mathbf{C}^{\mathrm{i}}\mathbf{D}^{\mathrm{i}}\mathbf{u}_{\mathrm{b}} = \mathbf{C}\mathbf{u}_{\mathrm{b}} = \text{const.}$ for all cavities. The following two calibration methods are considered below.

*Beam based absolute calibration*

The absolute calibration is performed with a probationary beam, under the assumption, that the beam component $\mathbf{u}_{\mathrm{b}}$ is the same for all cavities (ref. to 3.1-3 and 6.1-1). The output calibration procedure is executed *off-line*, between pulses, channel by channel, for a single cavity controlled according to the requirements for the normal operating condition. The *i*-th channel is calibrated separately excluding the others from the vector sum, by setting $\mathbf{C}^{\mathrm{j}\neq\mathrm{i}} = \mathbf{0}$.

The proposed calibration method is based on estimation of the beam component $\mathbf{C}^{\mathrm{i}}\mathbf{D}^{\mathrm{i}}\mathbf{u}_{\mathrm{b}}$, given by (6.2-14), for the respective *i*-th cavity. The recognized beam component is adjusted to the given reference value $\mathbf{C}\mathbf{u}_{\mathrm{b}}$, by the correction of the factor $\mathbf{C}^{\mathrm{i}}$ for *i*-th channel. Consequently, the required correction of the *i*-th channel, for the calibration purpose, is given by

$$\Delta\mathbf{C}^{\mathrm{i}} = \frac{\mathbf{C}\mathbf{u}_{\mathrm{b}}}{\mathbf{C}^{\mathrm{i}}\mathbf{D}^{\mathrm{i}}\mathbf{u}_{\mathrm{b}}}. \qquad (6.3\text{-}1)$$

Repeating the calibration procedure for all channels, the original signals of all cavities are restored with an accuracy of the constant factor **C**. Finally, the calibration factor **C** is matched to the scaling coefficient C (ref. to 6.1-7) and to the phase condition with respect to the actual beam (ref . to 6.3-7).

*Relative calibration without a beam*

A relative calibration is performed without a beam, under the assumption, that the incident phases $\left\{\angle\mathbf{v}_n^{\mathrm{i}}\right\}$ are correctly adjusted for all cavities, by means of the prior setting the

coupling factors $\{\mathbf{B}^{\mathrm{i}}\}$. In a case of diverse operating condition, the controlled cavities have diverse, time varying states, even for constant vector sum during the *flattop* range. So, the averaged values, over the *flattop* range, are considered for the calibration purpose. The primary assumption means, that the original signals $\{\underline{\mathbf{v}_n^{\mathrm{i}}}\}$, averaged over the *flattop* range, are collinear, in the vector representation for respective cavities. So, the input calibration, described later on, has been completed before.

The output calibration procedure is executed *off-line*, between pulses, simultaneously for all channels, considered for a vector sum open loop control (feed-forward). The measured *phasor* $\underline{\mathbf{v}_{\mathrm{d}n}^{\mathrm{i}}} = \mathbf{D}^{\mathrm{i}}\,\underline{\mathbf{v}_n^{\mathrm{i}}}$, averaged over the *flattop* range, for *i*-th channel of Output unit (ref. to fig. 6.1-2), is compared to the required reference *phasor* $\mathbf{v}_{\mathrm{r}}^{\mathrm{i}}$ of the respective channel. The reference absolute value $\left|\mathbf{v}_{\mathrm{r}}^{\mathrm{i}}\right|$ fits with the actual field gradient, averaged over the *flattop* range, given from an outside measurement system. The reference phase $\angle\mathbf{v}_{\mathrm{r}}^{\mathrm{i}} = \varphi_{\mathrm{r}}$, common one for all channels, equals to the given set-point value for the *flattop* range. The required set of calibration factors $\{\mathbf{C}^{\mathrm{i}}\}$ is estimated, and then implemented for all channels accordingly,

$$\left\{\mathbf{C}^{\mathrm{i}} = \frac{\mathbf{v}_{\mathrm{r}}^{\mathrm{i}}}{\underline{\mathbf{v}_{\mathrm{d}n}^{\mathrm{i}}}}\right\}. \tag{6.3-2}$$

The vector sum $\sum_{\mathrm{i}} \mathbf{v}_{\mathrm{c}n}^{\mathrm{i}}$ or mean value $\mathbf{v}_n = \overline{\mathbf{v}_{\mathrm{c}n}^{\mathrm{i}}}$, over all channels, is calculated with the obtained calibration factors. This virtual multi-cavity output is considered for the system model identification and control, resulting in the command input for a next pulse. The calibration procedure repeats for several pulses in the process of adaptive feed-forward control. Comparing the absolute value of vector sum, averaged over the *flattop* range, with the sum of the absolute values, averaged over the *flattop* range, for the respective channels, the calibration quality factor can be defined, as

$$\mathrm{Q_C} = \frac{\left|\sum_{\mathrm{i}} \underline{\mathbf{v}_{\mathrm{c}n}^{\mathrm{i}}}\right|}{\sum_{\mathrm{i}} \underline{\left|\mathbf{v}_{\mathrm{c}n}^{\mathrm{i}}\right|}} \le 1, \tag{6.3-3}$$

where underlining means average value, over the *flattop* range.

Comparing to the ideal value $Q_C = 1$, this factor can be used as a criterion for finishing of the calibration procedure. The relative calibration procedure can be repeated on request, for different condition, including feedback operation.

***Input calibration regarding to the signals co-linearity***

The main purpose of the input (high power) calibration is a required power distribution and a phase alignment of the cavities by proper correction of the coupling factors $\{\mathbf{B}^{\mathrm{i}}\}$. The signals co-linearity is necessary to match for the steady beam phase and for the reliable vector sum control.

In a case of diverse operating condition, discrepancies of amplitudes and phases are inevitable, so the averaged values, over the *flattop* range, are considered for the calibration purpose. The vector sum control tries to minimize the variance of the beam energy.

The input calibration can be performed without a beam, under the assumption, that the absolute, beam based output calibration has been completed before. The factors $\{\mathbf{B}^{\mathrm{i}}\}$ are correctly adjusted, under an actual operating condition, if the output *phasors* $\{\underline{\mathbf{v}^{\mathrm{i}}_{\mathrm{c}n}} = \mathbf{C}\underline{\mathbf{v}^{\mathrm{i}}_{n}}\}$, averaged over the flattop range, are equal to the given reference values $\{\mathbf{v}^{\mathrm{i}}_{\mathrm{r}}\}$, for all channels, so $\{\underline{\mathbf{v}^{\mathrm{i}}_{\mathrm{c}n}} = \mathbf{v}^{\mathrm{i}}_{\mathrm{r}}\}$. The reference phase $\angle\mathbf{v}^{\mathrm{i}}_{\mathrm{r}} = \varphi_{\mathrm{r}}$, common one for all channels, equals to the given set-point value for the *flattop* range. The absolute values may differ from each other according to requirements.

Analogously, like for the output relative calibration, the input calibration procedure is executed *off-line*, between pulses, simultaneously for all channels, considered for a vector sum open loop control (feed-forward).

The measured *phasor* $\underline{\mathbf{v}^{\mathrm{i}}_{\mathrm{c}n}}$, averaged over the *flattop* range, for *i*-th channel of Calibrator unit, is compared to the required reference *phasor* $\mathbf{v}^{\mathrm{i}}_{\mathrm{r}}$ of the respective channel. The required correction of the calibration factors $\{\mathbf{B}^{\mathrm{i}}\}$ is estimated and implemented for all channels accordingly,

$$\left\{\Delta\mathbf{B}^{\mathrm{i}} = \frac{\mathbf{v}^{\mathrm{i}}_{\mathrm{r}}}{\underline{\mathbf{v}^{\mathrm{i}}_{\mathrm{c}n}}}\right\}. \tag{6.3-4}$$

Analogously, like for the output relative calibration, the input calibration procedure repeats in the adaptive process by feed-forward control. The calibration quality factor $Q_B$ can be defined like the factor $Q_C$ by (6.3-3).

***Phase adjustment with respect to the beam***

The RF oscillating field is assumed to be synchronized with the charged bunch moving across the cavity (ref. to 2.1). Therefore, the cavities phases should be matched to the actual, constant beam phase. The requirement for the relative beam phase is given by

$$\varphi_b = \angle \mathbf{u}_b - \angle \overline{\mathbf{v}_n^i} = \angle \mathbf{C}\mathbf{u}_b - \angle \mathbf{C}\overline{\mathbf{v}_n^i}, \tag{6.3-5}$$

where $\overline{\mathbf{v}_n^i}$=const. is a stabilized mean value, over all cavities, $\mathbf{C}\overline{\mathbf{v}_n^i} = \mathbf{v}_r$=const. is a corresponding value for the multi-cavity output which equals to the reference value given by the *flattop* set-point. The beam component $\mathbf{C}\mathbf{u}_b$ is estimated by (6.2-15), and can be adjusted to the given reference value by the correction of the factor $\mathbf{C}$ (ref. to 6.3-1). Consequently, the required *flattop* phase of the multi-cavity output to be controlled is given by

$$\varphi_r = \angle \mathbf{v}_r = \angle \mathbf{C}\mathbf{u}_b - \varphi_b . \tag{6.3-6}$$

The *flattop* set-point phase can be set arbitrarily depending on the reference beam component $\mathbf{C}\mathbf{u}_b$ e.g.,

$$\varphi_r = -\varphi_b, \text{ if } \angle \mathbf{C}\mathbf{u}_b = 0 \qquad \text{or} \qquad \varphi_r = 0, \text{ if } \angle \mathbf{C}\mathbf{u}_b = \varphi_b . \tag{6.3-7}$$

## 6.4. Complex envelope detection

The *complex envelope* is a primary signal representation for the control purpose. The cavity voltage envelope is the fundamental data desired for the digital controller (ref. to 2.3). The effective algorithm for envelope detection is an important contribution to the optimization of the cavity control system.

***Quadrature detection***

The cavity RF signal is down-converted to an intermediate frequency $f_i$ preserving amplitude and phase information as follows (ref. to 2.3-1):

$$v(t) = v_m(t) \cdot \cos\left(2\pi f_i t + \varphi(t)\right), \tag{6.4-1}$$

where the amplitude $v_m(t)$ and the phase $\varphi(t)$ are slowly time-varying, relatively to the signal carrier with the angular frequency $\omega_i = 2\pi f_i$.

The *analytic signal* representation of v(t) is defined as

$$\breve{\mathbf{v}}(t) \equiv v(t) + \boldsymbol{j}\hat{v}(t) = \mathbf{v}(t) \cdot \exp(\boldsymbol{j}2\pi f_i t), \tag{6.4-2}$$

where $\hat{v}(t)$ is the *Hilbert transform* of v(t) and $\mathbf{v}(t) = v_m(t) \cdot e^{j\varphi(t)} = I(t)+\boldsymbol{j}Q(t)$ is the *complex envelope* representation (ref. to 2.3-2, 2.3-3 and 2.3-4). The *complex envelope* is determined by a complex demodulation of the *analytic signal* for a given frequency $f_i$, according to the expression:

$$\mathbf{v}(t) = \left(v(t) + \boldsymbol{j}\hat{v}(t)\right) \cdot \exp(-\boldsymbol{j}2\pi f_i t). \tag{6.4-3}$$

The digital signal processing applies the signal of intermediate frequency v(t) with sampling interval $T = 1/4f_i$ (four samples per period). Therefore, the *complex envelope* for discrete time t = nT is given by a digital demodulation

$$\mathbf{v}_n = \left(v_n + \boldsymbol{j}\hat{v}_n\right)(-\boldsymbol{j})^n = I_n + \boldsymbol{j}Q_n, \tag{6.4-4}$$

where, $\mathbf{v}_n = \mathbf{v}(nT)$, $v_n = v(nT)$, $\hat{v}_n = \hat{v}(nT)$, $I_n = I(nT)$, $Q_n = Q(nT)$ are signal samples respectively.

*Zero order complex envelope detection.*

Let's assume the stable value of an amplitude and phase of the cavity voltage for successive steps $n-1$ and $n$, so that $\mathbf{v}_{n-1} = \mathbf{v}_n$, what is expected for the *flattop* range. Two consecutive samples of the real signal $v_{n-1}$, $v_n$ are required for the *zero order* envelope detection, by digital demodulation, according to relations:

$$\left.\begin{aligned} \mathbf{v}_n &= \left(v_n + \boldsymbol{j}\hat{v}_n\right)(-\boldsymbol{j})^n \\ \mathbf{v}_n &= \left(v_{n-1} + \boldsymbol{j}\hat{v}_{n-1}\right)(-\boldsymbol{j})^{n-1} \end{aligned}\right\} \quad \Rightarrow \quad \mathbf{v}_n = \left(v_n + \boldsymbol{j}v_{n-1}\right)(-\boldsymbol{j})^n \tag{6.4-5}$$

*First Order Envelope Detection.*

A more accurate estimation of the *complex envelope* is considered for a fast varying amplitude and phase during the cavity *filling* time.

Let's assume a linearly time varying *complex envelope* for the successive steps $n$-1, $n$, $n$+1 with mutual difference of $\Delta\mathbf{v}$, as follows:

$$\mathbf{v}_{n-1} = \mathbf{v}_n - \Delta\mathbf{v}, \quad \mathbf{v}_{n+1} = \mathbf{v}_n + \Delta\mathbf{v}\,. \tag{6.4-6}$$

Three sequential samples of the real signal, $v_{n-1}$, $v_n$, $v_{n+1}$, are required for the *first order* envelope detection, by digital demodulation, according to relations:

$$\left.\begin{aligned} \mathbf{v}_n - \Delta\mathbf{v} &= \left(v_{n-1} + \boldsymbol{j}\widehat{v}_{n-1}\right)(-\boldsymbol{j})^{n-1} \\ \mathbf{v}_n &= \left(v_n + \boldsymbol{j}\widehat{v}_n\right)(-\boldsymbol{j})^{n} \\ \mathbf{v}_n + \Delta\mathbf{v} &= \left(v_{n+1} + \boldsymbol{j}\widehat{v}_{n+1}\right)(-\boldsymbol{j})^{n+1} \end{aligned}\right\} \Rightarrow \quad \mathbf{v}_n = \left(v_n - \boldsymbol{j}\frac{v_{n+1} - v_{n-1}}{2}\right)(-\boldsymbol{j})^{n} \tag{6.4-7}$$

*Offset removing*

A practical implementation of the *complex envelope* detection, requires removing an inevitable *offset* of the intermediate frequency signal. It can be a time-varying and modulated value. The differential form of the *complex envelope* expression, estimated as the average value $\mathbf{v}_n = \frac{\mathbf{v}_{n-1} + \mathbf{v}_{n+1}}{2}$, is proposed for the efficient *offset* removing.

Four sequential samples of the real signal, $v_{n-2}$, $v_{n-1}$, $v_n$, $v_{n+1}$, are required for the differential form of the *zero order* digital detection for the *complex envelope* expressed as

$$\mathbf{v}_n = \left(\frac{v_n - v_{n-2}}{2} - \boldsymbol{j}\frac{v_{n+1} - v_{n-1}}{2}\right)(-\boldsymbol{j})^{n}, \tag{6.4-8}$$

Five sequential samples of the real signal, $v_{n-2}$, $v_{n-1}$, $v_n$, $v_{n+1}$, $v_{n+2}$ are required for the differential form of the *first order* digital detection for the *complex envelope* expressed as

$$\mathbf{v}_n = \left(\frac{v_n - v_{n-2}}{4} - \frac{v_{n+2} - v_n}{4} - \boldsymbol{j}\frac{v_{n+1} - v_{n-1}}{2}\right)(-\boldsymbol{j})^{n}. \tag{6.4-9}$$

Comparing the measured sample $v_n$ from (6.4-7) with the corresponding expression of (6.4-9), the *offset* value is estimated as

$$v_{\text{off}\,n} = \frac{v_{n-2} + 2v_n + v_{n+2}}{4}\,. \tag{6.4-10}$$

It can be applied for *offset* compensation alternatively, if it is a repeatable value, in the next pulse.

The differential form of the *complex envelope* expression can be extended by averaging more values, resulting in better filtering of a noisy signal [38].

The algorithms for the digital detection of the *complex envelope* are determined without regard to causality and are useful for *offline* estimation required for the system identification between pulses. The causal form, required for the *online* implementation, is obtained by a delayed version of expressions (6.4-7), (6.4-8) or (6.4-9). The linear prediction by two steps ahead, $\mathbf{v}_n = 3\mathbf{v}_{n-2} - 2\mathbf{v}_{n-3}$, can be considered using (6.4-9), for a fast varying envelope during *filling* range. However, a higher intermediate frequency is a better solution for a delay reduction.

***Multi-sample detection***

A digital demodulation algorithm can be generalized applying N > 2 samples per period of the intermediate frequency signal. A stable value $\mathbf{v}_k$ of the *complex envelope*, during the period *k*, is assumed for the multi-sample detection. The discrete sample $\breve{\mathbf{v}}_n$ of the *analytic signal* representation for the step *n*, within the period *k*, is given by (ref. to 6.4-2):

$$\breve{\mathbf{v}}_n = \mathrm{v}_n + \boldsymbol{j}\hat{\mathrm{v}}_n = \mathbf{v}_\mathrm{k} \cdot \exp(\boldsymbol{j}\frac{2\pi}{\mathrm{N}}\mathrm{n}) . \tag{6.4-11}$$

Summing (6.4-11) together with the corresponding complex conjugate values gives

$$\mathbf{v}_\mathrm{k} \cdot \exp(\boldsymbol{j}\frac{2\pi}{\mathrm{N}}\mathrm{n}) + \mathbf{v}_\mathrm{k}^* \cdot \exp(-\boldsymbol{j}\frac{2\pi}{\mathrm{N}}\mathrm{n}) = 2\mathrm{v}_n . \tag{6.4-12}$$

Accordingly,

$$\mathbf{v}_\mathrm{k} = 2\mathrm{v}_n \cdot \exp(-\boldsymbol{j}\frac{2\pi}{\mathrm{N}}\mathrm{n}) - \mathbf{v}_\mathrm{k}^* \cdot \exp(-\boldsymbol{j}\frac{4\pi}{\mathrm{N}}\mathrm{n}) . \tag{6.4-13}$$

Summing over n = 0 : N−1 yields

$$\mathrm{N}\mathbf{v}_\mathrm{k} = 2\sum_{0}^{\mathrm{N}-1} \mathrm{v}_n \exp(-\boldsymbol{j}\frac{2\pi}{\mathrm{N}}\mathrm{n}) . \tag{6.4-14}$$

The differential form of the *zero order* digital detection for the *complex envelope* expressed by (6.4-8) is the solution case of (6.4-14) for N = 4.

***Experimental results***

The representative readouts, applying ACC1 module of FLASH setup, are presented below for typical operating condition. The down-converted 250 kHz signal of an RF mixer is approximated by 4 steps per period. Fig. 6.4-1 shows the original signals sampled by the 14

bits, 40 MHz analog-to-digital converters for vector sum control. The eight cavities channels and klystron channel are monitored by ADC fast readouts in 50 μs window within the *flattop* range. The analog, stairs-like signal of intermediate frequency 250 kHz, is sampled with a step of 25 ns and averaged over the synchronized window pulse with the resolution of 18 bits. The consequential secondary signal is decoded by a digital demodulation resulting in the *complex envelope* representation.

The signals for digital processing are demonstrated in fig. 6.4-2 for single cavity no. 8 controlled by feed-forward driving. The ADC secondary signal of intermediate frequency 250 kHz and estimated values of *offset* are shown with the resolution of 18 bits. The *complex envelope*, detected according to (6.4-9), is calibrated by phasing and scaling with MV unit. The zoomed *flattop* area shows raw, noisy data and estimated values, smoothed by the polynomial *spline* functions (ref. to Appendix).

## 6.5. Multi-cavity system control

The multi-cavity digital model, without a beam, driven by the controller output $\mathbf{x}_n$, is expressed recursively as (ref. to 6.1-11)

$$\mathbf{v}_{n+1} = \mathbf{A}_n \mathbf{v}_n + \mathbf{F}_n \mathbf{x}_n , \tag{6.5-1}$$

where the system factor is $\mathbf{A}_n = (1 - \omega_{1/2}\mathrm{T}) + \boldsymbol{j}\Delta\omega_n \mathrm{T}$ and the input factor is $\mathbf{F}_n$. The corresponding inverse model, useful for the control purpose, is derived as

$$\mathbf{x}_n = (\mathbf{v}_{n+1} - \mathbf{A}_n \mathbf{v}_n) \cdot \mathbf{F}_n^{-1} . \tag{6.5-2}$$

The required multi-cavity output and parameters of the plant determine uniquely the desired plant input, that is the controller output. The digital control conditions, derived from the continuous ones corresponding to table 4.2-1, are combined in table 6.4-1. The normalized values, dependent on substituted parameters: half-bandwidth and detuning of the multi-cavity, have been calculated for required output and desired input in the columns called set-point **v** and feed-forward **x** respectively. The three ranges of multi-cavity operation are separated in the rows: *filling*, *flattop* and *decay*. The common factor has been extracted for the ranges rows and feed-forward column respectively.

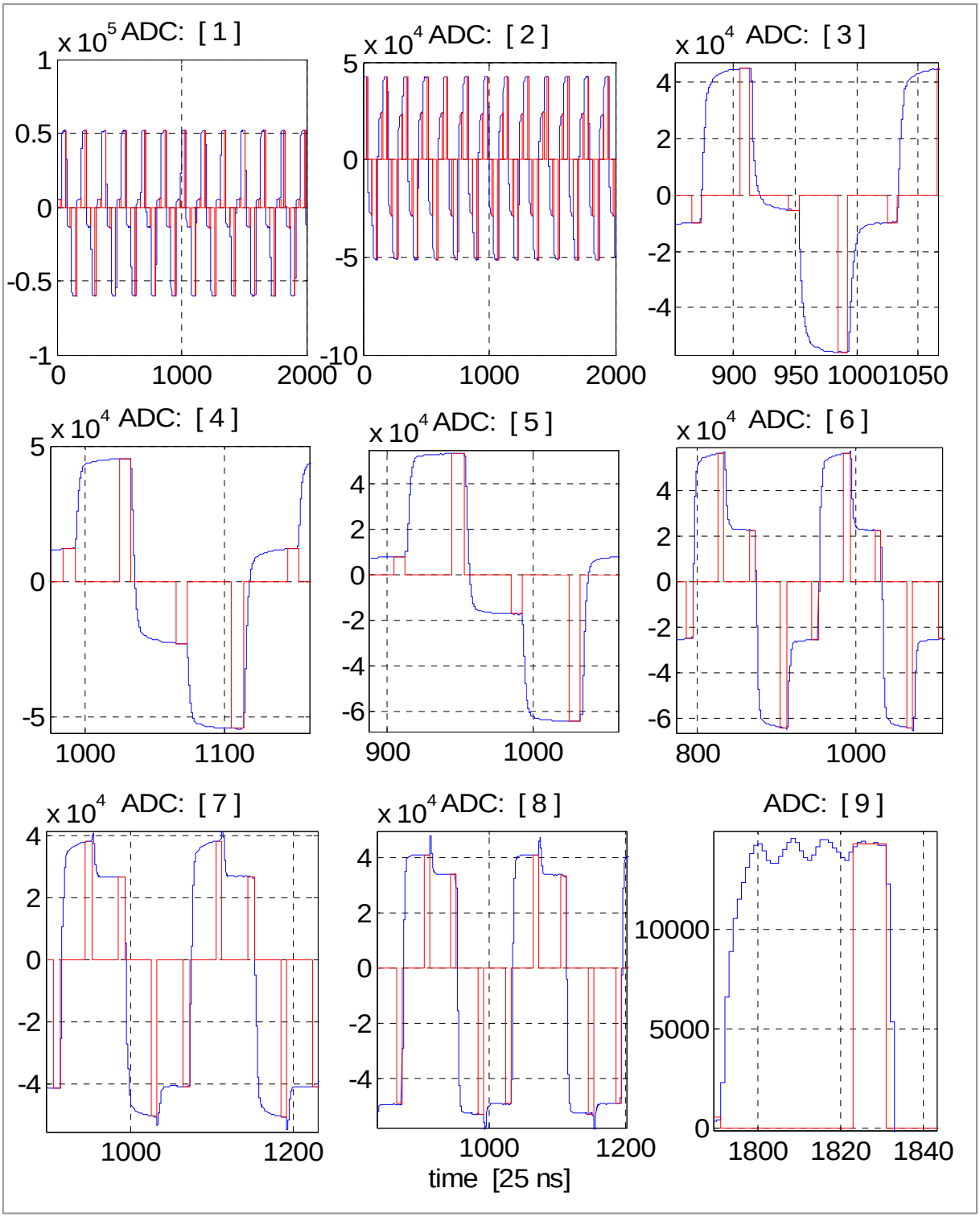


Fig. 6.4-1. Vector sum control. The eight cavities channels and klystron channel no. 9 are monitored by ADC fast readouts in 50 μs window within the *flattop* range. The analog, stairs-like signal of intermediate frequency 250 kHz, is sampled with a step of 25 ns (blue line) and averaged inside the synchronized window pulse (red line).

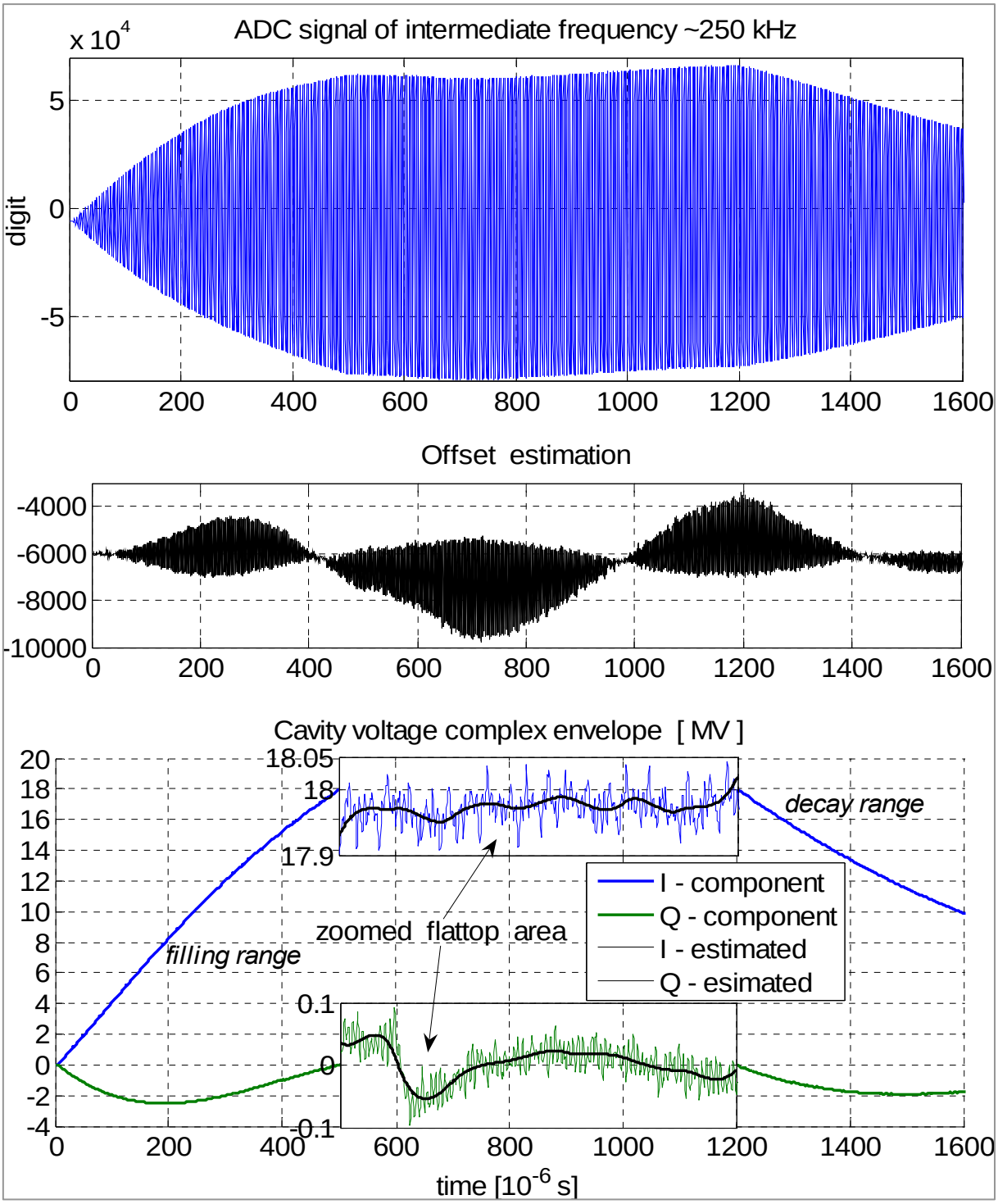


Fig. 6.4-2. Single cavity control by feed-forward driving. The secondary signal of intermediate frequency 250 kHz and estimated values of *offset* are shown with the resolution of 18 bits. The detected *complex envelope* is calibrated by phasing and scaling with MV unit. The zoomed *flattop* area shows noisy data and estimated values, smoothed by polynomial *spline* functions. A distortion, visible in the chart of Q – component, in the *flattop* area, is caused by the RF Gun *crosstalk*.

Table 6.5-1. The input – output condition of the digital control

| *Control* / *Range* | | Set-Point **v** | Feed-forward **x** $\mathbf{F}_n^{-1}$ | *common factor* |
|---|---|---|---|---|
| Filling | *exp* | $\frac{1-\exp(-\omega_{1/2}\mathrm{T}n)}{1-\exp(-\omega_{1/2}\mathrm{T}n_f)}$ | $\frac{\omega_{1/2}\mathrm{T}}{1-\exp(-\omega_{1/2}\mathrm{T}n_f)}$ | $\mathbf{v}_c^{\bullet}\exp\left(-\boldsymbol{j}\sum_{i=n}^{i=n_f}\Delta\omega_i\mathrm{T}\right)$ |
| | *lin* | $\frac{n}{n_f}$ | $\frac{1+\omega_{1/2}\mathrm{T}n}{\mathrm{T}n_f}$ | |
| | *sinh* | $\frac{\sinh(\omega_{1/2}\mathrm{T}n)}{\sinh(\omega_{1/2}\mathrm{T}n_f)}$ | $\frac{\exp(\omega_{1/2}\mathrm{T}n)}{\sinh(\omega_{1/2}\mathrm{T}n_f)}\omega_{1/2}\mathrm{T}$ | |
| Flattop | | 1 | $\omega_{1/2}\mathrm{T}-\boldsymbol{j}\Delta\omega_n\mathrm{T}$ | $\mathbf{v}_c^{\bullet}$ |
| Decay | | $\exp(-\omega_{1/2}\mathrm{T}m)$ | 0 | $\mathbf{v}_c^{\bullet}\exp\left(\boldsymbol{j}\sum_{i=0}^{i=m}\Delta\omega_i\mathrm{T}\right)$ |

For the *filling* range n = 0 : $n_f$, the multi-cavity is driven under the resonance condition in respect to the substituted detuning. Additionally, the following types of output trajectories: exponential, linear and hyperbolic sine, are selected for the *filling* range. For the *flattop* range n = $n_f$ : $n_p$, the multi-cavity output is stable in accordance with the reference value $\mathbf{v}_c^{\bullet}$. For *decay* range m = n − $n_p$ > 0, the controller is turned off and the multi-cavity output freely expires.

Due to a discrepancy of the multi-cavity model and unknown disturbances, the adaptive differential methods and feed-back support are necessary for a reliable control. All algorithms of the cavity control, presented in chapter 5, can be applied for the multi-cavity system driving. However, due to a limited access to a real accelerator, only some of them have been tested by experimental studying of ACC1 module in FLASH system [39].

***Adaptive Feed-Forward by direct inverse control***

The adaptive feed-forward by direct inverse control allows for a first recognition of the system and verification of the identification methods without a beam. The initial iterative control procedure requires simultaneous relative vector sum calibration (ref. to 6.3). Furthermore, a *predetuning* adjustment should be performed for a given operating condition

(ref. to 5.2). The controller output is determined by the inverse solution given by (6.5-2) for the required vector sum value, or directly by the rules from table 6.5-1.

*Filling operation*

A single cavity control, under the resonance condition, for a long *filling* range 1300 μs, is presented in fig. 6.5-1 for the cavity no. 8 of ACC1 module. The cavity amplitude and phase, klystron amplitude, forward and reflected power are showed for different following trajectories: linear, exponential and hyperbolic sine.

The multi-cavity performance has been studied for different durations of *filling* range. The vector sum control of 8 cavities of ACC1 module, under resonance condition, for *filling* ranges: 500 μs : 1300 μs is presented in fig. 6.5-2 for hyperbolic sine trajectory. The following basic characteristics of the plant: multi-cavity amplitude and phase, klystron phase, mean forward power, substituted parameters: half-bandwidth and detuning, are monitored for all ranges.

The relative expended energy as a function of *filling* time is presented in figure 6.5-4 for the following types of trajectory: exponential, linear and hyperbolic sine (optimal) (ref. to fig. 4.1-4).

The vector sum control for long *filling* 1000 μs and short *flattop* range 300 μs is presented in fig. 6.5-3 with basic characteristics.

*Flattop operation*

A single cavity control by adaptive feed-forward striving for *flattop* stabilization is presented in fig. 6.5-5 for five pulses of iteration.

The vector sum control of 8 cavities, with basic characteristics, is presented in fig. 6.5-6 for three amplitude values of multi-cavity output. An exponential trajectory has been chosen for the *filing* range under the resonance condition. Estimated detuning during *flattop* range indicates, that the multi-cavity is tuned for 12 MV, under-tuned for 14 MV, and over-tuned for 10 MV.

The repeated readout of basic characteristics from ten pulses is presented in fig. 6.5-7 for the vector sum control of 8 cavities. A linear trajectory has been chosen for the *filing* range under the resonance condition. A dispersion of multi-cavity characteristics is caused, mainly, by a detuning fluctuation due to cavities *microphonics*.

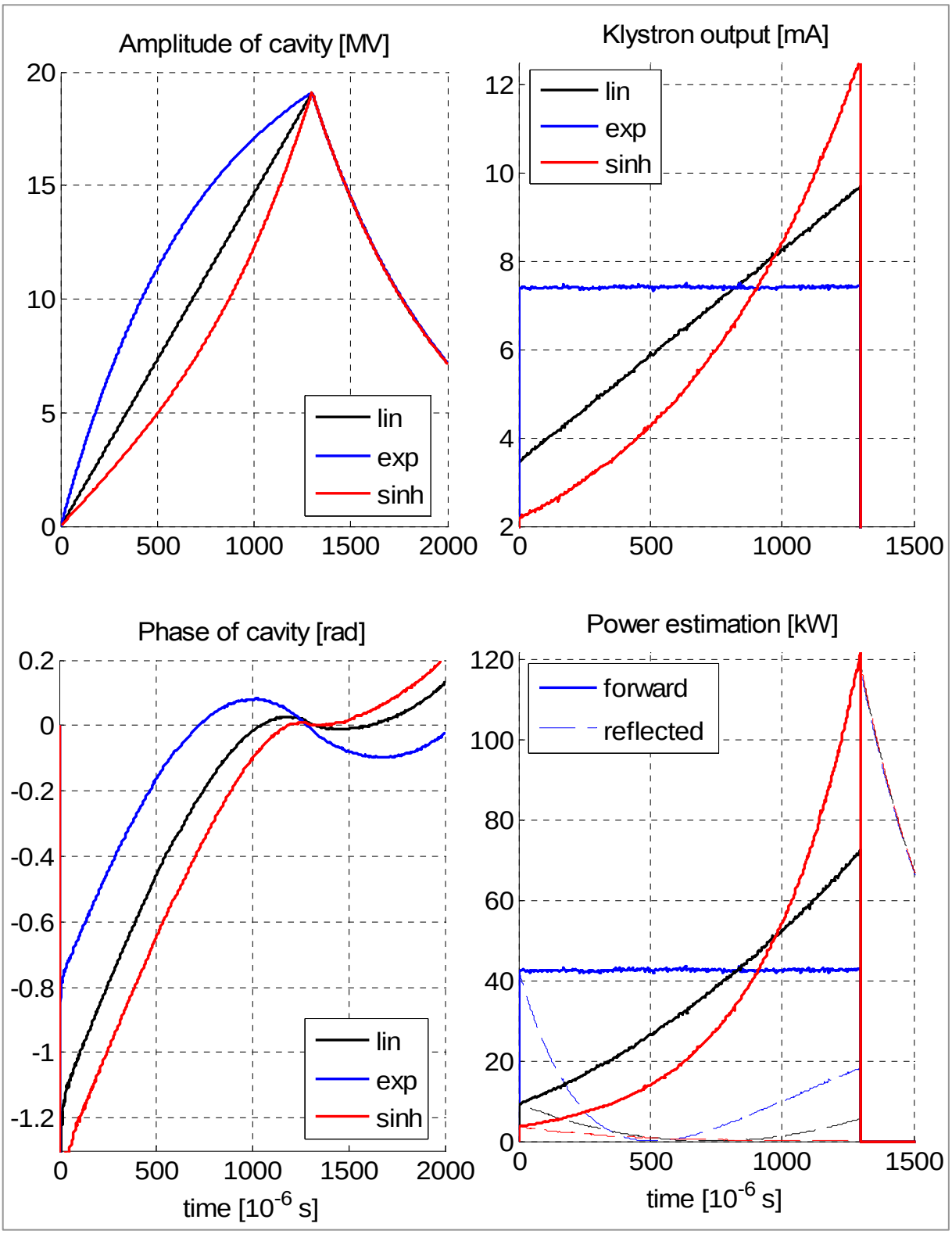


Fig. 6.5-1. Single cavity control, under resonance condition, by feed-forward driving for long *filling* range 1300 μs. The cavity amplitude and phase, klystron amplitude, forward and reflected power are showed for different following trajectories: linear, exponential and hyperbolic sine.

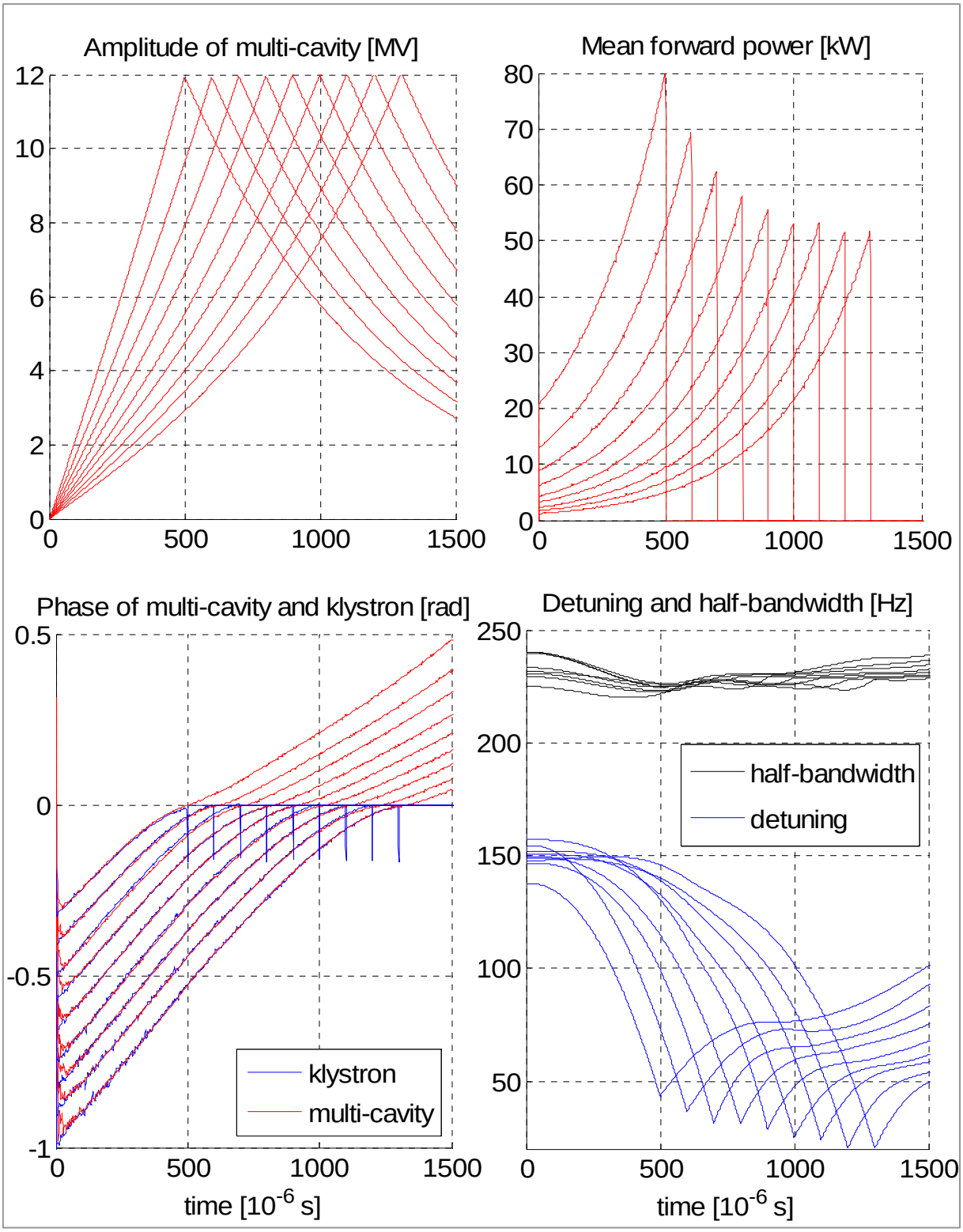


Fig. 6.5-2. Vector sum control of 8 cavities, under resonance condition, for *filling* ranges: 500 μs : 1300 μs for hyperbolic sine trajectory. The basic characteristics: multi-cavity amplitude and phase, klystron phase, mean forward power, substituted parameters: half-bandwidth and detuning, are monitored for all ranges.

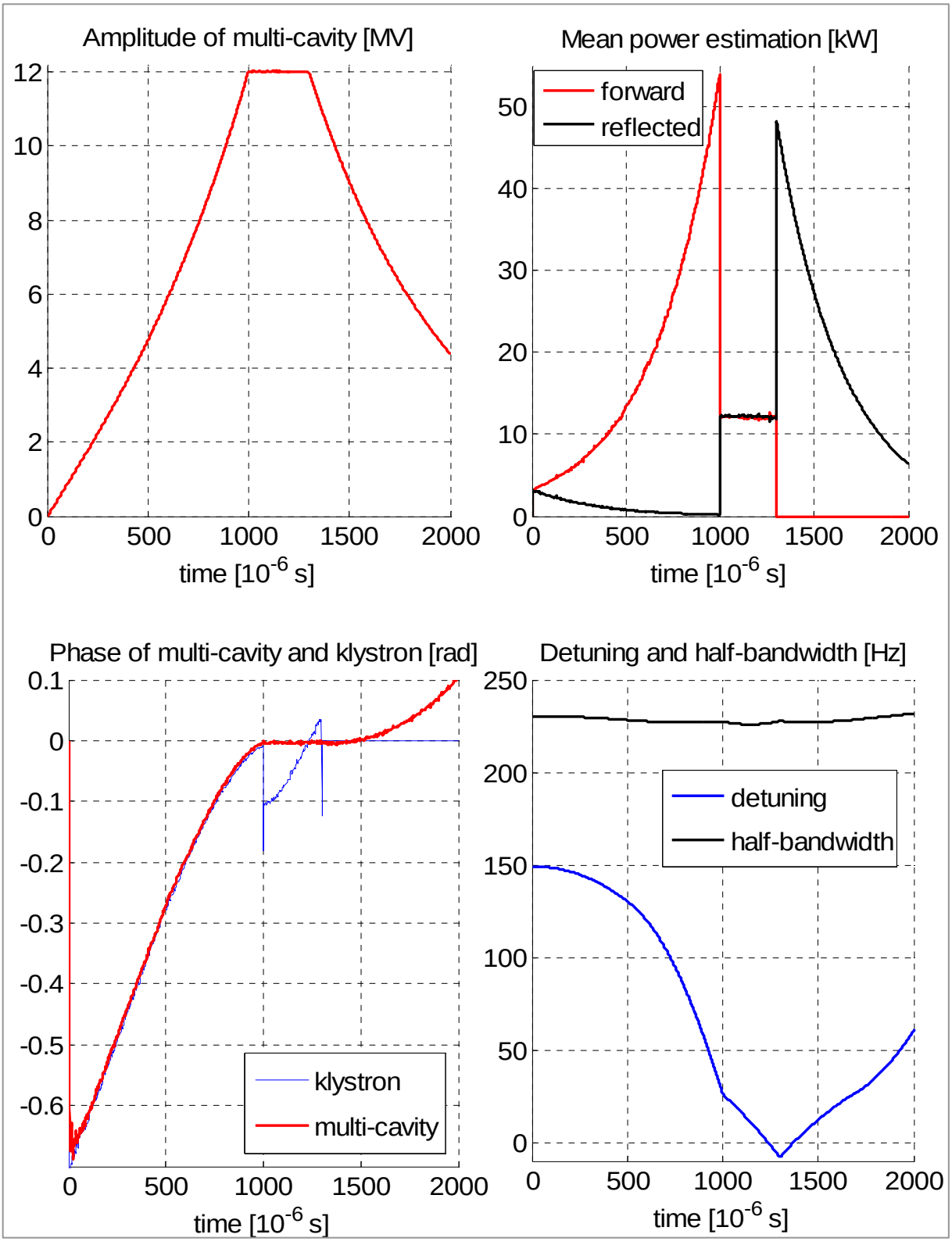


Fig. 6.5-3. Vector sum control of 8 cavities. The basic characteristics: multi-cavity amplitude and phase, klystron phase, forward and reflected mean power, substituted parameters: half-bandwidth and detuning, are monitored for long *filling* 1000 μs and short *flattop* range 300 μs.

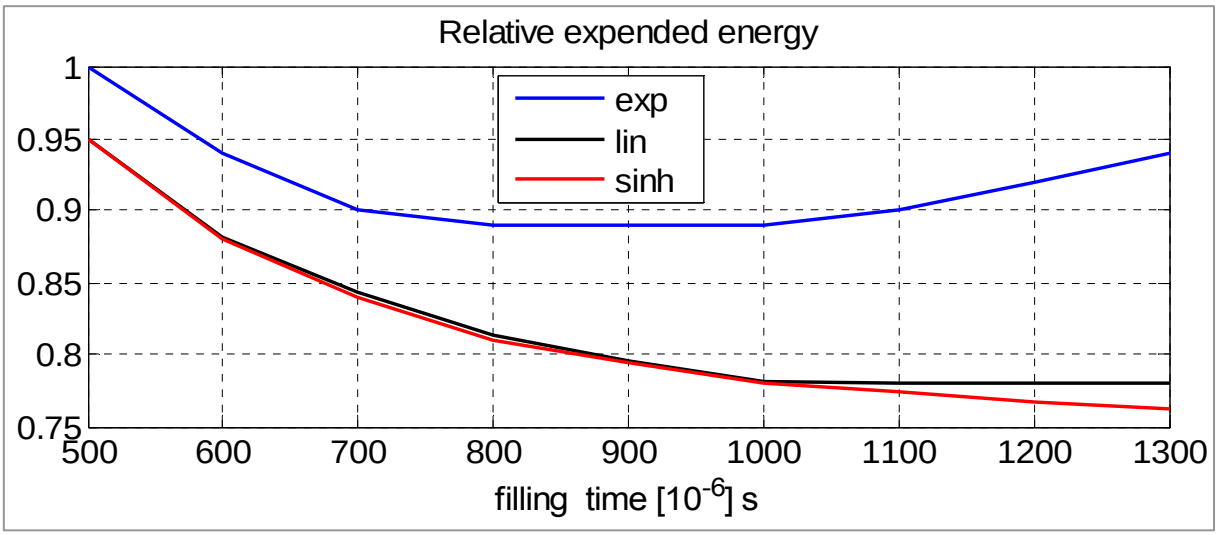


Fig. 6.5-4. The relative expended energy as a function of *filling* time for the following types of trajectory: exponential, linear and hyperbolic sine (optimal).

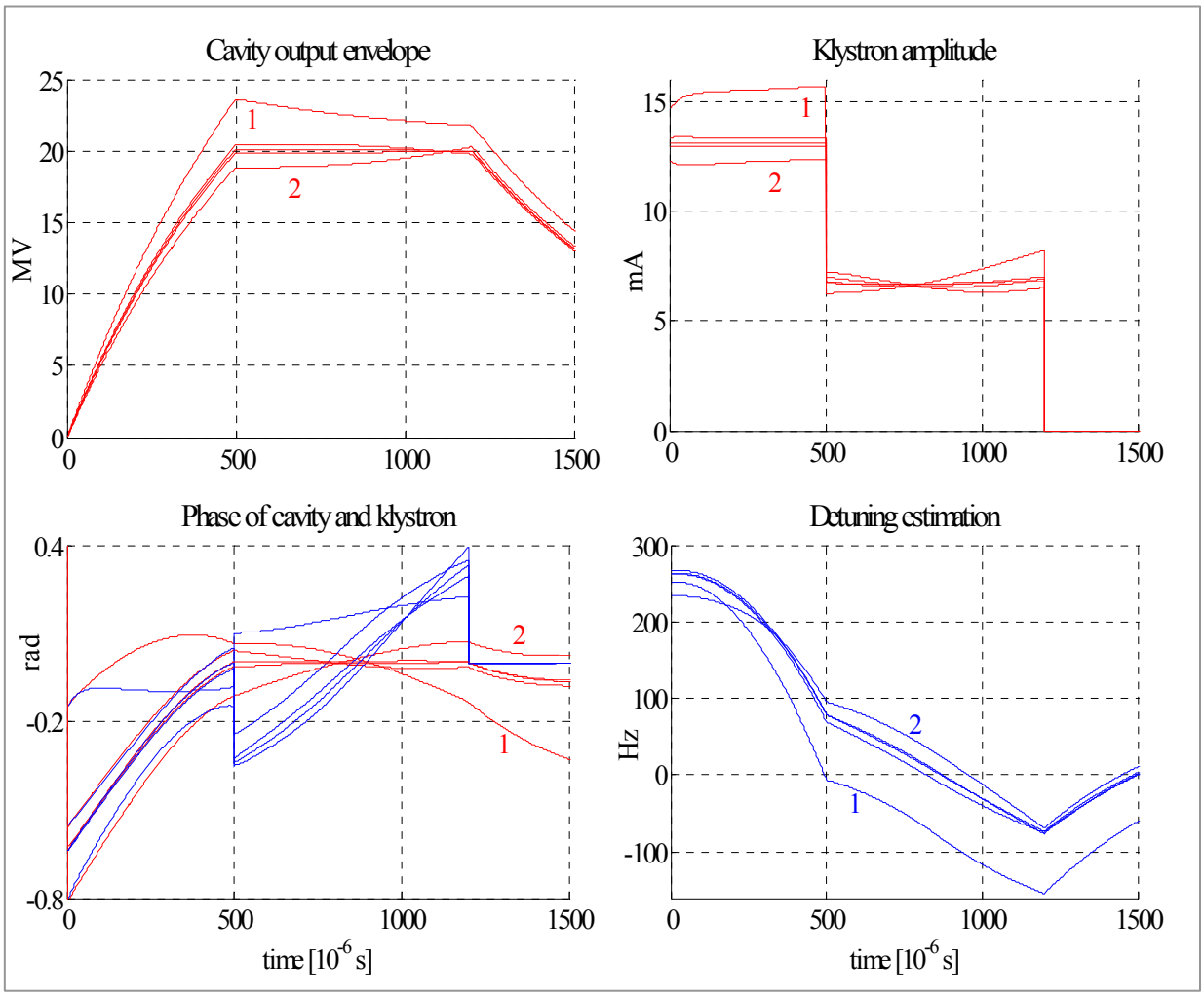


Fig.6.5-5. Single cavity control by adaptive feed-forward driving – five pulses of iteration.

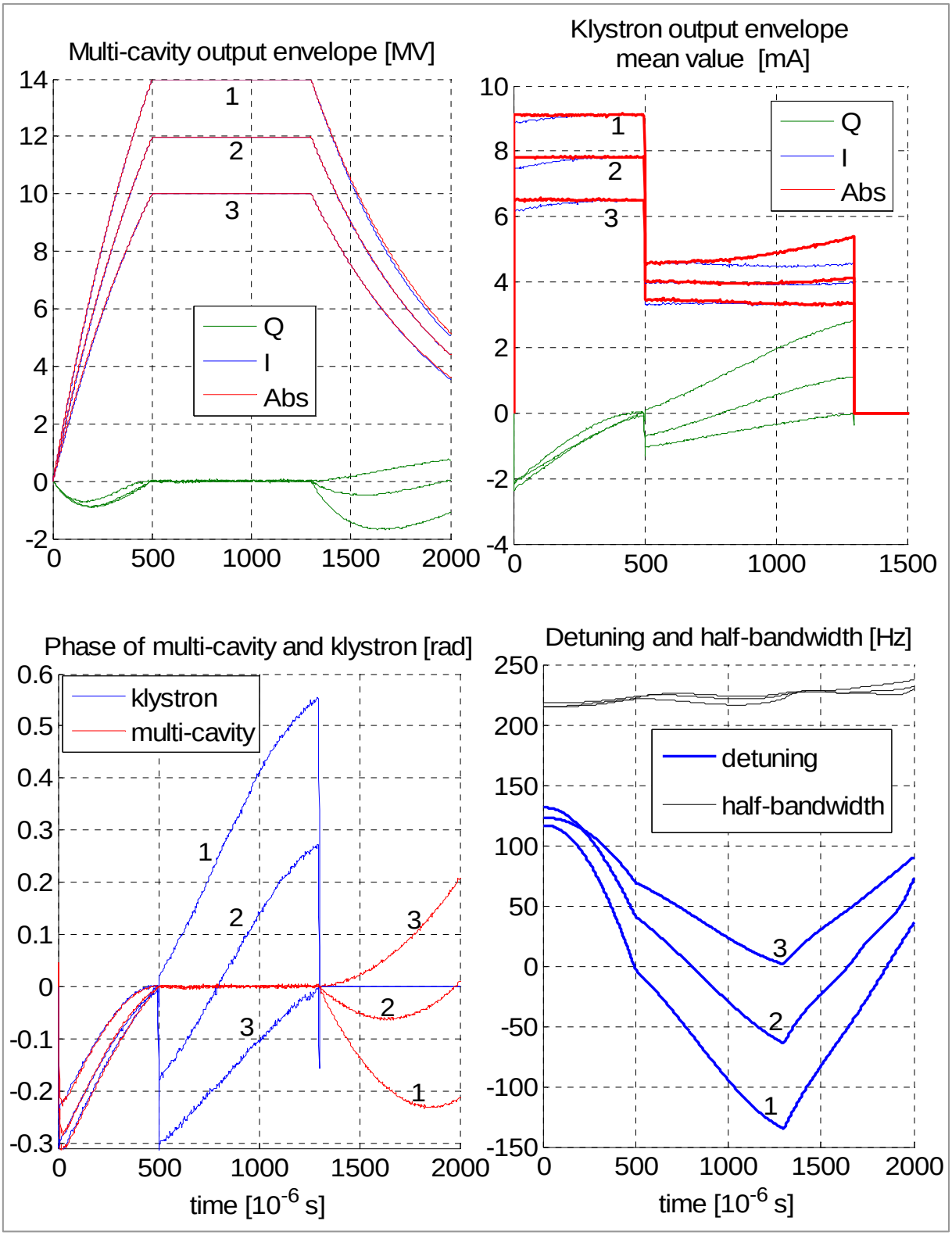


Fig. 6.5-6. The basic characteristics of vector sum control of 8 cavities, for three amplitude values of multi-cavity output. An exponential trajectory has been chosen for the *filing* range under the resonance condition. Estimated detuning during *flattop* range indicates, that the multi-cavity is: 1 − under-tuned for 14 MV, 2 − tuned for 12 MV, 3 − over-tuned for 10 MV.

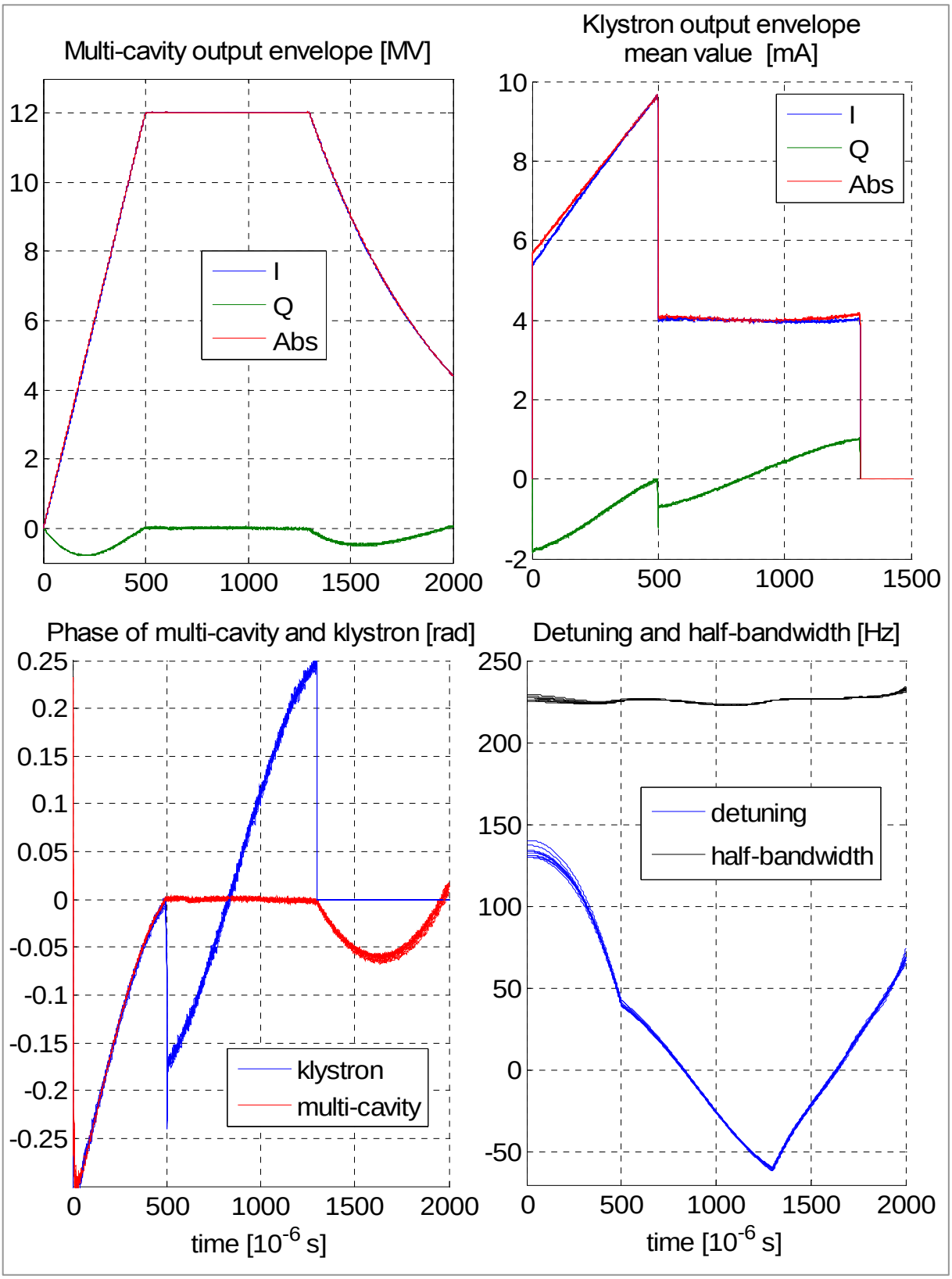


Fig. 6.5-7. Vector sum control of 8 cavities - repeated readout of basic characteristics from ten pulses. A linear trajectory has been chosen for the *filing* range under the resonance condition. A dispersion of multi-cavity characteristics is caused, mainly by a detuning fluctuation due to cavities *microphonics*.

***Conventional feedback supported by feed-forward control***

The complex control of the multi-cavity, modeled by (6.1-11), with the conventional feedback, supported by feed-forward driving, is presented in fig. 5.6-8, corresponding to fig. 5.5-1. Internal delay *d* is included in the model. All considerations of chapter 5.5 are valid for the feedback gain $\mathbf{G}_{f\,n} = \mathbf{F}_n \mathbf{G}_n$, where $\mathbf{F}_n$ is a multi-cavity input factor and $\mathbf{G}_n$ is a controller gain. The controller gain is determined by the given real value of resonant loop gain $G_{L0} \geq 0$ as follows (ref. to 5.5-6)

$$\mathbf{G}_n = G_{L0}\omega_{1/2}T\mathbf{F}_n^{-1}. \tag{6.5-3}$$

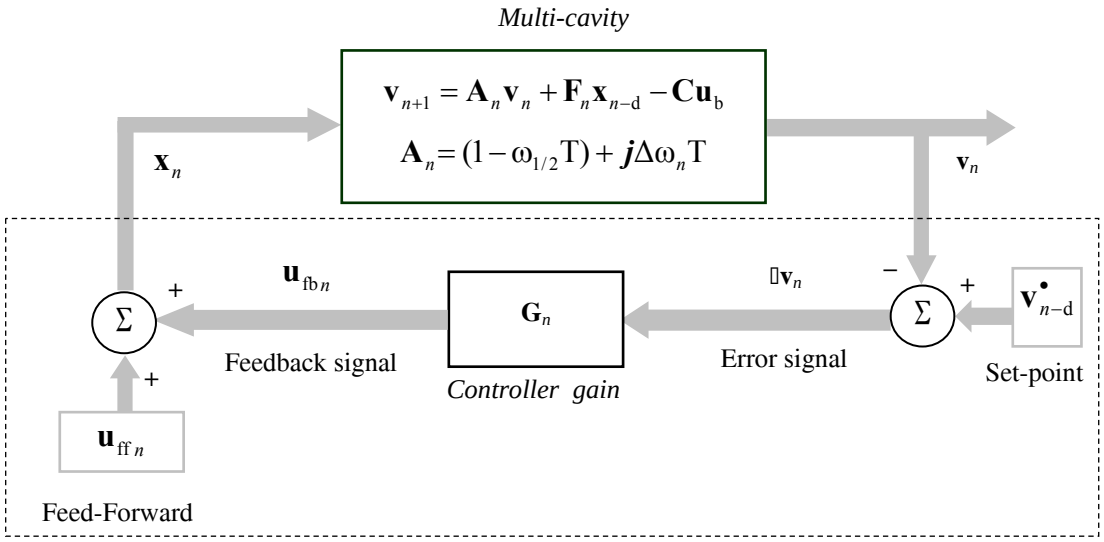


Fig.6.5-8. The complex control of the multi-cavity model, with the conventional feedback, supported by feed-forward driving.

The vector sum control of 8 cavities, without a beam, as a result of feedback supported by feed-forward driving, is presented in fig. 6.5-9, for the resonant loop gain $G_{L0}$ = 50. A linear trajectory has been chosen for the *filing* range under the resonance condition. The vector sum is stabilized within the long *flattop* range 1300 μs. The basic characteristics of the plant: envelope of the multi-cavity and klystron, substituted parameters: half-bandwidth and detuning, are monitored.

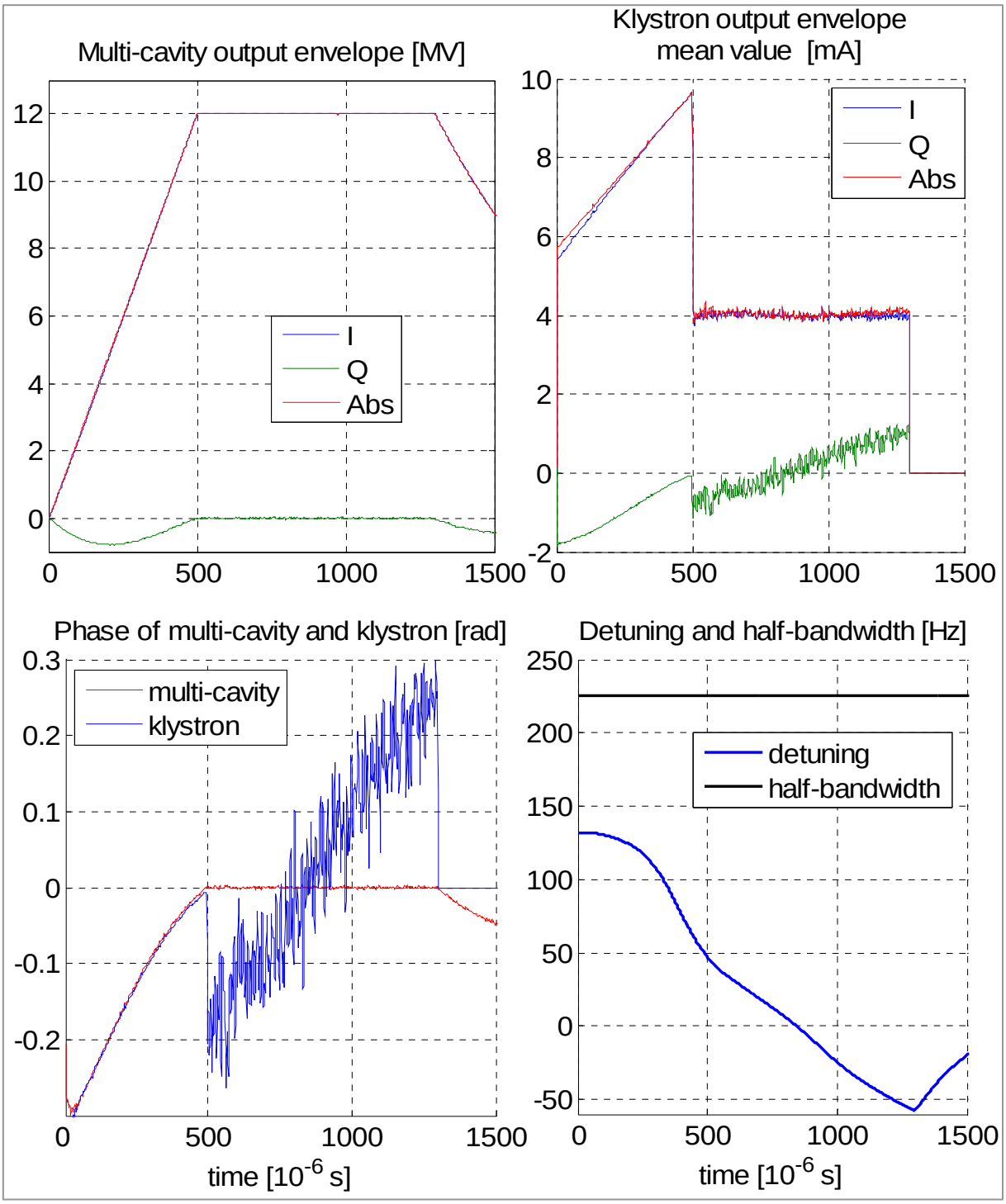


Fig. 6.5-9. The vector sum control of 8 cavities, without a beam, as a result of feedback with the resonant loop gain $G_{L0} = 50$, supported by feed-forward driving. A linear trajectory has been chosen for the *filing* range under the resonance condition. The vector sum is stabilized within the long *flattop* range 1300 μs. The basic characteristics of the plant: envelope of the multi-cavity and klystron, substituted parameters: half-bandwidth and detuning, are monitored. Not filtered noise of the multi-cavity output is amplified by the controller and klystron.

The selected amplitude and phase charts, within the zoomed *flattop* area, are presented in figure 6.5-10 for the following resonant loop gain values: $G_{L0}$ =: 0, 100, 300 (stability limit), of the multi-cavity control. The measured values, without a filter, are compared to the reference set-point. The relative *rms* error for amplitude and *rms* error for phase [rad] are estimated separately. The mean of the absolute error $\Delta v_c = \left| \mathbf{v}_c^{\bullet} - \mathbf{v}_c \right|$, related to set-point $v_c^{\bullet} = \left| \mathbf{v}_c^{\bullet} \right|$, for the *flattop* range, is estimated as follows: $\frac{\overline{\Delta v_c}}{v_c^{\bullet}} =: \sim 2 \cdot 10^{-3}, \sim 8 \cdot 10^{-4}, \sim 4 \cdot 10^{-3}$ for $G_{L0}$ =: 0, 100, 300, respectively. The multi-cavity output errors are dominated by disturbances of the measurement channel.

*Beam testing*

The vector sum control of ACC1 8 cavities, influenced by the beam loading, is presented in fig. 6.5-11, for feed-forward and feedback driving. The beam of 2 nC x 30 bunches (30 μs long) was injected in the beginning of the *flattop* range, at instance of 550 μs. The amplitude and phase charts, within zoomed *flattop* area, are selected for the following resonant loop gain values: $G_{L0}$ =: 0, 100, 250.

The measurements of beam energy stability was performed for a short beam. The cavity was activated with a pulse of 0.8 ms duration and repetition of 5 Hz. During the first stage of the operation (~0.5 ms *filling*), the cavity was driven with constant forward power and modulated phase, resulting in an exponential increase of the field under the resonance condition. The cavity voltage had reached the required final mean value ca. 13 MV, for a short *flattop* range (~0.3 ms). In the carried out experiment, two bunches of the beam were injected in the beginning of *flattop* range. An external *toroid* signal, induced by a beam, can activate the beam loading compensation, in the case of long bunches. The beam energy stability, measured in the BC2 (*bunch compressor*). while operating “on crest”, was tested as a function of the resonant loop gain (Fig. 6.5-12). The phase adjustment was carried manually according to the beam energy measurement system.

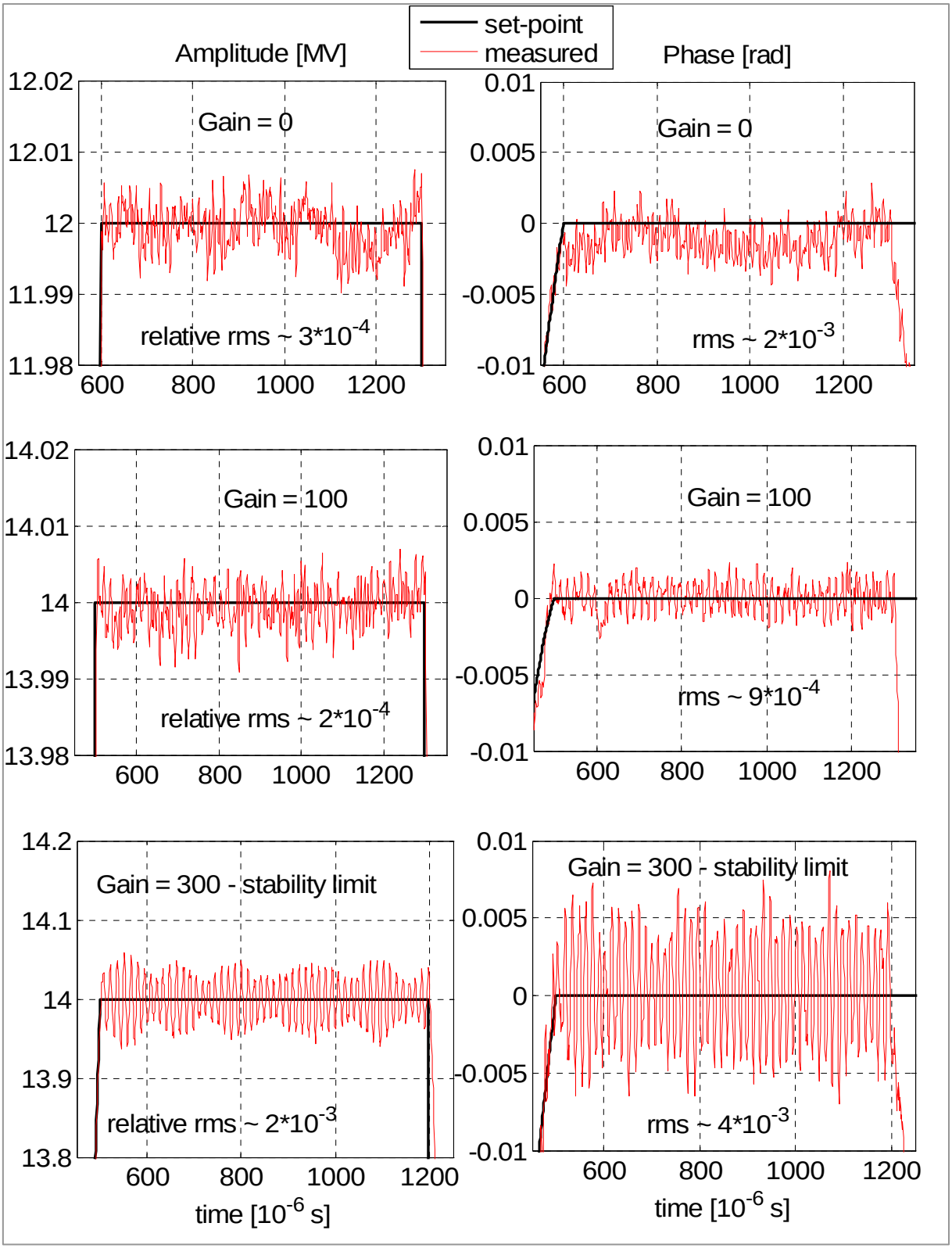


Fig. 6.5-10. The selected amplitude and phase charts, within zoomed *flattop* area, for the following resonant loop gain values: $G_{L0}$ =: 0, 100, 300 (stability limit) of the multi-cavity control. The measured values, without a filter, are compared to the reference set-point. The relative *rms* error for amplitude and *rms* error for phase [rad] are estimated separately.

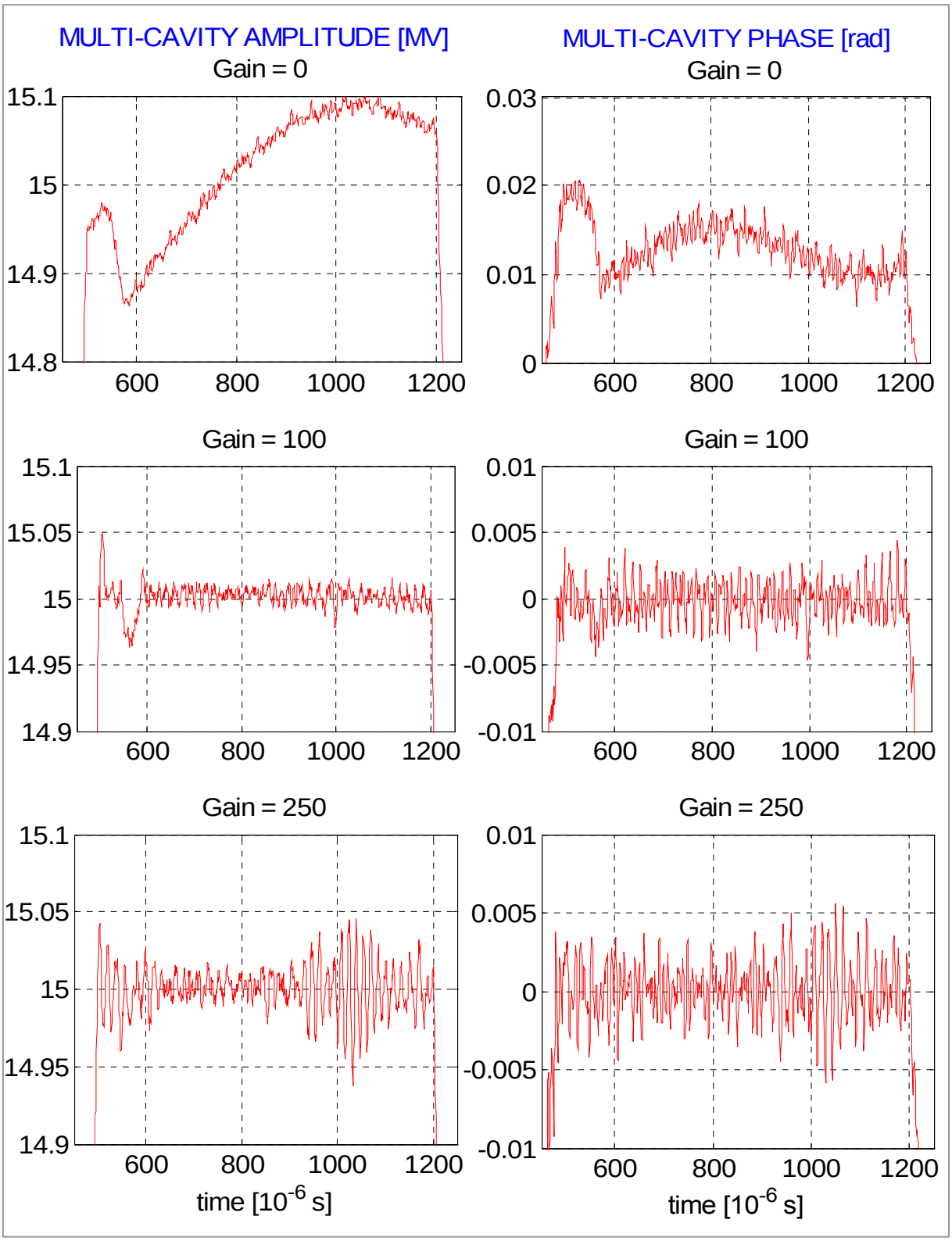


Fig. 6.5-11. The vector sum control of ACC1 8 cavities, influenced by the beam loading. The beam of 2 nC x 30 bunches (30 μs long) was injected in the beginning of the *flattop* range, at instance of 550 μs. The amplitude and phase charts, within zoomed *flattop* area, are selected for the following resonant loop gain values: $G_{L0}$ =: 0, 100, 250.

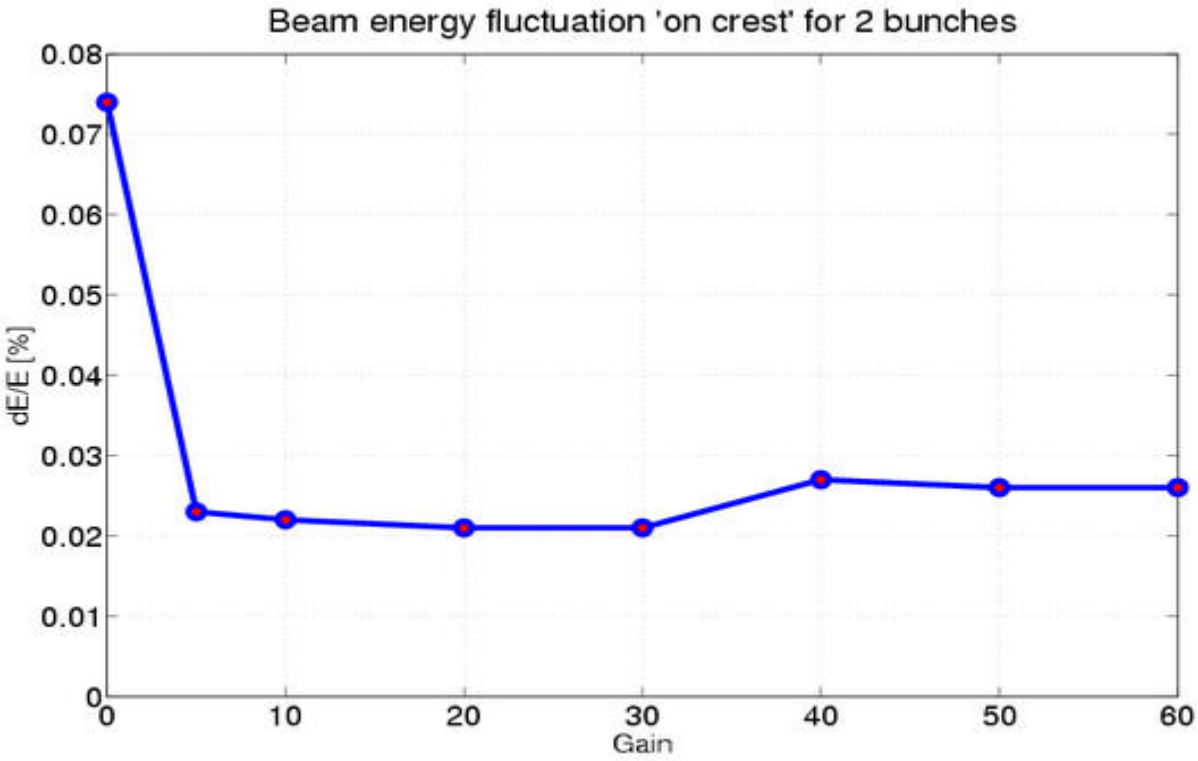


Fig. 6.5-12. The beam energy stability measured in the BC2 (*bunch compressor*), while operating “on crest”, versus resonant loop gain.

# 7. MULTI-CAVITY COMPLEX CONTROLLER

## 7.1. Multi-Cavity Complex Controller design

The Multi-Cavity Complex Controller (MCC) has been developed to investigate the optimal control methods for the LLRF system. The general concept of MCC is based on a novel firmware implementation and consists of two coordinated subsystems (fig. 7.1-1):

1. FPGA hardware layer (slave) – an actual controller, as a fast executor of the control algorithms. The cavity simulator, built in the same hardware platform, can be controlled, alternatively, instead of a real multi-cavity system.

2. MATLAB software layer (master) – an executive, arranging the control algorithms and supplementary procedures, providing control data and parameters for the controller.


Fig. 7.1-1. General idea of Multi-Cavity Complex Controller.

The control algorithms, introduced in chapter 5, determine the structure of the MCC system, which is presented in fig. 7.1-2. The FPGA-based controller executes a repeatable procedure of the feedback driving supported by feed-forward according to the prearranged control data loaded to the internal memories, called tables. The 8-channel multiplexer MUX switches the Test table, the Cavity Simulator, or ADC converters, as an input for the I/Q detector, respectively to a given mode of operation. A digital demodulation process applies a signal of the intermediate frequency 250 kHz for 8 channels. A detected *envelope* of the cavity voltage, represented by the [I, Q] components, is calibrated according to the given coefficients, by scaling and phasing of each channel. The vector sum, represented by the mean value over 8 channels, is filtered according to the filter factors (FIR or IIR) [38]. Consequently, the resultant, actual, multi-cavity output, is compared to the reference Set-Point creating an error signal. The Feedback unit, parameterized by Gain factors, has two modes of operation: by the differential inverse control according to fig. 5.4-1 and by the conventional feedback according to fig. 5.5-1. Superposition of the feedback signal and the signal of Feed-Forward table results in the controller output for the DAC converter.

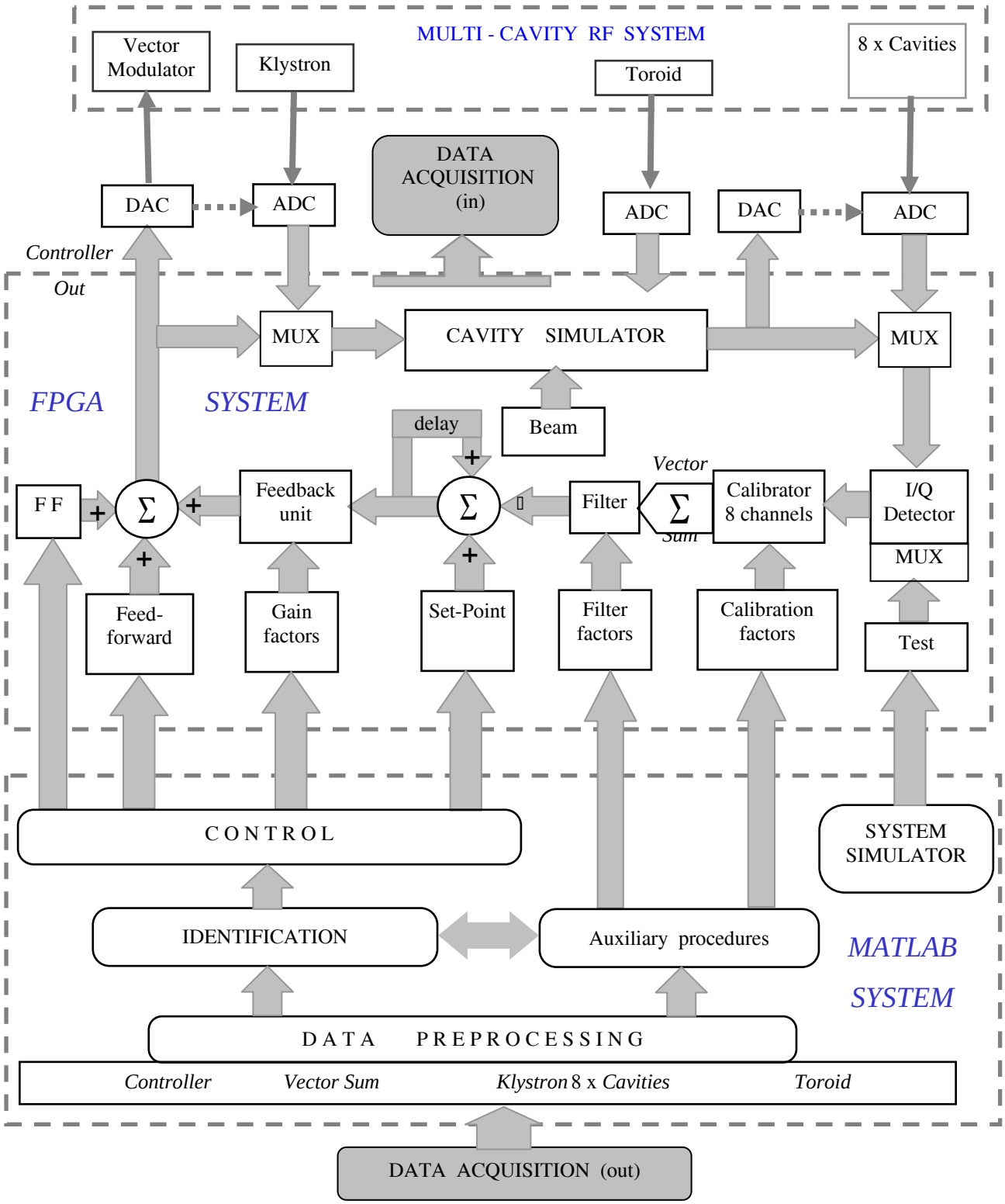


Fig. 7.1-2. The functional diagram of the Multi-Cavity Complex Controller.

The auxiliary feed-forward table FF is dedicated for compensation of deterministic additive disturbances: a beam loading and an input *offset* (caused by the DAC and vector modulator). The FPGA Cavity Simulator with Beam table (ref. to chapter 3) can be controlled by the internal or external modes of operation according to the MUX selection.

The Data Acquisition, implemented in an external RAM memory, acquires *on-line* data (in), during a pulse, from the selected internal channels (up to 64) of FPGA system. Subsequently, the data are read (out) from the RAM memory to MATLAB system. The main signals, related to the inputs or outputs of the Multi-Cavity subsystems and required for the control purpose, are as follows: controller output, multi-cavity output (vector-sum), klystron output, individual cavities and toroid signals.

The data *offline* processing is coded in 30 MATLAB files executed between pulses. The preprocessing of measured data includes the I/Q detection, calibration and smoothing by polynomial *splines* (ref. to Appendix). Preprocessed data are considered for the identification procedures, which comprise cavity parameters, klystron characteristics and beam loading identification. The auxiliary, but necessary procedures on request, include the input offset compensation, filter resolution, detuning adjustment, vector sum calibration, and the phase adjustment with respect to the beam. The control procedures arrange data for the set-point, gain and feed-forward tables according to the given control algorithms. Finally, the control data and parameters, after a proper scaling and formatting, are loaded to the internal registers of the FPGA based controller.

The System Simulator models the cavity and the controller processing, verifies the control algorithms and determines a reference pattern for FPGA implementation. In the diagnostic mode, the Test table and given control tables activate the controller, correspondingly to the reference process of System Simulator. The hardware readouts are compared with the software prototype. It is a necessary testing tool for the FPGA system development.

## 7.2. FPGA based integrated firmware engine

The integrated *firmware engine* for the controller and simulator system, called SIMCON, was realized in a form of modular, parameterized, connected structure of functional blocks in the VHDL (Very-high speed Integrated Circuit Hardware Description Language) design environment. A functional structure of the system was presented in fig. 7.2-1 [40].

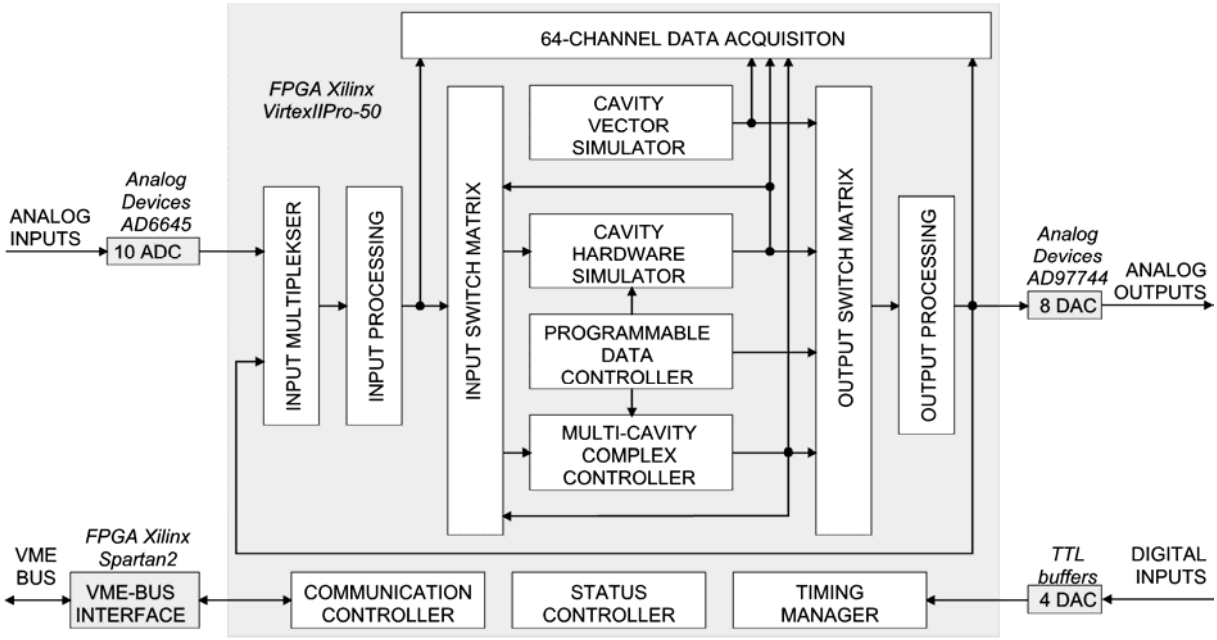


Fig. 7.2-1. Functional block diagram of the SIMCON *firmware engine* realized in VHDL.

The software engine services simultaneously ten 14-bit ADCs and eight DACs. The module TIMING MANAGER receives central clock signals of the accelerator and synchronizes the work of digital data processing channel of the LLRF system. The core of the system are the modules of MULTI-CAVITY COMPLEX CONTROLLER and CAVITY HARDWARE SIMULATOR. There were implemented hardware DSP algorithms based on fast, embedded multiplication 18x18 bit components. These components realize a single operation in 5ns. The parameters and control data are taken from the internal programmable registers and memory blocks called PROGRAMMABLE DATA CONTROLLER.

The communication and programming layer of all blocks in the SIMCON system is realized by the block COMMUNICATION CONTROLLER with a supervising computer system. The hardware based, data transmission channel, by VME-BUS protocol, is implemented in the block VME-BUS INTERFACE. The block INPUT MULTIPLEXERS provides a programmable choice of external ADC signals or internal data. The internal, digital

feedback loops may be realized due to the INPUT SWITCH MATRIX. The block OUTPUT SWITCH MATRIX provides the choice of signals output to DACs. The selected 64 internal signals are registered in the module of 64-CHANNEL DATA ACQUISITION.

***Communication INTERFACE between MATLAB and FPGA*** [40]

The software used to communicate with the controller was based on a client-server model, using TCP/IP network as a medium. During the tests, a TCP server was located on the SPARC CPU-56 computer embedded in the VME crate. As a client application, MATLAB has been used. To enable communication with the custom TCP server, it was necessary to write additional MATLAB Executable (MEX) modules.

Communication protocol has been designed to be textual, bi-directional, character stream. The protocol was made in a shell-like manner. It is possible to communicate with the server directly using only the telnet application, which is extremely useful for debugging. More complex client applications (MATLAB MEXes) have to emulate commands entered by the user, and parse human readable responses. This approach is easier than forcing the user to enter and understand binary content. The implementation of protocol engine on the server side was made using BISON and FLEX tools. This technology makes it possible to describe the protocol as a formal grammar, which makes the development and maintenance of the protocol easier. The server application is portable. Requirements for the platform to be able to host the server are following:

- C compiler
- POSIX threads (pthreads)
- BSD sockets implementation

These requirements are fulfilled on most (if not all) UNIX, Linux, and MS Windows systems. The presented solutions have been tested on the Linux, Solaris and MS Windows (the server has been tested on Linux and Solaris, while the MEX files has been tested on MS Windows, Linux and Solaris).

### 7.3. FPGA cavity simulator control

All control algorithms presented in chapter 5 have been verified by the System Simulator in MATLAB environment. Some of them were tested with the real accelerator by experimental studying of ACC1 module at FLASH system (ref. to chapter 6.5). A control process for the hardware cavity simulator, in the internal mode, is fully deterministic and, practically, copies the corresponding pattern process of the software System Simulator, in the 18-bit resolution version. But, the external mode of operation contributes to some analog uncertainty and offers a more realistic control conditions. So, all control algorithms have been reconsidered and verified applying FPGA cavity simulator in the external mode of operation. The scheme of testing circuit, corresponding to the real cavity control, is presented in fig. 7.3-1. The single cavity simulator is driven with the *controller* via DAC and ADC converters linked by cables. A digital complex modulation simulates the signal of intermediate frequency 250 kHz as a real part of the respective *analytic signal*. Modulated signals of the *klystron* and *cavity*, response to the controller via the DAC and ADC converters linked by cables.

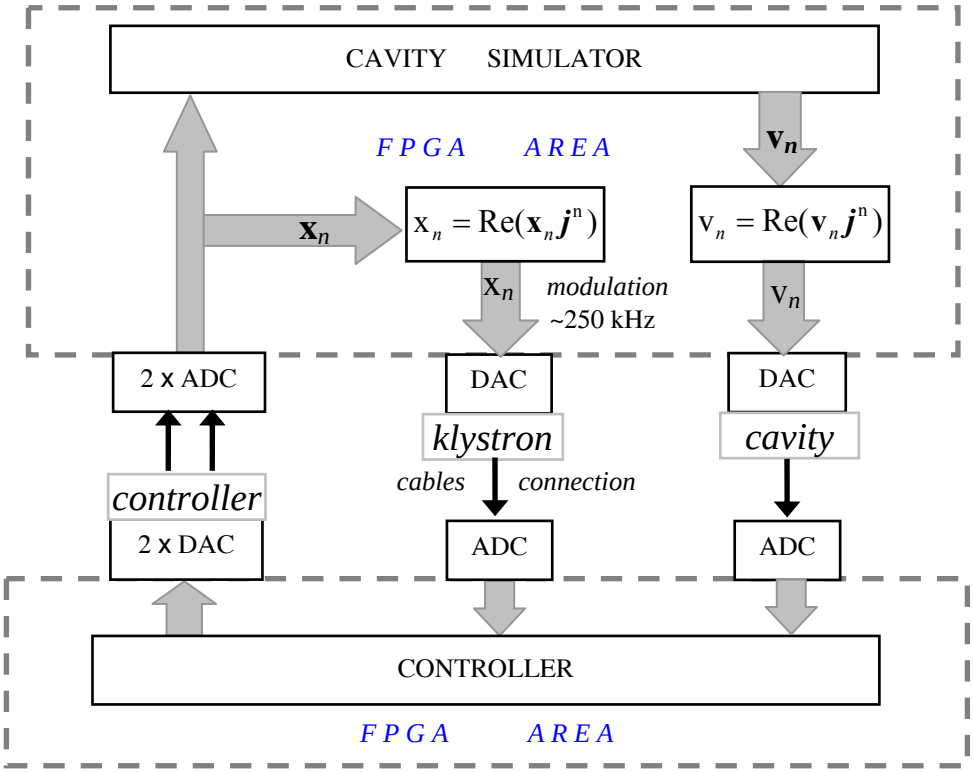


Fig.7.3-1. The scheme of testing circuit for the cavity simulator controlled in the external mode.

The cavity simulator driving has been carried out starting from the adaptive feed-forward by direct inverse control with the calibration procedure. The unknown, initial, cavity parameters have been taken arbitrarily. The cavity detuning within a pulse has been assumed as zero. The constant cavity driving with an exponential output has been chosen for the *filling* (500 μs) under the resonance condition. The required output has been set as equivalent to 20 MV level with zero phase within the *flattop* (800 μs) for the full range of 32 MV. The scaling factor C = 1.4107 has been established by the calibration procedure for the given internal cavity output. An initial phasing has no meaning for a single cavity without a beam and the phase has been set to zero rad. The value of *predetuning* has been set to 276 Hz according to the detuning adjustment procedure for the given stabilized *flattop* level. The simulation results, for the first three pulses of iteration, are presented in fig. 7.3-2, analogous to fig. 5.1-2. The main characteristics are plotted: cavity amplitude and phase, klystron amplitude and phase, cavity half-bandwidth and detuning. When the cavity output has started to fluctuate close to the ultimate state, the adaptive feed-forward, by differential inverse control, has been switched over. Finally, the feedback by differential inverse control has closed the loop, as the complex differential inverse control. The final results of simulation are presented in fig. 7.3-3. The main characteristics are plotted again: cavity complex envelope and phase with zoomed *flattop* area, klystron complex envelope and phase, cavity half-bandwidth and detuning for the real and estimated values. The cavity half-bandwidth has been estimated as ~4 Hz lower comparing to the constant actual value. However, the cavity detuning estimate fits quite well to the time-varying actual values.

The relative rms error for amplitude (~ $1.6 \cdot 10^{-4}$) and rms error for phase (~ $1.8 \cdot 10^{-4}$ rad) have been estimated separately for the *flattop* range. The relative mean error $\overline{\frac{\Delta v_c}{v_c^\bullet}}$ of *flattop*, as the mean of the absolute error $\Delta v_c = \left| \mathbf{v}_c^\bullet - \mathbf{v}_c \right|$, related to the absolute value of set-point $v_c^\bullet = \left| \mathbf{v}_c^\bullet \right|$ for the *flattop* range, is presented in figure 7.3-4, as a function of the pulse number, for the successive control processes. The errors are dominated by disturbances of the measurement channel. The noise rms of ADC converter, without input signal, was detected as ~ $6 \cdot 10^{-5}$, related to the 18-bit range.

Moreover, an efficiency of the adaptive feedback by differential inverse control is strongly limited by a nonlinear and unbalanced I/Q detector which causes alternately different delays for the I, Q-channels. In a case of time delay mismatch, between the plant and the

controller, the feedback signal is attenuated by the factor $\alpha = 0.3$ to keep the stability, in expense of an accuracy and a rate of convergence (ref. to 5.4-3). Additionally, the plant inverse is sensitive to high frequency noise, so the factor $f = 0.3$ has been set for the recursive filter (ref. to fig. 7.1-2).

Consequently, the conventional feedback supported by feed-forward seems to be a more reliable alternative of the cavity control. The relative mean error $\overline{\frac{\Delta v_c}{v_c^{\bullet}}}$ of *flattop* is presented in figure 7.3-5, as a function of the resonant loop gain for the conventional feedback supported by feed-forward control. The resonant loop gain $G_{L0} \approx 300$ has been reached for the stability limit, similarly like for a real multi-cavity system (ref. to fig. 6.5-10).

Adaptive feed-forward based directly on a feedback has been tested for a conventional case (ref. to 5.5-8) and differential inverse control (ref. to 5.4-2) giving similar results like for the autonomous feed-forward based on differential inverse control supported by the respective feedback. Generally, the subtle results diversity of the algorithms, tested in the Matlab system in chapter 5, is nearly lost by a noise of the measurement channel for the cavity simulator control.

***Beam testing***

An additional signal, from the FPGA memory table, has been switched on to the internal simulator input as the beam loading within the *flattop* range. The constant beam, which is unknown for the control system, has been set as equivalent to 6 mA of amplitude, which is close to the optimal value for the *flattop* energy efficiency (ref. to chapter 4.1). The adaptive feed-forward by differential inverse control, supported by a conventional feedback with resonant loop gain = 50, has been chosen for the beam loading compensation according to the procedure described in chapter 5.2. The following four stages of the simulation process are considered:

1. The stage before beam injection – the cavity output is stabilized according to the given set-point value for the *flattop*. Estimated cavity parameters and klystron output have been saved.

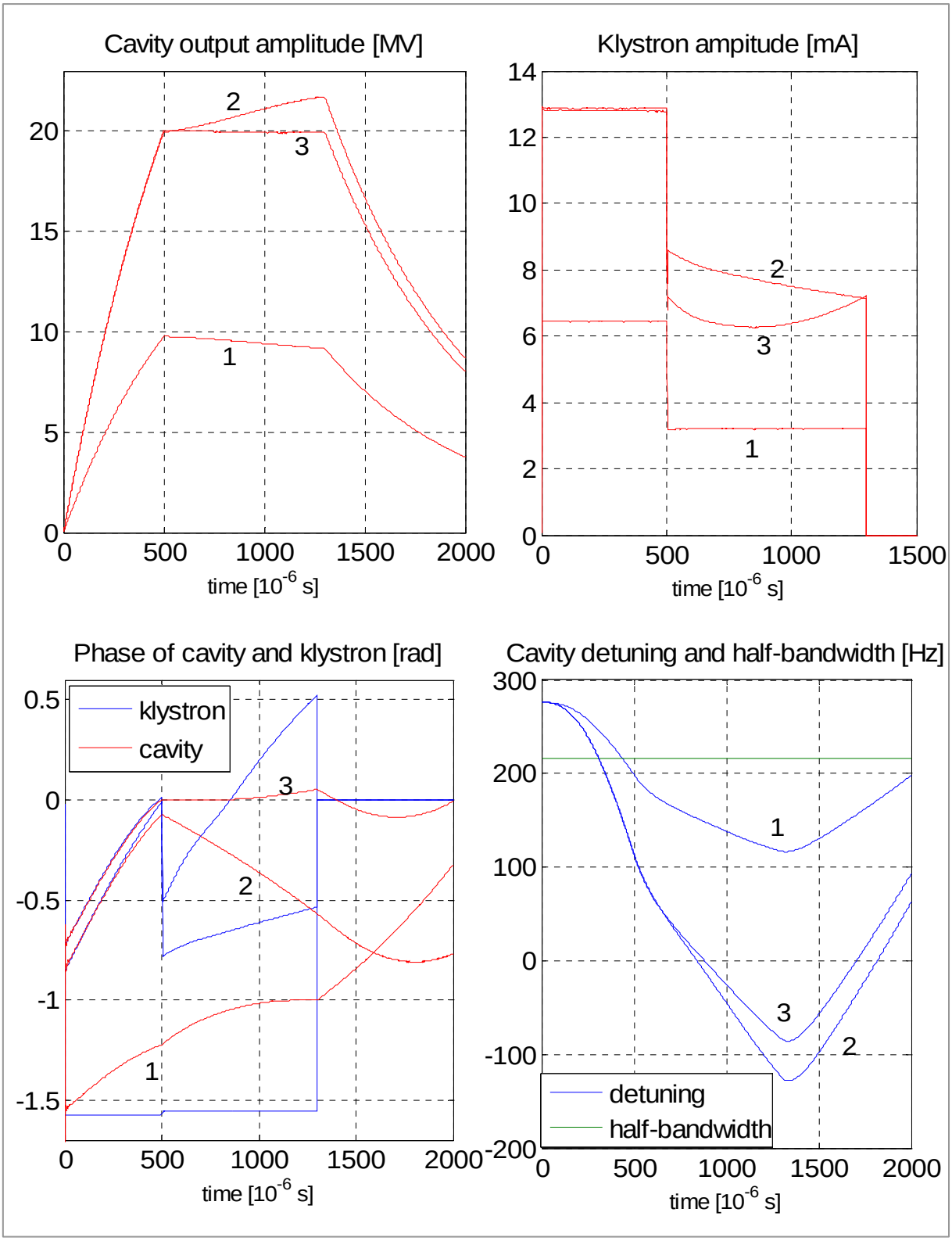


Fig.7.3-2. The cavity simulator control in the external mode by adaptive feed-forward driving. The main characteristics are plotted for the first three pulses of iteration: cavity amplitude and phase, klystron amplitude and phase, cavity half-bandwidth and detuning (actual values).

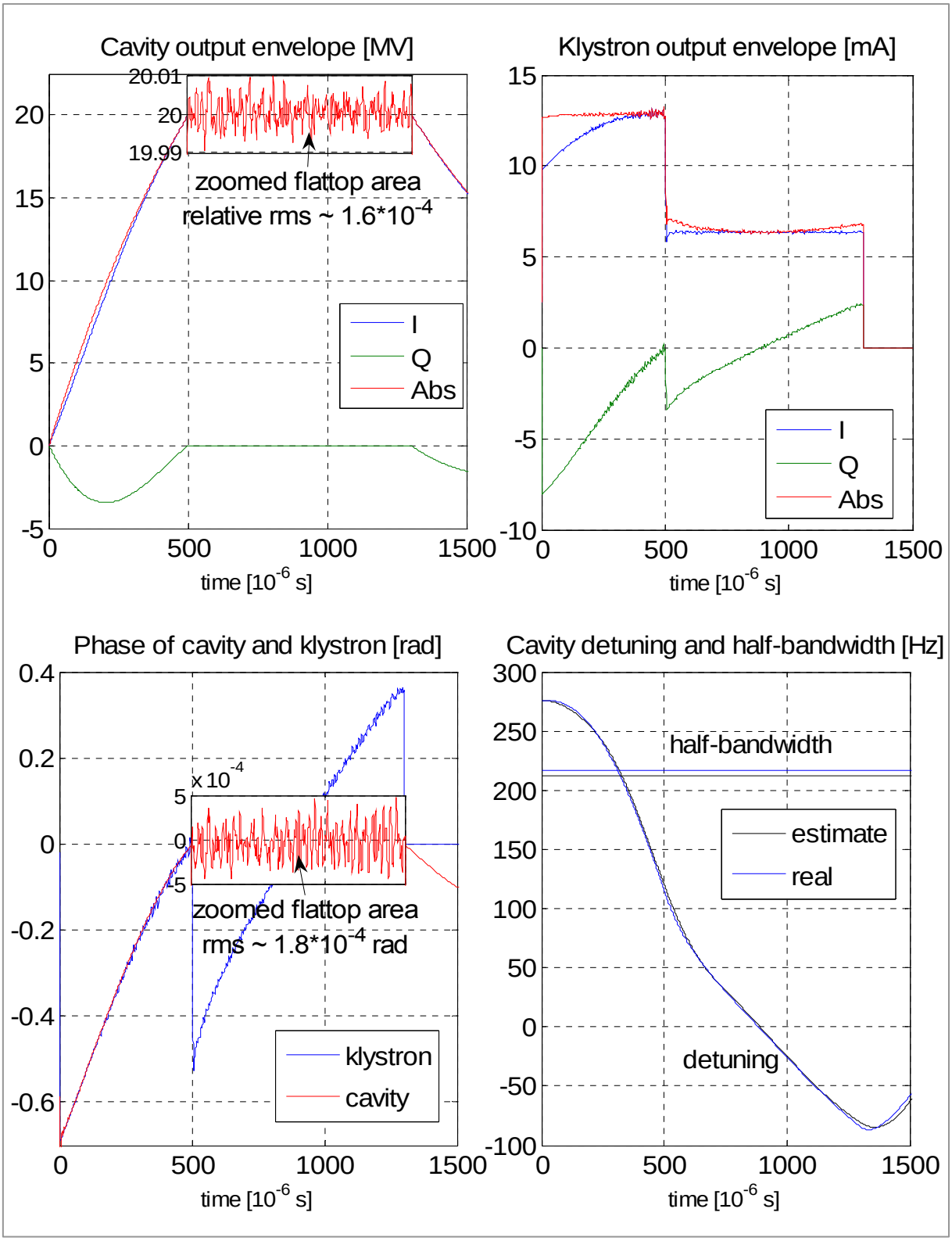


Fig.7.3-3. The final result of the cavity simulator driving by the complex differential inverse control. The main characteristics are plotted: cavity complex envelope and phase with zoomed *flattop* area, klystron complex envelope and phase, cavity half-bandwidth and detuning for the real and estimated values.

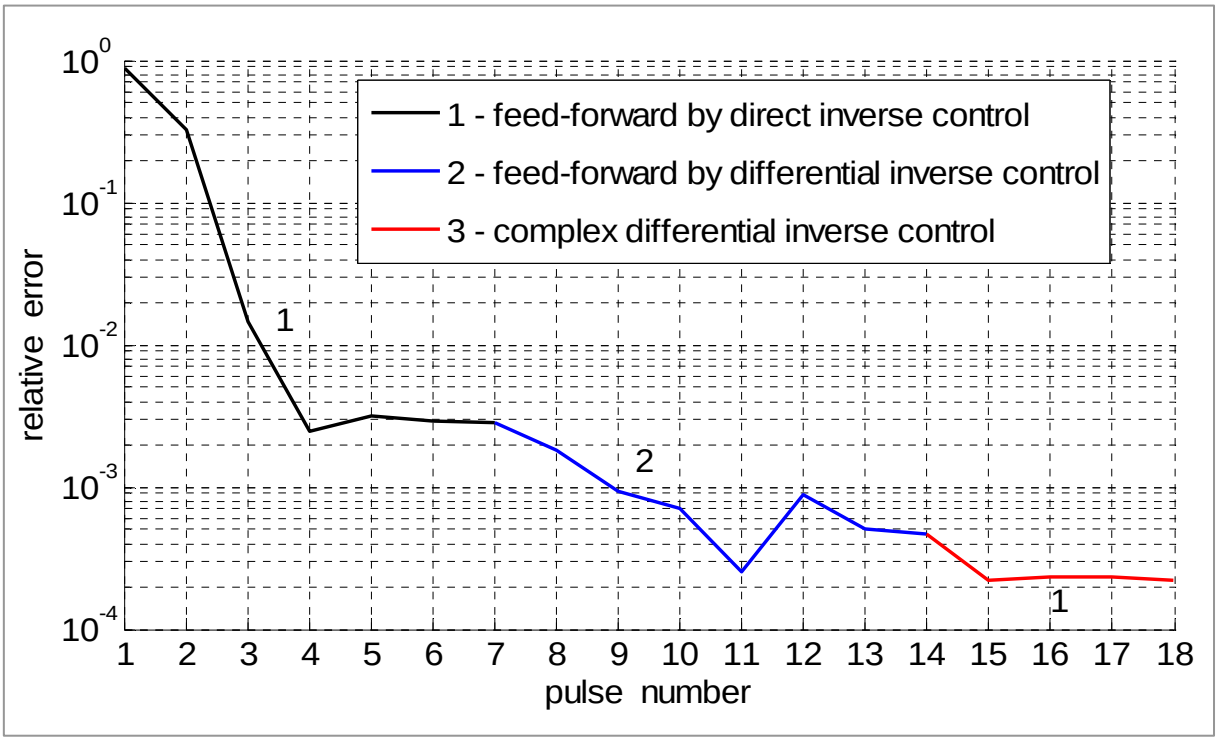


Fig. 7.3-4. The relative mean error of the *flattop*, as a function of the pulse number for the adaptive successive processes: 1 - feed-forward by direct inverse control, 2 - feed-forward by differential inverse control, 3 - complex differential inverse control.

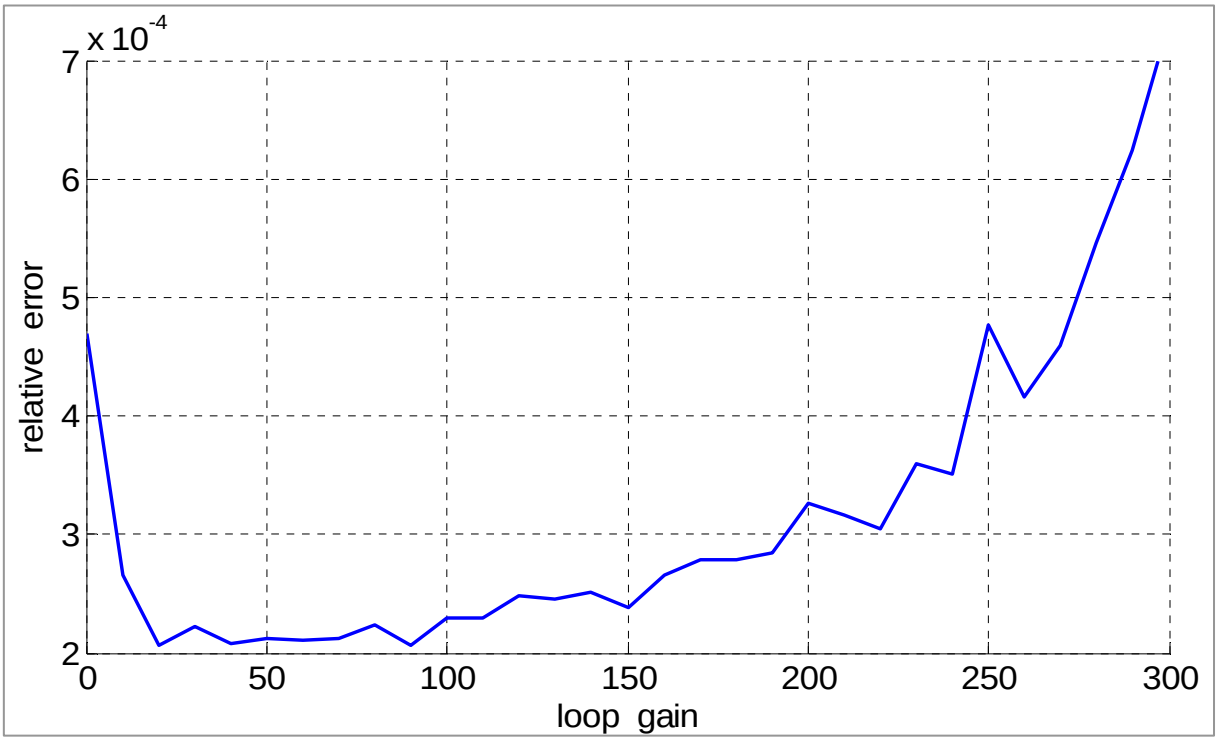


Fig. 7.3-5. The relative mean error of the *flattop*, as a function of resonant loop gain for the conventional feedback supported by feed-forward control.

2. The stage after beam injection – the iterative control process tries to compensate a sudden beam loading and the cavity state is recovered after several pulses of transient condition. Finally, the beam loading component has been estimated according to 6.2-15.

3. The stage after beam estimation and phase adjustment – the recognized beam component is adjusted to the reference phase value equal to zero, by the correction of the calibrator factor. The *flattop* set-point phase has not been changed for the relative beam phase equal to zero (injection *on crest*) (ref. to 6.3-7). But, the resultant input factor **B** (ref. to 6.1-9) has been changed respectively to the phase change of the calibrator factor **C**. Consequently, the cavity internal phase is adjusted with respect to the beam, after transient condition of the iterative control process.

4. The stage after beam stop – the iterative control process tries to decompensate a sudden disappearing of beam loading and the cavity state is recovered again after several pulses of the transient condition. But, the adjusted phase of the internal cavity output remains, ready for a next injection of a beam with the previous phase.

The results of the cavity simulator control with a beam equivalent to 6 mA of amplitude and 3 rad of phase are presented in fig. 7.3-6. The main characteristics are plotted as follows: cavity complex envelope and phase with zoomed *flattop* area, cavity half-bandwidth and detuning for the real and estimated values, klystron amplitude and phase for four stages with the stabilized cavity output: 1 – before beam injection, 2 – after beam injection, 3 – after beam estimation and phase adjustment, 4 – after beam stop. The relative rms error for the amplitude ($\sim 1.6 \cdot 10^{-4}$) and rms error for the phase ($\sim 1.6 \cdot 10^{-4}$ rad) have been estimated separately for the *flattop* range with the compensated beam loading.

The four stages of the simulation process are distinguished in figure 7.3-7 for the relative mean error $\overline{\frac{\Delta v_c}{v_c^{\bullet}}}$ of *flattop* against the pulse number. The maximum average deviation of amplitude reaches ~1% of the set-point value for the immediate beam loading changes.

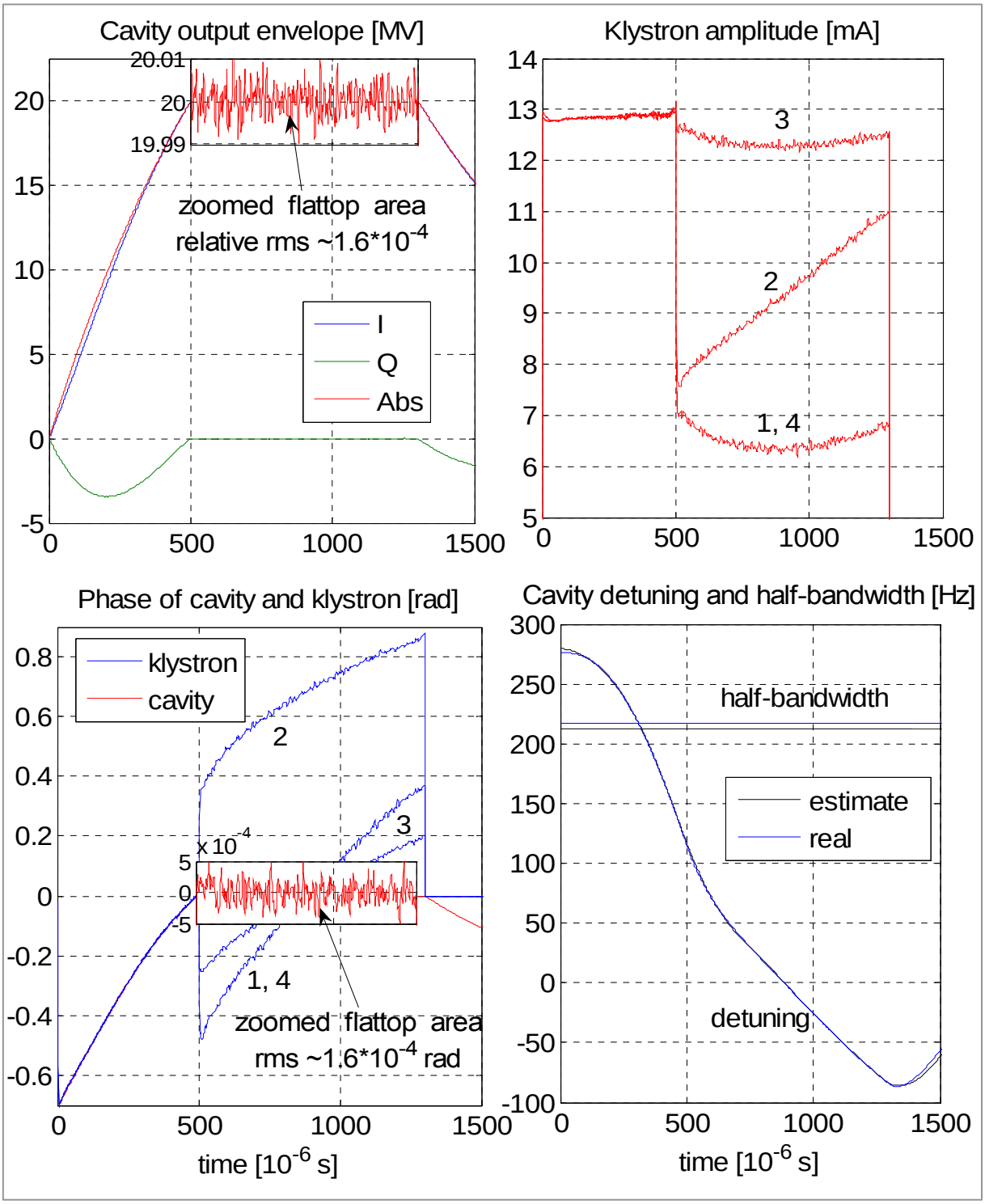


Fig.7.3-6. The results of the cavity simulator control with a beam equivalent to 6 mA of amplitude and 3 rad of phase. The main characteristics are plotted: cavity complex envelope and phase with zoomed *flattop* area, cavity half-bandwidth and detuning for the real and estimated values, klystron amplitude and phase for four stages with the stabilized cavity output: 1 – before beam injection, 2 – after beam injection, 3 – after beam estimation and phase adjustment, 4 – after beam stop.

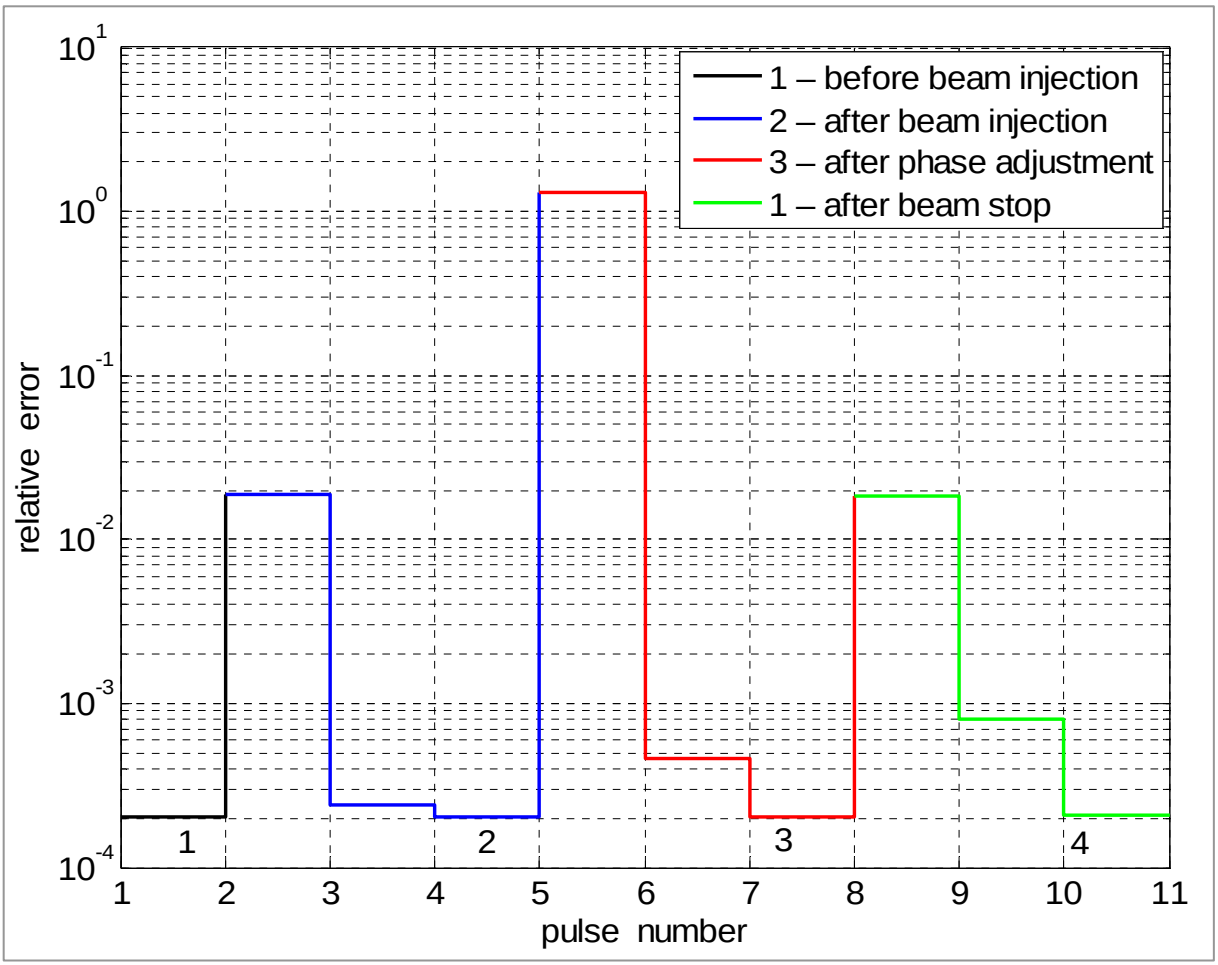


Fig. 7.3-7. The relative mean error of the *flattop*, as a function of pulse number for the successive control processes: 1 – before beam injection, 2 – after beam injection, 3 – after beam estimation and phase adjustment, 4 – after beam stop.

Similar results have been obtained by the complex differential inverse control, but with a gradual change of a beam to avoid under- and over-driving of the cavity simulator for the immediate beam loading changes.

The beam test has been repeated for the same amplitude but with different beam phases. An accuracy of the phase adjustment with respect to the beam depends on a beam component estimation (ref. to 6.2-15) and differs for diverse beam phases. A mean error of the phase adjustment has been estimated as $\sim 4 \cdot 10^{-3}$ rad.

*Phase adjustment by forward energy evaluation*

An alternative method of the phase adjustment with respect to the beam is based on the estimation of the forward energy expended during the *flattop* range as a function of the relative beam phase. The expended energy reaches maximal value for the beam injection *on crest*, so the relative beam phase is zero, on the condition of optimal detuning adjustment (average detuning is zero over the *flattop* range). In the proposed experiment, the beam component to be estimated is compensated for different phases of the reference value (set-point) selected in the vicinity of the expected optimum. The phase of the beam component equals to the respective reference phase, if the relative beam phase is zero (ref. to 6.3-6) . The simulation results are presented in fig. 7.3-8 for a beam phase $\angle \mathbf{u}_b = 0$ rad corresponding to the actual beam component phase $\angle \mathbf{C}\mathbf{u}_b = -\pi/2 \approx -1.571$. The relative expanded energy has been approximated by a parabolic curve within the range of $(-2 \div -1)$ rad of the set-point phase. The phase for the maximum value is estimated as $-1.533$ rad. The analogous evaluation by the primary method (ref. to 6.2-15) gives the value of $-1.566$ rad, what is much better estimation for that case.

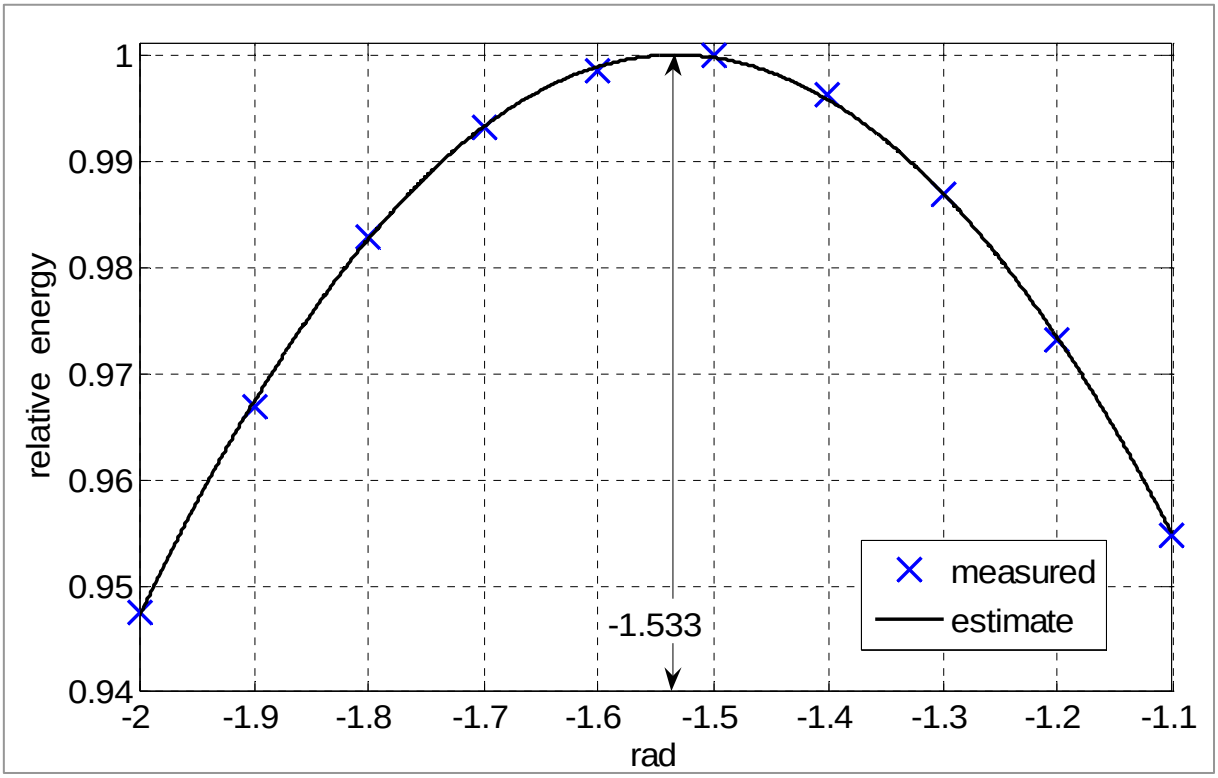


Fig. 7.3-8. The relative expanded energy approximated by a parabolic curve as a function of the set-point phase. The estimated maximum value corresponds to the zero rad of the relative beam phase.

# 8. SUMMARY

The cavity control system for the superconducting linear accelerator project is introduced in this thesis. Digital control of the superconductive cavity has been performed by applying FPGA technology system. The theoretical and experimental investigations focused their attention on the general identification of the cavity system characteristics and designed control methods. All of the most significant aspects have been carefully examined for the control purpose.

The standard electrical model of the single cavity has been reconsidered and verified. The signal model, based on the *complex envelope* concept, has been introduced and applied accordingly for all considerations. The multi-cavity model of the total system has been originally developed for the vector sum calibration and control. The deterministic phenomena of the first order have been carefully considered, consequently with the presented model. The control criteria, based on the energy efficiency, have been introduced. The optimal conditions for the *filling* and *flattop* ranges have been originally established. The original methods of the system identification have been presented and verified for the real plant, leading to the efficient control algorithms. Parameter identification algorithm was incorporated into the control system development. The time varying cavity detuning has been estimated by polynomial *splines*. The synthesis of the *spline* functions has been developed originally with general continuity conditions for polynomials of any degree.

Calibration and correction of the signal path are considered for the efficient driving of the multi-cavity system. Identification of the resonator parameters has been proven to be a successful approach in achieving the required performance, i.e. driving on the resonance during *filling* and the field stabilization during *flattop* time, while requiring reasonable levels of the power consumption. The feed-forward and feedback modes were successfully applied in operating of the cavity. Original methods by the differential inverse control have been introduced. Representative results of the experiments are presented for the typical operational condition.

A design of the digital controller, as the main part of the Low Level RF system, for superconducting cavities of a linear accelerator is presented. The FPGA based controller, supported by MATLAB system, was developed to investigate a novel firmware implementation. The complex control algorithm based on the time varying system identification is the proposal verified by the preliminary experimental results. The general

solution is implemented as the Multi-Cavity Complex Controller (MCC). The FPGA based controller executes the procedure according to the prearranged control tables: Feed-Forward, Set-Point and Feedback unit, to assure the required cavity performance. The adaptive control algorithm is applied for the feed-forward and feedback modes. The System Simulator and the testing procedures have been developed for an efficient verification of the FPGA controller structure.

All presented control algorithms have been verified in MATLAB environment. Some of them were tested by experimental studying of the real accelerator. Preliminary application tests of FPGA controller have been carried out using the superconducting cavity in the vertical CHECHIA laboratory setup in DESY. The cavity was driven with the feed-forward and feedback modes. Analogous, but more comprehensive, experiments have been repeated on the ACC1 module of the VUV-FEL (FLASH), and on remotely controlled FNPL Photo Injector cavity module at FERMILAB (USA). The achieved relative stabilization is $\sim 2 \cdot 10^{-4}$ for the amplitude and $\sim 9 \cdot 10^{-4}$ rad for the phase of the high-power RF accelerating signal. The adaptive feed-forward, by direct inverse control supported by conventional feedback, has been applied for the vector sum control of 8 cavities without a beam.

All the described control algorithms have been reconsidered and verified applying the FPGA cavity simulator in the external mode of operation. The beam testing has been carefully investigated including the phase recognition and adjustment. The best results have been achieved applying the adaptive feed-forward by differential inverse control supported by conventional feedback with the resonant loop gain equaled to 50. The experiments have offered quite reliable conditions for simulating of a real accelerator environment.

# APPENDIX

## ESTIMATION BY POLYNOMIAL SPLINES

Polynomial *spline* is defined by a linear combination of M base functions $\{w_m(t)\}$ with constant coefficients $\{\alpha_m\}$ as follows

$$w(t) = \sum_{m=1}^{M} \alpha_m w_m(t) , \tag{A-1}$$

where the base functions $w_m(t)$ are defined *piecewise* by the polynomials in separated intervals bounded by time points called the knots.

This kind of series is useful for estimation of measured signals by smoothing and for estimation of semi-signals, which are not measured directly, like the signal derivatives and time varying parameters.

A signal or a parameter, represented by the column vector of digital data $\mathbf{y} = \{y_n\}$, for n = 1:N, is approximated by a corresponding vector of the polynomial *spline* $\mathbf{w} = \{w(n)\}$, expressed in a matrix form

$$\mathbf{y} \cong \mathbf{w} = \mathbf{W} \cdot \boldsymbol{\alpha} , \tag{A-2}$$

where $\mathbf{W} = \{\mathbf{w}_m\}$ is N x M matrix of column vectors $\mathbf{w}_m = \{w_m(n)\}$, representing the polynomial base functions, and $\boldsymbol{\alpha} = \{\alpha_m\}$ is a column vector of M coefficients.

The classical *spline* type of degree $k$ , used in numerical analysis, has continuity $C^{k-1}$, which means that every two adjacent polynomial pieces meet in their value and first $k - 1$ derivatives at each knot.

The more general conditions of continuity or discontinuity in the given knots are considered for the series (A-1) and its time derivatives. All derivatives of the series (A-1) create new series of base functions, which are also *splines* of lower degrees, respectively. The simplest *spline* has the degree 0, what suggests the recovery of *antiderivatives* by successive integration starting from the step function.

***Base function synthesis by multiple integration***

The general assumptions for currently considered polynomial *spline* of *k*-th degree, denoted by $w^k$, are:

- *spline* $w^k$ is not continuous in the given discontinuity knots $\{n_j^k\}$, for j = 0: $J^k$,
- the knots $\{n_j^k\}$ determine $J^k$ the continuity ranges $\{n_{j-1}^k + 1 : n_j^k\}$, for j = 1: $J^k$ .

The proposed generation of base functions initiates from the "bottom", using *splines* of zero degree. These fundamental base functions consist of arbitrary constant values, within the consecutive continuity ranges determined by the knots $\{n_j^0\}$. An initial number of base functions is $M = J^0$. Generally, the synthesis of a *spline* of a higher degree is followed by the discrete integration of current base functions, independently within the given continuity ranges. The procedure is described iteratively for the *spline* of *k*-th degree within the given continuity range for the m-th base function

$$w_m^k(n) = \sum_{p=n_{j-1}^k+1}^{p=n} w_m^{k-1}(p) \quad \text{for} \quad n \in \left\{ n_{j-1}^k + 1 : n_j^k \right\}, \tag{A-3}$$

and for the resultant *spline* function

$$w^k(n) = \sum_{m=1}^{M} \alpha_m w_m^k(n) + \alpha_{M+1} c_{M+1} = \sum_{m=1}^{M+1} \alpha_m w_m^k(n), \tag{A-4}$$

where a value of formal product $\alpha_{M+1}c_{M+1}$ is a resultant constant of integration for an undetermined initial condition. An arbitrary constant value $c_{M+1}$ creates a next M+1 base function $w_{M+1}^k(n)$, determined within the given continuity range for $n \in \left\{ n_{j-1}^k + 1 : n_j^k \right\}$, and $\alpha_{M+1}$ is a parameter of a next M+1 degree of freedom. This integration proceeds for each *j*-th continuity range, for j = 1: $J^k$, increasing the number M of base functions (degrees of freedom) by one for each range. The number M of the base functions does not change, if an initial condition is set to zero for a given range. Finally, the previous *spline* $w^{k-1}$ becomes a derivative of the current *spline* $w^k$. The final number of the base functions is $M = \sum_{i=0}^{k} J^i$ for the *spline* of *k*-th degree. It is the minimal basis, assuming the undetermined initial conditions for all continuity ranges, which satisfies the required continuity conditions for the *spline* of k-degree and its all derivatives.

***Application for the cavity control system by estimation of signals, derivatives and time-varying parameters.***

The polynomial *spline* functions have been applied for estimation of typical data measured in the real accelerator by experimental studying of ACC1 module at FLASH system (ref. to chapter 6.5).

Taking into consideration the perturbed, measured data **y**, approximated by a *spline* $\mathbf{w} = \mathbf{W} \cdot \boldsymbol{\alpha}$ (ref. to A-2), the optimal solution for the coefficients **α**, with the minimal norm $\|\mathbf{y} - \mathbf{w}\|$, satisfies the orthogonal condition expressed by the scalar product:

$$(\mathbf{W}\boldsymbol{\alpha})^{\mathrm{T}} \cdot (\mathbf{y} - \mathbf{W}\boldsymbol{\alpha}) = 0\,, \tag{A-5}$$

where index "T" means, generally, a conjugate transpose. Excluding condition **α** = **0**, the final solution for approximated, smoothed data $\hat{\mathbf{y}} = \mathbf{w}$ is given by

$$\hat{\mathbf{y}} = \mathbf{W}\left(\mathbf{W}^{\mathrm{T}}\mathbf{W}\right)^{-1}\mathbf{W}^{\mathrm{T}}\mathbf{y}\,. \tag{A-6}$$

According to the LS method, it is the unique solution for the over-determined set of equations (A-2), where, in a practical application, N>>M.

Applying an orthogonalization process for the vectors $\{\mathbf{w}_m\}$ of the matrix **W** (e. g. by Gram–Schmidt method [27]), the expression (A-5) is simplified, for the orhonormal matrix **W**, as follows

$$\hat{\mathbf{y}} = \mathbf{W}\mathbf{W}^{\mathrm{T}}\mathbf{y}\,. \tag{A7}$$

The *splines* of different degrees have been tested for *offline* smoothing of the complex envelope for vector sum control of the multi-cavity setup. Some examples are selected below.

The complex envelope estimation by the *spline* of zero degree (k = 0) is presented in fig. A-1. The set of discontinuity knots is $\{n_j^0\}$ = {0, 200, 400, 500, 600, 800, 1000, 1200, 1500, 2000}, and the number of base functions is $M = J^0 = 9$.

The complex envelope estimation by the *spline* of first degree (k = 1) is presented in fig. A-2. The set of discontinuity knots is $\{n_j^1\}$ = {0, 2000}, and the number of base functions is $M = J^0 + J^1 = 10$.

The complex envelope estimation by the *spline* of second degree (k = 2) is presented in fig. A-3. The set of discontinuity knots is $\{n_j^1\}$ = {0, 500, 1200, 2000} ($J^1 = 3$) for the first derivative and $\{n_j^2\}$ = {0, 2000} ($J^2 = 1$) for the final *spline*. The number of base functions is $M = J^0 + J^1 + J^2 = 13$.

The complex envelope estimation by the *spline* of the third degree (k = 3) is presented in fig. A-4. The set of discontinuity knots is $\{n_j^1\}$ = {0, 500, 1200, 2000} ($J^1 = 3$) for the second derivative, $\{n_j^2\} = \{n_j^1\}$ ($J^2 = 3$) for the first derivative and $\{n_j^3\}$ ={0, 2000} ($J^3 = 1$) for the final *spline*. The number of base functions is $M = \sum_{i=0}^{3} J^i = 16$.

The complex envelope estimation by the *spline* of the third degree and all derivatives of {I,Q} components are presented in fig. A-5. The *spline* and its derivatives are continuous in the required ranges, stated above, respectively.

Multi-cavity phase and detuning estimation by the *spline* of the third degree are presented in fig. A-6. Estimation of the detuning for total range is compared with the detuning estimated as a phase derivative within the *decay* range. (ref. to chapter 6.2).

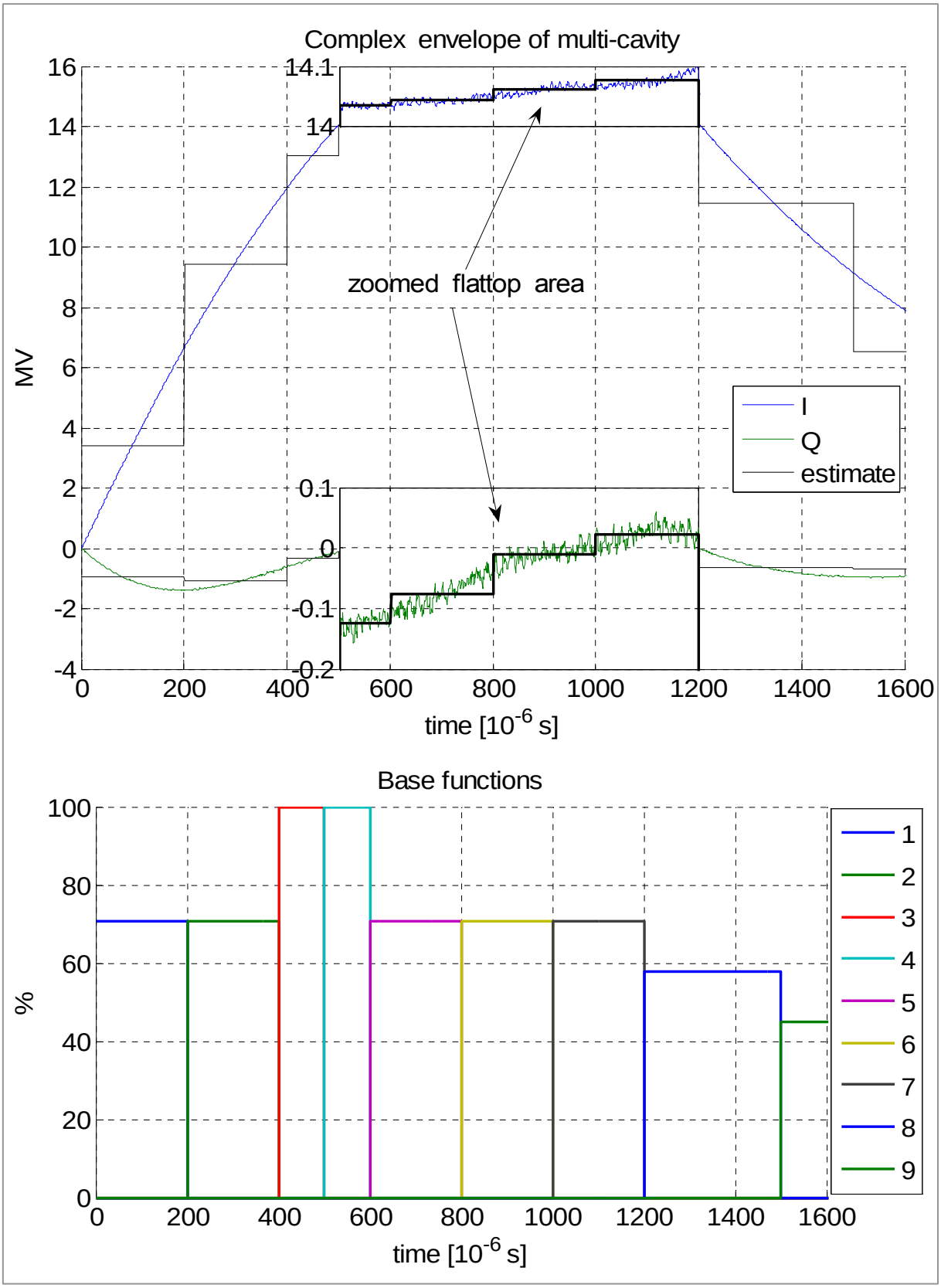


Fig. A-1. Complex envelope estimation by *spline* composed of 9 orthonormal base functions of zero-th degree.

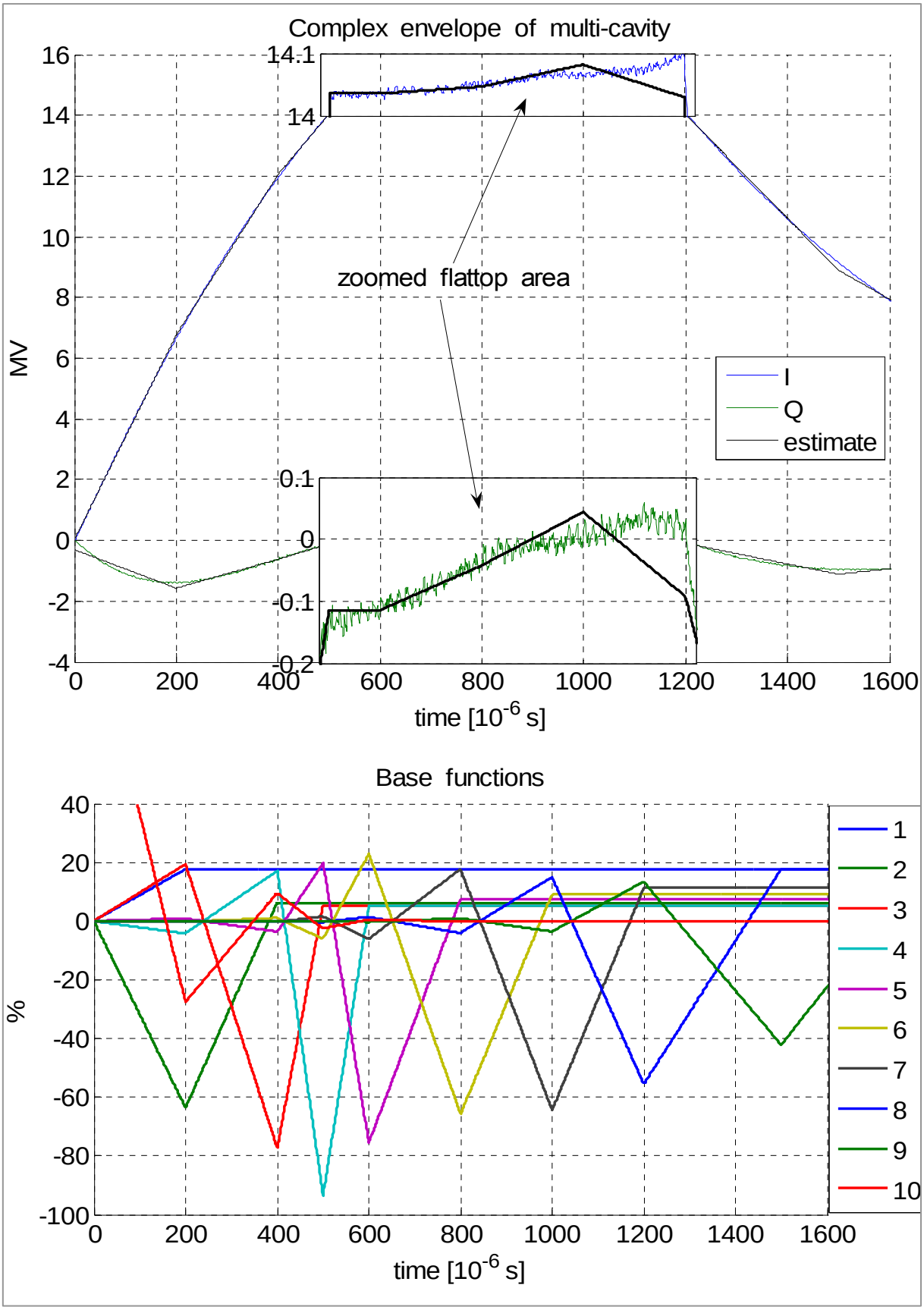


Fig. A-2. Complex envelope estimation by *spline* composed of 10 orthonormal base functions of first degree.

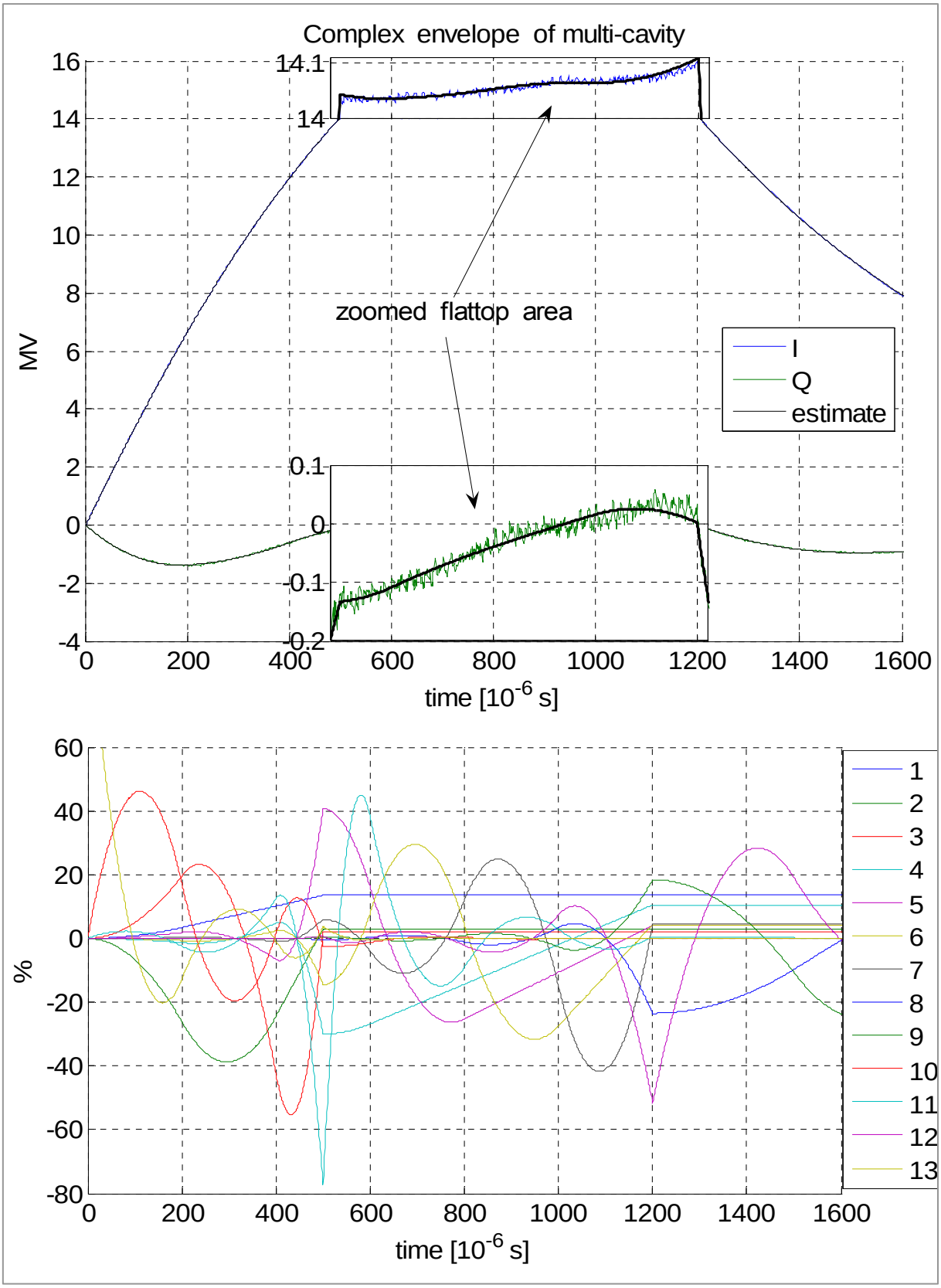


Fig. A-3. Complex envelope estimation by *spline* composed of 13 orthonormal base functions of second degree.

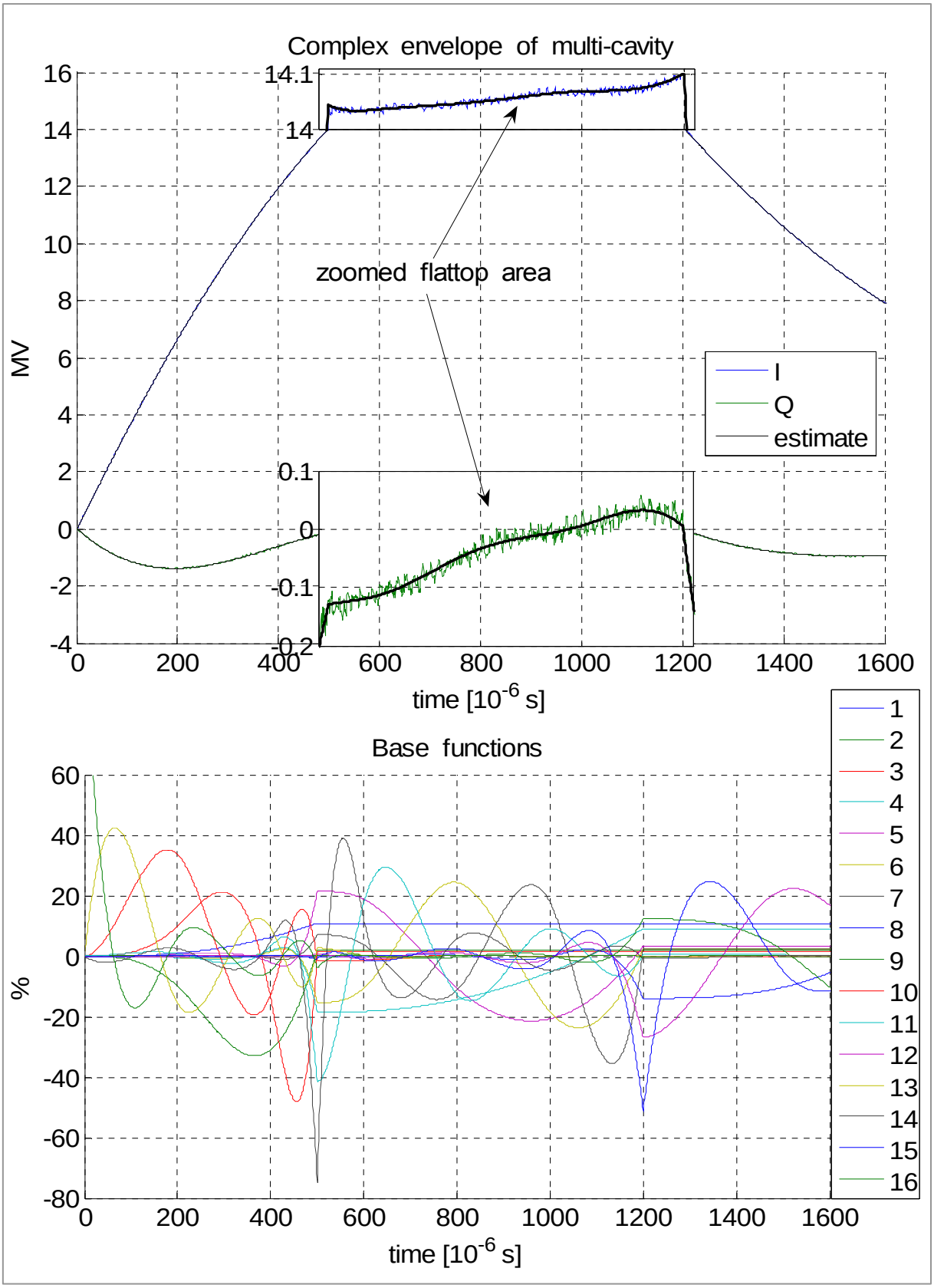


Fig. A-4. Complex envelope estimation by *spline* composed of 16 orthonormal base functions of third degree.

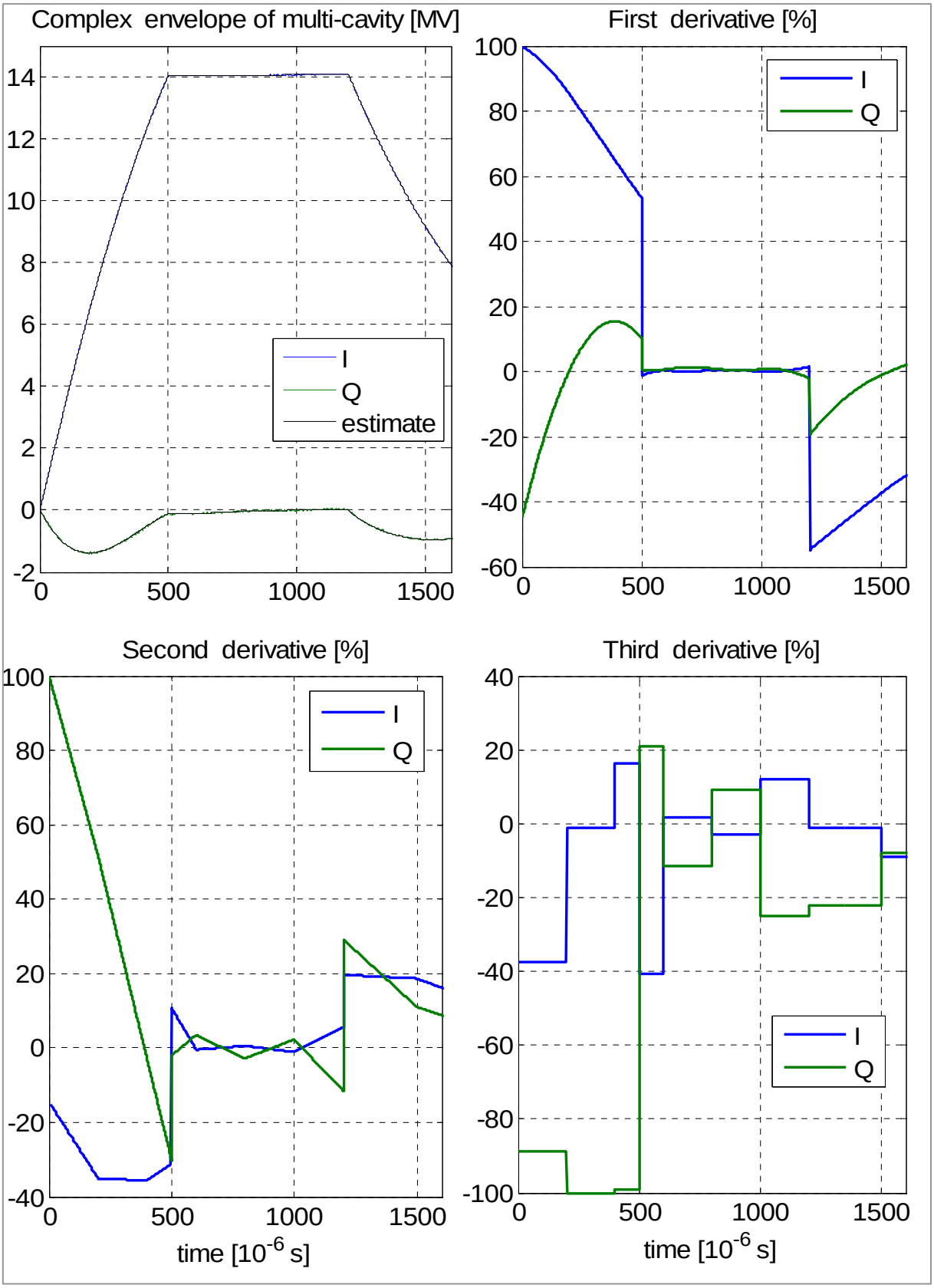


Fig. A-5. Complex envelope estimation by *spline* of third degree and all derivatives of {I, Q} components.

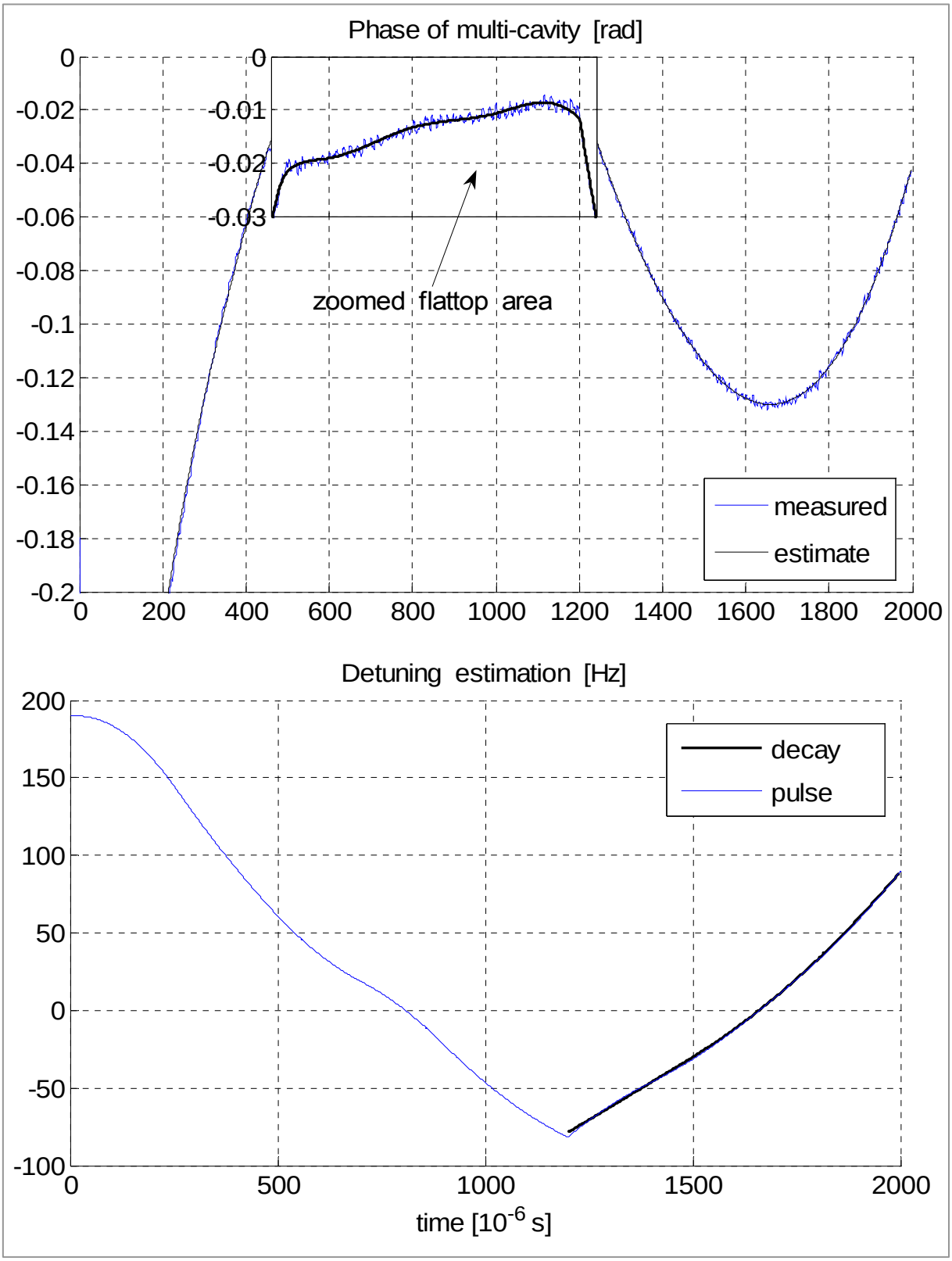


Fig. A-6. Multi-cavity phase and detuning estimation by *spline* of third degree. Estimation of the detuning for total range (pulse) is compared with the detuning estimated as a phase derivative within the *decay* range.

## REFERENCES


1. R.S.Romaniuk, K.Poźniak, T.Czarski, *Research activities within a frame of the CARE of Warsaw University of Technology,* Elektronika, Vol. XLVI, No. 2-3, 2005, pages 75 and II cover; (in Polish)
2. The European X-Ray Free Electron Laser *Technical Design Report*, July 2007, http://xfel.net
3. International Linear Collider, *Reference Design Report* (Draft), February 2007, http://media.linearcollider.org/rdr_draft_v1.pdf
4. TESLA *Technical Design Report*, Part II - The accelerator, March 2001 http://tesla.desy.de/new_pages/TDR_CD/start.htmlT.
5. J. Andruszkow et al. *First Observation of Self-Amplified Spontaneous Emission in a Free-Electron Laser at 109 nm Wavelength*, Physical Review Letters , Vol. 85, N. 18, 30 October 2000
6. W. Ackermann, at al. *Operation of a free electron laser from the extreme ultraviolet to the water window*, Nature Photonics vol. 1, 336 – 342,2007
7. A.H. Hofler**,** V. Ayvazyan, A. Brandt, S. Simrock, T. Czarski, J. R. Delayen, T. Matsumoto, *RF Control Modelling Issues for Future Superconducting Accelerators,* LINAC 2004 – Proceedings Lübeck, Germany, pp.180-182
8. Valeri Ayvazyan et al. *DSP-based Low Level RF Control as an Integrated Part of DOOCS Control System*, Proceedings of EPAC 2006, Edinburgh, Scotland, pp1450-2
9. S N Simrock, *Measurement for Low Level RF control Systems*, Measurement Science and Technology, 18 (2007), pp. 2320-2327
10. K.T.Pozniak, T.W.Czarski, R.S.Romaniuk, *System pomiarowo-kontrolny dla nadprzewodzącej, mikrofalowej wnęki rezonansowej akceleratora TESLA i europejskiego lasera XFEL,* Kwartalnik Elektroniki i Telekomunikacji PAN, Vol. 51, No 1, 2005, pp. 175-210
11. J. Sekutowicz, *TESLA superconducting accelerating structures*, Measurement Science and Technology, 18 (2007), pp. 2285-2292
12. S. Simrock and L. Merminga, *Radio Frequency Systems*, CEBAF, January 1994

13. T. Schilcher, *Vector Sum Control of Pulsed Accelerating Fields in Lorentz Force Detuned Superconducting Cavities*, Ph. D. thesis, Hamburg, 1998.

14. J. Szabatin, *Podstawy teorii sygnałów*. WKiŁ, Warszawa, wyd. 3, 2000.

15. Bracewell, R. *The Fourier Transform and Its Applications*, 2nd ed, 1986, McGraw-Hill.

16. J.C. Slater, *Microwave Electronics,* D. Van Nostrand Company, Inc. Princeton, New Jersey, USA, 1950

17. M. Liepe, W.D.-Moeller, S.N. Simrock, *Dynamic Lorentz Force Compensation with a Fast Piezoelectric Tuner,* in Proc. of the 2001 PAC Conference, Chicago, pp 1074-76

18. O. Kugeler , W. Anders, J. Knobloch, A. Neumann, *Microphonics Measurements in a CW-driven TESLA-type Cavity,* Proc. of EPAC 2006, Edinburgh, pp. 405-407

19. H. Gassot, *Mechanical Stability of the RF Superconducting Cavities*, Proc. of EPAC 2002, Paris, pp 2235-37

20. G. K. Davis, J. R. Delayen, *Piezoelectric Tuner Compensation of Lorentz Detuning in Superconducting Cavities*, Proc. of PAC 2003, Portland, pp. 1383-85

21. Przemysław Sękalski, *Smart Materials as Sensors and Actuators for Lorentz Force Tuning System,* Ph. D. thesis, Technical University of Łódź, Poland 2007

22. G. Devanz, P. Bosland, M. Desmons , E. Jacques, M. Luong, B. Visentin, *Compensation of Lorentz Force Detuning of a TTF 9-cell Cavity with a New Integrated Piezo Tuner*, Proc. of EPAC 2006, Edinburgh, Scotland, pp 378-380

23. T. Czarski, R.S. Romaniuk, K.T. Pozniak, and S. Simrock: *TESLA cavity modeling and digital implementation in FPGA technology for control system development*, Nuclear Instruments and Methods in Physics Research Section A: Accelerators, Spectrometers, Detectors and Associated Equipment -Volume 556, Issue 2, 15 January 2006, Pages 565-576.

24. A. Mosnier, SOLEIL, Gif/Yvette (France), *RF feedback systems for SC cavities*, www.cern.ch/accelconf/e98/PAPERS/WEZ02A.PDF

25. K.T. Pozniak, T. Czarski, R. S.Romaniuk, *Functional Analysis of DSP Blocks in FPGA Chips for Application in TESLA LLRF System*, TESLA Technical Note, 2003-29, DESY

26. K.T. Pozniak, R.S. Romaniuk, K. Kierzkowski, *Parameterized Control Layer of FPGA Based Cavity Controller and Simulator for TESLA Test Facility*, TESLA Technical Note, 2003-30, DESY

27. David G. Luenberger, *Optimization by Vector Space Methods*, 1969 John Wiley and Sons, Inc.

28. Zdzisław Bubnicki, *Teoria i algorytmy sterowania,* PWN, Warszawa 2002

29. Jacek Kudrewicz, *Analiza funkcjonalna dla automatyków i elektroników*, PWN, Warszawa 1977

30. T. Czarski, W. Koprek, K. Poźniak, R. Romaniuk, S. Simrock, A. Brandt, B. Chase, R. Carcagno, G. Cancelo, T. Koeth, *Superconducting Cavity Driving with FPGA Controller*, Nuclear Instruments and Methods in Physics Research Section A: Accelerators, Spectrometers, Detectors and Associated Equipment – Volume 568, Issue 2, 1 December 2006, Pages 854-862.

31. Bernard Widrow, Eugene Walach, *Adaptive inverse control*, Prentice Hall, New Jersey

32. A. Brandt, *Development of a finite state machine for the automated operation of the LLRF control at FLASH*, Ph. D. thesis, Hamburg, 2007.

33. T.Czarski, *Modelowanie i sterowanie wneką rezonansową akceleratora TESLA*. Elektronika, Vol. XLVI, No. 7, 2005, pages 65-68.

34. Tomasz Czarski, *Modelowanie systemu strerowania nadprzewodzącej wnęki rezonansowej akceleratora liniowego*; Kwartalnik Elektroniki i Telekomunikacji PAN, Vol. 52, No 4, 2006, pp 643-653.

35. T. Czarski, R.S. Romaniuk, K.T. Pozniak, S. Simrock: *Cavity parameters identification for TESLA control system development,* Nuclear Instruments and Methods in Physics Research Section A: Accelerators, Spectrometers, Detectors and Associated Equipment -Volume 548, Issue 3, 21 August 2005, Pages 283-618

36. Tomasz Czarski, *Superconducting cavity control based on system model identification***,** Measurement Science and Technology 18 (2007), pp. 2328-2335.

37. P.Pawlik, M.Grecki, S.Simrock, *System for high resolution detection of beam induced transients in RF signals*, Proceedings of Mixdes 2005, Kraków

38. Tomasz Stanisławski, *Metody odzyskiwania sygnału obwiedni zespolonej w eksperymencie XFEL z wykorzystaniem filtrów o skończonej odpowiedzi impulsowej*. Diploma thesis, Warszawa, luty 2009.

39. Tomasz Czarski; *Multi-Cavity Complex Controller for Low Level Radio Frequency System,* 2008-01-22 - FLASH Seminar; DESY http://flash.desy.de/meetings

40. T. Czarski; K.T. Pozniak; R.S. Romaniuk; J. Szewinski, *Multi-cavity complex controller with vector simulator for TESLA technology linear accelerator*, Proceedings of SPIE vol. 6937.